The Pennsylvania State University
The Graduate School

# GENERAL RELATIVISTIC HYDRODYNAMIC SIMULATIONS OF NEUTRON STAR MERGERS: FROM QUARKS TO GRAVITATIONAL WAVES

A Dissertation in
Physics
by
Aviral Prakash



Submitted in Partial Fulfillment
of the Requirements
for the Degree of

Doctor of Philosophy

August 2024

The dissertation of Aviral Prakash was reviewed and approved by the following:

David Radice
Assistant Professor of Physics and Astronomy & Astrophysics
Dissertation Advisor
Chair of Committee

B.S. Sathyaprakash
Elsbach Professor of Physics and Professor of Astronomy and Astrophysics

Steinn Sigurðsson
Professor of Astronomy and Astrophysics

Zoltan Fodor
Professor of Physics

Mauricio Terrones
George A. and Margaret M. Downsbrough Department Head, Evan Pugh University Professor, Professor of Chemistry and Materials Science and Engineering

# Abstract

With the advent of gravitational wave astronomy, it has become possible to study mergers of compact objects such as neutron stars in a new window of gravitational radiation. Gravitational waves carry imprints of the nuclear makeup of these compact objects which can be revealed in a merger. Such mergers can be studied in simulations and their observations (gravitational or electromagnetic) can help constrain the available models of nuclear physics. In this dissertation, we employ general relativistic neutrino-radiation hydrodynamic simulations of mergers of neutron stars, with a particular focus on understanding QCD phase transitions to deconfined quarks. To this aim, we compute gravitational wave signatures of such phase transitions and find that they manifest as an increase in a postmerger spectral frequency of the neutron star merger remnant. This increase, however, is modest at best for the equation of state employed. Additionally, the frequencies are degenerate with merger simulations of neutron stars with exclusively nucleonic (confined quarks) degrees of freedom. We also propose a multi-modal gravitational wave signature, in that, a non-detection or a detection of a feeble one-armed spiral instability in a merger remnant could point to the presence of phase transitions.

Further, we explore mergers of strange stars which are self-bound compact objects but find that the gravitational wave signatures of their mergers are difficult to distinguish from mergers of other neutron stars. We then examine thermal effects in a merger simulation of neutron stars and study their influence on the postmerger gravitational wave emission. In a Bayesian inference study, we find that at postmerger signal-to-noise ratios of 15, the next generation of gravitational wave detectors could potentially constrain such thermal effects. Next, we examine gravitational wave emission from multiple models of QCD phase transitions in a fully consistent Bayesian inference study and find that the next generation of gravitational wave detectors can reliably identify and distinguish particularly strong QCD phase transitions at postmerger signal-to-noise ratios as low as 10. Finally, we provide some important insights into how specific choices of constructions of phase transition models can manifest themselves in ways which could only be revealed in such simulations making numerical relativity an indispensable tool for the science cases of the next generation of gravitational wave detectors.

# Table of Contents

# List of Figures

# List of Tables

# Acknowledgements

At the very outset, I would like to express my deepest gratitude to my Ph.D. supervisor and mentor Prof. David Radice. I am deeply indebted to him for his resourcefulness, infinite patience (which I have tested many a time), excellent unbiased guidance and most importantly showing me how to inspire by action. Thank you David for instilling in me respect, not only for one's work but also for one's time. Apart from research, I have also learned valuable lessons in time management - most notably the Pomodoro (Italian for tomato) technique. I will however say that I am still working on my definition of 'management'. I remember, David once remarked that good coders are often very lazy as they write shell scripts to automate a lot of their workflow. I believe I have taken very seriously to the first piece of his advice.

I would also like to thank Prof. B.S. Sathyaparakash, Prof. Steinn Sigurðsson, and Prof. Zoltan Fodor for serving on my dissertation committee. Their valuable comments on my dissertation and their assistance, while I navigated through my graduate program, were instrumental in completing the requirements of my Ph.D. I also take this opportunity to thank the faculty members of the Institute for Gravitation and the Cosmos (IGC) which was my professional home for the last 5 years. In particular, Prof. Abhay Ashtekar whose many comments during my presentations have served to enhance my understanding of physics, Prof. Eugenio Bianchi for the excellent course on advanced general relativity and last but not least, Prof. Sarah Shandera under whose leadership, IGC offers a very stimulating atmosphere to grow both scientifically and professionally. A special vote of thanks to Prof. B.S. Sathyaparakash, 'Sathya' for countless scientific discussions, abundant help with data analysis, and showing me how to do back-of-the-envelope calculations which I have seen carried out everywhere right from his blackboard to a piece of tissue at Federal Taphouse. I thank him for being so warmly welcoming be it in his research group or dinners at his house and finally for being the go-to person to talk about life.

A special mention to all my professors from the first year of grad school: Prof. Dezhe Jin, Prof. Jorge Sofo, Prof. Irina Mocioiu, Prof. Chaoxing Liu, Prof. Cui-Zu Chang, and Prof. David Weiss who strengthened my foundation in the graduate physics curriculum through their many homework sets. A vote of thanks also to Prof. Richard Robinett and Prof. Irina Mocioiu for streamlining any administrative hurdles I faced. I express my deep gratitude to Prof. Miguel Mostafa for being my 'non-academic' mentor and showing me how to achieve a fantastic work-life balance. Just as before, I am still working on

my definitions of 'work', 'life', and most importantly 'balance'. The acknowledgments to professors are incomplete without mentioning Prof. Daniel Costantino and Prof. Michael Smitka, both of whom helped me grow as a teacher through my assignments with them as a teaching assistant.

I would then like to thank profusely the staff at the Physics department, in particular, Juli Mortimore who was, in ways more than one, a life-saver for all things administrative, Randi Neshteruk, Nicholas Mateer and Natasha Urabik for providing me all assistance when managing finances for travel and conferences, and finally, Melissa Diamanti for her help in getting my office space.

I express my gratitude to my collaborators Prof. Ignazio Bombaci, Prof. Domenico Logoteta, Prof. Sebastiano Bernuzzi, Prof. Albino Perego, and Dr. Matteo Breschi for their many inputs on my work and the years of fruitful collaboration. A shout-out to the members of the Numerical Relativity and CMA groups at Penn State: Estuti, Yi, Francesco, Rahul, Pedro, Jacob, Alireza, Maitraya, Mainak, Mukul, José, Abhishek, Kohta, Tetyana, Rossella, Andrew, Harshraj, Matt, Eduardo, and Peter.

I thank professors from my time as an undergraduate at IIT Madras, JNCASR and BIT Mesra, most importantly Prof. Chandra Kant Mishra 'Chandra', Prof. Sunethra Ramanan and Prof. Subir K. Das. If it were not for their constant encouragement and references, I would not have pursued my graduate studies at the time that I did. To Prof. Suresh Govindarajan, Prof. G. Aravind, Prof. S. Lakshmi Bala, Prof. V. Balakrishnan, Prof. S. Kasiviswanathan, Prof. Pattabiraman Murari 'Pattu', Prof. Jim Libby, Prof. Umesh Waghmare, Prof. Meher K. Prakash, Prof. Dawood Kothawala, Prof. Rahul Sharma, Prof. Arun A. Somasundaram and Prof. Swapan Konar, I express my deep gratitude for teaching me everything I know about science.

My flatmates Anirban, Rishabh and Ish deserve a special token of gratitude for bearing with me all these years and cooking super-delicious and at times super-pungent food. I would also like to acknowledge my cohort which formed an excellent support group. In particular, Divya, Becca, Rachael, Ruobing, Da, Mark, Dan, Ziggy, Kokkimidis, Kevin, Autumn, Bohan, Peng, Eli, Gavin, and Max, all of them have my deep affection. My friends from IGC: Ish, Sanika, Daniel, Monika, Arnab, Neev, Ssohrab, and Mauricio, all will always be remembered fondly. It is with great fondness that I also acknowledge my friends from BIT Mesra and IIT Madras, in particular, Pappa, Siddhu, Suraj, Shirsh, Penguin, Himanshu, Pandit, Mallesh, Lodoe, Anirban, Anof and Anand for keeping my sanity when life became stressful. This is the group that refuses to grow up, if growing up is ever an alternative, except for Penguin who has grown up too much.

I shall also be forever grateful to the Adventures Club at Penn State and in particular Danny Williams for instilling in me a deep sense of thrill towards white water rafting and exposing me to the natural beauty that is Pennsylvania. I shall forever remember the life-saving lesson, 'when in rapids, nose and toes'. A vote of thanks to the Shotokan Karate club at Penn State: Willard, Jake, Shabnam and Aditya as well as members of the RUF Fellowship who very graciously welcomed me to their dinners. A shout out to Matthew Wheaton for being a cherished friend in this regard. I would be remiss in my acknowledgements if I did not thank the excellent staff and doctors at the University

Health Services who have always been so kind and helpful to me.

My parents: Mr. Sajal Prakash and Mrs. Anvita Srivastava, whom I have missed dearly throughout my graduate studies and who were always there for me no matter what, to them, I express my love. I also thank my wonderful partner Vaishnavi for her love and affection, her help in maneuvering the copyright issues with this dissertation and especially for suffering me when I am predominantly insufferable.

Finally, to almighty for always keeping an eye out for me and blessing me with all the wonderful people I have mentioned above.

Numerical Relativity simulations presented in this dissertation were performed on PSC Bridges-2 (NSF XSEDE allocation TG-PHY160025), Comet, TACC's Stampede2 (NSF XSEDE allocation TG-PHY160025), SDSC Expanse (NSF XSEDE allocation TG-PHY160025) and NSF/NCSA Blue Waters (NSF AWD-1811236) supercomputers. Simulations for this research were also performed on the Pennsylvania State University's Institute for Computational and Data Sciences' Roar supercomputer. The simulations presented in this dissertation used resources from the National Energy Research Scientific Computing Center, a DOE Office of Science User Facility supported by the Office of Science of the U.S. Department of Energy under Contract No. DEAC02-05CH11231.

This material is based upon work supported by the U.S. National Science Foundation (NSF) under Award No. 2011725. Any opinions, findings, and conclusions or recommendations expressed in this publication are those of the author and do not necessarily reflect the views of the U.S. National Science Foundation (NSF).

In addition, I would also like to acknowledge support from Pennsylvania State University's Department of Physics in the form of several fellowships. These fellowships include the David C. Duncan Graduate Fellow Scholarship in Physics (2024), the Dr. John Randall Shuman Troxell Memorial Scholarship in Physics (2023), and the Edward A. and Rosemary A. Mebus Graduate Fellowship in Physics (2022).

# Chapter 1
# Introduction

## 1.1 Relativistic Hydrodynamics

A merger of binary neutron stars (BNS) is one of the most energetic events in the cosmos, emitting copious amounts of energy in gravitational waves [1], short gamma-ray bursts (GRB), and kilonovae [2] that may outshine entire galaxies. It should come as no surprise that modeling such violent phenomena is one of the most challenging problems in computational astrophysics. One of the reasons why such mergers are so interesting is that they offer a scenario wherein all 4 fundamental forces of physics play a decisive role. To say that integrating the physics of all 4 forces and their manifestations in a simulation is extremely non-trivial, is no exaggeration.

Modeling such mergers is also a problem that holistically encompasses unparalleled time and length scales across which these phenomena occur. For instance, one may go from the sub-femto meter ($< 10^{-15}$m) length scales in studying the dynamics of sub-atomic particles like protons, neutrons, electrons, and quarks that make up the composition of neutron star matter to studying gravitational wave radiation on astronomical length scales hundreds of Mpc ($\sim 10^{24}$m). On one hand, one may encounter neutrino interactions taking place on the sub-microsecond timescale and on the other hand, an afterglow evolution from a neutron star merger on the time scale of up to years.

The strong nuclear force, governing the interactions between quarks that make up neutrons and protons manifests itself in the nuclear equation of state (EoS). Its influence can be particularly pronounced when neutron star interiors or the remnants of their mergers probe extreme temperatures ($\sim 10^{11} - 10^{12}$ K) and densities (several times the nuclear saturation density of $2.7 \times 10^{14}$g cm$^{-3}$). Under such conditions, it is conceivable that quarks and gluons that were confined within hadrons such as protons and neutrons can undergo a transition into a phase of deconfined quarks where the boundaries between

individual hadrons diminish, much like the situation of conducting electrons in a lattice. This dissertation is a small step toward exploring the dynamics of such a phase transition and the possible consequences it may have.

Other forces such as the weak nuclear force influences the radiation transport of neutrinos and manifests in out-of-equilibrium effects encountered in the bulk of a merger remnant. At large length scales, the weak nuclear force affects the properties of neutron star matter ejected in such a merger such as their composition or entropy. It may also impact electromagnetic signatures resulting from a radioactive decay of such ejecta. Neutron stars are also one of the strongest magnetized objects in the universe with typical magnetic field strengths $\gtrsim 10^{12}$G. The electromagnetic force thus plays a decisive role in the magnetohydrodynamics of the neutron star plasma as well as in the aftermath of a merger e.g. properties of relativistic jets, short GRBs, etc.

Finally, all of the above takes place within the purview of extremely strong gravity, necessitating a description in the language of general relativity. As a result, the primary equations to solve for a consistent description of BNS mergers are those of general-relativistic neutrino-radiation magnetohydrodynamics, a problem that is as daunting as its name. Throughout this dissertation, however, we are going to make several simplifying assumptions. Most notably, our simulations of neutron star mergers are devoid of magnetic fields which is a reasonable assumption if we are not interested in the large-length scale phenomena such as the launching of jets or short GRBs. On a short ($\sim$ 5km) length scale corresponding to the size of a neutron star's core, magnetic fields are not expected to produce extreme effects [3]. Our simulations solve for general relativistic hydrodynamics with approximate neutrino transport wherein, instead of solving for the full Boltzmann equation, we only solve for the $0^{\text{th}}$ and $1^{\text{st}}$ moments of the distribution function.

This chapter begins with a quick summary of the preliminary concepts from general relativity and then the 3+1 decomposition of spacetime is described. Following this, the general relativistic framework of hydrodynamics is presented which, together with the equations for the evolution of spacetime, forms the backbone of our simulation infrastructure. Then, a detailed overview of the neutron star EoS models is provided that culminates in a description of QCD Phase transitions. We finally conclude this chapter with a brief introduction to the methods of neutrino radiation transport.

### 1.1.1 Preliminaries from General Relativity

We will commence with a scant description of the fundamental concepts from general relativity while pointing the reader to excellent references for their perusal that include but are not limited to [4–6]. Within the theory of general relativity (GR), space and time are placed on an equal footing and treated as dimensional facets of the same object called 'spacetime', the properties of which are described by tensorial quantities e.g. metric, curvature, etc. An important attribute of tensors and tensorial equations derived within the framework of GR is their covariance which means that upon changing a coordinate system, the tensors and the forms of tensor equations remain unchanged even though the tensor's components themselves may be modified. This is an important fact because only those quantities may qualify as measurables by observation or experiment that do not change with the choice of a particular coordinate system or gauge.

As is customary in numerical relativity literature, the alphabets $a-h$ and $o-z$ are used for the indices of a 4-dimensional spacetime and range from 0-3 whereas the alphabets between $i-n$ are reserved for spatial indices ranging between 1-3.

We begin with the most fundamental tensor of all encountered in general relativity which is the metric tensor $\vec{\vec{g}}$. The metric provides a quantitative measure of the distance between two points (called events) in a curved spacetime along a curve $\mathcal{C}$. In other words,

$$\int_{\mathcal{C}} ds = \int_{\mathcal{C}} (g_{ab} dx^a dx^b)^{1/2} \tag{1.1}$$

wherein we have also assumed Einstein's summation convention over repeated indices. Another useful quantity that is related to the first derivative of the metric is called the Christoffel Connection $\Gamma$ whose components are given by

$$\Gamma^c_{ab} = \frac{1}{2} g^{cd} \left( \partial_a g_{db} + \partial_b g_{ad} - \partial_d g_{ab} \right) \tag{1.2}$$

With this definition in mind, we can proceed to define the covariant derivative in curved spacetime for a contravariant vector and its dual one-form as

$$\begin{aligned} \nabla_a A^b &= \partial_a A^b + \Gamma^b_{ac} A^c \\ \nabla_a A_b &= \partial_a A_b - \Gamma^c_{ab} A_c \end{aligned} \tag{1.3}$$

Analogously, we can define the same operation on a mixed rank-2 tensor $\vec{\vec{T}}$ like

$$\nabla_a T^b_c = \partial_a T^b_c + \Gamma^b_{ad} T^d_c - \Gamma^d_{ac} T^b_d \tag{1.4}$$

We remark here that the covariant derivative operator $\nabla$ is metric compatible meaning $\nabla_a g_{bc} = 0$. Next, we define the Reimann curvature tensor which measures the local curvature of the spacetime as

$$R^a_{bcd} = \partial_c \Gamma^a_{bd} - \partial_d \Gamma^a_{cb} + \Gamma^a_{ec} \Gamma^e_{bd} - \Gamma^a_{fd} \Gamma^f_{bc} \tag{1.5}$$

Contractions of the Riemann tensor are also very useful and are given by the Ricci tensor and the Ricci scalar which are respectively defined as

$$R_{ab} = R^c_{acb} = \partial_c \Gamma^c_{ab} - \partial_b \Gamma^c_{ac} + \Gamma^c_{ab} \Gamma^d_{cd} - \Gamma^c_{ad} \Gamma^d_{bc} \tag{1.6}$$

and

$$R = R^a_a = R_{ab} g^{ab}. \tag{1.7}$$

Finally, the Einstein tensor is given as

$$G_{ab} = R_{ab} - \frac{1}{2} R g_{ab} \tag{1.8}$$

The equations central to general relativity, called the Einstein's equations, relate the curvature of spacetime to its source: the matter fields. The equations are written as

$$G_{ab} = 8\pi T_{ab} \tag{1.9}$$

The matter fields sourcing the spacetime are encapsulated within the energy-momentum tensor, also called the stress-energy tensor. The essence of general relativistic dynamics was very eloquently put by John Archibald Wheeler in a famous quote, "matter tells spacetime how to curve and spacetime tells matter how to move". Another interesting attribute of these equations is that they are an analog of Poisson's equation in Newtonian gravity which describes the Newtonian gravitational potential $\varphi_N$ as a result of a given density configuration specified by $\rho$.

$$\nabla^2 \varphi_N = 4\pi\rho \tag{1.10}$$

'Gravity' and 'matter' appear on either side of both of these equations, i.e., the Poisson

equation and Einstein's equations. Another thing to note is that the metric may be considered a relativistic analog of the gravitational potential as its second derivatives (and quadratic terms of first derivatives) appear in Einstein's equations just like the second derivative of $\varphi_N$ in Newtonian gravity.

There can be multiple prescriptions for the energy-momentum tensor depending upon the specific problem at hand. We are interested in the relativistic dynamics of fluids and hence adopt a simple prescription, that of the perfect fluid which is given as

$$T^{ab} = (e + p)u^a u^b + pg^{ab} \tag{1.11}$$

where $e$ represents the total energy density of the fluid which is further expressed as a contribution from the rest mass energy density and the internal energy. Specifically, $e = \rho(1 + \epsilon)$ where $\rho$ represents the rest-mass density and $\epsilon$ is the specific internal energy. In the above equation, $p$ is an isotropic pressure and $u^a$ is the fluid 4-velocity. The rest mass density$\rho$ can be further expressed in terms of baryon number density $n$ as $\rho = nm_B$, with $m_B$ being a fiducial baryonic mass. We define a perfect fluid as a fluid that is devoid of shear stresses (isotropic pressure), heat conduction, and viscosity. We remark that the energy-momentum tensor considered is that of a perfect fluid however, both liquids and gases can be classified as fluids. It should be emphasized that we are only interested in fluids that change their volume under pressure, i.e., the fluids should be compressible. Since liquids are incompressible to a large extent, the perfect fluid in our simulations is gaseous. It comes, therefore, as no surprise that the very first equation of state that a relativistic hydrodynamics code is tested on is indeed an ideal gas equation of state. This distinction between liquids and gases is not made explicit in contemporary literature, however, we will use the term fluid to refer to compressible fluids.

In this subsection, we have assumed geometrized units, i.e., $G = c = 1$. However, for better clarity, we will temporarily restore the speed of light $c$ in our equations for section 1.2.

#### 1.1.1.1 Gravitational Waves

We conclude this section with a brief description of radiative solutions to Einstein's equations 1.9, also called gravitational waves. A wave-like solution to these equations is only possible in the linearized regime that is for an asymptotically flat vacuum spacetime. Not to say that the gravitational waves do not exist in the strong-field regime (in the vicinity of the source of gravitational waves), they do, however, the strong field regime

necessitates the solution of the full non-linear equations which has to be done numerically. In other words for an asymptotically flat spacetime, we have

$$g_{ab} = \eta_{ab} + h_{ab} + \mathcal{O}(h_{ab}^2) \tag{1.12}$$

where linearized gravity is enforced by requiring $|h_{ab}| \ll 1$. $h$ here represents perturbations to the flat metric $\eta$. This would essentially imply that we neglect the terms that are quadratic or higher in the computation of the Christoffel connections or the curvature tensor. Specifically, the Christoffel connection in linearized gravity reads

$$\Gamma^c_{ab} = \frac{1}{2}\left(\partial_a h^c_b + \partial_b h^c_a - \partial^c h_{ab}\right) \tag{1.13}$$

and likewise, the Ricci tensor is

$$R_{ab} = \frac{1}{2}\left(\partial_d\partial_b h^d_a + \partial_c\partial_a h^c_b - \partial_c\partial^c h_{ab} - \partial_a\partial_b h\right) \tag{1.14}$$

where $h = \eta^{cd}h_{cd}$ is the trace of the metric perturbations. The Ricci scalar is given by

$$R = R_{ab}g^{ab} \approx R_{ab}\eta^{ab}. \tag{1.15}$$

Employing the expressions computed above and introducing the tensor $\bar{h}_{ab}$ defined as $\bar{h}_{ab} = h_{ab} - \frac{1}{2}\eta_{ab}h$, Einstein's equations 1.9 can be cast into the following form

$$-\partial_c\partial^c\bar{h}_{ab} - \eta_{ab}\partial^c\partial^d\bar{h}_{cd} + \partial^c\partial_a\bar{h}_{bc} + \partial^c\partial_b\bar{h}_{ac} = 16\pi T_{ab}. \tag{1.16}$$

At this point, we can use the gauge freedom inherent in GR by choosing a gauge where the divergence of the metric perturbations $\bar{h}$ vanish. This means $\partial^a\bar{h}_{ab} = 0$ and the gauge is referred to as the Lorenz gauge. Within the Lorenz gauge, the linearized field equations take the form

$$\Box\bar{h}_{ab} = -16\pi T_{ab} \tag{1.17}$$

where $\Box = \partial_c\partial^c$ is the D'Alembertian operator. For a vacuum spacetime, this equation reduces to

$$\Box\bar{h}_{ab} = 0 \tag{1.18}$$

and the plane wave solutions can be expressed as

$$\bar{h}_{ab} = A_{ab}\exp(i\kappa_c x^c) \tag{1.19}$$

where $\kappa$ is a null 4-vector, i.e., $\kappa_a\kappa^a = 0$ and $A$ is the amplitude tensor for the gravitational wave. The solution tells us that perturbations to the flat metric propagate as a plane wave in a direction along $(\kappa_x, \kappa_y, \kappa_z)$ and a frequency $\omega = \kappa^0 = (\kappa_j\kappa^j)^{1/2}$. Owing to the fact that $h$ is a symmetric tensor, the amplitude tensor $A$ too is a symmetric and rank-2 tensor in 4 dimensions. This means that it has 10 degrees of freedom. For planar wave propagation, we require that $A$ and $\kappa$ should be orthogonal, i.e., $A_{ab}\kappa^b = 0$ which constrains 4 degrees of freedom. An additional 4 degrees of freedom are constrained by infinitesimal coordinate transformations within the Lorenz gauge and requiring that the new coordinates too satisfy the vanishing divergence criterion of the Lorenz gauge (See ref. [7]). In the end, we are left with only two degrees of freedom for $A_{ab}$ and therefore $h$. These are the $+$ and $\times$ polarizations of the gravitational wave strain.

We have remarked that owing to the strong non-linearity of Einstein's equations in the strong field regime, the linearized description cannot be used to compute gravitational waves. To compute gravitational waves in this regime, we solve the full non-linear Einstein's equations in a 3+1 formalism to get the evolution of $g_{ab}$. Following this, we utilize the Newman Penrose formulation [8] wherein the GW strain can be computed from

$$\ddot{h}_+ - i\ddot{h}_\times = \Psi_4 = -C_{abcd}n^a\bar{m}^b n^c\bar{m}^d \tag{1.20}$$

where $\Psi_4$ is the Weyl scalar constructed from the Weyl tensor projected onto a given null frame $\{\vec{l}, \vec{n}, \vec{m}, \vec{\bar{m}}\}$ . The Weyl tensor is given by

$$C_{abcd} = g_{ea}C^e_{bcd} = g_{ea}\left(R^e_{bcd} - \left(\delta^e_{[c}R_{d]b} + g_{b[d}R^e_{c]}\right) + \frac{R}{3}\delta^e_{[c}g_{d]b}\right) \tag{1.21}$$

The null frame $\{\vec{l}, \vec{n}, \vec{m}, \vec{\bar{m}}\}$ is derived from a spherical polar orthonormal basis in 3-space, i.e., $\{\hat{e}_r, \hat{e}_\theta, \hat{e}_\varphi\}$ along with a timelike vector $\hat{e}_t$ which is normal to the spatial hypersurface. The basis vectors are given by

$$\vec{l} = \frac{1}{\sqrt{2}}(\hat{e}_t - \hat{e}_r), \quad \vec{n} = \frac{1}{\sqrt{2}}(\hat{e}_t + \hat{e}_r), \quad \vec{m} = \frac{1}{\sqrt{2}}(\hat{e}_\theta - i\hat{e}_\varphi), \quad \vec{\bar{m}} = \frac{1}{\sqrt{2}}(\hat{e}_\theta + i\hat{e}_\varphi) \tag{1.22}$$

Typically a radius of $400M_\odot$ is used for the extraction $\Psi_4$, from which the gravitational wave strain can be computed.

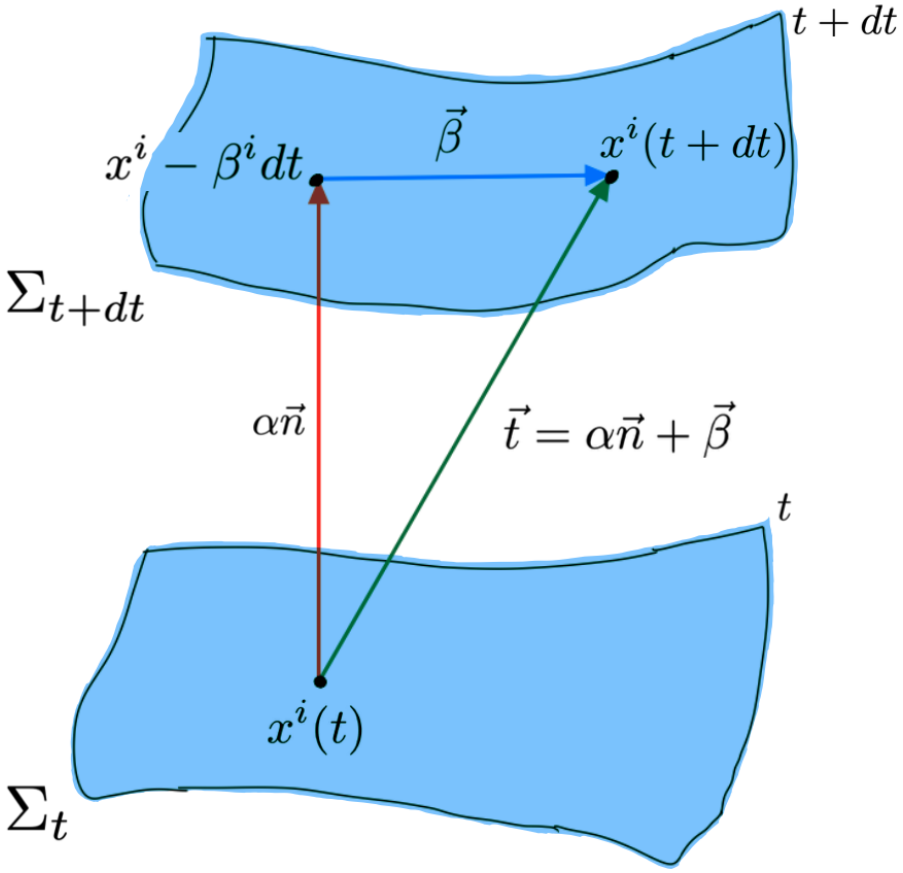


**Figure 1.1.** The 3+1 decomposition of spacetime.

### 1.1.2 The 3+1 Decomposition of spacetime

In this subsection, we shall introduce the 3+1 decomposition of spacetime which is the fundamental vocabulary of numerical relativity literature. We have remarked that in general relativity, spatial and temporal coordinates are equivalent which renders a covariance to the theory. Numerical relativity is, however, the art of solving these covariant equations for astrophysical scenarios. Owing to the high non-linearity of the Einstein's equations, analytical solutions are scarce and one needs to compute solutions numerically. A majority of equations encountered in numerical relativity including Einstein's equations are hyperbolic partial differential equations (PDEs), and there exist comprehensive works including but not limited to [9,10] regarding the mathematical structure of such equations as well as their numerical solutions. To harness these numerical methods, one needs to cast Einstein's equations as an initial value problem which can only be done when we make a conscious distinction between the time and space coordinates thereby lending the name 3(spatial) + 1(temporal) decomposition of spacetime. Before commencing

with the details of the 3+1 decomposition, we would like to provide the reader with references to several standard works on numerical relativity for additional details. These are ref. [7, 11–13].

In figure 1.1, we show a schematic for the 3+1 decomposition of spacetime. The spacetime is characterized by a manifold $\mathcal{M}$ and a metric $g$ in 4-dimensions. The essence of a 3+1 decomposition is to segment the spacetime into spatial foliations $\Sigma_t$ which are parameterized by a constant value of the time coordinate $t$. In figure 1.1, we show a spatial slice $\Sigma_t$ which after a time interval $dt$, evolves into $\Sigma_{t+dt}$. We define a unit, time-like 4-vector $n^a$ which is normal to each point in $\Sigma_t$ and is defined such that its dual one-form $n_a$ is proportional to the gradient of the time coordinate $t$, i.e., $n_a \propto \partial_a t$. Being a unit time-like vector, $n^a$ satisfies $n^a n_a = -1$.

At this stage, we shall introduce the two building blocks of the 3+1 decomposition namely the lapse function $\alpha$ and the shift vector $\beta^a$. The lapse function gives us the rate of change of coordinate time along the direction of $n^a$. Technically put, the vector $n^a$ when amplified by the lapse $\alpha$ takes us from $\Sigma_t$ to $\Sigma_{t+dt}$ along the worldline of an Eülerian observer (whom we shall define momentarily). The shift vector on the other hand is a purely spatial vector meaning $\beta^t = 0$ that tracks the spatial coordinates $x^i$ as they change from $\Sigma_t$ to $\Sigma_{t+dt}$. In terms of the lapse $\alpha$ and the shift vector $\beta^i$, vector $n^a$ can be given as

$$n^a = \frac{1}{\alpha} \begin{pmatrix} 1 \\ -\beta^i \end{pmatrix}_{4\times 1} \tag{1.23}$$

and the corresponding one-form $n_a$ is defined as

$$n_a = (-\alpha, 0, 0, 0)_{1\times 4} \tag{1.24}$$

Using these quantities, we define the time coordinate basis vector which gives the direction of evolution as

$$t^a = \alpha n^a + \beta^a. \tag{1.25}$$

Armed with these definitions, we also define the spatial 3-metric $\gamma_{ab}$ corresponding to the constant-time hypersurface $\Sigma_t$ as

$$\gamma_{ab} = g_{ab} + n_a n_b \tag{1.26}$$

where $g_{ab}$ are the components of the full 4-dimensional metric. From the above definition, one can also write the spatial projection operator $\gamma^a_b$ which is used to project vectors and

tensors onto the spatial hypersurface $\Sigma$ as

$$\gamma^a_b = \delta^a_b + n^a n_b. \tag{1.27}$$

We note that $\gamma^{0a} = 0$, $\gamma_{ij} = g_{ij}$ and $\gamma^{ab} n_a = 0$. Finally, we have all the pieces to write the line element of a metric in the language of 3+1 decomposition. Such a line element is given by

$$ds^2 = g_{ab} dx^a dx^b = (-\alpha^2 + \beta_i \beta^i) dt^2 + 2\beta_i dx^i dt + \gamma_{ij} dx^i dx^j \tag{1.28}$$

where the metric $g_{ab}$ and its inverse $g^{ab}$ are given as

$$g_{ab} = \begin{pmatrix} -\alpha^2 + \beta^i \beta_i & \beta_i \\ \beta_i & \gamma_{ij} \end{pmatrix}_{4\times 4}, \quad g^{ab} = \begin{pmatrix} -1/\alpha^2 & \beta^i/\alpha^2 \\ \beta^i/\alpha^2 & \gamma^{ij} - \beta^i \beta^j/\alpha^2 \end{pmatrix}. \tag{1.29}$$

We shall now describe an Eülerian observer, whose dynamics help compute the explicit form of the 4-velocity of a fluid. Let us consider an inertial observer that is observing a relativistic fluid moving with a 4-velocity $u^a$. An observer is said to be Eülerian if they move in such a way that they see the fluid's velocity $v^a$ to be purely spatial, i.e., $v^t = 0$ in the Eülerian frame. To do that, the Eülerian observers themselves have a time-like velocity (say $n^a$) with respect to the inertial observer. It can be shown [14] that $u^a = W(n^a + v^a)$ where $W$ is the relativistic Lorentz factor $1/\sqrt{1 - v_i v^i}$. We report now (without derivation) the expression for the fluid 4-velocity from an inertial frame as

$$u^a = \frac{W}{\alpha} \begin{pmatrix} 1 \\ \alpha v^i - \beta^i \end{pmatrix}. \tag{1.30}$$

#### 1.1.2.1 The ADM Formulation

Having discussed the 3+1 decomposition of spacetime, we shall conclude this subsection by providing a summary of the main equations while casting Einstein's equations in the 3+1 formalism, i.e., as an initial value problem. To begin with, we define the covariant derivative $D_a$ on the spatial foliation $\Sigma$ by its action on a mixed tensor $T^b_c$ as

$$D_a T^b_c = \gamma^d_a \gamma^b_e \gamma^f_c \nabla_d T^e_f \tag{1.31}$$

This covariant derivative is also compatible with the 3-metric $\gamma_{ab}$, i.e., $D_a \gamma^{bc} = 0$. We can now define the 3-dimensional analogs of the Christoffel connections and the Riemann

tensor as

$$
\begin{aligned}
{}^{(3)}\Gamma^c_{ab} &= \frac{1}{2}\gamma^{cd}\left(\partial_a\gamma_{db} + \partial_b\gamma_{ad} - \partial_d\gamma_{ab}\right) \\
{}^{(3)}R^a_{bcd} &= \partial^{(3)}_c\Gamma^a_{bd} - \partial^{(3)}_d\Gamma^a_{cb} + {}^{(3)}\Gamma^a_{ec}\ {}^{(3)}\Gamma^e_{bd} - {}^{(3)}\Gamma^a_{fd}\ {}^{(3)}\Gamma^f_{bc}.
\end{aligned} \tag{1.32}
$$

Likewise, the 3-dimensional Ricci tensor and Ricci scalar are defined by ${}^{(3)}R_{ab} = {}^{(3)}R^c_{acb}$ and ${}^{(3)}R = {}^{(3)}R^a_a$. We shall now define the extrinsic curvature tensor $K_{ab}$ which gives us the curvature of the spatial hypersurface itself that is embedded in the 4-dimensional spacetime. $K_{ab}$ can be defined as

$$
K_{ab} = -\gamma^c_a\nabla_c n_b \tag{1.33}
$$

For brevity, we shall skip here the explicit derivation of the equations of the 3+1 ADM formalism which can be readily found in references [7, 11–13, 15]. We report below the main equations.

The 6 evolution equations are those of the spatial metric $\gamma_{ij}$ and the extrinsic curvature $K_{ij}$ and are given by

$$
\begin{aligned}
\partial_t\gamma_{ij} &= -2\alpha K_{ij} + D_i\beta_j + D_j\beta_i \\
\partial_t K_{ij} &= -D_iD_j\alpha + \beta^k\partial_k K_{ij} + K_{ik}\partial_j\beta^k + K_{kj}\partial_i\beta^k + \alpha\left({}^{(3)}R_{ij} + KK_{ij} - 2K_{ij}K^k_j\right) \\
&\quad + 4\pi\alpha\left(\gamma_{ij}(S-E) - 2S_{ij}\right)
\end{aligned} \tag{1.34}
$$

wherein the quantities $S_{ij}$, $S$ and $E$ are the different components of the energy-momentum tensor and are given by

$$
\begin{aligned}
S_{ab} &= \gamma^c_a\gamma^d_b T_{cd} \\
S_a &= -\gamma^b_a n^c T_{bc} \\
S &= S^a_a \\
E &= n^a n^b T_{ab}
\end{aligned} \tag{1.35}
$$

Apart from the evolution equations, we also have the following 4 constraint equations that, once specified for an initial time-step, should in principle hold for each time step, i.e., they hold for all spatial foliations $\Sigma_t$. They are given by the Hamiltonian and

momentum constraint which can be expressed as

$$
\begin{aligned}
{}^{(3)}R + K^2 - K_{ij}K^{ij} &= 16\pi E \\
D_j \left( K^{ij} - \gamma^{ij} K \right) &= 8\pi S^i
\end{aligned}
\tag{1.36}
$$

The fundamental building blocks of the 3+1 decomposition of the metric, the lapse function $\alpha$, and the shift vector $\beta^i$ are also called gauge-dependent quantities because they depend upon a particular choice of the coordinate system and hence are not measurable by experiment or observation. They are not constrained by Einstein's equations and represent the 4-fold gauge freedom inherent in GR. Specifying $\alpha$ and $\beta^i$ is equivalent to choosing a particular gauge (or coordinate system). The constraint equations are independent of these gauge-dependent quantities because they should be satisfied on each hypersurface whereas the $\alpha$ and $\beta^i$ link together two adjacent hypersurfaces. As has already been mentioned, given that the constraint equations are satisfied at the initial time step, they should in principle hold at all time steps. In numerical computations, however, solving both hyperbolic (the evolution equations) and elliptic (the constraint equations) PDEs is prohibitively expensive, and therefore instead of requiring a solution of constraint equations at each time step (constrained evolution), contemporary numerical codes only monitor violations in the Hamiltonian and momentum constraints from the initial time step. If the violation is within a specified tolerance, the metric and extrinsic curvature are evolved freely.

We should conclude with brief analogies for the evolution and constraint equations in the 3+1 ADM formulation. The extrinsic curvature $K_{ij}$ can be expressed as a lie derivative of the spatial metric [7,11–13]. For the initial value problem, we require $\gamma_{ij}$ and $K_{ij}$ at an initial time $t = 0$, following which they are evolved using equations 1.34. This is a general relativistic analog of the Newtonian scenario that states that given initial positions and velocities, the time evolution of the system can be prescribed by Newton's second law. Additionally, the decomposition of Einstein's equations into evolution and constraint equations is also an attribute that is observed in classical electromagnetism for Maxwell's equations where we have 2 evolution equations for the electric and magnetic fields (Faraday-Lenz law and Ampere-Maxwell's law) and 2 constraint equations (Gauss' law) for the divergence of electric and magnetic fields.

#### 1.1.2.2 The 3+1 Valencia Formulation

In this subsection, we shall describe the basic equations for general relativistic hydrodynamics. Coupled with the evolution equations for the metric and extrinsic curvature, the 3+1 Valencia formulation [16] forms the backbone of calculations in a numerical relativity infrastructure. It can be instructive from a comparison point of view to write down the equations for Newtonian hydrodynamics for a self-gravitating system, i.e., a system where the dynamics of the fluid influences the gravitational potential. The equations are the conservation of rest mass, energy, and momentum and Poisson's equation for the gravitational potential given a density configuration. These conservation laws, also called as the Eüler equations of gas dynamics are given in terms of the densities of conserved variables as

$$\begin{aligned} \partial_t \rho + \partial_i(\rho v^i) &= 0 \\ \partial_t(\rho v^i) + \partial_j(\rho v^i v^j + p^{ij}) &= -\rho \partial^i \varphi \\ \partial_t E + \partial_i\left((E+p)v^i\right) &= -\rho v^k \partial_k \varphi \\ \partial_i \partial^i \varphi &= 4\pi\rho \end{aligned} \tag{1.37}$$

where we have assumed isotropic pressure, i.e., $p^{ij} = p\delta^{ij}$. Additionally, $\rho$ is the rest mass density and $E$ is the total energy density given by $E = \rho\epsilon + (1/2)\rho v^2$ with $\epsilon$ being the specific internal energy. Finally, $\varphi$ represents the Newtonian gravitational potential sourced from $\rho$. In the above system, there are 7 unknowns namely $\rho$, 3 components of $v^i$, $p$, $\epsilon$ and $\varphi$ but only 6 equations. Therefore, in order to close the system, an equation of state needs to be supplied which has the form of $p = p(\rho, \epsilon)$. The concept of an equation of state is so central to this dissertation, that we have devoted an entire section (section 1.2) to discuss in detail, the properties of equations of state.

The equations of general relativistic hydrodynamics have a one-to-one correspondence with the system of equations 1.37. The Poisson's equation is analogous to the 10 Einstein's equations whose 3+1 decomposition into evolution and constraint equations, we saw in the previous section. The conservation of rest mass, energy, and momentum are encapsulated as

$$\begin{aligned} \nabla_a J^a &= 0 \\ \nabla_a T^{ab} &= 0. \end{aligned} \tag{1.38}$$

Here, $J^a = n m_B u^a$ is the rest-mass 4-current and $T^{ab}$ as we have seen before, is the

energy-momentum tensor of a perfect fluid. The 3+1 Valencia formulation casts the set of equations 1.38 in a 3+1 formalism. The equation for the conservation of rest mass is easy to derive as

$$\begin{aligned}
&\nabla_a \left(n m_B u^a\right) = 0 \\
&\implies \frac{1}{\sqrt{-g}} \partial_a \left(\sqrt{-g} n m_B u^a\right) = 0 \\
&\implies \partial_t \left(\alpha \sqrt{\gamma} n m_B u^t\right) + \partial_i \left(\alpha \sqrt{\gamma} n m_B u^i\right) = 0 \\
&\implies \partial_t \left(\sqrt{\gamma} D\right) + \partial_i \left(\sqrt{\gamma} D (\alpha v^i - \beta^i)\right) = 0
\end{aligned} \tag{1.39}$$

where we have utilized the property of the 4-divergence and used the definition $D = n m_B \alpha u^t = \rho W$ for the conservative variable $D$. We have also used the 3+1 definition of the fluid 4-velocity from equation 1.30. The 3+1 equations for the conservation of energy and momentum are a bit more involved and we refer the reader to Chapter 7 of reference [7] for the details of the derivation. In a nutshell, following a similar derivation as for the rest mass, the equations for energy and momentum conservation respectively read

$$\begin{aligned}
\partial_t(\sqrt{\gamma} E) + \partial_i \left(\sqrt{\gamma}(\alpha S^i - \beta^i E)\right) &= -\sqrt{-g} T^{ab} \nabla_a n_b \\
\partial_t(\sqrt{\gamma} S_j) + \partial_i \left(\sqrt{\gamma}(\alpha S^i_j - \beta^i S_j)\right) &= \frac{1}{2} \sqrt{-g} T^{ab} \partial_j g_{ab}
\end{aligned} \tag{1.40}$$

In these equations, we have made use of the 3+1 form of the components of $T^{ab}$. They are given as follows

$$\begin{aligned}
S^{ab} &= \rho h W^2 v^a v^b + p \gamma^{ab} \\
S^a &= \rho h W^2 v^a \\
E &= \rho h W^2 - p
\end{aligned} \tag{1.41}$$

with $h = 1 + \epsilon + p/\rho$ being the relativistic specific enthalpy of the fluid.

In summary, the equations for the conservation of rest mass, energy, and momentum, can be cast into a compact form of

$$\partial_t(\sqrt{\gamma} \vec{U}) + \partial_i(\sqrt{\gamma} \vec{F}^i) = \vec{S} \tag{1.42}$$

where $\vec{U}$ is a vector of the conservative variables, whose volume integrals represent the

conserved quantities, $\vec{F}^i$ is a vector of fluxes corresponding to conservative variables along the $i^{\text{th}}$ direction, and $\vec{S}$ represents the source terms. They are given by

$$\vec{U} = \begin{pmatrix} \rho W \\ \rho h W^2 v_j \\ \rho h W^2 - p \end{pmatrix}, \quad \vec{F}^i = \begin{pmatrix} \alpha v^i D - \beta^i D \\ \alpha S^i_j - \beta^i S_j \\ \alpha S^i - \beta^i E \end{pmatrix} \tag{1.43}$$

and

$$\vec{S} = \begin{pmatrix} 0 \\ (1/2)\sqrt{\gamma}\alpha S^{ik}\partial_j \gamma_{ik} + S_i \sqrt{\gamma}\partial_j \beta^i - E\sqrt{\gamma}\partial_j \alpha \\ \alpha\sqrt{\gamma} S^{ij} K_{ij} - \sqrt{\gamma} S^j \partial_j \alpha \end{pmatrix} \tag{1.44}$$

Following the same arithmetic as before, an equation of state of the form $p = p(\rho, \epsilon)$ is required to close the system.

We shall conclude this section with an important comment. Hyperbolic PDEs with a vanishing source term are exact conservation laws e.g. the conservation of rest mass. On the other hand, the conservation of energy and momentum have a finite source term on their RHS which makes them a balance law. This means that up to round off error, such a 3+1 formulation will conserve the rest mass but not conserve energy and momentum. We re-iterate, that the energy and momentum are still conserved in nature as well as in the covariant sense where the equations are written in 4-dimensional coordinates. It is only when they are converted to a 3+1 format, do they lose their conservative nature up to a round-off error. This is a numerical limitation rather than a limitation of the equations themselves. Indeed, conservative formulations e.g. to the system of Eüler equations in Newtonian gravity have shown good promise in conserving the energy to a round of error [17]. A conservative formulation for general relativistic hydrodynamics also exists [18] which aims to cast the non-zero source terms as the divergence of an effective flux. However, an implementation of such a formulation in contemporary codes is yet to be made.

## 1.2 The Equation of State

Put succinctly, an equation of state (EoS) describes the equilibrium behavior of a system. If the system is composed of multiple species in equilibria, there exists an EoS for each species which in turn contributes to the overall EoS. This is usually the case with neutron star matter where we have a host of species like protons, neutrons, electrons, photons, hyperons, and possibly even deconfined quarks contributing to the overall dynamics

of the fluid. The precise definition of this equilibrium behavior will be elaborated in subsection 1.2.3 when we discuss equilibrium distribution functions and how EoSs are derived from them. Before we can proceed with the properties of an EoS, it is beneficial to briefly recapitulate the fundamentals of thermodynamic potentials as well as the classical textbook example of phase transitions in water. The definitions provided in the following two subsections will come in very handy when we compute the properties of equations of state in subsection 1.2.4.

### 1.2.1 Thermodynamic Potentials: A quick review

The thermodynamic potentials or the thermodynamic state functions, coupled with a given equation of state help us in computing the equilibrium properties of a system. We will start with the first law of thermodynamics which is essentially a re-statement of the energy conservation principle. For a system with a single species of particles, it can be mathematically expressed as

$$dU + pdV - TdS = \mu dN \tag{1.45}$$

where $dU$ represents the change in the internal energy of the system, $dV$ is the change in volume under the application of a pressure $p$, $dS$ is the change in the system's entropy and $dN$ represents the change in the number of particles as a result of some reaction process. $T$ represents the system's temperature and $\mu$ is the chemical potential which is a measure of change in the system's energy as a result of a change in the number of particles of a particular species. If the system instead were to be composed of multiple species, the first law of thermodynamics would be modified as

$$dU + pdV - TdS = \sum_i \mu_i dN_i \tag{1.46}$$

where $\mu_i$ and $N_i$ are the chemical potential and number of particles for the $i^{\text{th}}$ species respectively. Considering the simpler case of a single particle species, we define $U = Nm\epsilon$ and $S = Nms$ where $N$ is the total number of particles and $m$ is the mass of each particle. In numerical relativity literature, $\epsilon$ represents the specific internal energy of a fluid and $s$ is the specific entropy. Using these definitions and the fact that $V = Nm/\rho$ where $\rho$ is the fluid's rest mass density, we can express equation 1.45 as

$$d\epsilon = Tds - pd(1/\rho) = Tds + (p/\rho^2)d\rho. \tag{1.47}$$

Here we have made the simplifying assumption that the number of particles remains a constant, i.e., $dN = 0$. Equation 1.47 will come in very handy when we compute the sound speed of different EoS formulations. We have seen in subsection 1.1.1, that the total energy density is given by $e = \rho(c^2 + \epsilon)$ where we have maintained the dimensionality of the equation. At this point, we recall the relativistic specific enthalpy $h$ which is defined as

$$h = c^2 + \epsilon + p/\rho \tag{1.48}$$

Using the above definition of specific enthalpy and equation 1.47 it is possible to re-cast the first law of thermodynamics into other useful forms

$$dp = \rho dh - \rho T ds \tag{1.49}$$

$$de = h d\rho + \rho T ds. \tag{1.50}$$

Finally, we define the internal energy $U$ of the fluid as a thermodynamic state function dependent on $S$, $V$, and $N$, i.e., $U = U(S, V, N)$ (equation 1.45) which further implies the following definitions

$$T = \left(\frac{\partial U}{\partial S}\right)_{V,N}, \quad p = -\left(\frac{\partial U}{\partial V}\right)_{S,N}, \quad \mu = \left(\frac{\partial U}{\partial N}\right)_{S,V}. \tag{1.51}$$

There are a few more thermodynamic potentials that are important for our purposes and we enumerate them as follows:

- The total enthalpy $H$ of a system is expressed as $H = U + pV$ where the symbols have their usual meaning. In a total differential form, we can write

$$dH = dU + pdV + Vdp = TdS + Vdp + \mu dN \tag{1.52}$$

  where for the second equality, we have utilized equation 1.45. This relationship also helps express $H$ as a state function of $S$, $p$, and $N$, i.e., $H = H(S, p, N)$ which further allows for the following definitions

$$T = \left(\frac{\partial H}{\partial S}\right)_{p,N}, \quad V = \left(\frac{\partial H}{\partial p}\right)_{S,N}, \quad \mu = \left(\frac{\partial H}{\partial N}\right)_{S,p}. \tag{1.53}$$

- The Gibbs free energy $G$ helps compute a measure of the thermodynamic feasibility of a process. For isolated systems, a thermodynamic process is feasible when $dG \leq 0$. As a potential, it is defined as $G = H - TS$, and in a differential form we have

$$dG = dH - TdS - SdT = \mu dN + Vdp - SdT \tag{1.54}$$

where again we have utilized the first law of thermodynamics. Given $G = G(N, p, T)$, we can have the following definitions

$$\mu = \left(\frac{\partial G}{\partial N}\right)_{T,p}, \quad V = \left(\frac{\partial G}{\partial p}\right)_{N,T}, \quad S = -\left(\frac{\partial G}{\partial T}\right)_{N,p}. \tag{1.55}$$

- The Helmholtz's Free energy $F$ is defined as $F = U - TS$ which in a differential form is written as

$$dF = dU - TdS - SdT = -SdT - pdV + \mu dN. \tag{1.56}$$

As a state function, $F = F(T, V, N)$ which allows for the following defintions

$$S = -\left(\frac{\partial F}{\partial T}\right)_{V,N}, \quad p = -\left(\frac{\partial F}{\partial V}\right)_{T,N}, \quad \mu = \left(\frac{\partial F}{\partial N}\right)_{T,V} \tag{1.57}$$

- Finally, we define the grand canonical potential $\Omega$ defined as $\Omega = F - \mu N$. As we shall see in chapter 2, the grand canonical potential is employed to define the equilibrium properties of a deconfined quark phase - the dynamics of which in neutron star mergers is the main crux of this dissertation. As a total differential,

$$d\Omega = dF - \mu dN - Nd\mu = -SdT - pdV - Nd\mu \tag{1.58}$$

Just like we did for all the previous thermodynamic potentials, $\Omega$ as a state function is given by $\Omega = \Omega(T, V, \mu)$ which paves the way for the following definitions

$$S = -\left(\frac{\partial \Omega}{\partial T}\right)_{V,\mu}, \quad p = -\left(\frac{\partial \Omega}{\partial V}\right)_{T,\mu}, \quad N = -\left(\frac{\partial \Omega}{\partial \mu}\right)_{T,V} \tag{1.59}$$

We conclude this section by commenting on the equilibrium conditions for an isolated system. An isolated system in equilibrium is under thermal, chemical, and mechanical equilibrium. In other words, the temperature, chemical potential, and pressure of the system are the same throughout. This is a direct consequence of the fact that the system's entropy increases and is maximal ($dS = 0$) for equilibrium. An equivalent criterion is the decrease of the system's Gibbs free energy to a minimum, i.e., $dG = 0$ for equilibrium.

### 1.2.2 Phase Transitions: A quick review

In this subsection, we shall briefly review the fundamental properties of phase transitions. A phase is any state of matter like solid, liquid, or gas that is characterized by a distinct set of thermodynamic state functions. Other examples of phases include diamagnetic or paramagnetic phases in materials or for that matter, confined (within hadrons) phases and deconfined phases of quarks in strongly interacting matter. A transition between two phases occurs due to a change in one or more thermodynamic state functions that characterize a phase. Such a change may be sudden or discontinuous as happens in a first-order phase transition or take place gradually for higher-order phase transitions. A phase boundary or a coexistence curve in the phase structure separates the two phases and along such a coexistence curve, the two phases coexist in equilibrium.

The Ehrenfest classification of phase transitions provides a quantitative definition for the order of a phase transition. It states that the order of a phase transition is the lowest order of the derivative of Gibbs free energy which is discontinuous across the phase boundary. The Gibbs free energy $G$ itself varies continuously across a phase boundary. For two phases $A$ and $B$, a phase transition from $A$ to $B$ is of the $n^{\text{th}}$ order if the following two conditions are satisfied

$$\left(\frac{\partial^m G_A}{\partial p^m}\right)_{N,T} = \left(\frac{\partial^m G_B}{\partial p^m}\right)_{N,T}, \quad \left(\frac{\partial^m G_A}{\partial T^m}\right)_{N,p} = \left(\frac{\partial^m G_B}{\partial T^m}\right)_{N,p}, \quad \left(\frac{\partial^m G_A}{\partial N^m}\right)_{T,p} = \left(\frac{\partial^m G_B}{\partial N^m}\right)_{T,p} \tag{1.60}$$

where $m = 1, 2, ..., n-1$ and

$$\left(\frac{\partial^n G_A}{\partial p^n}\right)_{N,T} \neq \left(\frac{\partial^n G_B}{\partial p^n}\right)_{N,T}, \quad \left(\frac{\partial^n G_A}{\partial T^n}\right)_{N,p} \neq \left(\frac{\partial^n G_B}{\partial T^n}\right)_{N,p}, \quad \left(\frac{\partial^n G_A}{\partial N^n}\right)_{T,p} \neq \left(\frac{\partial^n G_B}{\partial N^n}\right)_{T,p} \tag{1.61}$$

Another important property of a first-order phase transition is the existence of latent heat.

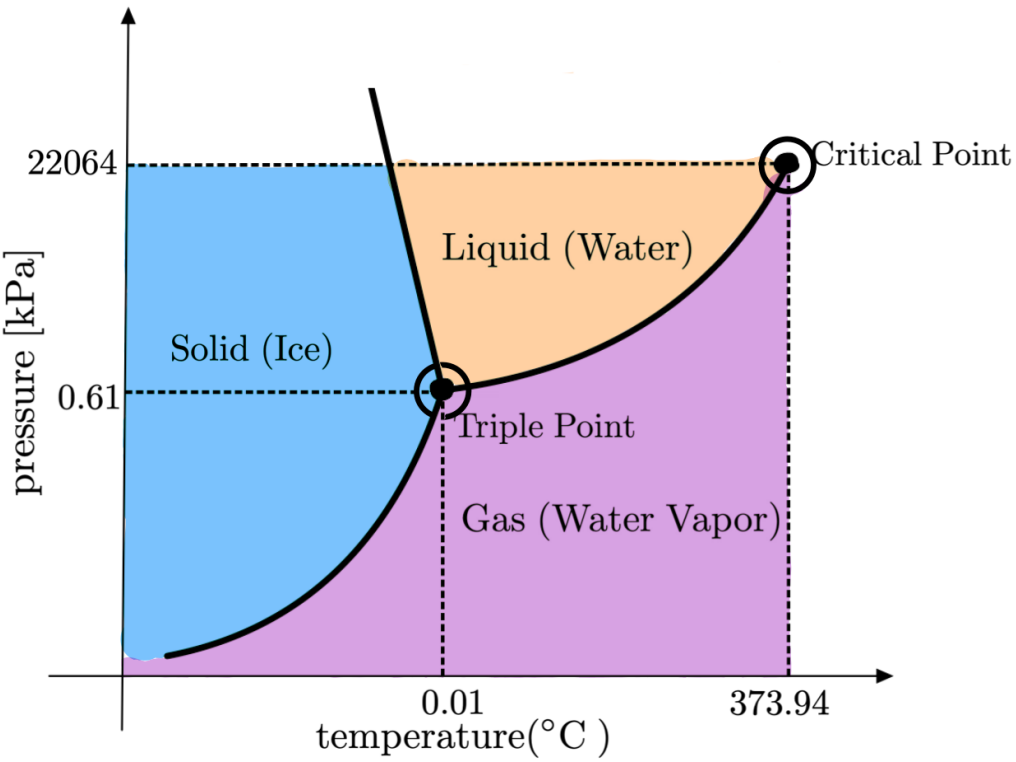


**Figure 1.2.** A schematic diagram showing the phase structure of water projected onto the pressure-temperature plane at a constant volume.

"Latent" heat meaning hidden heat is the heat given to a system to bring about a change of phase at a constant temperature. Mathematically, the latent heat $\Delta Q_L$ measures the change in a system's entropy at a constant temperature, i.e., $\Delta Q_L = T_0 \Delta S$. For higher-order phase transitions, entropy is continuous across a phase boundary resulting in no latent heat.

We will now consider the simple example of a first-order phase transition in water. This is a system with a single conserved charge which is the number of water molecules $N$ such that $dN = 0$. Many a time in contemporary phase transition literature, the term "charge" is used in a general sense to denote a conserved quantity for instance the number of particles (like baryon number), electric charge, or even strangeness. In figure 1.2, we show the phase structure of water projected onto the pressure-temperature plane at a constant volume. The full phase structure depends on pressure $p$, temperature $T$, and volume $V$. The figure shows the three phases in which water exists, i.e., solid, liquid, and gas. They are separated by coexistence curves along which the two phases on either side are in equilibrium. The solid-liquid phase transition (melting), the liquid-vapor phase transition (vaporization), as well as the solid-vapor phase transition (sublimation), all

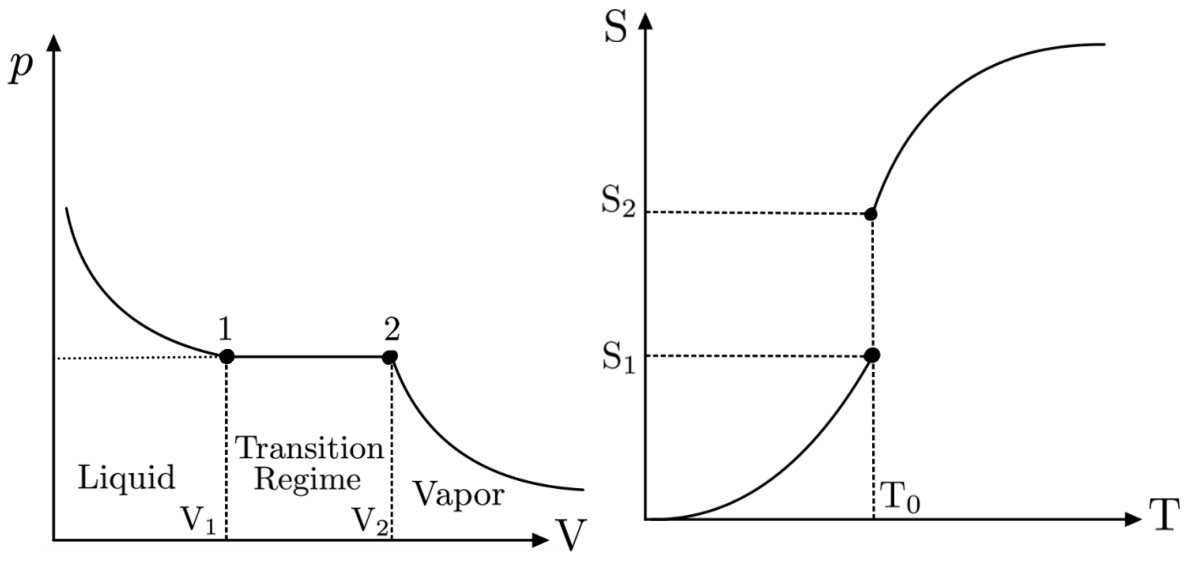


**Figure 1.3.** *Left panel*: The projection of the phase diagram of water on the pressure-volume space at a constant temperature shows a discontinuity in volume across the phase boundary. Typically, phase transitions with a single conserved charge (here $N$) proceed at a constant pressure. *Right panel*: The discontinuity in entropy at the transition temperature $T_0$ at a constant pressure.

three are of the first order. The coexistence curves intersect at the triple point at which all three phases of water are in equilibrium. The liquid-vapor phase transition terminates at a critical point at which the phase transition becomes second-order.

For the first-order liquid(1)-vapor(2) phase transition in water (see figure 1.3) ($N$ being a constant) at the point $(T_0, p_0)$ in the phase diagram, we have the following conditions:

- The Gibbs free energy $G(T, p)$ changes continuously across the phase transition boundary, i.e., $G_1(T_0, p_0) = G_2(T_0, p_0)$
- The entropy $S = -\left(\partial G/\partial T\right)_p$ is discontinuous across the phase boundary, i.e., $S_1 \neq S_2$
- The volume (or equivalently density) $V = \left(\partial G/\partial p\right)_T$ is discontinous across the phase boundary. i.e., $V_1 \neq V_2$ (or $\rho_1 \neq \rho_2$)
- There exists a latent heat given by $\Delta Q_L = T_0(S_2 - S_1)$.

We conclude this subsection with a remark about the criterion for the coexistence of phases at the phase boundary. We know that pressure $p$ and temperature $T$ will be continuous across the phase boundary owing to mechanical and thermal equilibrium

respectively. The total Gibbs free energy at a specific point $(T_0, p_0)$ on the coexistence curve is given by

$$G(T_0, p_0, N) = G_1(T_0, p_0, N_1) + G_2(T_0, p_0, N_2) = \mu_1 N_1 + \mu_2 N_2 \tag{1.62}$$

where $N_1$ and $N_2$ are the numbers of particles in the liquid and vapor phases respectively and $N_1 + N_2 = N$ is a constant. We recall that a condition for equilibrium is that Gibbs free energy attains a steady state, i.e., $dG = 0$. At a constant $(T_0, p_0)$, this implies

$$dG = \mu_1 dN_1 + \mu_2 dN_2 = 0 \tag{1.63}$$

Since $dN = dN_1 + dN_2 = 0$, we have another condition for the coexistence of phases as $\mu_1 = \mu_2$ which is the condition for chemical equilibrium. This condition will be central to the construction of mixed phases of confined and deconfined quarks when we discuss the Maxwell and Gibbs constructions in subsection 1.2.5.2.

### 1.2.3 Boltzmann Equation and distribution functions

Mergers of neutron stars are an unambiguously complex problem involving several physics models in synchronization. EoS models in competent merger simulations typically include the effects of multiple particles also called degrees of freedom. These include protons, neutrons, electrons, positrons, photons, and neutrinos. There have been several works that have investigated the appearance of more exotic degrees of freedom such as hyperons [19, 20], muons [21], and deconfined quarks (see references in chapters 2 and 6). Each of these particles has a dynamics of its own, which at the most fundamental level, is governed by the distribution function.

A distribution function, put simply, is a time-dependent measure of the number of particles of a given species in a 6-dimensional volume of coordinate and velocity (or momentum) space. More clearly, a distribution function $f = f(t, x^i, u^j)$ is such that $f(t, x^i, p^j) d^3x d^3u$ is the number of particles within the 6-dimensional volume of $d^3x d^3u$. Therefore, the total number of particles in the phase space is given by

$$N = \int \int f(t, x^i, u^j) d^3x d^3u. \tag{1.64}$$

The evolutionary dynamics of $f$ in 7 dimensions (one of time and the 6-dimensional phase space) is governed by the Boltzmann equation, which for classical mechanics (where the relativistic effects are not important) takes the following form

$$\partial_t f + u^i \partial_i f + (F^j/m)\partial_{u^j} f = \Pi(f). \tag{1.65}$$

Here $F^j$ is a velocity-independent force that acts on each particle and the term $\Pi(f)$ on the right-hand side is called a collisional term which takes into account the interactions (called collisions generically) of particles. A collisionless Boltzmann equation is one with a vanishing $\Pi$ which corresponds to a homogeneous advection equation for $f$ in the 6-dimensional phase-space.

In cases where relativistic effects need to be taken into consideration, the Boltzmann equation (assuming a flat spacetime) takes the following form

$$p^a \partial_a f + m\partial_{p^b}(F^b f) = \Pi(f). \tag{1.66}$$

Here $p^a$ represents the 4-momentum of the particle of rest mass $m$ and $F^b$ is the four-force which may or may not depend on $p^a$. The explicit form of the collisional integral is not important here but may be found in references such as [7, 22]. The above equation has been written for a flat spacetime and can be extended to curved spacetimes in general relativity, however for brevity we shall omit it here.

For systems that are out of equilibrium, the distribution function is time-dependent and the full Boltzmann equation needs to be solved. Complete numerical solutions of the Boltzmann equation are computationally expensive and in conjunction with merger simulations of neutron stars, even more so. Therefore, extensive work has been done to solve equation 1.66 in general relativity, either by using truncated moment formalisms [23–25] or by employing Monte-Carlo methods [26–28]. However, recent approaches such as finite element methods [29] show significant promise in solving the full transport equation.

In a neutron star merger, out-of-equilibrium effects [30–32] such as the bulk viscous damping of the remnant's oscillations are introduced by neutrino interactions. Trapped neutrinos before equilibrating with the neutron star matter as well as free-streaming neutrinos need to be accounted for by solving equation 1.66 in full general relativity. However, other species such as nucleons, protons, electrons, etc. are largely in thermodynamic equilibrium. In the language of kinetic theory, equilibrium means that the distribution function for the corresponding species is stationary and can be computed by requiring $\Pi(f_0) = 0$. This equilibrium distribution function, which from now on we shall denote by $f_0(p)$, forms the basis of an equation of state. This means that equilibrium properties for a particle species such as their number density $n$, pressure $p$ or energy density $e$ can be

derived once an equilibrium distribution function is known. The involvement of neutrinos in out-of-equilibrium phenomenon is the reason, why one usually does not encounter phrases such as a 'neutrino EoS' as an EoS is intimately related to equilibrium behavior of a species. However, trapped neutrinos, once in weak and thermal equilibrium with matter and radiation can be effectively treated with an EoS of a massless ideal Fermi gas [21], something which we shall explore in detail in subsection 1.2.4.3.

The equilibrium distribution functions computed for the relativistic Boltzmann equation 1.66 depend upon whether for a particle species, quantum mechanical effects need to be considered or not. To provide a measure for the same, we introduce two quantities by the name of fugacity ($\alpha_f$) and coldness ($\zeta_c$) as follows

$$\alpha_f = \left(\frac{\mu}{k_B T}\right), \zeta_c = \left(\frac{mc^2}{k_B T}\right) \tag{1.67}$$

where $k_B$ is the Boltzmann's constant and the other symbols have their usual meaning. Qualitatively, $\alpha_f$ is proportional to the significance of quantum mechanical effects for the dynamics of the fluid and $\zeta_c$ is inversely proportional to the importance of special relativistic effects. To this aim, we can classify the typical fluids of interest in the case of neutron star mergers as follows:

- If $\alpha_f \gg 1$ and $\zeta_c \ll 1$, we have a degenerate and relativistic fluid where both quantum mechanical effects and relativity need to be considered.
- If $\alpha_f \ll 1$ and $\zeta_c \ll 1$, we have a non-degenerate and relativistic fluid where quantum mechanical effects may be neglected however relativistic effects need to be taken into account.
- If $\alpha_f \ll 1$ and $\zeta_c \gg 1$, we have a non-degenerate and non-relativistic fluid wherein we can safely ignore both quantum mechanical and relativistic effects and treat the fluid within a classical framework.

One should emphasize that the above classification is only qualitative and serves to provide a sound logic to the study of the different types of equilibrium distributions in numerical relativity. Excluding the explicit details of computing the equilibrium solutions to the full Boltzmann equation, we report the equilibrium distributions most often encountered, in the order of the classification mentioned above.

- For $\alpha_f \gg 1$ and $\zeta_c \ll 1$, equilibrium solutions to equation 1.66 are the well-known

Fermi-Dirac and Bose-Einstein distribution functions expressed as

$$f_0(p) = \frac{g_s}{h_p^3}\left(\frac{1}{\exp(-\alpha_f - cp^a u_a/k_B T) \pm 1}\right). \tag{1.68}$$

Here +1 corresponds to fermions like baryons and leptons which obey the Fermi-Dirac statistics and Pauli's exclusion principle, and -1 in the denominator is for bosons like mesons, photons, etc. which obey the Bose-Einstein statistics.

- For $\alpha_f \ll 1$ and $\zeta_c \ll 1$, the equilibrium distribution is the Maxwell-Jüttner distribution given by

$$f_0(p) = \frac{g_s}{h_p^3}\left(\frac{1}{\exp(-\alpha_f - cp^a u_a/k_B T)}\right). \tag{1.69}$$

- For $\alpha_f \ll 1$ and $\zeta_c \gg 1$, we have the classical Maxwell-Boltzmann distribution function, often employed for computing the properties of classical systems such as a classical monoatomic fluid. It is expressed as

$$f_0(p) = 4\pi\left(\frac{m}{2\pi k_B T}\right)^{3/2} n \exp\Big(-p^2/2mk_B T\Big) \tag{1.70}$$

In the above distributions, $g_s$ stands for the degeneracy factor of the particle species given by

$$g_s = \begin{cases} 2s+1, m \neq 0 \\ 2s, m = 0 \end{cases} \tag{1.71}$$

and $h_p$ is the Plancks' constant. We should emphasize here that while $p^a$ represents the 4-momentum of the particle, $u_a$ represents the 4-velocity of the 'fluid' as a whole, which in the local fluid frame can be written as $u_a = (-1, 0, 0, 0)$. This makes $-cp^a u_a = wmc^2 = E$ with $w$ being the relativistic Lorentz factor and $E$ the total relativistic energy. Armed with these definitions, we can condense the relativistic equilibrium distributions (both degenerate and non-degenerate) in a single expression as

$$f_0(p) = \frac{g_s}{h_p^3}\left(\frac{1}{\exp((E-\mu)/k_B T) + \varepsilon}\right). \tag{1.72}$$

where $\varepsilon$ differentiates between the different kinds of distributions, i.e.,

$$\varepsilon = \begin{cases} +1, \text{for Fermi} - \text{Dirac distribution} \\ -1, \text{for Bose} - \text{Ensitein distribution} \\ 0, \text{for Maxwell} - \text{Jüttner distribution} \end{cases} \tag{1.73}$$

### 1.2.4 Equation of State

Before we start to elucidate the properties of several EoS models, we introduce here two definitions that are going to come in handy.

The very first definition is that of specific heat. Put simply, it measures the capacity of a system to absorb heat from its surroundings. Mathematically, it is expressed as the change in heat per unit mass per unit temperature, i.e., $C_{\text{heat}} = dQ/(NmdT)$. From equation 1.47, we can write

$$\frac{dQ}{Nm} = Tds = d\epsilon + pd(1/\rho) = C_{\text{heat}}dT \tag{1.74}$$

from where we can write $C_{\text{heat}}$ assuming $\epsilon = \epsilon(\rho, T)$ as

$$C_{\text{heat}} = \frac{1}{dT}\left[\left(\frac{\partial\epsilon}{\partial T}\right)_{\rho} dT + \left(\left(\frac{\partial\epsilon}{\partial\rho}\right)_{T} - \frac{p}{\rho^2}\right) d\rho\right] \tag{1.75}$$

The specific heat can be computed at a constant volume or a constant pressure. At a constant volume (or equivalently a constant density), the heat capacity $C_v$ is given by

$$C_v = \left(\frac{\partial\epsilon}{\partial T}\right)_{V} = T\left(\frac{\partial s}{\partial T}\right)_{V} \tag{1.76}$$

Likewise, at constant pressure, the heat capacity $C_p$ is given as

$$\begin{aligned} C_p &= \frac{1}{dT}\left[\left(\frac{\partial\epsilon}{\partial T}\right)_{\rho} dT + \left(\left(\frac{\partial\epsilon}{\partial\rho}\right)_{T} - \frac{p}{\rho^2}\right) d\rho\right] \\ &= C_v + \left[\left(\frac{\partial\epsilon}{\partial\rho}\right)_{T} - \frac{p}{\rho^2}\right]\left(\frac{\partial\rho}{\partial T}\right)_{p} \\ &= \left(\frac{\partial h}{\partial T}\right)_{p} = T\left(\frac{\partial s}{\partial T}\right)_{p} \end{aligned} \tag{1.77}$$

wherein we have employed the first law of thermodynamics as stated in equations 1.49 and 1.50. An important quantity of interest is the ratio of the two specific heats described

which is called the adiabatic index $\Gamma$. In other words

$$\Gamma = C_p/C_v \tag{1.78}$$

The second important property of an equation of state is its sound speed whose relativistic definition is given as

$$C_s^2 = \left(\frac{\partial p}{\partial e}\right)_s \tag{1.79}$$

which reduces to $(C_s^2)_N = (\partial p/\partial \rho)_s$ in the Newtonian theory. Finally using equations 1.49 and 1.50, it is trivial to show that

$$\begin{aligned} C_s^2 &= \left(\frac{(C_s^2)_N}{h}\right) \\ &= \frac{1}{h}\left[\left(\frac{\partial p}{\partial \rho}\right)_\epsilon + \frac{p}{\rho^2}\left(\frac{\partial p}{\partial \epsilon}\right)_\rho\right] \end{aligned} \tag{1.80}$$

We will now begin to discuss several model equations of state that one encounters in contemporary numerical relativity research.

#### 1.2.4.1 The Ideal Gas equation of state

We begin with the simplest model of the equation of state namely that of an ideal gas where the fluid pressure is directly proportional to temperature at a constant volume. In more concrete terms, the pressure $p$ is given as

$$p = nk_BT \tag{1.81}$$

where $n$ stands for the number density of the fluid. The number of particles $N$ in an ideal gas EoS is a constant. Such an equation of state is an apt model to describe non-degenerate systems irrespective of whether they are non-relativistic, relativistic, or ultrarelativistic. From the analysis of a classical mono-atomic gas (for which we refer the reader to section 2.4 in [7]), it is possible to express the adiabatic index $\Gamma$ as $\Gamma = 1 + k_B/(mC_v)$. Using this and equation 1.76, we can also express the pressure of a classical monoatomic fluid as

$$p = \rho\epsilon(\Gamma - 1) \tag{1.82}$$

with the corresponding specific enthalpy given by $h = c^2 + \epsilon\Gamma$ (equation 1.48). For a classical (non-degenerate) monoatomic gas, adiabatic index $\Gamma$ takes the values of 5/3 for a non-relativistic fluid, a value between 4/3 and 5/3 for a relativistic fluid, and 4/3 for an ultrarelativistic fluid. The two expressions for pressure also allow us to define a one-to-one correspondence between the specific internal energy $\epsilon$ and temperature $T$ as follows

$$T = \frac{m}{k_B}(\Gamma - 1)\epsilon \tag{1.83}$$

Typically, numerical relativity simulations evolve the specific internal energy $\epsilon$ within the 3+1 Valencia formulation and the temperature is computed from it.

We can also estimate the specific entropy of a fluid obeying the ideal gas EoS from the first law of thermodynamics (equation 1.47) and plugging in the definitions of pressure from equation 1.82

$$\frac{m}{k_B} ds = \left( \frac{d\epsilon}{\epsilon(\Gamma - 1)} - \frac{d\rho}{\rho} \right) = d\left( \ln \left[ \frac{\epsilon^{1/(\Gamma-1)}}{\rho} \right] \right) \tag{1.84}$$

which can be integrated to obtain

$$s = \frac{k_B}{m} \ln \left( \frac{\epsilon^{1/(\Gamma-1)}}{\rho} \right) + C \tag{1.85}$$

upto a constant of integration C. Finally, we will conclude this subsection with a computation of the sound speed for an ideal gas EoS. Using equation 1.80, it is trivial to show that

$$C_s^2 = \frac{\epsilon\Gamma(\Gamma - 1)}{c^2 + \Gamma\epsilon} \tag{1.86}$$

#### 1.2.4.2 The Polytropic equation of state

The polytropic equation of state is one of the most widely used ansatz for representing the equilibrium behavior of fluids in relativistic simulations. One of the reasons for their popularity is the phenomenological flexibility they provide to emulate several nuclear phenomena (for instance QCD phase transitions, the appearance of hyperons, etc.) when rigorous methods to model these from first principles are not available. A phenomenological approach gives a good idea of the qualitative behavior to be expected of these nuclear processes and how they manifest in the context of neutron star mergers.

The pressure $p$ in a polytropic EoS is given by

$$p = K\rho^{\Gamma} \tag{1.87}$$

where K is called the polytropic constant and $\Gamma$ is the adiabatic index.

To further emphasize the utility of a polytropic EoS, we report the leading order contribution to the pressure of a fully degenerate and non-relativistic electron fluid [7] which behaves like a non-relativistic polytrope ($\Gamma = 5/3$) and is given by

$$p(\rho) = \frac{1}{5}\left(\frac{3h_p^3}{4\pi g_s m^4}\right)^{2/3}\rho^{5/3} \tag{1.88}$$

Likewise, the leading order contribution to the pressure of a fully degenerate ultrarelativistic fluid of electrons is also a polytrope with $\Gamma = 4/3$. A rigorous treatment of such fluids would typically involve computing the properties ($p$, $n$, or $e$) of an ideal (non-interacting) relativistic Fermi gas under the assumption of complete degeneracy. However, as far as the leading order contribution is concerned, a polytropic ansatz would suffice.

As we can see from equation 1.87 there is no temperature dependence in pressure. This implies that there is an inherent freedom in choosing temperature which can be assumed to be 0 perfectly well. This is the reason why polytropic EoSs are reasonable models for cold and $\beta-$ equilibrated neutron stars. However, if one assumes the condition of an isentropic flow, i.e., the specific entropy is the same across the whole fluid, then the ideal gas EoS and the polytropic EoS are the same formulations and indeed one can be derived from the other provided $ds = 0$. The condition of an isentropic flow and coincidence with an ideal gas EoS, helps us to attribute a specific internal energy (or equivalently temperature) to a polytropic fluid. In particular, we can show from 1.47 that for a polytropic fluid which is also isentropic, the specific internal energy is given by

$$\epsilon = \frac{K\rho^{\Gamma-1}}{\Gamma - 1} \tag{1.89}$$

Likewise, the sound speed can be computed as

$$C_s^2 = \frac{(C_s^2)_N}{h} = \frac{p\Gamma(\Gamma-1)}{\rho(\Gamma-1)+\Gamma p} \tag{1.90}$$

Needless to say, when the polytropic EoS coincides with the ideal gas EoS for isentropic

flows, their entropies are the same and are given by equation 1.85. To provide greater flexibility to the polytropic equations of state so as to emulate nuclear processes, we can construct sequences of polytropic equations of state. Such an ansatz is called a piecewise polytropic equation of state expressed as

$$p(\rho) = \bigcup_{i}^{J} K_i \rho^{\Gamma_i} \tag{1.91}$$

where J is the total number of polytropic segments and each polytrope is valid within a given range of densities. The operator $\bigcup$ is the union operator on the collection of all polytropic segments. For self-consistency, we require that in such an EoS, the pressure and energy density (or equivalently the specific internal energy) be continuous at the point of transition between two polytropes. The sound speed (first derivative of pressure), however, will be discontinuous across the transition in general. The condition for the continuity of pressure at the transition density $\bar{\rho}_i$ is trivial and is expressed as

$$\begin{aligned} p_{i+1}(\bar{\rho}_i) &= p_i(\bar{\rho}_i) \\ K_{i+1} &= K_i \bar{\rho}_i^{\Gamma_i - \Gamma_{i+1}} \end{aligned} \tag{1.92}$$

Likewise, from the first law of thermodynamics 1.47 for an isentropic flow, we can derive the continuity condition for the energy density as

$$e_{i+1}(\bar{\rho}_i) = e_i(\bar{\rho}_i) \tag{1.93}$$

where $e_i(\rho) = K_i \rho^{\Gamma_i}/(\Gamma_i - 1) + C_i \rho$ and $C_i$ is a constant of integration given by

$$C_i = \frac{e_{i-1}(\bar{\rho}_{i-1})}{\bar{\rho}_{i-1}} - \frac{K_i \bar{\rho}_{i-1}^{\Gamma_i - 1}}{\Gamma_i - 1} \tag{1.94}$$

Temperatures in a neutron star merger typically reach several tens of MeV and the equilibrium behavior of matter cannot be sufficiently described by a cold EoS. To this aim, we conclude this subsection with a note on adding thermal effects to a cold EoS. This is done in a sort of hybrid formalism wherein a thermal component is added to a cold piecewise polytropic EoS. This thermal component (denoted by a subscript 'th') has a simple form given by the pressure-temperature relationship of an ideal gas. In concrete

terms, the total pressure and specific internal energy of a hybrid EoS (assuming a single polytrope) is expressed as

$$\begin{aligned} p &= p_{\rm c} + p_{\rm th} = K_{\rm c}\rho^{\Gamma_{\rm c}} + \rho\epsilon_{\rm th}(\Gamma_{\rm th} - 1) \\ \epsilon &= \epsilon_{\rm c} + \epsilon_{\rm th} \end{aligned} \tag{1.95}$$

where $K_{\rm c}$ and $\Gamma_{\rm c}$ are the polytropic constant and adiabatic index for the cold polytropic EoS and $\epsilon_{\rm th}$, $\Gamma_{\rm th}$ are the specific internal energy and adiabatic index for the thermal ideal gas correction. Typically a numerical relativity infrastructure evolves $\epsilon$ within the 3+1 Valencia formulation and $\epsilon_{\rm th}$ is computed from the difference $\epsilon - \epsilon_{\rm c}$ which is then utilized to compute the thermal correction to the pressure $p_{\rm th}$.

#### 1.2.4.3 The Equation of State for a degenerate relativistic fluid

In this subsection, we report on the EoS for a degenerate relativistic fluid, i.e., a fluid for which both quantum mechanics and relativistic effects are vital to describe its dynamics. We shall not make a distinction between the specific kind of species (like Fermions or Bosons) the particles belong to or what distribution function one should choose rather, we will present results for a generic class of relativistic fluids. We will also describe certain limits to the results obtained in full generality which can be suitable for a particular species for instance the massless approximation to describe an EoS for particles like photons or light quarks.

Speaking more concretely, we are interested in the class of fluids with large fugacity ($\alpha_f \gg 1$) and small relativistic coldness ($\zeta_c \ll 1$). Before embarking on the details of the procedure that constructs the EoS, it is useful to describe a class of integrals that we will encounter time and again in this subsection. The integral reads as follows

$$J_{nm}(\alpha_f, \zeta_c) = \int_0^\infty dx \frac{\sinh^n x \ \cosh^m x}{\exp(-\alpha_f + \zeta_c \cosh x) + \varepsilon} \tag{1.96}$$

In general, these integrals need to be evaluated numerically (see references [7, 22]) and we will leave our results in terms of $J_{nm}$ however, there do exist some limiting cases in which closed-form analytic expressions for these integrals are possible e.g. the zero temperature limit or the massless limit (see references [22, 33]).

Any model for the EoS should provide us with three equilibrium properies: the pressure $p$, the energy density $e$, and the number density of particles $n$ (or equivalently the rest mass density $\rho$). Using thermodynamic relations which we have described in

subsection 1.2.1, it is possible to compute all other quantities of interest such as entropy density or sound speed. Since we are not differentiating between the different kinds of distribution functions, it is optimal to consider a generalized form of the distribution function $f_0(p)$ given by equation 1.72.

Integrals involving relativistic distribution functions are evaluated over the Lorentz invariant quantity $d^3p/p^0$ which corresponds to the relativistic 4-momentum $p^a = (wmc, wmv^i)$ of a particle and where $p = p^i p_i$. The number density current 4-vector for a given distribution function $f_0(p)$ is defined as

$$N^a = \int c p^a f_0(p) \frac{d^3p}{p^0} \tag{1.97}$$

Likewise, we can re-define the energy-momentum tensor for the fluid in terms of a relativistic distribution function as follows

$$T^{ab} = \int c p^a p^b f_0(p) \frac{d^3p}{p^0} \tag{1.98}$$

The number density is given by $n = N^0/c$. Plugging the form of the generalized relativistic distribution function, we have

$$n = \int p^0 f_0(p) \frac{d^3p}{p_0} \tag{1.99}$$

At this stage, we will introduce a change of variables of the type $p^0 = mc\cosh x$ for $x \geq 0$. From special relativity, we know $p^0 = E/c$ and therefore from the equation of relativistic energy $E^2 = p^2c^2 + m^2c^4$ , it follows that $p = (p^i p_i)^{1/2} = mc\sinh x$. We also employ spherical coordinates in momentum space to write $d^3p = 4\pi p^2 dp$ so we have

$$\begin{aligned} n &= \frac{g_s}{h_p^3} 4\pi \int_0^\infty \frac{m^3c^3 \cosh x \sinh^2 x}{\exp(-\alpha_f + \zeta_c \cosh x) + \varepsilon} dx \\ &= 4\pi \frac{g_s}{h_p^3} (mc)^3 J_{21}(\alpha_f, \zeta_c) \end{aligned} \tag{1.100}$$

Next, we present a calculation for the energy density of a degenerate relativistic fluid by recalling the form of the energy-momentum tensor $T^{ab} = (e+p)u^a u^b + p g^{ab}$. Considering a flat spacetime ($\eta_{ab}$) and recalling the property for normalization of 4-velocity, the energy density can be computed as follows

$$e = T^{ab} u_a u_b$$

$$
\begin{aligned}
&= c\frac{g_s}{h_p^3}\int_0^\infty \frac{(p^a u_a)(p^b u_b)4\pi p^2}{\exp(-\alpha_f - cp^d u_d/k_B T)+\varepsilon}\frac{d^3p}{p^0} \\
&= 4\pi c\frac{g_s}{h_p^3}(mc)^4\int_0^\infty \frac{\sinh^2 x\cosh^2 x}{\exp(-\alpha_f+\zeta_c\cosh x)+\varepsilon}dx \\
&= 4\pi c\frac{g_s}{h_p^3}(mc)^4 J_{22}(\alpha_f,\zeta_c) \qquad (1.101)
\end{aligned}
$$

wherein we have utilized the relation $p^a u_a = -p^0 = -mc\cosh x$ which is valid in the local fluid frame. Finally, the pressure for the fluid can be computed from the above two definitions of $n$ and $e$ by using

$$
p = \frac{1}{3}\left(T^{ab}\eta_{ab} + e\right) \qquad (1.102)
$$

The first term will be simplified to

$$
\begin{aligned}
T^{ab}\eta_{ab} &= -4\pi c\frac{g_s}{h_p^3}(mc)^4\int_0^\infty \frac{\sinh^2 x}{\exp(-\alpha_f+\zeta_c\cosh x)+\varepsilon}dx \\
&= -4\pi c\frac{g_s}{h_p^3}(mc)^4 J_{20}(\alpha_f,\zeta_c) \qquad (1.103)
\end{aligned}
$$

which gives the pressure as

$$
\begin{aligned}
p &= \frac{1}{3}4\pi c\frac{g_s}{h_p^3}(mc)^4\left(J_{22}(\alpha_f,\zeta_c) - J_{20}(\alpha_f,\zeta_c)\right) \\
&= \frac{1}{3}4\pi c\frac{g_s}{h_p^3}(mc)^4 J_{40}(\alpha_f,\zeta_c). \qquad (1.104)
\end{aligned}
$$

Here we have made use of a property (see reference [22]) of the integrals of the form 1.96 that $J_{22} - J_{20} = J_{40}$. This is something that can be cross-verified from the finite temperature expressions for the same system found in reference [34].

The framework we have introduced in this subsection and the expressions we have derived for $n$, $e$, and $p$ for a degenerate relativistic fluid can be used to model an ideal (i.e. interaction-free) behavior of several nuclear species at finite temperature e.g., neutrons, protons, electrons, photons, deconfined quarks, trapped neutrinos in weak and thermal equilibrium, etc. Contemporary nuclear EoS models derived from formalisms such as relativistic mean field theory or chiral effective field theory, take the above ideal behavior as a starting point and add interaction terms in an attempt to emulate a degree of realism. A description of these models is well beyond the scope of our work and for our purposes, they will only be correction terms to the ideal behavior.

**The massless limit**

We will now turn to discuss an important limit to the properties of a degenerate relativistic fluid which is the masless limit or the ultrarelativistic limit. This limit is very useful to model the properties of particles with extremely small masses such as trapped neutrinos in $\beta-$equilibrium, light quarks, ideal Bose gas models of a gas of gluons, a gas of photons etc. Any dependence on the rest mass vanishes in this limit as we shall see. Another interesting attribute of the ultrarelativistic limit is the fact that pressure and energy density are directly proportional according to $p = e/3$. This is also a result that holds for a radiation fluid such as a gas of photons.

In terms of the relativistic coldness, the ultrarelativistic limit is $\zeta_c \ll 1$. Here, we make yet another change of variables which is $z = \zeta_c \cosh x$ and assert that $(z/\zeta_c)^2 \approx \cosh^2 x - 1 = \sinh^2 x$. We can then recast the integral 1.96 as follows

$$\begin{aligned} J_{nm}(\alpha_f, \zeta_c) &= \int_0^\infty dx \frac{\sinh^n x \ \cosh^m x}{\exp(-\alpha_f + \zeta_c \cosh x) + \varepsilon} \\ &= \frac{1}{\zeta_c^q} \int_0^\infty \frac{z^{q-1}}{\exp(-\alpha_f + z) + \varepsilon} dz \\ &= K_q(\alpha_f) \end{aligned} \tag{1.105}$$

where $q = m + n$. Here we will express our results in terms of the integral $K_q(\alpha_f)$ which for $\varepsilon = 1$ becomes the Fermi integral. Using the standard procedure for the computation of $n$, $e$ and $p$ outlined above, we will now present the results for these quantities in the ultrarelativistic limit.

- $n = 4\pi(g_s/h_p^3)\left(k_B T/c\right)^3 K_3(\alpha_f)$
- $e = 4c\pi(g_s/h_p^3)\left(k_B T/c\right)^4 K_4(\alpha_f)$
- $p = (4c/3)\pi(g_s/h_p^3)\left(k_B T/c\right)^4 K_4(\alpha_f) = e/3$

**The zero temperature limit**

We will conclude this subsection with another important limit that of the zero temperature. Many a time it is not very desirable to include the entirety of finite temperature treatment (by the evaluation of integrals of the type 1.96) to get a qualitative idea of the dynamics in a merger. For instance, reasonable estimates in a merger simulation may be obtained by adding an ideal gas thermal component to a cold EoS model. To do so, one needs to have a reasonable model for the equilibrium behavior at zero temperature. This may be achieved either by a sequence of polytropes (1.2.4.2) or by taking the zero

temperature limit of the expressions for $n$, $e$ and $p$ obtained in this subsection. A zero temperature limit is only taken for Fermionic species and in the most precise terms, it is the assumption of complete degeneracy. This means that all states below the Fermi energy have been occupied. We caution the reader that when we mention zero temperature, we are not referring to an absolute zero. Isolated neutron stars in equilibrium may be cold enough so that their temperatures are in the keV regime which is effectively 3-5 orders of magnitude smaller on the high-energy temperature scale of 10s-100s of MeV (set by mergers of neutron stars and heavy ion collisions) and is effectively negligible.

In the following, we describe the zero temperature limit of the expressions for $n$, $e$, and $p$ for an ideal Fermi Gas (that is $\varepsilon = +1$). A vanishing temperature is equivalent to imposing the condition $\exp(-\alpha_f + \zeta_c) \to 0$ and consequently, the Fermi-Dirac distribution function 1.72 becomes a step function, i.e., unity for values of energy less than Fermi energy i.e. $E/\mu \leq 1$ and 0 for $E/\mu > 1$. Another convenient facet of these integrals in the limit of zero temperature is that closed-form analytic expressions are readily available in references such as [35].

In the zero temperature limit, the number density now reads

$$n = 4\pi \frac{g_s}{h_p^3} \int_0^{p_F} p^2 dp = \frac{4\pi}{3} \frac{g_s}{h_p^3} p_F^3 = \frac{1}{3} \frac{g_s}{2\pi^2} k_F^3 \tag{1.106}$$

where in the last step, we have expressed our results in the units of $G = c = \hbar = 1$. We will begin to drop these constants as the expressions begin to get too cumbersome to keep track of them. The upper limit of the integral $p_F = \hbar k_F$ is the Fermi momentum provided by the relation $p_F = (\mu_F^2 - m^2)^{1/2}$ and $\mu_F$ is the same as Fermi energy $E_F$.

The expression for energy density in the zero temperature limit is now given by

$$\begin{aligned} e &= \frac{g_s}{2\pi^2} \int_0^{k_F} \left(k^2 + m^2\right)^{1/2} k^2 dk \\ &= \frac{g_s}{2\pi^2} \left[ k_F \left(k_F^2 + m^2\right)^{3/2} - \frac{1}{2} m^2 k_F \left(k_F^2 + m^2\right)^{1/2} - \frac{1}{2} m^4 \ln \left( \frac{(k_F^2 + m^2)^{1/2} + k_F}{m} \right) \right] \end{aligned} \tag{1.107}$$

Finally, the pressure $p$ in the zero-temperature limit is given by

$$p = \frac{1}{3} \frac{g_s}{2\pi^2} \int_0^{k_F} \frac{k^4}{(k^2 + m^2)^{1/2}} dk$$

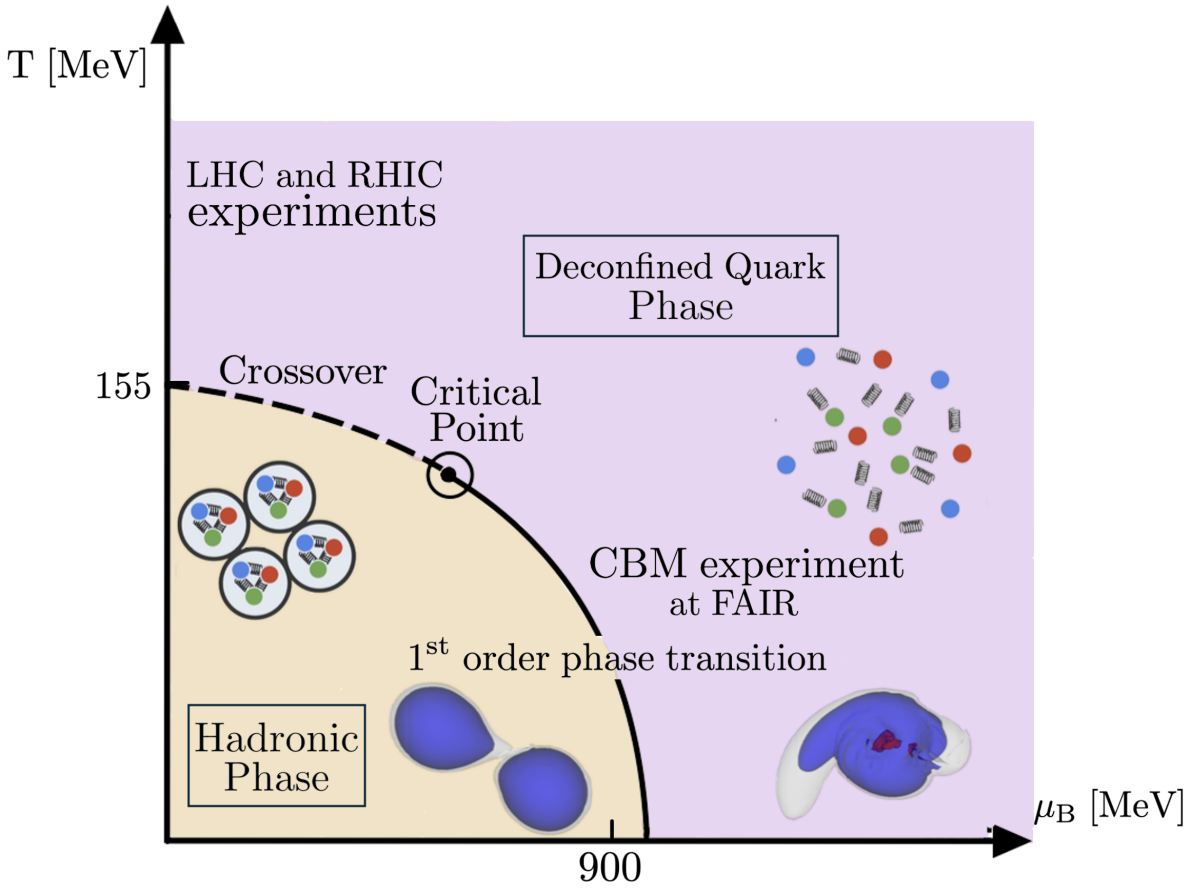


**Figure 1.4.** A schematic diagram of the phases of strongly interacting matter. Shown is a phase boundary between a deconfined quark phase and a confined hadronic phase which terminates at a critical point. The precise position of the critical point is, as of now, not well understood at finite baryon chemical potential. We also show the approximate positions occupied by a merger of neutron stars assuming a first order phase transition were to take place. The figures are not to scale in length.

$$= \frac{1}{3}\frac{g_s}{2\pi^2}\frac{1}{4}\left[k_F^3\left(k_F^2+m^2\right)^{1/2} - \frac{3}{2}m^2k_F\left(k_F^2+m^2\right)^{1/2} + \frac{3}{2}m^4\ln\left(\frac{(k_F^2+m^2)^{1/2}+k_F}{m}\right)\right] \tag{1.108}$$

### 1.2.5 QCD Phase Transitions

One of the long-standing problems in quantum chromodynamics (QCD) is a precise determination of the phases of strongly interacting matter. The vast majority of matter in our day-to-day lives is hadronic which is to say that the elementary quarks (the up quark $u$ and the down quark $d$) that make up protons and neutrons exist in confined states with the strong nuclear force between them being mediated by gluons. These confined

states are characteristic of the hadronic phase: the low-temperature and the low-density region in the phase structure of QCD as reported in figure 1.4. The adjective 'low' here is relative to the MeV energy scales in high-energy physics wherein temperatures of the order of keV (about $10^7$ K) are considered low. The theory of QCD is asymptotically free which means that at large enough energies including temperatures reaching tens of MeVs and/or densities reaching several times that of nuclear saturation ($2.7 \times 10^{14}\text{gcm}^{-3}$), the strong interactions holding the quarks together begin to weaken. Therefore at such energy scales, it is conceivable that confined states of quarks may undergo a transition to a phase of deconfined quarks. The precise nature of this transition, i.e., whether it is of the first order as in a liquid-vapor phase transition or whether it proceeds continuously is an area of active research. Lattice QCD calculations and heavy ion collision experiments have provided valuable insight into the nature of such a phase transition at vanishing densities and high temperatures. As such, it is fairly well established that the transition to a phase of deconfined quarks at vanishing densities proceeds through a crossover with a critical temperature near 155 MeV. However, the inapplicability of QCD methods at finite densities, makes it currently challenging to determine the precise nature of this phase transition.

Fortunately, with the advent of gravitational wave astronomy, it has now become possible to observe mergers of neutron stars using gravitational waves. Neutron stars and their mergers occupy the cold and dense part of the phase structure of QCD, thereby providing us with density scales that are impregnable by any terrestrial laboratory. In this and the following subsections, we shall be discussing a model of an EoS for a phase of deconfined quark matter as well as the two important constructions for a first order phase transition that are used to stitch together a hadronic EoS at low densities with a quark EoS at high densities. As we will notice, the choice of a particular construction has a profound impact on the stellar structure of a neutron star. Further, an exploration of how this choice manifests in a merger of two neutron stars is what forms the crux of this dissertation.

#### 1.2.5.1 The quark matter EoS: MIT Bag Model

The MIT Bag model [36] provides us with a simple phenomenological method to model the equilibrium behavior of strongly interacting matter at high densities where the dominant degrees of freedom are deconfined quarks consisting of the three lightest flavors, i.e., the up quark ($u$), the down quark ($d$) and the strange quark ($s$). Despite its simplicity as compared to involved models of nuclear theory formalisms that are used to describe the

hadronic phase (corrections to the ideal Fermi gas that we referred to in the previous subsection), the MIT Bag model can provide robust insights into the nature of the deconfined quark phase. The model states that the energy associated when quarks are present in a volume $V$ consists of two contributions. The mere presence of quarks in a volume $V$ has an energy budget of $BV$ where the energy density $B$ is called the Bag constant. The second contribution comes from the kinetic motion of quarks. When quarks are confined within hadrons, it is assumed that they are free to move but no current crosses the hadronic boundary. When the quarks are deconfined, the kinetic contribution to their energies is modeled by an ideal Fermi gas which we have discussed at length in the previous subsection.

It turns out that the precise value for $B$ is important. There are admissible values for $B$ which may result in the energy per nucleon being less than that of the most bound Fe-56 nucleus thereby implying that ordinary matter is in a metastable state of decay to the so-called strange quark matter. This is called the Bodmer-Witten hypothesis and forms the subject matter of investigation in chapter 4. According to the MIT Bag model, the $n$, $e$, and $p$ of an ideal Fermi gas of deconfined quarks is given by the following expressions (in $G = c = \hbar = 1$) units [34]:

$$n = \sum_i \frac{1}{3} \frac{g_s}{2\pi^2} \int_0^\infty k^2 E_i(k) \left( f_0(k, \mu_i) + f_0(k, -\mu_i) \right) \frac{dk}{m_i E_i} \tag{1.109}$$

$$e = \sum_i \frac{g_s}{2\pi^2} \int_0^\infty k^2 E_i(k)^2 \left( f_0(k, \mu_i) + f_0(k, -\mu_i) \right) \frac{dk}{E_i} + B \tag{1.110}$$

$$p = \sum_i \frac{1}{3} \frac{g_s}{2\pi^2} \int_0^\infty k \frac{\partial E_i(k)}{\partial k} k^2 \left( f_0(k, \mu_i) + f_0(k, -\mu_i) \right) dk - B \tag{1.111}$$

$$\tilde{s} = S/V = \left( \frac{\partial p}{\partial T} \right)_{V, \mu_i} \tag{1.112}$$

In these expressions, a factor of $1/3$ accounts for the fact that there are 3 quarks per baryon, and the degeneracy factor for quarks $g_s$ is 6 for each quark flavor. The summation index $i$ runs over $u, d$, and $s$ quarks. The expression $E_i(k) = (k^2 + m_i^2)^{1/2}$ is the total relativistic energy of the $i^{\text{th}}$ quark flavor and $f_0(k, -\mu_i)$ is the distribution function for the antiparticle. It is easy to establish an analogy with the equations of a degenerate relativistic fluid in subsection 1.2.4.3. Finally, $\tilde{s}$ in these equations represents an entropy density not to be confused with the specific entropy $s$.

A very interesting facet of this model can be noted from the expression for pressure

where the Bag constant $B$ appears with a negative sign. In the case where the Bag model describes a strange star which is a compact object made up entirely of $u, d$ and $s$ quark matter (and will be explored in detail in chapter 4), this implies that the Bag 'pressure' assists the inward gravitational pressure to balance the outward Fermi pressure of the quarks. This also means that strange stars are self-bound in that such stars can maintain their shape even in the absence of gravity. This is contrary to the standard compact objects with which we are familiar like white dwarfs or neutron stars that are instead gravitationally bound.

We conclude this subsection with a brief comment. We have considered a model for the three lightest quark flavors. Many a time (e.g. in chapter 2 and 4), the up quark and the down quark are considered massless as they are much lighter relative to the strange quark. This is a direct application of the zero-mass limit for an ideal Fermi gas that we mentioned in section 1.2.4.3, the exact expressions for which can be found in the reference [34]. In addition to this, in chapter 4, we have contrasted the finite temperature EoS of strange quark matter described by the MIT Bag model with the hybrid EoS of strange quark matter. For the latter case, we have made use of the zero temperature limit of the same EoS and corrected it with an ideal gas thermal correction, another direct application of the complete degeneracy approximation we saw in subsection 1.2.4.3.

#### 1.2.5.2 Stitching the hadronic and quark phases: Maxwell and Gibbs constructions

Having discussed robust formulations for the low-density hadronic EoS and the high-density quark EoS, we now turn our attention to the methods that are used to match these equations of state in a coexistence region (mixed quark phase). We shall discuss two such constructions that are commonly used in the modeling of $1^{\text{st}}$ order phase transitions from a hadronic phase to a deconfined phase of quarks. These constructions are called the Maxwell construction and the Gibbs construction. Drawing from the analogy of the classic example of $1^{\text{st}}$ order phase transitions in water, we recall that such a phase transition proceeds by maintaining a constant pressure through the transition densities. This is in effect a re-statement of the fact that volume (or equivalently density), a derivative (inverse derivative) of Gibbs Free energy at a constant temperature undergoes a discontinuity. Indeed, when the possibility of phase transitions inside the cores of neutron stars was first considered, a model of the constant-pressure phase transition was proposed to explain such behavior. However, there exists a caveat with this picture which is that the general relativistic stellar structure equations (the TOV equations)

for a compact object such as a neutron star mandate that the pressure in the interior of a neutron star be monotonically increasing as one descends from the surface to the core. A region of constant pressure for a range of densities would essentially imply that an annular volume of neutron star material is mapped onto the same radial surface which is contradictory to the structure of a neutron star. Thus the constant pressure configurations are not stable configurations for a neutron star.

Another important aspect of the problem is that the phase transitions for water exist in a simple system with one conserved charge meaning that the number of water molecules is constant. A neutron star is a more complex system in that there can be multiple conserved charges like baryon number and electric charge. Corresponding to each conserved charge, there exists a chemical potential and in the case of neutron stars these are the baryon chemical potential $\mu_B$ and the electric chemical potential $\mu_q$. The total chemical potential $\mu_i$ for a particle of species $i$ can be expressed as

$$\mu_i = B_i\mu_B + q_i\mu_q \tag{1.113}$$

where $B_i$ is the baryon number of $i$ and $q_i$ is its electric charge in units of e - the electronic charge. From the above equation, it is straightforward to see that $\mu_B = \mu_n$, the chemical potential of a neutron, and $\mu_q = -\mu_e$ is the negative of the chemical potential of an electron. Armed with these definitions, we can express the chemical potentials of the $u, d$ and $s$ quarks in terms of $\mu_n$ and $\mu_e$ as follows

$$\mu_u = \frac{1}{3}\mu_n - \frac{2}{3}\mu_e \tag{1.114}$$

$$\mu_d = \frac{1}{3}\mu_n + \frac{1}{3}\mu_e \tag{1.115}$$

$$\mu_s = \frac{1}{3}\mu_n + \frac{1}{3}\mu_e = \mu_d \tag{1.116}$$

The chemical potential too is one of the derivatives of Gibbs free energy at a constant temperature and pressure and if it is discontinuous across a phase boundary, it can be used in the construction of a first-order phase transition. This is precisely the difference between Maxwell and Gibbs constructions for the mixed phase. Maxwell construction enforces charge neutrality in the two phases separately but not in the transition region. In other words, there is local charge neutrality but not global charge neutrality. Mathematically, the conditions for a mixed phase constructed using the

Maxwell construction are as follows [37]

$$\begin{aligned} p_H &= p_Q \\ T_H &= T_Q \\ \mu_{B,H} &= \mu_{B,Q} \\ \mu_{q,H} &\neq \mu_{q,Q} \end{aligned} \tag{1.117}$$

where the subscripts $H$ and $Q$ mean that the corresponding quantities are to be computed for the hadronic and quark phases respectively. Thus we see that owing to a discontinuity in the electric chemical potential across the phase boundary, a motion of electrons from a region of higher electric chemical potential to lower electric chemical potential takes place, thereby developing a strong electrostatic field.

Gibbs construction on the other hand enforces global charge neutrality thereby requiring that both $\mu_B$ and $\mu_q$ be continuous across the phase transition boundary. The conditions for the same are as follows

$$\begin{aligned} p_H &= p_Q \\ T_H &= T_Q \\ \mu_{B,H} &= \mu_{B,Q} \\ \mu_{q,H} &= \mu_{q,Q} \end{aligned} \tag{1.118}$$

Enforcing global charge neutrality typically has the effect of producing a large mixed phase where deconfined quarks exist in conjunction with hadrons.

It is essential to compare the attributes of the two constructions for phase transitions in neutron stars. The Maxwell construction results in a gravitational separation of the confined quark phase and the pure deconfined quark phase as a result of the constant pressure configurations being excluded from stable configurations. This also means that the pure quark phase is easier to access by the fluid's thermodynamic state - either in a dense neutron star or in a merger remnant. In this regard, the Maxwell construction is closer to the first-order phase transition in water. On the other hand, even though Gibbs construction preserves the global charge neutrality of a star as well as the monotonicity of pressure, it may result in such a highly energetic pure quark phase that is inaccessible to the neutron star fluid. This is precisely the case with the EoS model employed in chapter 2.

In figure 1.5, we show the differences between the Maxwell and Gibbs construction for

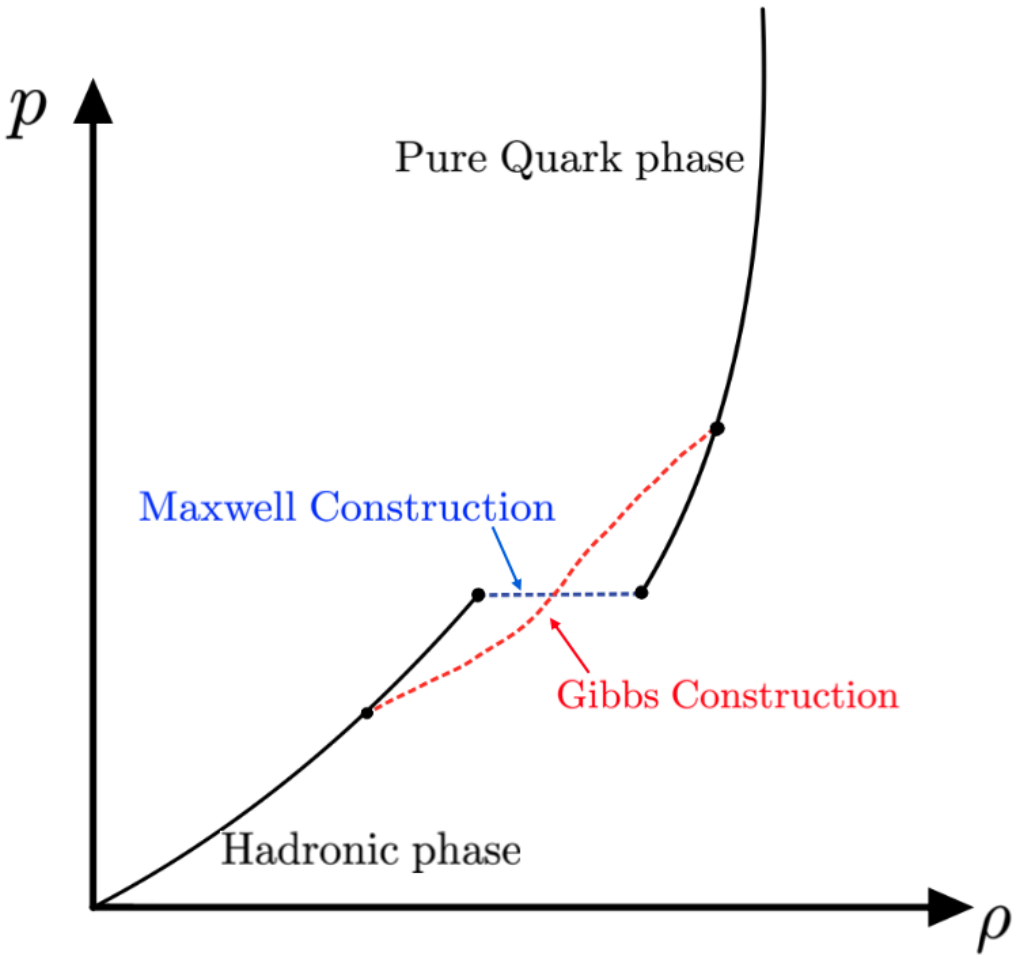


**Figure 1.5.** A schematic diagram comparing the cold pressure-density profiles for a hadron-quark hybrid EoS constructed from Maxwell and Gibbs constructions.

a mixed phase in the pressure-density phase space. While Maxwell construction resembles the familiar constant pressure phase transition found in water, Gibbs construction ensures the monotonicity of pressure as required by TOV equations. We refer the reader to references [37, 38] for an elaborate discussion comparing the two constructions of first-order phase transitions. Reference [37] uses the MIT Bag model for the high-density pure quark phase and shows that upon increasing the Bag's constant, the mixed phase with Gibbs construction widens and the EoS becomes softer. This is to be expected because now the inward gravitational pressure is assisted by a stronger degeneracy pressure to compactify the star. The authors also report the TOV sequences for the two constructions of deconfinement phase transitions. Owing to the constancy of pressure in the Maxwell construction, the mixed phase in an isolated non-spinning neutron star is ruled out and this results in an unstable branch with the Maxwell construction with a positive M-R

slope (figure 4 in reference [37]).

To conclude, the stellar structure is indeed very sensitive to the choice of construction employed for the phase transition. One of the main objectives of this dissertation is to investigate the sensitivity of these choices in the context of neutron star mergers. As we shall see in this dissertation, there will be profound impacts of the type of phase transition, i.e., a GIbbs construction or a Maxwell construction and the exact models used for the hadronic and pure quark phases on the outcomes of neutron star mergers. We shall postpone more on this discussion to the conclusions in chapter 7.

### 1.2.6 The Tolman Oppenheimer Volkoff (TOV) Equations

We shall now begin with a discussion of the equations for stellar structure. Different classes of stars need slightly different modeling to describe their structure, which in all cases, is premised upon the requirement of hydrostatic equilibrium. The precise physics that governs such an equilibrium is based on the nature of the star in question. For instance, main sequence stars need a balance between the radially outward gaseous and radiation pressure sourced from nuclear fusion and the inward pressure of gravity. To describe their structure, classical physics for the gas pressure and Newtonian gravity for the inward pressure may suffice. Moving to the stellar graveyard, we encounter compact objects such as White dwarfs. Here too, one can comfortably get along with just Newtonian gravity for the inward gravitational pressure, but the radially outward electron degeneracy pressure is a quantum mechanical effect that comes from Pauli's exclusion principle. A classical treatment (Maxwell-Boltzmann distribution) will need to be abandoned. An even more compact category is that of the neutron stars where the electrons and protons combine to form neutrons and the electron degeneracy pressure is now replaced by a much stronger neutron degeneracy pressure. Here, owing to the substantial curvature of spacetime, one needs to resort to a general relativistic description of the gravitational force in tandem with quantum mechanics for the structure of the star. Yet another interesting category of compact objects is that of the still-theorized strange stars that are made up entirely of deconfined quark matter. A description of their stellar structure will require, like neutron stars, quantum mechanics to account for the outward 'quark' degeneracy pressure and a general relativistic description of gravity.

We do however caution the reader that such a classification of the importance of quantum mechanics and general relativity models is qualitative at best and indeed very sensitive to the type of problem at hand. For instance, general relativity may not be very useful to describe the structure of the sun any better than Newtonian gravity however, if

we were to consider planetary orbits, the precession of Mercury is a general relativistic effect.

We begin with a brief comment on the stellar structure equations of white dwaefs. Isolated and non-spinning white dwarfs have a rather simple description of the underlying equation of state. Having an average temperature of $10^4$ K, white dwarf matter can be modeled as completely degenerate electrons and is an ideal candidate to be described by a zero-temperature equation of state as we discussed in subsection 1.2.4.3. As we have seen, to first order, the equation of state can be given as a polytrope with $\Gamma = 4/3$ or $5/3$ depending upon whether the electrons are ultra-relativistic or non-relativistic. S. Chandrashekar described the stellar structure of a white dwarf [39] using an interpolation between these two polytropes and employing the Lane-Emden equations which are given by

$$\frac{1}{r^2}\frac{d}{dr}\left(\frac{r^2}{\rho}\frac{dp}{dr}\right) = -4\pi\rho \tag{1.119}$$

Given a central density $\rho_c$ and a cold EoS, $p = p(\rho)$, the lane-Emden equations solve for $\rho = \rho(r)$ which then provides $p = p(r)$. The radius of the star $R$ is computed by requiring a vanishing pressure at the surface, i.e., $p(r = R) = 0$. Finally, the mass of the white dwarf is given by

$$M = \int_0^R \rho(r) 4\pi r^2 dr. \tag{1.120}$$

A fixed value of $\rho_c$ corresponds to a given configuration of a white dwarf. We can construct a sequence of white dwarf configurations by solving the Lane-Emden equations iteratively corresponding to a sequence of $\rho_c$s. It turns out that for a completely degenerate Fermi (electron) gas, the sequences from Lane-Emden equations predict a vanishing radius at a mass called the Chandrashekhar mass which is around $1.4M_\odot$. This mass sets a limit to the maximum mass of an isolated and non-rotating white dwarf in equilibrium and is also called the Chandrashekhar limit. It is straightforward to show a derivation of the equation 1.119 from Eüler equations of gas dynamics in Newtonian gravity and assuming spherical symmetry. For brevity, we shall skip the derivation here and point the reader to Chapter 12 in the reference [7] for the same.

We now turn our attention to the relativistic generalization of equation 1.119 called the Tolman Oppenheimer and Volkoff equation, whose contemporary form was first derived by J. Robert Oppenheimer and George Volkoff in [42]. The TOV equation describes the structure of a spherically symmetric object in general relativity. They have found applications in describing the structures of cold and $\beta-$ equilibrated neutron stars and more recently, strange stars. Here too we shall be using as input, the cold EoS which

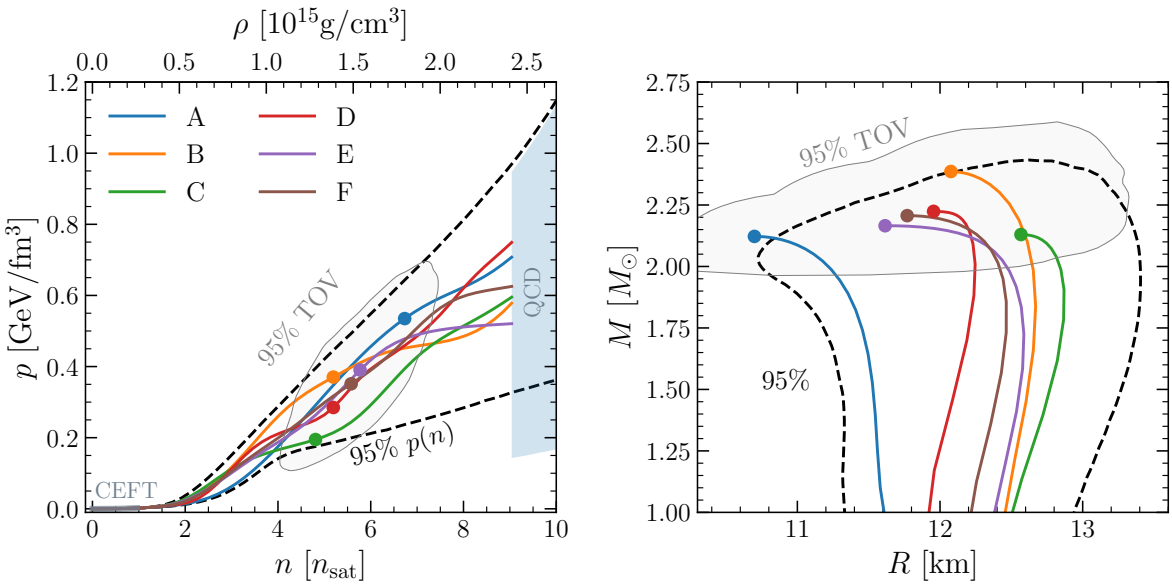


**Figure 1.6.** *Left Panel*: Shown in solid colored lines are the cold equations of state in the pressure-number density space taken from the reference [40]. These EoSs are representative of the entire EoS dataset, whose 95 % credible intervals have been shown with black dotted lines. Also shown are bounds from the Chiral effective field theory (CEFT) and QCD. *Right Panel*: The mass-radius sequences of isolated and non-spinning neutron star configurations corresponding to the EoSs shown in the left panel. The grey contour in both panels represents the 95% credible interval of a joint probability distribution of pressure-density (left panel) and mass-radius (right panel). Colored circles correspond to the maximum mass configurations in both panels. The image has been reproduced from the reference [41] under the terms of the Creative Commons CC BY 4.0 license.

is to say, the neutron star matter is composed of a completely degenerate Fermi fluid of neutrons providing an outward neutron degeneracy pressure.

We begin with the metric of spacetime in the exterior of a static (non-rotating) and spherically symmetric star. Birkhoff's theorem states that the only vacuum solution for Einstein's equation which is static and spherically symmetric is the Schwarzschild solution. Therefore the spacetime in the exterior of the star, i.e., $\forall r \geq R$ in spherical polar coordinates can be given by

$$ds^2 = g_{ab}dx^a dx^b = -\left(1 - \frac{2M}{r}\right)dt^2 + \left(1 - \frac{2M}{r}\right)^{-1} dr^2 + r^2 d\theta^2 + r^2 \sin^2\theta d\varphi^2 \quad (1.121)$$

where the metric $g_{ab}$ is the Schwarzschild metric given by

$$g_{ab} = \begin{pmatrix} -\left(1-\frac{2M}{r}\right) & 0 & 0 & 0 \\ 0 & \left(1-\frac{2M}{r}\right)^{-1} & 0 & 0 \\ 0 & 0 & r^2 & 0 \\ 0 & 0 & 0 & r^2\sin^2\theta \end{pmatrix}. \tag{1.122}$$

and the constant $M > 0$ has the interpretation of the total gravitational mass of the star. Such a metric is straightforward to derive from the Einstein's equations under the assumptions of a static and spherically symmetric spacetime. The metric $g$ will set the necessary boundary conditions required for a numerical solution of the TOV equations.

Now within the star, the metric is still spherically symmetric and static however, we no longer have a vacuum but matter described by the energy-momentum tensor $T_{ab}$ sourcing the curvature of spacetime. Nevertheless, the metric in the interior of the star, i.e, $\forall r < R$ can be expressed as follows

$$g_{ab} = \begin{pmatrix} -e^{2\phi(r)} & 0 & 0 & 0 \\ 0 & e^{2\lambda(r)} & 0 & 0 \\ 0 & 0 & r^2 & 0 \\ 0 & 0 & 0 & r^2\sin^2\theta \end{pmatrix}. \tag{1.123}$$

where $\phi$ and $\lambda$ are exclusively functions of the radial coordinate and are called the metric potentials. Given this metric, one can now compute the Einstein tensor and write Einstein's equations (in the fluid frame) 1.9 (see [43] for a reference) as

$$\begin{aligned} G^t_t &= \frac{1}{r^2}\left(e^{-2\lambda}-1\right) - \frac{2}{r}\frac{d\lambda}{dr}e^{-2\lambda} = 8\pi T^t_t = -8\pi e \\ G^r_r &= \frac{1}{r^2}\left(e^{-2\lambda}-1\right) + \frac{2}{r}\frac{d\phi}{dr}e^{-2\lambda} = 8\pi T^r_r = 8\pi p \\ G^\theta_\theta &= G^\varphi_\varphi = \left(\frac{d^2\phi}{dr^2} + \left(\frac{d\phi}{dr}+\frac{1}{r}\right)\left(\frac{d\phi}{dr}-\frac{d\lambda}{dr}\right)\right)e^{-2\lambda} = 8\pi p \end{aligned} \tag{1.124}$$

Integrating the equation for the time-time component (assuming $\lambda(r)$ to be analytic at 0) and introducing the mass function $m(r)$ as the mass contained within a radius r as

$$m(r) = \int_0^r e(s)4\pi s^2 ds, \tag{1.125}$$

we get

$$e^{-2\lambda(r)} = \left(1 - \frac{2}{r}m(r)\right) \forall r \leq R. \tag{1.126}$$

Substituting this in the equation for the radial-radial component, it is straightforward to show that

$$\frac{d\phi}{dr} = \frac{4\pi r^3 p(r) + m(r)}{r(r - 2m(r))}. \tag{1.127}$$

At this stage, we invoke the conservation of energy and momentum, i.e, $\nabla_a T^{ab} = 0$. We can compute the spatial projection of this equation as

$$h^c_b \nabla_a T^{ab} = 0 \tag{1.128}$$

where $h_{ab} = g_{ab} + u_a u_b$. From this equation, it follows that

$$(e + p)a^c = -h^{ac}\partial_a p \tag{1.129}$$

where $a^b$ is the four acceleration of the fluid defined as $a^b = u^c \nabla_c u^b$. This equation tells us that the relativistic acceleration is proportional to the gradient of pressure, a result that resonates with the Newtonian picture of hydrostatic equilibrium. One may also show that the only non-trivial equation from the above relation corresponds to the index $c$ being the radial coordinate. In other words,

$$-(e + p)\frac{d\phi}{dr} = \frac{dp}{dr}. \tag{1.130}$$

Substituting this equation in equation 1.127, one gets the standard form of the TOV equation as

$$\frac{dp}{dr} = \frac{-(e(r) + p(r))(m(r) + 4\pi r^3 p(r))}{r(r - 2m(r))} \tag{1.131}$$

Given a specification of a cold EoS and a central energy density $e_c$, the TOV equation, just like the Lane-Emden equations can also be used to solve for pressure and density profiles of an isolated non-rotating neutron star. Likewise, for a sequence of $e_c$, one may construct sequences of mass and radii of multiple non-rotating neutron star configurations that obey the same EoS. In figure 1.6, we show the mass-radius sequences computed by iterative solutions of the TOV equations for a set of cold $\beta-$ equilibrated equations of state. These equations of state have been taken from ref. [40] and have been constructed to cover a large parameter space of contemporary nuclear models consistent with constraints from nuclear theory.

We conclude this subsection with a comment on the computation of total mass and radii. Like the Newtonian case, the radius of a compact object from TOV equations can be computed by requiring a vanishing pressure, i.e., $p(r = R) = 0$. There are, however, two notions of mass: a gravitational mass which appears in the metric, and the Baryonic mass which is the total mass of all species comprising the star. In a Newtonian framework, these are the same thing, however in a relativistic framework, the gravitational mass is always smaller than the baryonic mass because the deficit is released as the binding energy to form a stable system. The gravitational and Baryonic masses are respectively given by

$$\begin{aligned} M_G &= \int_0^R 4\pi r^2 e(r) dr \\ M_B &= \int_0^R \frac{4\pi r^2 e(r)}{\left(1 - \frac{2m(r)}{r}\right)^{1/2}} dr > M_G \end{aligned} \tag{1.132}$$

## 1.3 Neutrino Radiation Transport

We shall now provide a quick overview of the details of neutrino transport in our merger simulations. As we have remarked earlier, neutrinos are involved in weak reactions that produce out-of-equilibrium effects [30–32]. Consequently, to describe their transport consistently, the full Boltzmann equation needs to be solved. This is, unfortunately, easier said than done. The Boltzmann equation is an equation in 7 variables and solving it in tandem with the equations of general relativistic hydrodynamics is computationally very prohibitive. All the simulations presented in this dissertation have been performed using a neutrino leakage + M0 scheme see ref. [23, 24] and the references therein except for the simulations in chapter 5 which have been performed with the more advanced M1 [25] scheme. We also direct the reader to an excellent review [28] on the state-of-the-art neutrino transport algorithms in neutron star mergers.

In the absence of weak reactions, in addition to the baryon number being conserved, the proton number given as $n_p = n_e = nY_e$ is also conserved. Here $n$ is the baryon number density and $Y_e$ is the electron fraction of the fluid. In other words,

$$\begin{aligned} \nabla_a (n u^a) &= 0 \\ \nabla_a T^{ab} &= 0 \end{aligned} \tag{1.133}$$

However, in the presence of weak reactions, the proton number is not conserved and is instead evolved along with $Y_e$ as

$$\begin{aligned} \nabla_a(nu^a) &= 0 \\ \nabla_a(nY_e u^a) &= R \\ \nabla_a T^{ab} = \Psi^a &= Q u^a \end{aligned} \tag{1.134}$$

where $R$ is the net lepton number emission or absorption rate per unit volume in the rest-frame of the fluid, i.e., $u_a = (-1, 0, 0, 0)$ and $Q$ is the net neutrino cooling or heating rate per unit volume in the rest frame of the fluid. In our code, `WhiskyTHC`, neutrinos are classified into trapped neutrinos (trapped within the remnant) which are treated with a leakage scheme, and free-streaming neutrinos, the $0^{\text{th}}$ moment of whose distribution functions is evolved by the M0 scheme. Neutrinos are considered massless and therefore the free-streaming neutrinos follow null-geodesics along radial rays that are spherically symmetric. Flavorwise, we divide the neutrinos into three categories: the electron neutrinos $\nu_e$, the anti-electron neutrinos $\bar{\nu}_e$ and all other heavy neutrinos are grouped as $\nu_x$. The quantities $R$ and $Q$ are given as

$$\begin{aligned} R &= (\kappa_{\nu_e} n_{\nu_e} - \kappa_{\bar{\nu}_e} n_{\bar{\nu}_e}) - \left(R^{\text{eff}}_{\nu_e} + R^{\text{eff}}_{\bar{\nu}_e}\right) \\ Q &= (\kappa_{\nu_e} n_{\nu_e} E_{\nu_e} + \kappa_{\bar{\nu}_e} n_{\bar{\nu}_e} E_{\bar{\nu}_e}) - \left(Q^{\text{eff}}_{\nu_e} + Q^{\text{eff}}_{\bar{\nu}_e} + Q^{\text{eff}}_{\nu_x}\right) \end{aligned} \tag{1.135}$$

where the effective emissivities $R^{\text{eff}}$ and $Q^{\text{eff}}$ and the neutrino absorption opacity $\kappa$ are provided by the leakage scheme. $n$ is the number density of free streaming neutrinos of a given species, and $E$ is their average energy in the rest frame of the fluid. To solve for $n$ and $E$, we evolve the $0^{\text{th}}$ moment of the free-streaming neutrino distribution function. The M0 scheme effectively provides us with hyperbolic PDEs for the evolution of $n$ and $E$ for the free-streaming neutrinos.

Since the neutrinos are massless, their 4-momenta $p^a$ is given by

$$p^a = E_\nu k^a \tag{1.136}$$

where $E_\nu = -p^c u_c$ is the neutrino energy in the rest-frame of the fluid and $k^a$ is a null vector that can be decomposed into a timelike velocity $u^a$ and a unit spacelike vector $r^a$ as $k^a = u^a + r^a$. Since the free-streaming neutrinos are only evolved over radial rays, $r$ is the spatial degree of freedom. Like subsection 1.2.4.3, we can again define a number

current for a neutrino with flavor X as

$$N_X^a = -\int f_X p^a \frac{d^3p}{p^0} \tag{1.137}$$

from which the neutrino number density (in the rest frame of the fluid) can be computed as $n_X = -u_a N_X^a = N_X^t$. It can be shown [44], that $N_X^a$ satisfies

$$\nabla_a N_X^a = R_X^{\text{eff}} - \kappa_X n_X. \tag{1.138}$$

Using the 3+1 decomposition, the equation for the number density of neutrinos can be expressed as

$$\partial_t \left(\alpha\sqrt{\gamma} n_X k^t\right) + \partial_r \left(\alpha\sqrt{\gamma} n_X k^r\right) = \alpha\sqrt{\gamma}\left(R_X^{\text{eff}} - \kappa_X n_X\right) \tag{1.139}$$

where the symbols have their usual meaning and $N_X^a = n_X k^a$ is a restatement of the fact that the free-streaming neutrinos travel at the speed of light. Likewise, the equation for the energy transport can be written assuming a stationary spacetime, i.e., a spacetime that is time-translation invariant. This further implies that $\partial_t^a$ being the Killing Vector field, the energy of free-streaming neutrinos along their worldlines should be a constant, i.e., $-p_a t^a$ is a constant along a free-streaming neutrino worldline. Finally, the energy transport equation can be given as

$$n_X k^t \partial_t(-E_X k_a t^a) + n_X k^r \partial_r(-E_X k_a t^a) = \left(-k_c t^c Q_X^{\text{eff}} + E_X k_a t^a R_X^{\text{eff}}\right) \tag{1.140}$$

In this chapter, we have provided a review of all the moving parts in a cogwheel that is a relativistic hydrodynamic simulation. Starting from the evolution of spacetime to hydrodynamics to the equilibrium of matter and finally neutrino transport. In multiple places, we have skipped detailed derivation in the interest of brevity and pointed the reader to exhaustive resources. However, the themes that are central to this dissertation like the equations of state and QCD phase transitions have been discussed in sufficient detail.

# Part I

# Numerical Relativity Simulations

# Chapter 2
# QCD Phase Transitions: Gravitational Wave and Electromagnetic Signatures

## 2.1 Introduction

Strong interacting matter, described by quantum chromodynamics (QCD), possesses a rich phase structure [45–47]. At low enough temperatures and densities, the QCD phase diagram is populated by hadronic matter, i.e., a phase where quarks and gluons are confined within baryons and mesons. High precision QCD calculations on a space-time lattice at zero baryon chemical potential (i.e. zero baryon density) have clearly shown that at high temperature and for physical values of the quark masses, quarks and gluons become the most relevant degrees of freedom. The transition to this quark-gluon plasma phase is a crossover [48, 49] rather than a real phase transition with a pseudo-critical temperature of about 155 MeV. The phase with deconfined quarks and gluons has been observed in heavy-ion collision experiments at very high beam energies probing the high temperature and low-density region of the QCD phase diagram (see e.g. [50] and the references therein).

A transition to a phase with deconfined quarks and gluons is also expected in the region with low or moderate temperatures ($T = 0$ – $100\,\mathrm{MeV}$) and large densities (several times the nuclear saturation density $\rho_{nuc} \sim 2.7 \times 10^{14}\mathrm{g\ cm^{-3}}$). This is the region of the QCD phase diagram that is mapped by neutron star (NS) interiors, the hot and dense matter formed during core-collapse supernovae, and binary neutron star (BNS) mergers. In fact, since a long time it has been proposed that quark matter composed of the three

lightest quark flavors, namely up ($u$), down ($d$) and strange ($s$) quarks, can exist inside the cores of heavy NSs (the so-called hybrid stars) or form a new type of self-bound compact object called a strange star, which is completely made up of strange quark matter (see e.g., [34]). Whether in this region of the QCD phase diagram, the quark deconfinement phase transition is of the first order with a critical endpoint, or whether it proceeds smoothly through a crossover is still an open question. The latter cannot be answered by lattice QCD calculations due to the so-called "sign problem", which makes all known lattice QCD methods at finite baryon chemical potential inapplicable. New dedicated experiments under construction at future facilities such as the Compressed Baryonic Matter (CBM) experiment [51] at the Facility for Antiproton and Ion Research (FAIR) will clarify this and other fundamental questions on dense QCD matter in the upcoming years.

The discovery of gravitational waves (GWs) from the BNS merger GW170817 by Advanced LIGO and Advanced VIRGO [1], complemented by the subsequent observations of electromagnetic (EM) counterparts by a host of earth and space-based telescopes [2], has ushered in the new field of multi-messenger astrophysics with GWs. It is now possible to indirectly probe the nature of the dense and hot matter created in BNS mergers through multi-messenger observations. Numerical simulations with state-of-the-art physics models are required to model the highly dynamic post-merger evolution of BNSs and bridge the gap between the fundamental physics of mergers and observational data.

The works by Most et al. [52,53], Bauswein et al. [54,55], Weigh et al. [56], Liebling et al. [3], and Blacker et al. [57] extensively studied QCD phase transitions in BNS mergers by contrasting simulation results obtained with equation of state (EOS) models in which the QCD phase transition was included or excluded. Most et al. [52, 53] employed a chiral mean field model with a first-order phase transition from hadrons to quarks, which also included hyperons. They found that, for their particular choice of EOS, a first-order QCD phase transition induced similar qualitative differences in the postmerger dynamics and the associated GW signal as the appearance of hyperons [19, 20]. In particular, the appearance of quarks was rapidly followed by black hole (BH) formation in their studies. They also identified a small dephasing in the postmerger GW signal, which was claimed to be a unique signature of the formation of quarks. However, it is not clear that such a dephasing is significant given the numerical uncertainties in their simulations.

The studies of Bauswein et al. [54, 55] differed from the previous ones in several aspects. They employed an EOS that contained an extended mixed phase of quarks and hadrons [58], while the EOS adopted by Most et al. [52, 53] had a rapid transition to

pure quark matter. Bauswein et al. [54, 55] also used a smoothed particle hydrodanamics (SPH) code instead of a grid based code and employed the conformally flat approximation to general relativity (GR). The simulations of Bauswein et al. [54, 55] resulted in the formation of quadrupolarly deformed hybrid remnants with hadronic envelopes and deconfined quarks in their cores that did not immediately collapse to BHs. These remnants were found to emit GWs at a substantially higher frequency than their hadronic counterparts. In particular, the GW signal from hybrid remnants violated empirical relations between certain properties of the binaries that can be measured from the inspiral signal and their postmerger peak frequencies [59–63]. Since these relations are known to hold for all hadronic EOSs [64], the detection of a signal violating them would be a smoking gun evidence for the presence of a first order phase transition.

The apparent discrepancies between the results of Most et al. [52, 53] and Bauswein et al. [54, 55] have been addressed by Weih et al. [56]. This study considered a purely phenomenological description of the EOS using a piecewise polytropic ansatz. Weih et al. [56] found that, depending on the characteristic of the EOS and of the phase transition, there can be different possibilities. A shift in the postmerger peak GW frequency was found to occur only for models in which the phase transition is not immediately followed by BH formation. Moreover, in the cases in which the phase transition was delayed from the onset of the merger it was possible for the postmerger GW spectrum to display two peaks: one associated with the hadronic remnant prior to the phase transition, and one associated with the hybrid remnant after the phase transition. More recently, Liebling et al. [3] used the same phenomenological ansatz as Weih et al. [56]. They confirmed the previous findings and also studied the impact of phase transitions on the topology of the magnetic field of the stars.

A recent work by Blacker et al. [57] attempted to derive a methodology to constrain the onset density of a deconfinement phase transition in BNS mergers. They investigated the effects of quark deconfinement over a substantial range of NS masses. They used EOS framework as Refs. [54, 55], but varied some of the model parameters. They claimed that with several measurements of the postmerger peak frequency for different binary masses it would be possible to constrain the density threshold for quark deconfinement at zero temperature.

The related scenario of a merger of self-bound compact stars or strange stars was considered by Bauswein et al. [65, 66] and Zhu et al. [67], while the merger between hadronic NSs and strange quark stars was considered in De Pietri et al. [68]. These studies highlighted some potential GW and EM signatures for strange quark stars. Such

scenarios could be independently constrained from upper bounds on the flux of strangelets generated in such mergers [65, 69].

A concordant picture has started to emerge on the possible role of QCD phase transitions in BNS mergers. However, there are still many open questions. What are the prospects for constraining a phase transition given a realistic BNS population? How generic are the signatures identified by Bauswein et al. [65, 66] and Blacker et al. [57]? Can EM counterparts and nucleosynthesis yield provide an independent constraint? In this chapter we begin to address some of these questions using BNS merger simulations in full general relativity. We use a state-of-the-art microphysical nuclear EOS for the hadronic phase and a phenomenological bag model for the quark phase. These are coupled to an approximate formalism for neutrino transport. We focus on a wider range of total binary mass and mass ratios than what has been considered in the past and study, for the first time, the possible signature of phase transitions in kilonovae, r-process nucleosynthesis yield, and afterglows of BNS mergers. We confirm that QCD phase transitions could leave a detectable imprint on the postmerger GW signal. However, such signatures might not be easily identifiable. Indeed, the differences between our hadronic and mixed quark binaries are of the same order as differences between different hadronic models already presented in the literature. Bauswein et al. [70] also investigated the mass ejection rates from BNS mergers in the context of EOSs with deconfined quarks and reported on the absence of characteristic signatures resulting from quark deconfinement. Likewise, we do not find any smoking gun evidence of a phase transition in the kilonova or nucleosynthesis yields, but we find that the onset of a QCD phase transition can lead to more energetic bounces of the remnant. These, in turn, result in the ejection of a small amount of material to very high velocities which could power particularly bright non-thermal afterglows. However, this effect cannot be presently used to constrain phase transition in mergers owing to the large uncertainties in the physics of the shock launched by the ejecta in the interstellar medium (ISM).

This chapter is organized as follows. In the subsequent sections 2.2 and 2.3, we describe, respectively, the details of the EOSs and the numerical infrastructure for the calculations presented in this chapter. In section 2.4, we describe the dynamics of the merger. In particular, in sub-section 2.4.1 we comment upon the qualitative features of the evolution of a BNS merger with a QCD phase transition, and in sub-section 2.4.2, we probe the thermodynamic properties of the matter produced in mergers using Lagrangian tracer particles. Section 2.5 is devoted to the study of the GW signatures of such a phase transition. A discussion about the properties of the outflow from such mergers and

accretion disks surrounding the remnant follows in section 2.6. Section 2.7 is dedicated to the discussion of possible EM signatures coming from mergers exhibiting a QCD phase transition. In particular, we compute the kilonova lightcurves at early times after the merger and the late-time afterglow in sub-sections 2.7.1 and 2.7.2 respectively. We finally culminate the chapter with conclusions in section 2.8.

## 2.2 Equations of State

### 2.2.1 Hadronic matter

In the first case (hadronic matter) we assume that the dense and hot matter formed during BNS mergers can be modeled, up to the relevant temperatures and densities, as a uniform electric-charge-neutral fluid of neutrons, protons, electrons, positrons, and photons. Recently a new microscopic EOS for this system has been obtained in Bombaci et al. [71] (hereafter the BL EOS) for the zero temperature case, using the Brueckner-Hartree-Fock (BHF) quantum many-body approach (see [71] and references therein) starting from modern two-body and three-body nuclear interactions derived within chiral effective field theory (ChEFT) (e.g. [72, 73]). These chiral nuclear interactions reproduce with high accuracy the nucleon-nucleon (NN) scattering data and the experimental binding energies of light (A = 3, 4) atomic nuclei. The BL EOS reproduces the empirical properties (energy per nucleon, symmetry energy and its slope parameter $L$, incompressibility) of nuclear matter at saturation density ($n_0 = 0.16\,\mathrm{fm}^{-3}$; see Logoteta et al. [74]), it does not violate causality (i.e. $v_s < c$, with $v_s$ being the speed of sound in the nuclear medium), and it is consistent (see figure 2 in [71]) with the measured elliptic flow of matter in heavy-ion collisions experiments [75].

When computing static neutron star configurations, the BL EOS (for the $\beta$-stable case) gives: (i) a maximum mass $\mathrm{M_{max}} = 2.08\ \mathrm{M_\odot}$ and a corresponding radius $\mathrm{R(M_{max})} = 10.22\,\mathrm{km}$; (ii) a quadrupolar tidal polarizability coefficient $\Lambda_{1.4} = 385$ (for the 1.4 $\mathrm{M_\odot}$ neutron star [76]) compatible with the constraints derived from GW170817 [1]; and (iii) a threshold mass for the prompt collapse of a $q = 1$ BNS system to BH as $\mathrm{M_{threshold}} = 2.925\ \mathrm{M_\odot}$ (Section 2.4.1) indicating that GW170817 is compatible with being a NS-NS system if NSs are described by this EOS. With the addition of a thermal contribution, using the so-called $\Gamma$-law, the BL EOS has been used in BNS merger simulations by Endrizzi et al. [77].

Very recently, the BL EOS has been extended to finite temperature and to arbitrary

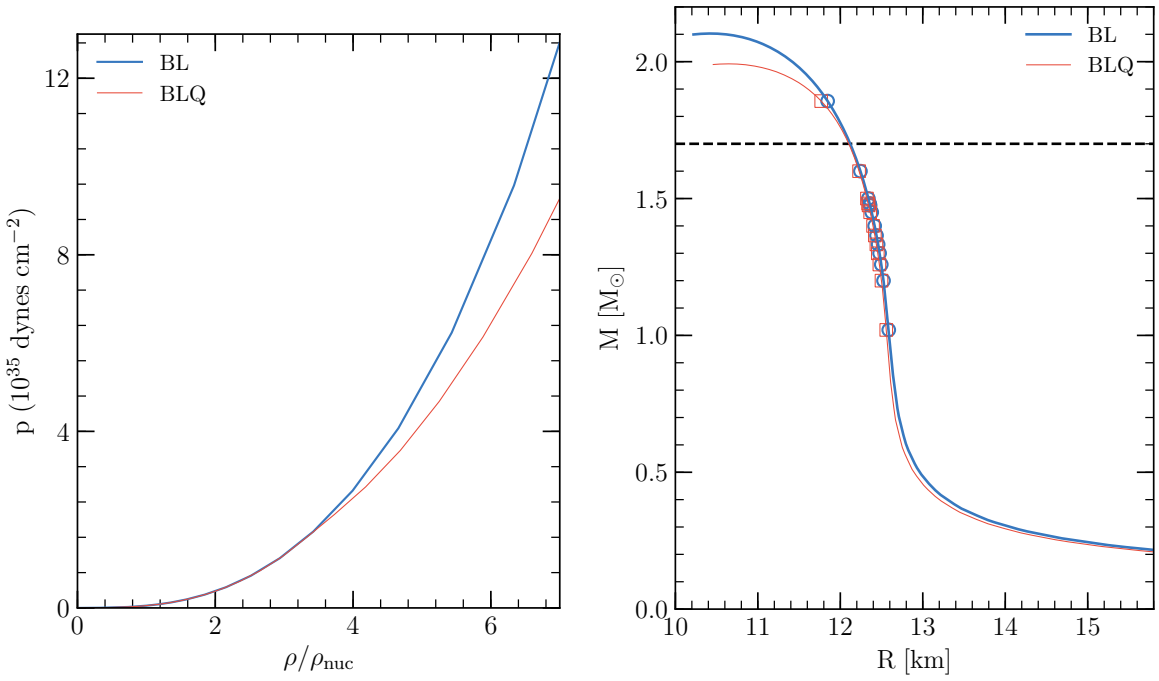


**Figure 2.1.** The pressure-density variation at $T = 0$ and the mass-radius relationship for isolated, cold ($T = 0$), $\beta$-equilibrated, and spherically symmetric neutron stars constructed with the two equations of state used in this work. The circle and square markers represent the individual masses of the neutron stars simulated for BL and BLQ EOS respectively. The BLQ mass-radius sequence departs from the BL sequence for neutron stars having a mass M $\gtrsim$ 1.7 M$_\odot$. These stars possess in fact a core made of hadron-quark mixed matter.

proton fractions [78]. In the following we will refer to this finite-temperature EOS model as the BLh EOS. The BLh EOS has been applied in Bernuzzi et al. [79,80] to asymmetric neutron star mergers ($q \neq 1$) with chirp mass 1.188 M$_\odot$ corresponding to the measured one in the case of GW170817.

### 2.2.2 Deconfined quark matter

The second EOS model (hereafter the BLQ EOS) used in our work describes the thermodynamic properties of hadronic-quark hybrid matter. We assume that at high enough temperatures and densities reached during a BNS merger, stellar matter undergoes a transition to a phase with deconfined quarks (quark matter) and in addition, we assume this phase transition to be of the first order. Quark matter could also be present in the NS cores prior to the merger in the case of sufficiently massive NSs (see figure 2.1) and for particular choices of the quark matter EOS parameters. To describe the hadronic phase (i.e. quarks confined in neutrons and protons in our case) of hybrid matter we

make use of the BLh EOS described above.

To model the quark phase we use an extended version of the phenomenological bag model EOS which includes the effects of gluon-mediated QCD interactions between quarks up to the second order in the QCD coupling $\alpha_s$ [81–83]. The grand canonical potential per unit volume can be written as (we use units where $\hbar = c = 1$):

$$\Omega = \sum_{i=u,d,s,e} \Omega_i^0 + \frac{3}{4\pi^2}(1 - a_4)\mu^4 + B_{\rm eff}\,, \tag{2.1}$$

where $\Omega_i^0$ is the grand canonical potential density for $u$, $d$, $s$ quarks and electrons (and their antiparticles), described as ideal relativistic Fermi gases. The second term on the right hand side of Eq.(2.1) accounts for the perturbative QCD corrections to $\mathcal{O}(\alpha_s^2)$ [81–83] and its value represents the degree of deviations from an ideal relativstic Fermi gas EOS, with $a_4 = 1$ corresponding to the ideal case. The chemical potential $\mu$ in Eq. (2.1) can be written in terms of the $u$, $d$ and $s$ quark chemical potentials as $\mu = (\mu_u + \mu_d + \mu_s)/3$. The term $B_{\rm eff}$ is an effective bag constant that takes into account, in a phenomenological way, the nonperturbative aspects of QCD.

At finite temperature, the ideal gas contributions to $\Omega$ provided by fermions and antifermions can be calculated by computing the corresponding Fermi integrals for a given temperature $T$ and chemical potential $\mu_i$ (see e.g. [84]):

$$\begin{aligned} \Omega_i^0(T,\mu_i) &= -\frac{1}{3}\frac{g_i}{2\pi^2}\int_0^\infty k^2 dk\ k\,v \\ &\times \ [f(k,\mu_i) + f(k,-\mu_i)] \end{aligned} \tag{2.2}$$

where $v = k/E_i$ is the particle velocity (with $E_i(k) = (k^2 + m_i^2)^{1/2}$), and $f(k, \pm\mu_i)$ are the Fermi distribution functions with chemical potentials for particles $(+\mu_i)$ and antiparticles $(-\mu_i)$:

$$f(k,\pm\mu_i) = \frac{1}{e^{(E_i(k)\mp\mu_i)/T} + 1}, \tag{2.3}$$

the degeneracy factor is $g_i = 2$ for electrons and $g_i = 6$ for each quark flavor. We neglect the temperature dependence of the last two terms in Eq.(2.1).

The total entropy density

$$s = \sum_{i=u,d,s,e} s_i \tag{2.4}$$

can be calculated using the ideal Fermi gas approximation for each fermionic particle

species [85]:

$$\begin{aligned} s_i(T,\mu_i) &= -\frac{g_i}{2\pi^2}\int_0^\infty k^2 dk\,[f(k,\mu_i)\ln f(k,\mu_i) \\ &+ (1-f(k,\mu_i))\ln(1-f(k,\mu_i)) \\ &+ f(k,-\mu_i)\ln f(k,-\mu_i) \\ &+ (1-f(k,-\mu_i))\ln(1-f(k,-\mu_i))] \end{aligned} \tag{2.5}$$

Using standard thermodynamical relations, the energy density can be written as:

$$e = \Omega + \sum_{i=u,d,s,e} \mu_i n_i + Ts, \tag{2.6}$$

where $n_i$ is the number density for each particle species which can be calculated as:

$$n_i = -\left(\frac{\partial\Omega}{\partial\mu_i}\right)_{T,V} \tag{2.7}$$

and the total baryon number density is:

$$n_B = \frac{1}{3}(n_u + n_d + n_s)\,. \tag{2.8}$$

We next assume a first order hadron-quark phase transition and, following Glendenning [38], we require global electric charge neutrality of bulk stellar matter. An important consequence of imposing global charge neutrality is that the hadronic and the quark phases can coexist for a finite range of pressures. This treatment of the phase transition is known in the literature as the Gibbs construction for the hadron-quark mixed phase. In this case the Gibbs conditions for phase equilibrium can be written as [38]:

$$\mu_{b,H} = \mu_{b,Q} \equiv \mu_b\,, \tag{2.9}$$

$$\mu_{q,H} = \mu_{q,Q} \equiv \mu_q\,, \tag{2.10}$$

$$T_H = T_Q \equiv T\,, \tag{2.11}$$

$$P_H(\mu_b,\mu_q,T) = P_Q(\mu_b,\mu_q,T)\,, \tag{2.12}$$

where the subscript $H$ and $Q$ refer to physical quantities in the hadronic and in the quark phase respectively, while the baryon chemical potential, $\mu_b$, and the electric chemical potential, $\mu_q$, are two independent chemical potentials corresponding respectively to the global conservation of the baryon number and the electric charge. In the pure hadronic

phase $\mu_b = \mu_n$, the neutron chemical potential, and $\mu_q = \mu_e$, the electron chemical potential. In the quark phase the quark chemical potentials can be written as:

$$\mu_u = \frac{1}{3}(\mu_b - 2\mu_q) = \frac{2}{3}\mu_p - \frac{1}{3}\mu_n \,, \tag{2.13}$$

$$\mu_d = \frac{1}{3}(\mu_b + \mu_q) = \frac{2}{3}\mu_n - \frac{1}{3}\mu_p \,. \tag{2.14}$$

Weak reactions of the type:

$$d + u \leftrightarrow u + s \tag{2.15}$$

$$u + e^- \leftrightarrow s + \nu_e \tag{2.16}$$

will change the strangeness content of the just deconfined quark matter [86] to minimize the energy per baryon of the system. Since the typical time-scale for weak interaction processes $t_w \lesssim (10^{-8}\text{–}10^{-10})\,\mathrm{s}$ is significantly shorter than the hydrodynamics timescales inside the remnant, we neglect detailed reaction rates involving quarks and neutrinos, and we consider $\beta$-stable strange quark matter with the strange quark chemical potential $\mu_s = \mu_d$.

In the present work we take $m_u = m_d = 0$, $m_s = 100$ MeV, $B_{\rm eff}^{1/4} = 180\,\mathrm{MeV}$ and $a_4 = 0.4$. With these values of the EOS parameters for the quark phase, and with the BL EOS for the hadronic phase, we obtain the NS mass-radius curves shown in figure 2.1. In particular, we find identical radii and NS structure for BL and BLQ when considering stars with masses up to $\mathrm{M} \simeq 1.7\ \mathrm{M}_\odot$. That is, up to the onset of the phase transition. After the onset of the phase transition, the BLQ EOS becomes less stiff than BL and predicts more compact NSs and a lower maximum mass of $\mathrm{M}_{\rm max} = 1.99\ \mathrm{M}_\odot$. The corresponding radius is $\mathrm{R}(\mathrm{M}_{\rm max}) = 10.46$ km. The threshold for prompt BH formation for a $q = 1$ BNS merger with BLQ EOS is found to be $2.825\ \mathrm{M}_\odot$ (see Section 2.4.1).

## 2.3 Numerical Setup

We evolve our systems in full general relativity along with high-order convergence schemes for general relativistic hydrodynamics using the `WhiskyTHC` code [23, 24, 87–89]. The spacetime metric is evolved using the Z4c formulation [90, 91] of Einstein's equations implemented in the `CTGamma` thorn [92, 93] of the `EinsteinToolkit` [94]. Our simulations make use of the `Carpet` adaptive mesh refinement (AMR) framework [95, 96], which implements the Berger-Oliger scheme with refluxing [97, 98]. For the

relativistic hydrodynamics, `WhiskyTHC` evolves proton number and neutron number densities separately to ensure detailed conservation given by:

$$\nabla_\mu (n_{p,n}\, u^\mu) = R_{p,n} \tag{2.17}$$

where $n_{p,n}$ are the number densities of (free or bound) protons and neutrons respectively, $u^\mu$ is the fluid four-velocity and $R_{p,n}$ are the net lepton number deposition rates due to the emission and absorption of electron neutrinos and anti-neutrinos. Due to charge neutrality, the relative amount of neutrons and protons is expressed in terms of $\mathrm{Y}_e$, i.e. the electron fraction given by $n_p/(n_p + n_n)$. The evolution of the energy-momentum tensor takes the following form:

$$\nabla_\mu T^{\mu\nu} = Q u^\nu \,, \tag{2.18}$$

where $Q$ is the net energy deposition rate due to the emission and absorption of neutrinos and anti-neutrinos of all flavors. We consider the relativistic fluid of the neutron star to be a perfect fluid with no shears, viscosity, or heat conduction, that is:

$$T^{\mu\nu} = (e + p) u^\mu u^\nu + p g^{\mu\nu}. \tag{2.19}$$

Here $e$ is the total energy density, $p$ the isotropic pressure and $g^{\mu\nu}$ the spacetime metric. For additional details on the numerical schemes used to discretize the above equations and the specifics of the neutrino leakage scheme, we refer to Radice et al. [24] and the references therein.

In order to record the thermodynamic history of the relativistic flow in and around the remnant's core, we inject Lagrange tracer particles in the fluid frame. These are fiducial particles that are advected with the flow according to:

$$\frac{\mathrm{d}x^i}{\mathrm{d}t} = \alpha v^i - \beta^i. \tag{2.20}$$

Here $\alpha$ is the lapse function, $v^i$ is the three-velocity of the fluid, and $\beta^i$ is the shift vector.

The initial data for all our simulations is constructed from irrotational binaries in quasi-circular orbits at an initial separation of 45 km. These are constructed using the `LORENE` code by Gourgoulhon et al. [101] which provides classes to solve for a wide variety of partial differential equations using multi-domain spectral methods. We use the BL EOS to construct the initial data for all our systems, including those simulated with the

**Table 2.1.** A summary of the properties of non-spinning isolated NSs used for constructing the initial data with the BL EOS. $M_1$ represents the primary (heavier) mass in the binary and $M_2$ is the secondary mass. M represents the total mass whereas q and $\nu$ represent the mass ratio and the symmetric mass ratio of the binary. $\Lambda_i$s ($i \in \{1, 2\}$) are the respective quadrupolar tidal polarizability coefficients of the individual stars and $\widetilde{\Lambda}$ is a parameter defined in Eq(5) of [99]. $\xi$ is a tidal parameter constructed in [64] from $\Lambda_i$s.

| $M_1$ $[M_\odot]$ | $M_2$ $[M_\odot]$ | M $[M_\odot]$ | q | $\nu$ | $\Lambda_1$ | $\Lambda_2$ | $\widetilde{\Lambda}$ | $\xi$ |
|---|---|---|---|---|---|---|---|---|
| 1.3 | 1.3 | 2.6 | 1.0 | 0.25 | 696 | 696 | 696 | 130 |
| 1.3325 | 1.3325 | 2.67 | 1.0 | 0.25 | 595 | 595 | 595 | 111 |
| 1.365 | 1.365 | 2.73 | 1.0 | 0.25 | 510 | 510 | 510 | 95 |
| 1.4 | 1.4 | 2.8 | 1.0 | 0.25 | 432 | 432 | 432 | 81 |
| 1.45 | 1.45 | 2.9 | 1.0 | 0.25 | 341 | 341 | 341 | 63 |
| 1.475 | 1.475 | 2.95 | 1.0 | 0.25 | 303 | 303 | 303 | 56 |
| 1.5 | 1.5 | 3.0 | 1.0 | 0.25 | 269 | 269 | 269 | 50 |
| 1.6 | 1.6 | 3.2 | 1.0 | 0.25 | 168 | 168 | 168 | 31 |
| 1.4 | 1.2 | 2.6 | 1.17 | 0.25 | 432 | 1137 | 711 | 133 |
| 1.482 | 1.259 | 2.74 | 1.18 | 0.25 | 293 | 849 | 510 | 95 |
| 1.856 | 1.02 | 2.88 | 1.82 | 0.23 | 46 | 2896 | 505 | 92 |

BLQ EOS. We simulate 11 BNS configurations varying both in their total mass and mass ratios (table 2.1). These include binaries with total gravitational masses ranging from 2.6 $M_\odot$ to 3.2 $M_\odot$ and covering a mass ratio range of 1 to 1.82. Among our simulations there are three systems that are targeted to GW170817, namely 1.365 $M_\odot - 1.365$ $M_\odot$, 1.482 $M_\odot - 1.259$ $M_\odot$ and 1.856 $M_\odot - 1.020$ $M_\odot$. Each of these binaries have a chirp mass of 1.18 $M_\odot$ that is compatible with the observations for GW170817 [1]. Additionally, we also simulate a binary 1.4 $M_\odot - 1.2$ $M_\odot$ that is consistent with the observations of the relativistic binary pulsar PSR J1829+2456 [102].

We employ an AMR structure composed of 7 refinement levels. Of these, the three outer levels are fixed, while the inner four levels are comoving with the stars during their inspiral. The finest refinement levels covers entirely the stars during the inspiral and the centrally condensed part of the remnant after the merger. We simulate the binaries at two spatial resolutions (see tables 2.2 and 2.3): with grid resolutions of 184.6 m (standard resolution; SR) and 246.1 m (low resolution; LR) in the finest refinement level. The binary 1.4 $M_\odot - 1.2$ $M_\odot$ is only simulated at SR. The time step is determined by the Courant-Friedrichs-Lewy (CFL) coefficient which is taken to be 0.125. This small

CFL, in combination with the positivity preserving limiter of `WhiskyTHC`, guarantees the positivity of the density [89].

## 2.4 Merger Dynamics

### 2.4.1 Qualitative Dynamics

We start with a discussion of the qualitative dynamics of a BNS merger with a phase transition. To this aim, we show in figure 2.2 the postmerger evolution for the 1.3325 $M_\odot$ − 1.3325 $M_\odot$ binary, which is representative of our set of simulations. The figure shows the thermodynamic properties of matter in the equatorial plane. All of the binaries we have considered, with the exception of 1.856 $M_\odot$ − 1.020 $M_\odot$, have no deconfined quark matter during the inspiral up until merger. This is expected since, as discussed in Section 2.2, phase transition at zero temperature occurs only for stars more massive than about 1.7 $M_\odot$.

The inspiral evolutions of the BLQ and BLh binaries are identical, with the exception of 1.856 $M_\odot$ − 1.020 $M_\odot$, which is discussed later. As the orbit of the binary shrinks the stars become increasingly deformed. In high mass ratio systems the deformations lead to mass transfer and the disruption of the secondary star [79]. In the case of comparable mass binaries there is no mass transfer between the stars up to contact.

As the stars merge, their collisional interface is heated to temperatures of up to 40 MeV [52, 103–106]. This hot interface is the first site of quark matter production. Over the next few milliseconds, a massive remnant begins to form with increasing densities and temperatures in and around the core. At this stage, the spatial distribution of the quark phase is largely determined by regions of high temperature and this feature is found to be a robust characteristic of all our simulations. These temperature hot-spots evolve further into a ring-like structure over the next several milliseconds which is also a feature observed in [52, 104, 105]. The hot-spots continue to dictate the spatial distribution of the quark phase, but now the extreme density in the core of the remnant, reaching up to five times the nuclear saturation density, also starts to play a role in producing quark matter and determining their distribution in space. Noteworthy is the fact that both temperature and density can trigger a production of deconfined quark phase. For example, according to our EOS, for typical electron fractions $Y_e \simeq 0.01$ and density of 3 $\rho_{\rm nuc}$, quark deconfinement can occur at temperatures as low as ∼20 MeV. On the other hand, at densities of the order of the nuclear saturation density, quark deconfinement

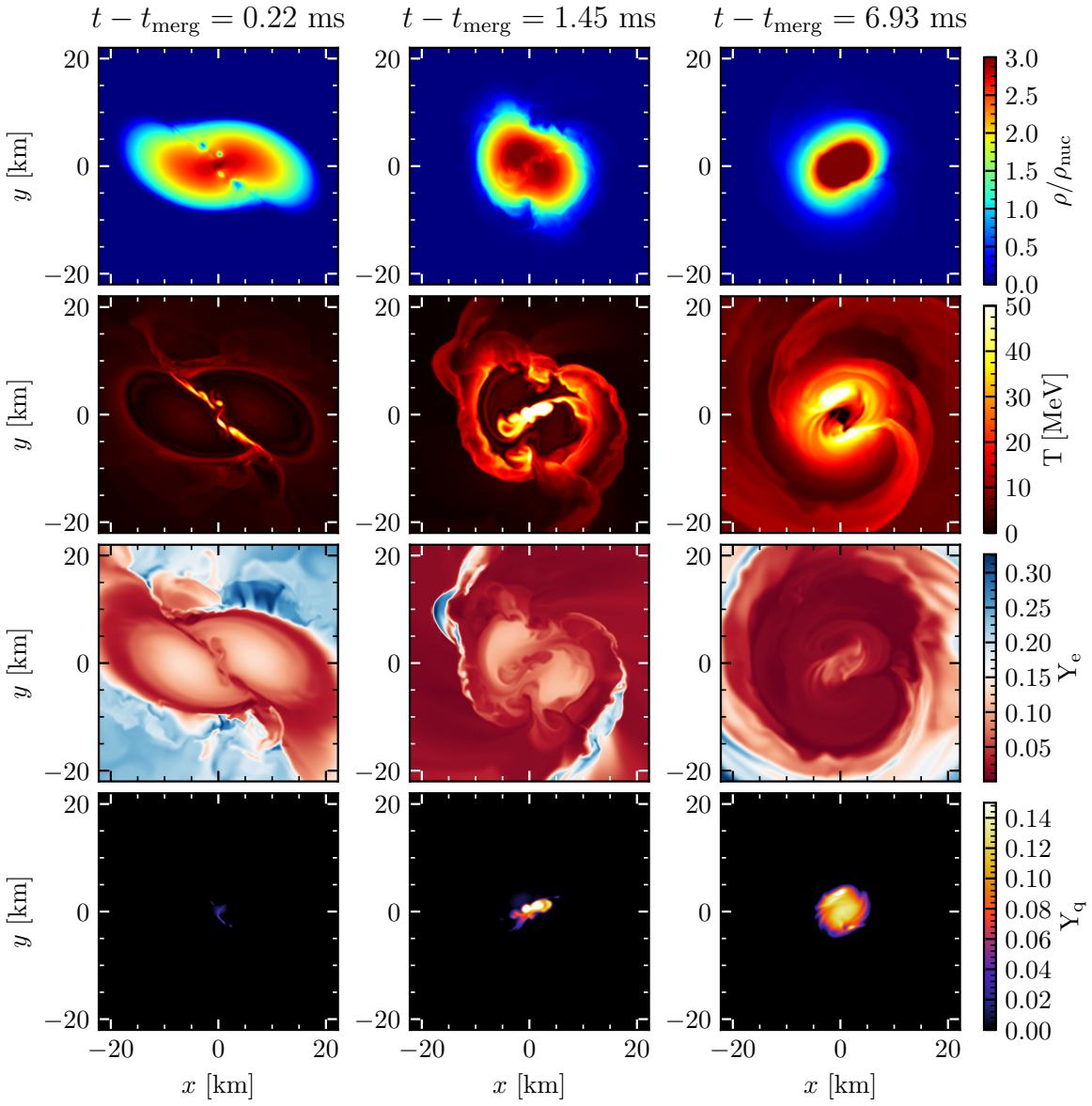


**Figure 2.2.** Evolution of the remnant's density, temperature, electron fraction and quark fraction across the xy plane for a merger of the 1.3325 $M_\odot$ − 1.3325 $M_\odot$ binary. Deconfined quarks appear as matter is compressed and heated up during the merger. The quark distribution strongly correlates with the temperature distribution in the middle panel, indicating that quarks are formed due to heating during the merger. At later times, the quark distribution is centrally condensed and most strongly correlated with the density.

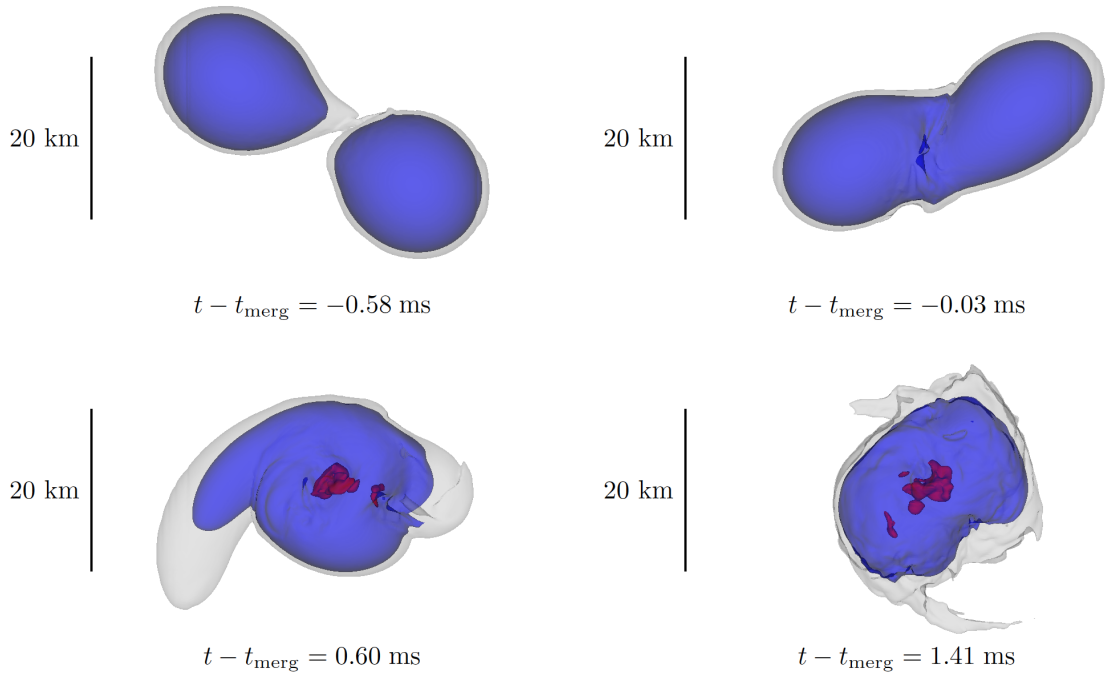


**Figure 2.3.** Evolution of a BNS merger of masses 1.4 $M_\odot$ and 1.2 $M_\odot$ evolved with the BLQ EOS. The mass configuration corresponds to the pulsar PSR J1829+2456 [102]. The blue and grey colour-scales represent iso-density surfaces corresponding to densities $10^{14}$ g cm$^{-3}$ and $10^{13}$ g cm$^{-3}$ respectively. The deconfined quark phase that appears near the core of the remnant after merger is represented in red.

requires temperatures above ∼70 MeV. We explore this interplay between density and temperature for the production of quarks in more detail in subsection 2.4.2.

As another representative example of the dynamics of the BLQ binaries, we show the evolution of the 1.4 $M_\odot - 1.2$ $M_\odot$ binary in figure 2.3. This merger proceeeds in a similar way as that of the previously discussed 1.3325 $M_\odot - 1.3325$ $M_\odot$ binary. However, a qualitative difference between the dynamics of an equal and an unequal mass merger is that the quark distribution is asymmetric in the latter case. This follows from the fact that the hot-spots in unequal mass mergers are no longer spatially symmetric with respect to the remnant's centre, as also pointed out in [52].

A generic feature of all of our simulations is that the remnants of the BLQ binaries are more compact and collapse earlier to a BH than the BLh binaries, for which the QCD phase transition is absent. This is because the appearance of quarks tends to soften the EOS making the NSs more compact and hence more susceptible to BH formation. Measuring the lifetimes of NS merger remnants could provide important constraints on the NS EOS. Indeed hierarchical inference studies done on collapsing neutron star models

using the X-ray afterglow studies of short gamma ray bursts show evidence of a quark EOS [107].

Binaries with mass above a critical threshold undergo prompt collapse to a BH, which we define as the absence of any bounce of the merger remnant prior to BH formation. When prompt BH formation occurs it is difficult to differentiate between systems with or without a QCD phase transition solely on the basis of postmerger GW signal, since it is effectively absent. However, the differences between the BLh and BLQ EOS manifest as a lowering of the mass threshold for the prompt BH collapse from $M = 2.925\,M_\odot$ for BLh EOS to $M = 2.825\,M_\odot$ in the case of BLQ EOS (see tables 2.2, 2.3 and Kashyap et al. [108]). This is in agreement with the claim that phase transitions can lower the threshold towards prompt BH collapse by Bauswein et al. [55].

### 2.4.2 Dynamics of the phase transition

We follow a methodology along the lines of [52, 53, 106, 109] to study thermodynamic conditions reached in BNS mergers and to identify whether or not these conditions are conducive towards the production of deconfined quark matter. In particular, as discussed in section 2.3, we track the thermodynamic properties of the NS material in and around the core using Lagrange tracer particles. This allows us to record the thermodynamic evolution of individual "fluid elements". We primarily discuss the case of the $1.3325\ M_\odot - 1.3325\ M_\odot$ binary, which is representative of most of our simulations.

The BLQ EOS provides the quark fraction $Y_q$ as a function of density ($\rho$), matter temperature T, and electron fraction $Y_e$, i.e. $Y_q = Y_q(\rho, T, Y_e)$. As the dynamics of the phase transition takes place in and around the core of the remnant, where $Y_e$ does not exceed 0.15 (see figure 2.2), it is reasonable to approximate the full phase diagram of the EOS with a two-dimensional analog obtained by averaging $Y_e$ over the range $Y_e \in [0.0, 0.15]$. We remark that this is done for illustrative purposes only and that no such approximation is made in the simulations. There are no qualitative differences between the $Y_e$-averaged $\langle Y_q \rangle$ and $Y_q$ in the range of $Y_e$'s considered here.

The result of this procedure comprises the background color map used in figures 2.4 and 2.5. The figures show the thermodynamic trajectory of a Lagrange tracer which is representative of the evolution of tracer particles located near (within a radial distance of 7.3 km) the core of the remnant. Before the merger, corresponding to negative $t - t_{\rm merg}$ and coordinate distances $R \gtrsim 7$ km, the particle is in the hadronic phase. As the stars merge, matter undergoes repeated cycles of compression and expansion, during which it crosses the phase boundary repeatedly. After a few oscillations, the remnant becomes

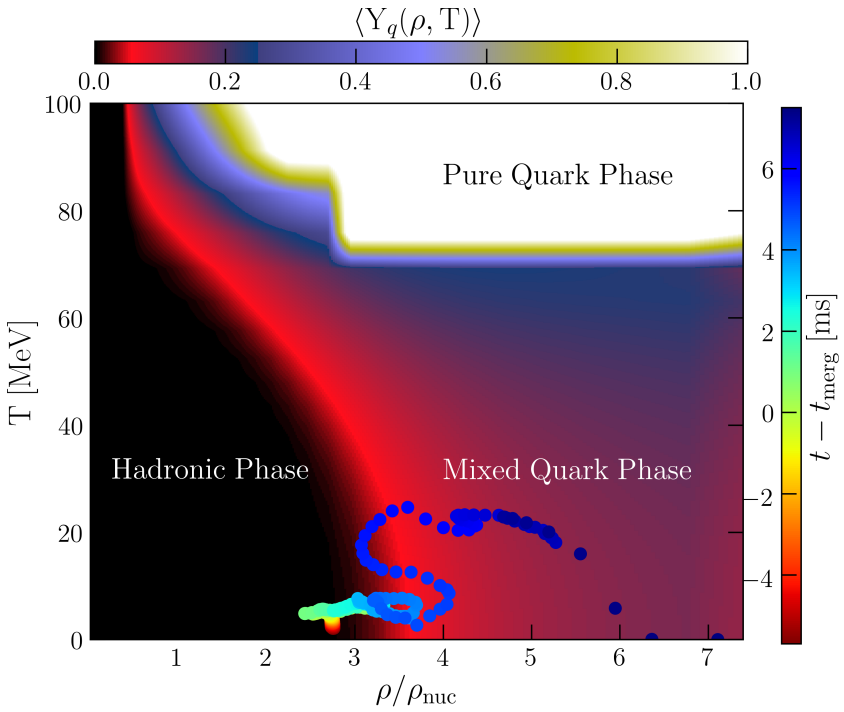


**Figure 2.4.** Thermodynamic trajectory of a representative tracer particle from the binary system 1.3325 $M_\odot$ – 1.3325 $M_\odot$. The trajectory is superposed on a $Y_e$ weighted equilibrium slice of the BLQ EOS. The trajectories themselves are color-coded according to the relative time from the merger. Matter in the NS cores crosses the phase boundary several times starting from the moment of merger and until the time of collapse and BH formation.

unstable and starts to collapse. Matter is compressed to large densities and BH formation takes place. As the tracer evolves, the radial distance oscillates between 4 km and 6 km from the remnant's centre, signifying that as the tracer is moving in and out of the quark phase, it is also moving in and around the remnant's core. Finally, just before the final collapse, the tracer particle is found in the hadron-quark mixed phase of the EOS. The occurrence of mixed quark phases is a consequence of modelling the phase transition by imposing global charge neutrality or the Gibbs construction. Gibbs construction was also utilized in the work by Blacker et al. [57] which resulted in mixed quark phases with different onset densities (at $T = 0$) in their quark EOSs. This is an important difference with respect to the models used in some of the earlier works [52, 53], in which the transition to pure quark matter occurred within a narrow range of densities and temperatures.

This trend of matter repeatedly crossing the phase boundary is generic across our set of simulations. Such behavior was expected to take place on the basis of the analysis of thermodynamic trajectories from simulations that employed purely hadronic EOSs [109].

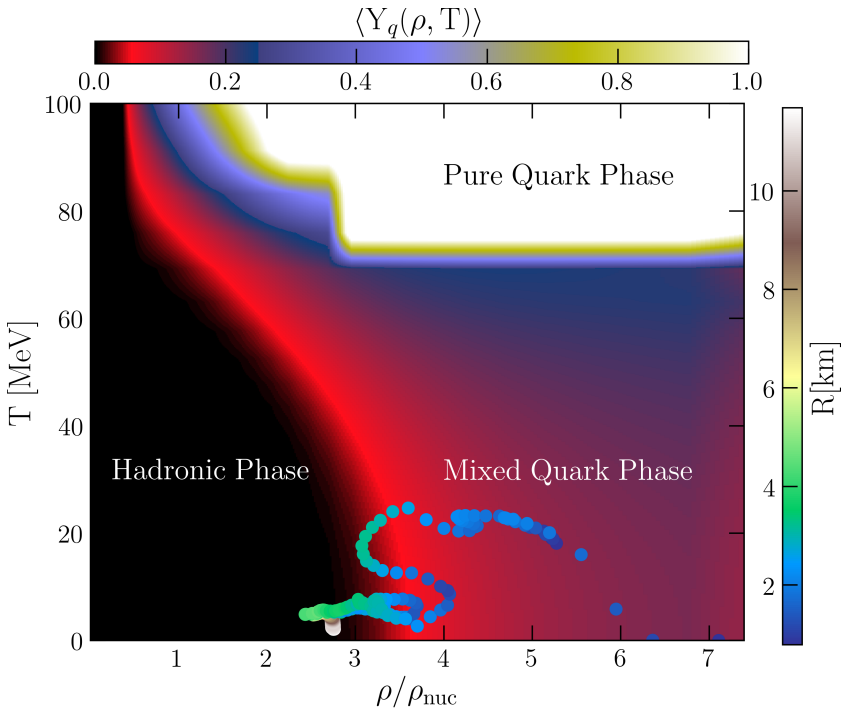


**Figure 2.5.** Same figure as fig. 2.4 but now the trajectory of the tracer is color-coded with the radial distance of the tracer from the center of the remnant.

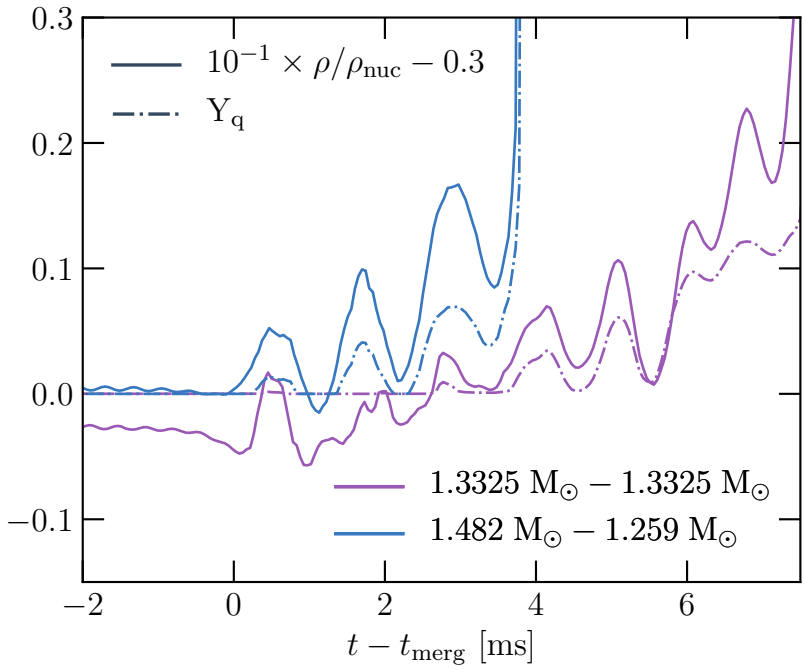


**Figure 2.6.** Time evolution of quark fraction and density of fluid elements traced by Lagrangian tracers for 2 binary neutron star systems 1.482 $M_\odot$-1.259 $M_\odot$ and 1.3325-1.3325 $M_\odot$. Noticeable is the fact that the period of oscillations of density matches the period of oscillations of quark fraction.

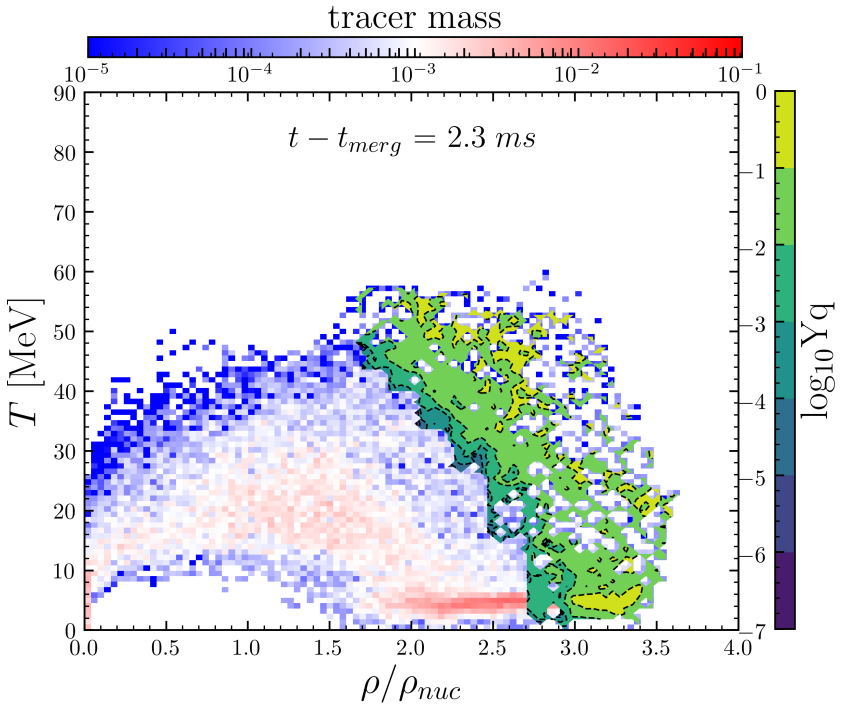


**Figure 2.7.** A two-dimensional histogram of the thermodynamic variables $\rho$ and T and weighted by bins of tracer mass. Also shown are the contours of quark fraction. Both the bulk of the remnant's core and the periphery of the core can exhibit deconfined quark matter depending upon $\rho$ and T.

It is now confirmed for the first time in our work. This process is also illustrated in figure 2.6, where we show the evolution in time for the quark fraction and density for two tracer particles: one from the 1.3325 $M_\odot$ − 1.3325 $M_\odot$ binary and one from the 1.482 $M_\odot$ − 1.259 $M_\odot$ binary. We find that the oscillations in $Y_q$ are in phase with the density oscillations. This suggests that the repeated crossing of the phase boundary is triggered by the oscillations of the remnant after its formation. Indeed, we find that the density oscillations of the tracer particles closely track those of the maximum density. These density oscillations either result in a BH formation or are damped over a timescale of ∼10−20 ms [103].

Figure 2.7 also shows a complementary analysis of the phase diagram for the 1.3325 $M_\odot$ − 1.3325 $M_\odot$ binary. Instead of showing the thermodynamic trajectories of a specific fluid element, we provide a snapshot of the entire star at a fixed time, 2.3 ms after the merger. In particular, we show a histogram of the 2-dimensional distribution of density and temperature from all the tracers in the simulation. The color represents the sum of all the masses of tracer particles in a particular temperature and density range. We also plot the contours of the quark fraction on and above the threshold for

the deconfinement phase transition. The red streak at low temperature ∼10 MeV in the range of densities between $2\rho_{\rm nuc}-3\rho_{\rm nuc}$ represents the thermodynamic state of the bulk of the remnant's core. This extends to sufficiently high densities to cross the phase boundary according to our adopted EOS. However, quarks are also formed at lower densities in the high-temperature regions (T $\sim$ 50 MeV) that have been heated during the merger phase. These hot layers are located at the periphery of the quark core [103]. Our data shows that, if indeed the phase transition to deconfined quarks is of the first order, then, depending upon the particular location of the critical point in the QCD phase diagram (to be constrained from future experiments like FAIR), matter could simultaneously undergo both a first order and a crossover phase transition in different parts of the remnant. We remark here that these hot and cold regions of deconfined quark matter in and around the remnant's core were also observed by Blacker et al. [57] in their rest mass distributions over a density-temperature plane of DD2F-SF EOSs.

We define certain characteristic times in our simulations as follows. $t_{\rm merg}$ is the time of merger, taken to be the time when the amplitude of the $l = 2, m = 2$ mode of the GW strain attains a maximum. This point approximately coincides with a minima in the maximum density of the stars, as the NSs are plunging towards each other [110]. This expansion phase is followed by a very rapid and strong compression as the stars collide (see figure 2.8). $t_{\rm BH}$ is the time of formation of a black hole in the simulation marked by the formation of an apparent horizon, which we approximately take to be the time when the lapse function drops below 0.2. We denote by $t_{\rm coll}$ the time when the $l = 2, m = 2$ mode of the radiation effectively shuts off which we take to be the time when the amplitude drops below 0.5 % of its maximum value. $t_{\rm end}$ is the terminal point of our simulations where we cease to evolve the system. These times scales are reported in milliseconds from merger in tables 2.2 and 2.3.

## 2.5 Gravitational Waves

In this section, we discuss the potential imprints that a QCD phase transition may have on the gravitational wave emission from a merger of binary neutron stars. Figure 2.8 shows the instantaneous frequency and the amplitude of the dominant ($l = 2, m = 2$) mode of the GW strain for the 1.3325 $\rm M_\odot - 1.3325\ M_\odot$ binary, as well as the maximum density, and the binary binding energy. The latter is computed by subtracting the energy radiated in GWs from the initial binding energy of the binary, i.e., $E_b = \rm M_{ADM} - (M_1 + M_2) - E_{GW}$ following [103, 111]. We find that the inspiral dynamics for the BLQ binary is identical

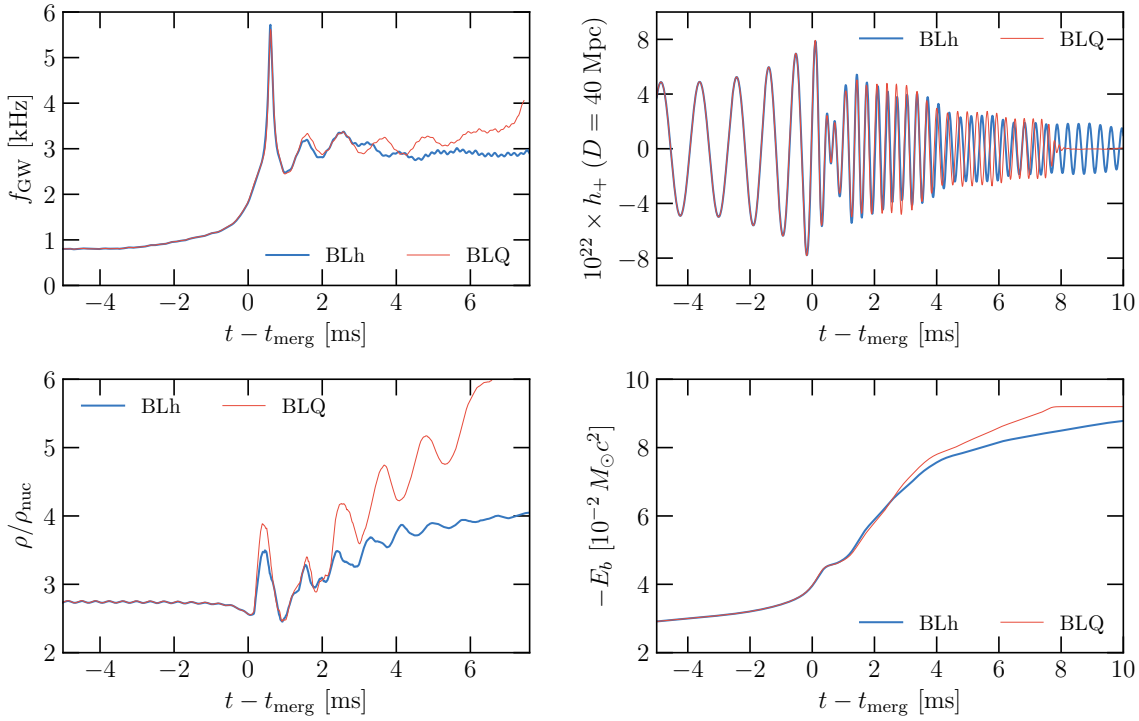


**Figure 2.8.** Evolution of the instantaneous GW frequency $f_{\rm GW}$, the"+" polarization strain amplitude for the $(l = 2, m = 2)$ mode of the GW signal, the central density $\rho$, and the binding energy $E_b$ of the 1.3325 $M_\odot$ − 1.3325 $M_\odot$ binary. The inspiral ($t \leq t_{\rm merg}$) evolution predicted by both the BLh and BLQ EOSs is identical. The appearance of quarks is imprinted on the postmerger dynamics and GW signal.

to that of the BLh binary. This is expected, because for this binary, as well as for most of the binaries considered in this study, the two EOSs are identical over the range of densities and temperatures reached in the inspiral. Nevertheless, this is an important consistency check, given that we simulate both the BLh and BLQ binaries starting from the same initial data. That is, we do not start the BLQ simulations from pre-merger snapshots of the BLh simulations.

The only exception is the 1.856 $M_\odot$ − 1.020 $M_\odot$ binary (figure 2.9), in which quarks are already present during the inspiral according to the BLQ EOS. For this binary we find the pre-merger maximum quark fraction to be $Y_q \simeq 0.06$. The maximum density in the BLQ binary is $\sim 7\%$ larger than that of the BLh binary. Despite these differences, the orbital evolution for the 1.856 $M_\odot$ − 1.020 $M_\odot$ BLh and BLQ binaries are essentially indistinguishable. In particular, the dephasing between the two associated waveforms is smaller than our numerical precision. This is also not surprising given that the phase transition only impacts the primary component of this binary, whose tidal parameter $\Lambda_1$

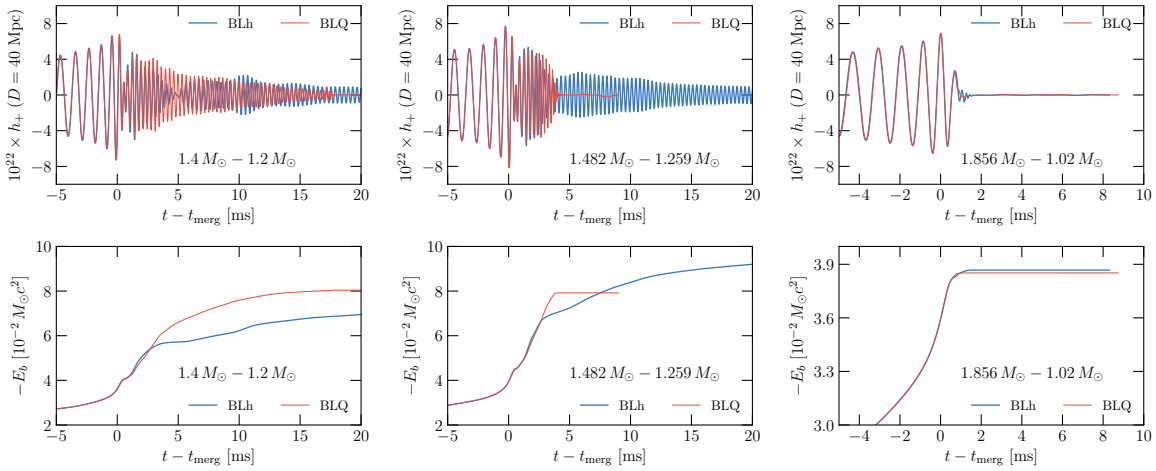


**Figure 2.9.** Amplitude of the $(l = 2, m = 2)$ mode of the GW strain $h_+$ and binding energies for the 1.4 $M_\odot$ - 1.2 $M_\odot$, 1.482 $M_\odot$ - 1.259 $M_\odot$, and 1.856 $M_\odot$ - 1.020 $M_\odot$ binaries. As the binaries become more massive or more asymmetric, the length of the postmerger signal decreases. The postmerger is further shortened by an onset of deconfinement phase transition.

is in any case very small $\simeq 45$.

The postmerger evolution of the BLh and BLQ binaries are instead very different. This is shown in figure 2.8 for the 1.3325 $M_\odot - 1.3325$ $M_\odot$ binaries. The phase transition to deconfined quarks in the BLQ binaries is accompanied by a loss of pressure support. This in turn causes the BLQ remnants to undergo violent cycles of gravitational contraction and centrifugal bounces, while at the same time becoming progressively more compact. This ultimately leads to the collapse to BH. The progressive contraction of the remnant is accompanied by a drift in the instantaneous peak frequency of the $(l = 2, m = 2)$ mode of the GW signal and by an increase in the overall GW luminosity, as evidenced by the evolution of $E_b$ in figure 2.8.

Figure 2.9 shows the general trends of the $(l = 2, m = 2)$ component of the GW strain and of the binary binding energies across our set of simulations. We do not find any significant difference in the inspiral GW signal between the BLh and BLQ binaries. This also includes the 1.856 $M_\odot$ - 1.020 $M_\odot$ binary for which quarks are also present in the inspiral, as discussed above. Significant differences are present in the postmerger for all the binaries, with the exception of the 1.856 $M_\odot$ - 1.020 $M_\odot$ binary, which results in prompt BH formation. For the latter, the postmerger signal is consistent with the ring down of the formed BH. The phase transition is imprinted in the duration of the postmerger signal and as a change in the peak frequency and overall amplitude of the signal. All BLQ binaries form BHs during our simulation time (see also tables 2.2 and

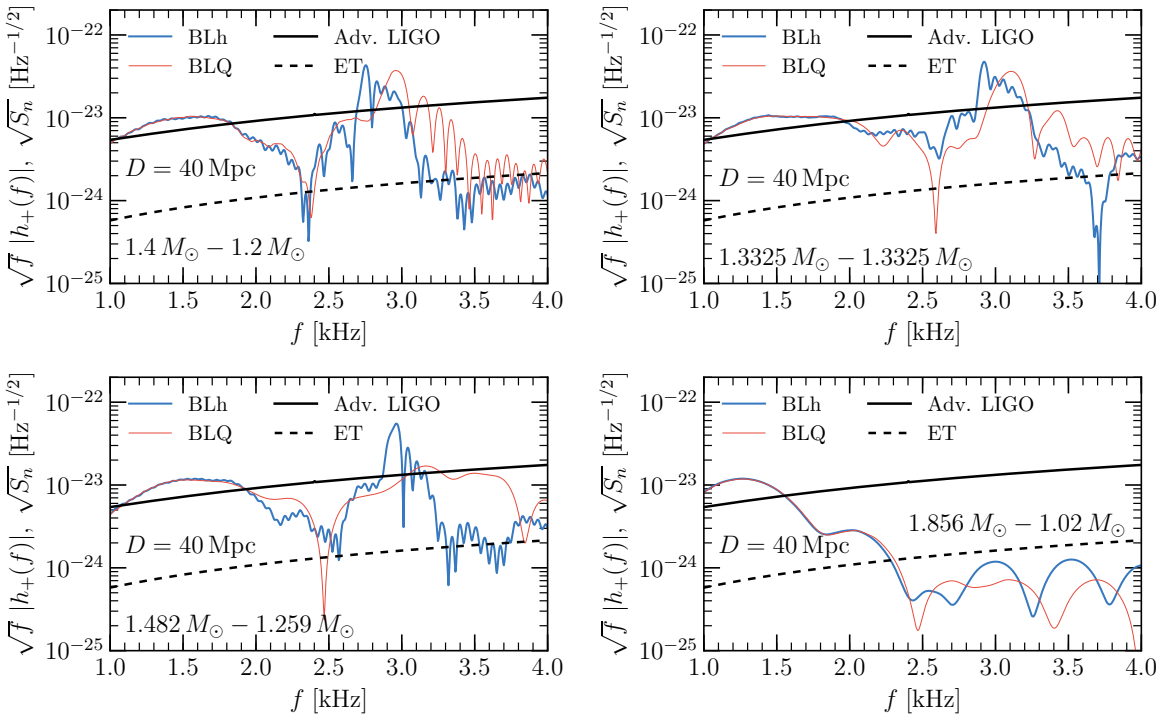


**Figure 2.10.** Power spectrum of the $(l = 2, m = 2)$ mode of the GW strain for the 1.4 $M_\odot$ − 1.2 $M_\odot$, 1.3325 $M_\odot$ − 1.3325 $M_\odot$, 1.482 $M_\odot$ − 1.259 $M_\odot$, and 1.856 $M_\odot$ − 1.020 $M_\odot$ binaries. An exponential filter was applied to the data to remove the inspiral signal. The difference in the peak frequency between the BLQ and the BLh binaries in the top panels is sufficiently large to be measured. On the other hand, because of the short length of the BLQ postmerger signals, the differences in the peak frequency for the binaries in the bottom panels is smaller than the nominal uncertainty of the Fourier transform, so they cannot be measured.

2.3). The change in the amplitude of the GW signal is similar to that reported by Radice et al. [20], who studied the impact of the appearance of hyperons in mergers. However, in the case of a first order transition, the change in the amplitude is accompanied by a change in the peak frequency of the postmerger signal [54].

More specifically, the works by Sekuguchi et al. [19] and Radice et al. [20] found that the appearance of hyperons lead to a softening of the EOS which is qualitativaly similar to that induced by a first order quark deconfinement phase transition and documented here. Indeed, like the quark deconfinement phase transition, the creation of hyperons lead to more compact remnants that are more prone to collapse. However, because the thermodynamic potentials of matter remain smooth, the appearance of hyperons does not impact the peak frequency of the postmerger signal of the remnants, if not for the fact that binaries simulated with hyperons typically results in earlier BH formation.

The GW power spectra for a representative set of binaries are shown in figure 2.10.

A characteristic feature in the postmerger spectra of NS mergers is the existence of a postmerger peak frequency $f_2$ [59, 60, 112–120] in the range of 2-4 kHz that is related to the rotational frequency of the remnant. As is evident from figure 2.10, there is a characteristic shift in this postmerger peak frequency due to the appearance of quarks in binaries evolved with the BLQ EOS. This is in qualitative agreement with the findings of Bauswein et al. [54], who found that such shift is a distinctive signature of a phase transition. However, the maximum shift in $f_2$ among our simulations is only 0.21 kHz (tables 2.2 and 2.3). This is to be contrasted with the range of shifts (0.2-0.6 kHz) in $f_2$ observed by Bauswein et al. [54]. These differences could arise due to the differences in the EOS models used in this study and in Bauswein et al. [54], or they could be due to differences in the methodologies of our simulations. We cannot verify this since the EOS models used by Bauswein et al. [54] are not available to us.

We remark that these shifts in the postmerger peak frequencies can only be observed for binaries with a sufficiently long postmerger, where the Fourier uncertainty principle would imply a finite localization of power spectral density (PSD) peaks in the frequency domain. For a short-lived remnant, the uncertainty principle dictates that there would be a spread of PSD over a wide range of frequencies and hence the peaks would be too broad to observe any shifts (See figure 2.10). The uncertainty in the Fourier transform is the reciprocal of the length of the postmerger signal, i.e., $\Delta\mathrm{FT} = 1/(t_{\mathrm{coll}} - t_{\mathrm{merg}})$. For long lived remnants, i.e., 1.30 $\mathrm{M}_\odot - 1.30$ $\mathrm{M}_\odot$, 1.3325 $\mathrm{M}_\odot - 1.3325$ $\mathrm{M}_\odot$ and 1.4 $\mathrm{M}_\odot - 1.2$ $\mathrm{M}_\odot$, the shift in peak frequency between BLh and BLQ EOS satisfies $\Delta f_2 > \Delta\mathrm{FT}$ and hence $f_2$ shift can be a robust signature of a phase transition. For shorter lived remnants, like 1.482 $\mathrm{M}_\odot - 1.259$ $\mathrm{M}_\odot$ and 1.365 $\mathrm{M}_\odot - 1.365$ $\mathrm{M}_\odot$, $\Delta f_2 \leq \Delta\mathrm{FT}$ and so the frequency shifts are not good indicators of phase transitions here. Finally, for systems with very little to no postmerger, like the equal mass binaries from 1.4 $\mathrm{M}_\odot - 1.4$ $\mathrm{M}_\odot$ to 1.6 $\mathrm{M}_\odot - 1.6$ $\mathrm{M}_\odot$, and 1.856 $\mathrm{M}_\odot - 1.020$ $\mathrm{M}_\odot$, $t_{\mathrm{coll}} \to t_{\mathrm{merg}}$, so the frequency distribution of the postmerger signal is too broad to compute any robust signature. We find that this criterion for comparing the shifts in $f_2$ with uncertainties in the Fourier transform of the time domain signal holds across the two spatial resolutions we have investigated (see tables 2.2 and 2.3).

To eliminate additional sources of these $f_2$ shifts, we perform a simulation of the 1.365 $\mathrm{M}_\odot - 1.365$ $\mathrm{M}_\odot$ binary (tables 2.2 and 2.3) using the subgrid-scale turbulence model of Radice [100], which was calibrated using the GRMHD simulations of Kiuchi et al. [121]. We find that the introduction of viscosity can result in the appearance of secondary peaks in the postmerger spectrum that are formed in the first few milliseconds

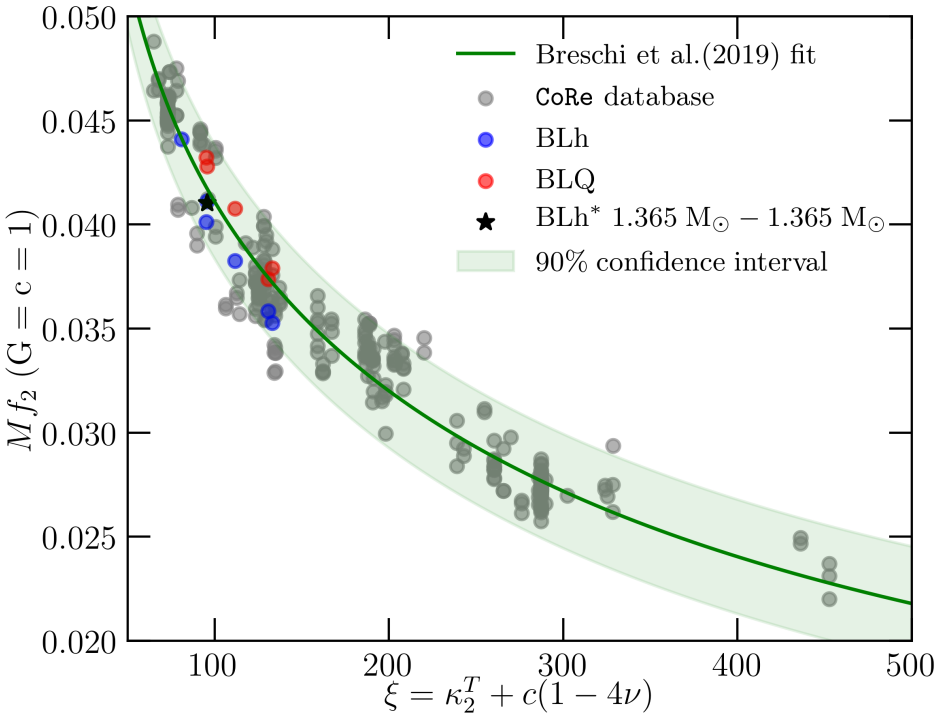


**Figure 2.11.** Correlations between the total mass-scaled postmerger peak frequency $Mf_2$ and the tidal parameter $\xi$. Also shown is the fit from the quasi universal relation presented in [64] along with its 90% confidence interval. The grey points correspond to simulations catalogued in the CoRe database [123]. It can be seen that deviations in $f_2$ (red circles) by virtue of phase transitions are not large enough to violate the quasi-universal relation.

after the postmerger. However, the $f_2$ peak frequency is not affected, in agreement with our previous findings [122]. In this chapter, we denote the results from this run with an asterisk to the EOS name as BLh* (see tables 2.2, 2.3, 2.4, 2.5, and figures 2.11, 2.14).

The $f_2$ peak frequency has been shown to be tightly correlated with the NS radius and tidal properties of a binary [59–63, 113, 124, 125]. These empirical, quasi-universal relations are interesting because they correlate the tidal properties of a binary, which are characteristic of the inspiral, to the postmerger peak frequency $f_2$ of the remnant. A significant departure from these relations caused by shifts in $f_2$ can provide conclusive evidence for deconfinement phase transitions [54–57]. We test the quasi-universal relation proposed in Breschi et al. [64] against our $f_2$ frequencies and present the results in figure 2.11. In line with the terminology presented in [64], we plot our postmerger peak

frequencies from BLh and BLQ binaries against the tidal parameter $\xi$ defined by:

$$\xi = \kappa_2^T + c(1 - 4\nu)\,, \tag{2.21}$$

where $c$ is a fitting parameter, $\nu = M_1 M_2/(M)^2$ is the symmetric mass ratio, and $\kappa_2^T$ is the tidal polarizability parameter defined by

$$\kappa_2^T = 3\left(\Lambda_1 X_1^4 X_2 + \Lambda_2 X_2^4 X_1\right). \tag{2.22}$$

Here $X_i = M_i/M$. The functional form of the quasi-universal relation is given as:

$$M f_2 = F_0 \frac{1 + n_1\xi + n_2\xi^2}{1 + d_1\xi + d_2\xi^2} \tag{2.23}$$

where $F_0, n_1, n_2, d_1, d_2$ and $c$ are fitting parameters specified in [64]. As mentioned previously, the shifts in $f_2$ (when observed i.e. when $\Delta f_2 > \Delta\mathrm{FT}$) have been very modest as compared to Bauswein et al. [54, 55] and Blacker et al. [57] and are found to be described very well by Eq. (2.23). We do not find any evidence of strong deviations from the fit as a consequence of deconfinement phase transitions. Our results show that the absence of deviations in the $f_2$ from the expected universal relations cannot be used to rule out the presence of phase transitions or to constrain their density threshold, as instead claimed by Blacker et al. [57]. Additionally, we would like to remark that the quasi-universal relation presented in figure 2.11 describes a larger dataset of BNS mergers than any of the previous studies by including simulations from 14 EOSs (including hyperonic and quark EOSs) and a large sampling of mass ratios ranging from 1 to 2.06 to describe asymmetric binaries which are consistently taken into account by the parameter $\xi$. Finally, we caution the reader that, even though shifts in $f_2$ have not been reported in the literature for purely hadronic EOSs, we cannot exclude the possibility that such shifts might occur for hadronic EOSs exhibiting a sudden change in their stiffness at several times the saturation density.

## 2.6 Dynamical Ejecta and Disks

### 2.6.1 Ejecta and Nucleosynthesis

We now describe the properties of the outflow from a merger with a deconfinement phase transition which will eventually help calculate possible EM counterparts of such mergers.

To this aim, we calculate the asymptotic velocity, the specific entropy, the angle with the orbital plane, and the electron fraction of the matter ejected on a dynamical timescale in our simulations. In particular, we record the properties of matter that crosses a coordinate sphere of radius 200 $G\,\mathrm{M}_\odot/c^2$ ($\simeq 295.34$ km) and that is unbound according to the geodesic criterion, i.e., with $u_t < -1$. We refer to [126–128] for a discussion of other possible choices.

We summarize the results of this analysis in tables 2.4 and 2.5. We report the mean ejecta properties from our simulations. When comparing the BLh and the BLQ binaries, we do not find systematic differences in the total ejecta mass, or in the average entropy, composition, or angular distribution. The only robust trend appears in the velocity distribution of the ejecta. For this purpose, we define the fast moving ejecta as the baryonic matter which follows the condition $W\beta > 1$ where $W$ is the Lorentz factor and $\beta = v/c$. The bulk ejecta from both the BLh and the BLQ binaries are subrelativistic, with asymptotic velocities in the range $0.1-0.3$ $c$, in agreement with previous findings [23,24,79,80,129,130]. However, we also observe that a small fraction of the ejecta (up to $10^{-4}\,\mathrm{M}_\odot$) achieves asymptotic velocities as large as $0.8$ $c$ [24,131–134]. It is in this latter component of the ejecta that we find a systematic difference between the BLh and the BLQ binaries. In particular, the BLQ binaries that do not undergo prompt collapse produce larger amounts of ejecta with velocity $W\beta > 1$ than the corresponding BLh binaries. The total kinetic energy of this component of the ejecta is also larger for the BLQ EOS. This fast-moving tail of the ejecta is launched when the remnant bounces back after the merger [24,134], so we speculate that the differences between the BLh and BLQ binaries in this component of the outflow is due to the stronger oscillations experienced by the BLQ remnants after merger. We remark that a similar effect was reported by [24]. In that case, it was the appearance of hyperons that caused the merger remnant to bounce more strongly, while here the stronger bounce of the BLQ binaries is caused by the QCD phase transition.

Figure 2.12 shows histograms of the properties of the outflows for three representative binaries. The $1.3\ \mathrm{M}_\odot - 1.3\ \mathrm{M}_\odot$ binary is representative of a low-mass merger for which the appearance of deconfined quarks does not lead to qualitative changes in the dynamics during the first milliseconds from the merger. This is due to the relatively low densities achieved by this binary ($\rho_{\rm max} \lesssim 4\ \rho_{\rm nuc}$) in the first $\sim$5 ms of the merger. As the stars merge, the quark fraction $\mathrm{Y_q}$, in phase with central density, attains a maximum of 0.3. Further oscillations in density are constrained between $2.8\rho_{\rm nuc} - 4\rho_{\rm nuc}$ and are not conducive for the formation of a large amount of deconfined quarks whose fraction

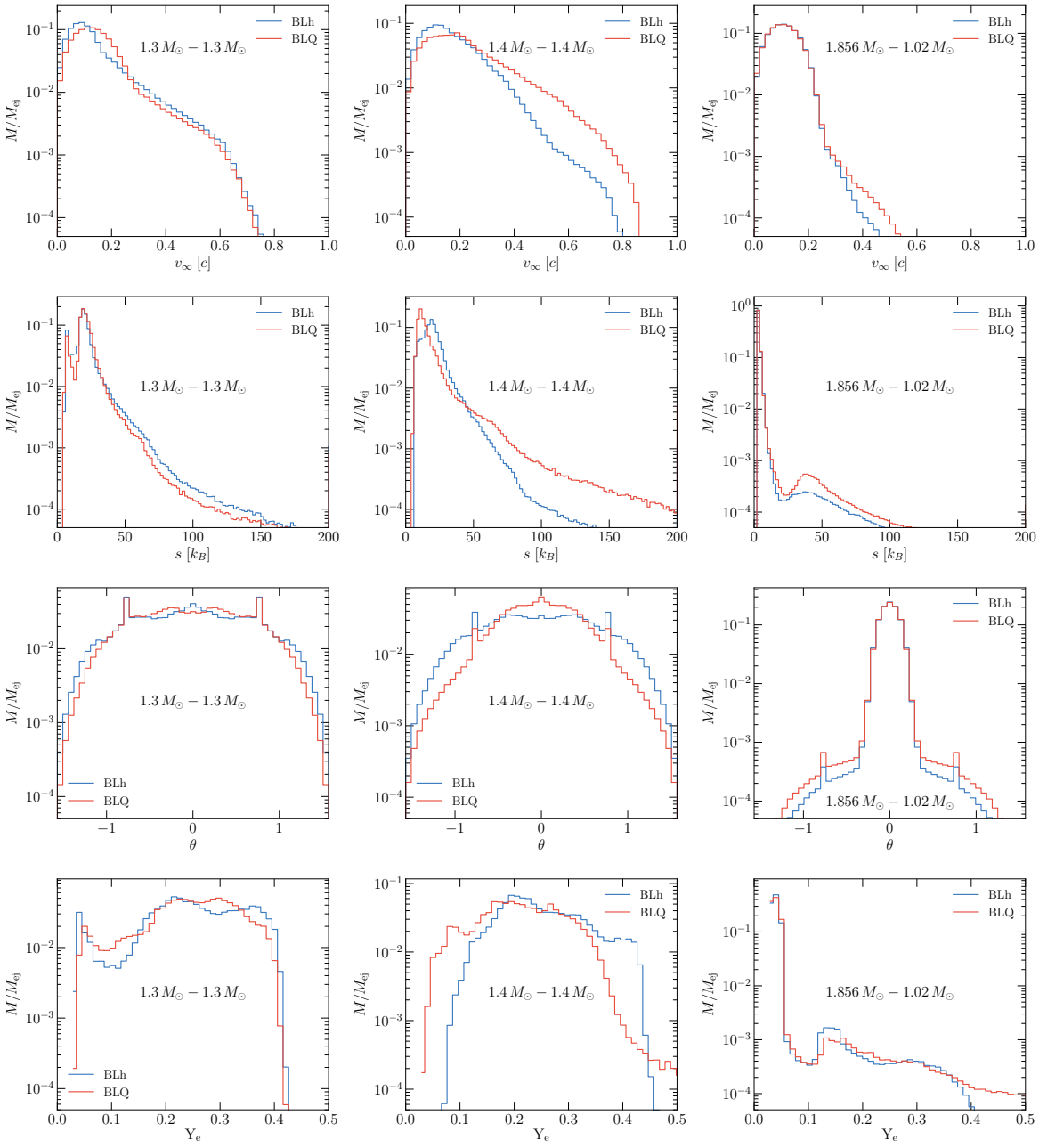


**Figure 2.12.** Histograms of the asymptotic velocity $v_\infty$, specific entropy $s$, angle with the orbital plane $\theta$, and electron fraction $Y_e$ of the ejecta for three representative binary configurations evolved with the BLh and BLQ EOSs. The most significant differences are seen in the 1.4 $M_\odot$ - 1.4 $M_\odot$ binary, for which the BLQ EOS predicts rapid BH formation, while the BLh EOS predicts a long-lived remnant. We note that $M$ here represents the mass of the ejecta in the corresponding bins normalized to $M_{ej}$ i.e. the total ejecta mass as reported in tables 2.4 and 2.5.

oscillates between $0 - 0.15$ for $t - t_{\rm merg} < 5$ ms. It is important to emphasize that the presence of a phase transition still leads to a qualitative change in the outcome of the 1.3 $M_\odot$ – 1.3 $M_\odot$ merger. Indeed, the BLQ binary collapses to BH after ∼15 ms of the merger, while the BLh binary forms a long-lived remnant (see tables 2.2 and 2.3). However, these differences manifest themselves on somewhat longer timescales than those relevant for the production of the dynamical ejecta, which is launched within ∼1−5 ms of the merger [24].

The 1.4 $M_\odot$ – 1.4 $M_\odot$ binary is representative of a binary for which the impact of quark deconfinement leads to dramatic qualitative differences in the dynamics of the merger. The BLh binary forms a long-lived remnant that does not collapse within our simulation time, while the BLQ binary experiences a catastrophic loss of pressure support as hadrons are converted to quarks and forms a BH within ∼2 ms of the merger. Neither is a case of prompt BH formation: the 1.4 $M_\odot$ – 1.4 $M_\odot$ BLQ binary still experiences one violent bounce before collapsing. The more violent merger of the BLQ binary is reflected in a significantly larger amount of fast moving ejecta (figure 2.12 and tables 2.4, 2.5). This interpretation is confirmed by the presence of a significant excess of high-entropy, shock-heated, material in the BLQ ejecta. The ejecta distribution is also more concentrated close to the orbital plane, as expected for the fast-tail of the shock driven ejecta [24, 134]. Interestingly, the electron fraction in the ejecta of the 1.4 $M_\odot$ – 1.4 $M_\odot$ BLQ binary is smaller than that of the corresponding BLh binary. This is because the BLh ejecta are irradiated by neutrinos from the massive NS remnant, which is absent in the BLQ binary (due to the early BH formation).

The 1.856 $M_\odot$ – 1.020 $M_\odot$ binary is an example of a merger resulting in prompt BH formation with both the BLh and BLQ EOSs. The dynamical ejecta is entirely driven by tidal torques on the secondary NS, so we do not expect any effect due to the phase transition. Indeed, the differences between the 1.856 $M_\odot$ - 1.020 $M_\odot$ BLh and BLQ binaries shown in figure 2.12 are not robust with resolution. However, our simulation reveal another interesting effect. The ejecta has two components. A low electron fraction, low entropy component with most of the ejecta mass and a high electron fraction $Y_e > 0.3$ and high entropy $s \gtrsim 25\ k_B$ component. The presence of a second component in the ejecta in highly asymmetric binaries was already reported in Refs. [79, 120, 135], where it has been attributed to the presence of a residual shock driven component of the outflows. However, a careful analysis of the evolution of the ejecta in the orbital plane as a function of time suggests that, at least for the binaries considered here, this second component is due to the presence of internal shocks in the tidal debris.

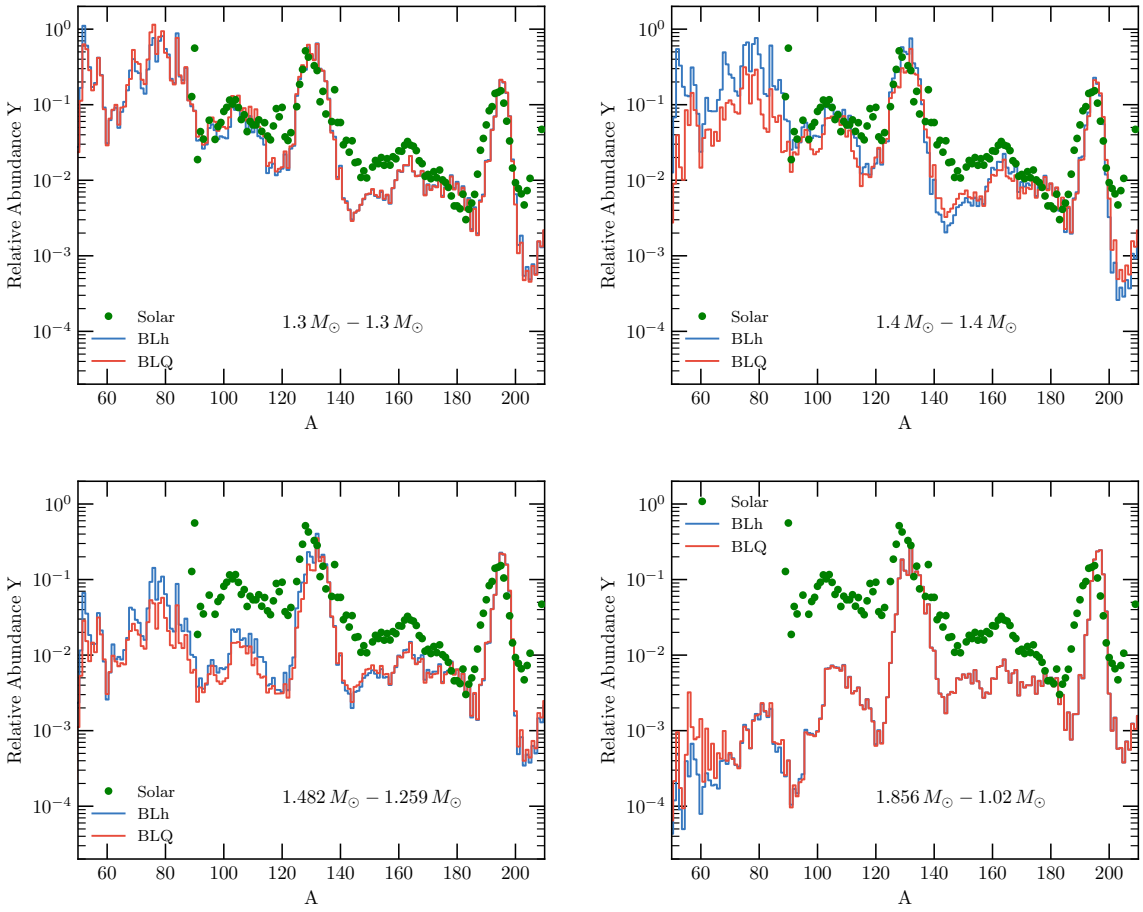


**Figure 2.13.** Nucleosynthesis yields of the dynamical ejecta from selected binaries. The final relative abundances in the ejecta are insensitive to the appearance of quarks, but are instead sensitive to the binary mass-ratio. Comparable-mass binaries produce r-process elements with relative abundances close to Solar $r$-process residual, while high-mass ratio binaries show ratios of heavy to light r-process abundances that are significantly larger than the Solar $r$-process residual. We normalize the yields at a given A with respect to the yields in the $3^{rd}$ r-process peak i.e. A $\in [180, 200]$ to report the relative abundance Y.

The outflow from BNS mergers realizes the conditions for the production of heavy elements via the rapid neutron capture process [136]. We use the methodology described in detail in Refs. [23] and [24] to compute the relative abundances of heavy nuclei produced in the dynamical ejecta from our simulations. Our results are shown in figure 2.13. We find that the presence of deconfined quarks in the BLQ binaries does not leave a significant imprint on their nucleosynthesis yields. Even in the case of the 1.4 $M_\odot - 1.4$ $M_\odot$ binaries, for which the phase transition has a strong impact on the merger dynamics, we find that the differences in the yields are only modest. The variation in the relative elemental

abundances in the ejecta as the mass ratio of the binary is varied, is significantly larger. Indeed, we find that while the dynamical ejecta from binaries with mass ratio $q \simeq 1$ robustly produce elements with relative abundances close to Solar $r$-process residual, the higher mass ratio mergers tend to overproduce second and third r-process peak elements. This is because asymmetric binaries produce a larger amount of neutron rich, cold, tidal ejecta [24, 134].

### 2.6.2 Remnant Disks

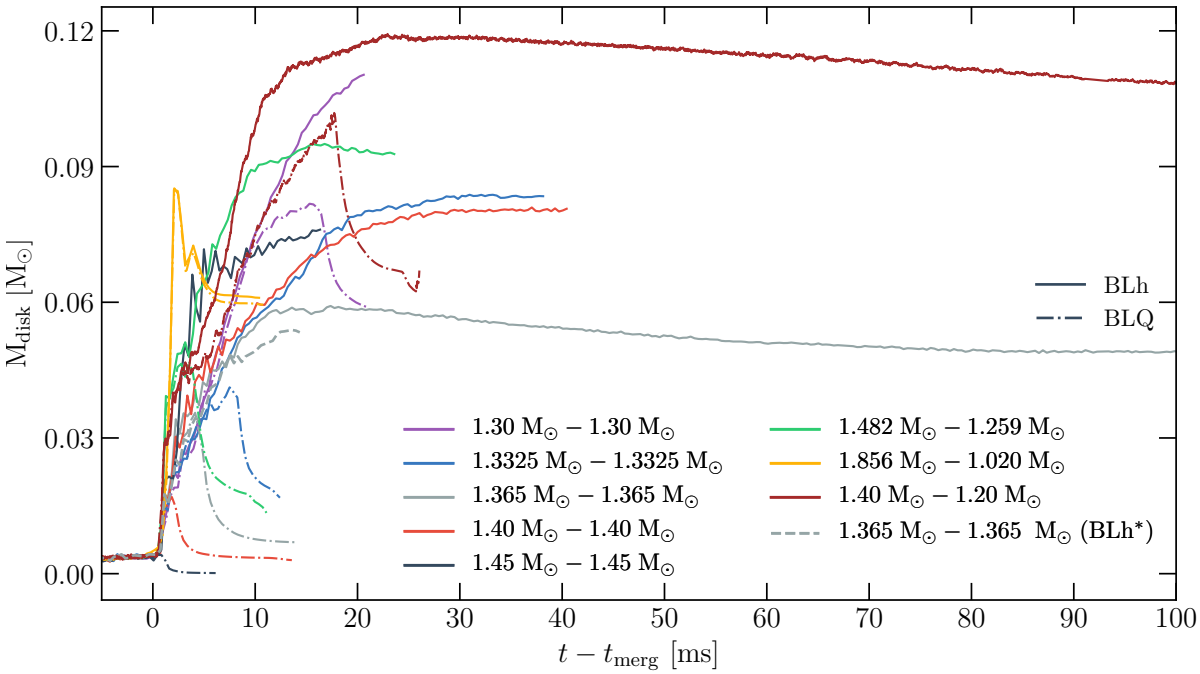


**Figure 2.14.** Evolution of disk mass for a subset of our simulations. Binaries with the BLh EOS (solid lines) form stable, long-lived remnants with disks evolving on long timescales. The binaries with deconfined quarks (dotted lines) result in the formation of BHs. The gravitational collapse is accompanied by the accretion of a significant fraction of the disk over a timescale of few milliseconds. Binaries where remnants from both EOSs undergo prompt collapse do not show significant differences in their disk mass evolution.

Following the conventions in [137], we define the accretion disk as all baryonic matter with rest mass density $\rho < 10^{13}$g cm$^{-3}$. We remark that this density threshold corresponds to the approximate location where the angular velocity of the remnant becomes Keplerian [104]. In the case of BH remnants, all of the matter outside of the BH has $\rho < 10^{13}$g cm$^{-3}$. Furthermore, we exclude all matter enclosed by the BH apparent

horizon i.e. we only include regions where $\alpha \geq 0.3$. In other words,

$$M_{\rm disk} = \int \sqrt{\gamma}\, W\, \rho\, dx\, dy\, dz \tag{2.24}$$

where $\gamma$ represents the determinant of the spatial metric and $W$ is the Lorentz factor. The integration is carried out over all matter in the region defined above.

As discussed in detail in Radice et al. [24], the remnant accretion disk is formed of material that is squeezed out of the collisional interface between the NSs during and shortly after the merger. So the disk mass initially increases with time, as shown in figure 2.14. For those binaries that do not form BHs, the disk mass peaks within 10−20 ms of the merger. Over longer timescales the angular momentum transport due to spiral density waves drives accretion and a secular outflow from the disk [80, 128]. Angular momentum transport due to MHD turbulence is also expected to contribute to this process, however our simulations did not include magnetic fields, so they cannot describe this phenomenon. At the same time, we remark that in our previous study we found that in the first ∼100 ms of the merger the spiral waves are expected to be the dominant mechanism for angular momentum transport [128].

The dynamics is very different for binaries that form BHs. When the central part of the remnant collapses a significant fraction of the disk is accreted within a few milliseconds (figure 2.14), as also reported in Ref. [80]. Since the BLQ EOS predicts early BH formation for all binaries considered in this study, while most of the BLh binaries form long-lived remnant, this process leads to significant differences between the remnant disks for the BLh and BLQ binaries. Exceptions to these are the massive equal-mass binaries that collapse promptly for both the BLh and BLQ EOS resulting in a rapid disk accretion post merger and the 1.856 $M_\odot$ − 1.020 $M_\odot$ system, for which the disk is formed from the tidal disruption of the secondary NS in the late inspiral, prior to the production of a significant amount of deconfined quarks.

## 2.7 EM Signatures

### 2.7.1 Kilonova Light Curves

For the purpose of computing kilonova light curves, we compute the ejecta properties using the Bernoulli criterion, which allows us to include both the dynamical ejecta discussed above and the wind ejecta emerging at later times in our simulations [126–128]. We also assume that 20% of the disk mass at the end of the simulation is unbound

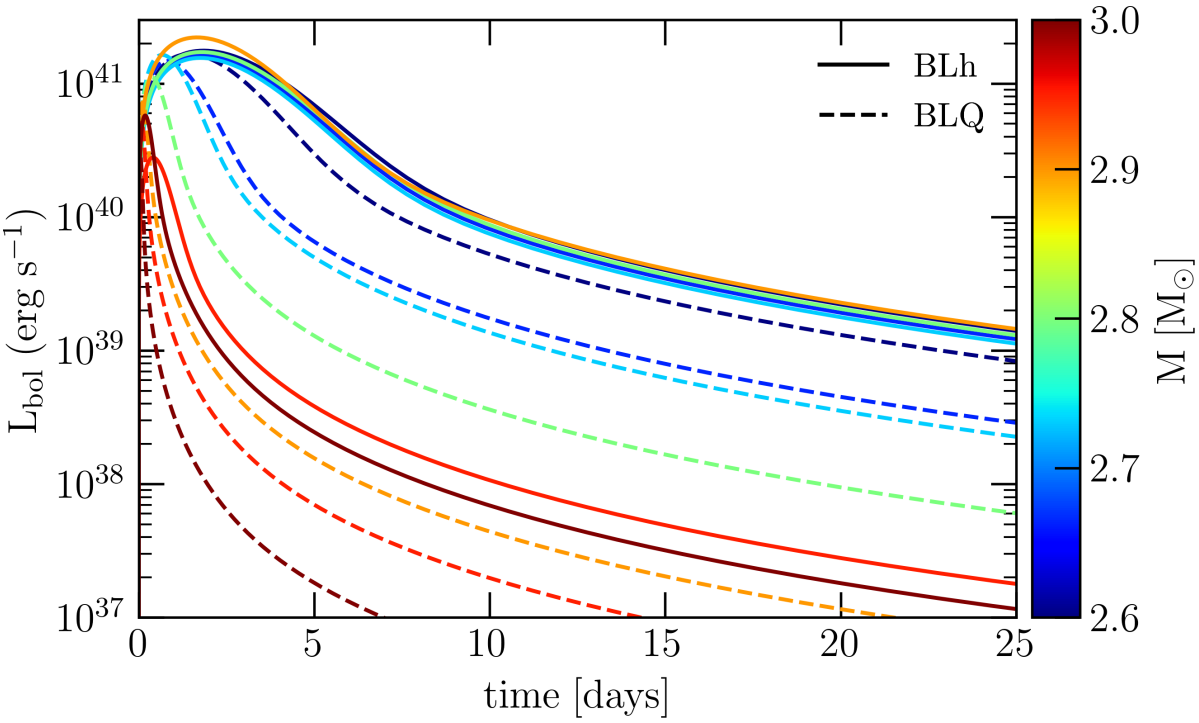


**Figure 2.15.** Kilonova light curves for a subset of our simulations with $q = 1$. The colour code represents the total mass of the binary with the dashed (solid) curves indicating models with (without) a QCD phase transition. In general, BLh binaries are more luminous and the brightness decreases with increasing mass.

by winds [138–140]. For the wind component of the ejecta, we assume mass-averaged electron fraction and velocity to be 0.2 and $0.1c$ respectively [141]. We calculate bolometric luminosities using a single component kilonova light curve model, whose basic equations are given in Refs. [142–144]. In addition to the total ejecta mass, we also extract from the simulations, the mass-averaged velocity and electron fraction of the outflow. The latter is used to calculate the matter opacities using an analytic fit to the results of Ref. [145]. The input heating rate and thermal efficiency of the ejecta used here are taken from Refs. [146] and [147], respectively.

We show bolometric lightcurves for models with q = 1 in figure 2.15. Generically, we find that the BLh binaries lead to more luminous and slowly evolving kilonovae than their counterparts with the BLQ EOS. However, these differences are entirely attributable to the differences in life time between the BLh and BLQ remnants. Indeed, we also observe that the kilonova becomes dimmer for more massive binaries. Equal mass binaries undergoing prompt BH formation have very small ejecta and disk masses, owing to which their kilonovae are very dim. Kilonova observations are powerful probes to determine the life time of BNS merger remnants [148]. However, the time to collapse for a merger

remnant might depend on factors other than a phase transition such as particular features in the hadronic EOS or magnetic and neutrino effects [149].

We observe that the kilonova corresponding to the binary merger of 1.45 $M_\odot$−1.45 $M_\odot$ with the BLh EOS is the brightest among all our models as shown in figure 2.15. This may be attributed to the fact that the ejecta from this model is the most energetic (see table 2.4) of all our systems. It is important to note that the binary is very close to the prompt collapse threshold for the BLh EOS and hence is subjected to large uncertainties arising from spatial resolution which also levies large uncertainties in the calculation of disk masses. Indeed, we observe that at standard resolution (SR) the binary is long-lived with a lifetime of $\gtrsim 14$ ms (table 2.2). However, with the low resolution (LR) grid setup, it collapses to a BH on a much shorter time scale of $\sim 3$ ms. Another aspect to note here is that this is the only binary where the BLQ remnant collapses promptly to a BH but the BLh remnant does not.

### 2.7.2 Kilonova Afterglow

The fast-moving tail of the ejecta is expected to drive shocks in the ISM which might produce synchrotron radiation over a wide range of the EM spectrum over a timescale of months to years from the merger. This is the so-called kilonova afterglow [132, 134, 150–152]. This scenario has been invoked to explain the recent deviation of the X-ray afterglow in GW170817 from the theoretical expectations for a relativistic jet [134, 153], although other interpretations of this data are not excluded [153, 154]. The properties of the kilonova depend sensibly on the ejecta mass and velocity distributions. It is therefore conceivable that late time observations of BNS mergers could probe the presence of phase transitions in the EOS of dense matter.

We calculate the lightcurves of the synchrotron radiation arising from the interaction between the dynamical ejecta and the ISM with the semi-analytic code `PyBlastAfterglow` [134, 153]. The code computes the synchrotron radiation that arises from electrons accelerated in the amplified magnetic field in the forward shock, i.e., in the shock between the expanding blast wave and ISM. The total flux density is computed by integrating the flux from each element of the solid angle over equal-time arrival surfaces. The ISM is assumed to be cold and uniform with density $n_{\rm ISM}$. The equipartition microphysical parameters, describing the energy conversion efficiency between the shock and the magnetic fields and electrons, $\epsilon_e$ and $\epsilon_B$ respectively, are assumed to be constant. The initial conditions for the code are given by the kinetic energy and angular distribution of the ejecta from the merger simulations. Its evolution is computed assuming only

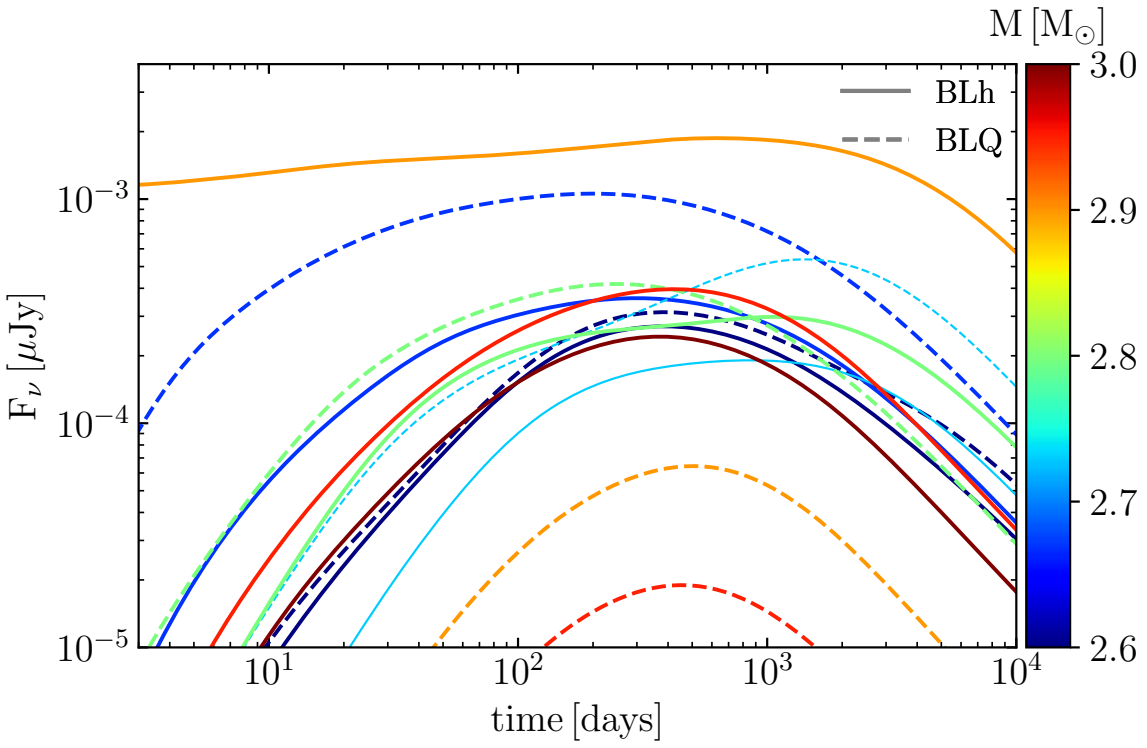


**Figure 2.16.** Kilonova afterglow light curves at 1 keV for a set of equal mass models. The models' total mass is color-coded. Dashed (solid) curves indicate models with (without) phase transition. The plot shows that the afterglow of models with phase transition in general is brighter and more extended in time.

adiabatic energy losses and no lateral spreading.

We set the free parameters as follows. The observational angle, namely the angle between the line of sight and the polar axis of the BNS system, is $\theta_{\rm obs} = 30\,{\rm deg}$, which is consistent with the observational geometry for GW170817 [1]. We consider a source at 40 Mpc with the redshift $z = 0.0099$. The ISM density and microphysical parameters are set as $n_{\rm ISM} \in (10^{-3}, 10^{-2})\,{\rm cm}^{-3}$, $p = 2.15$, $\epsilon_e = 0.2$, and $\epsilon_B = 5 \times 10^{-3}$. These values are chosen from the respective credibility intervals inferred for GRB170817A [155]. Note however, that the kilonova afterglow might have different microphysical parameters as compared to the gamma ray burst (GRB) afterglow. Indeed, recent observations suggest the onset of the spectral evolution of the synchrotron emission from GW170817 [153].

Figure 2.16 shows the kilonova lightcurves from a set of representative equal mass models with total mass ranging from $2.6\,{\rm M}_\odot$ to $3.0\,{\rm M}_\odot$. Notably, the kilonova properties of low mass models with BLh EOS are rather independent of M, peaking at $\lesssim 10^3$ days and reaching flux density $\simeq 10\,\mu$Jy. The inclusion of a phase transition in these models,

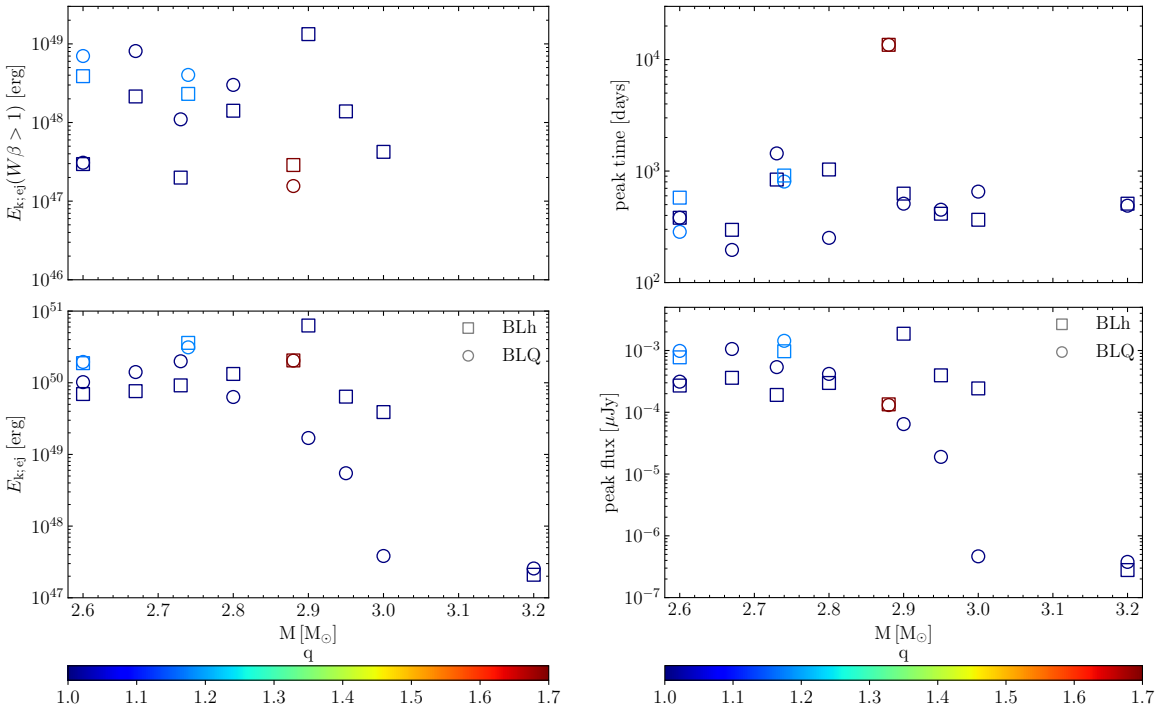


**Figure 2.17.** The ejecta kinetic energy (*left two panels*) and kilonova properties (*right two panels*) for the simulations with and without phase transition (BLQ and BLh, respectively). The kinetic energy is shown separately for the entire ejecta (*lower subpanel*) and for the fast component only (*upper panel*). The kilonova properties are the lightcurves' peak time (*upper panel*) and flux (*lower panel*). Circle (squre) markers indicate models with (without) phse transition, i.e., models with BLQ (BLh) EOS. The plot shows a correlation between the peak flux and the total kinetic energy. The effect of the phase transition is very prominent at high mass binaries, where the softening of EOS leads to prompt collapse, reducing the ejecta kinetic energy and peak flux.

generally, leads to broader and slightly brighter kilonova lightcurves, as the fast tail of the ejecta of these models becomes more energetic (as discussed previously and as shown in the left panel of figure 2.17). This is especially apparent for the model with $\mathrm{M} = 2.67\,\mathrm{M}_\odot$, where the inclusion of the phase transition leads to a considerably more energetic fast ejecta tail (see table 2.4 and upper left panel of figure 2.17), which in turn leads to a significantly broader lightcurves.

The general properties of the kilonova lightcurves, i.e., the peak flux $F_{\rm peak}$ and the peak time time $t_{\rm peak}$ are shown in figure 2.17 (right panel) for all models. Notably, $F_{\rm peak}$ is well correlated with $E_{\rm ej;kin}$, a trend that is much less clear in simulations with large mass ratio [134]. The plot shows that indeed, among the low mass models, the inclusion of the phase transition raises $F_{\rm peak}$. However, a difference of $\leq 10\,\mu$Jy is smaller than the

systematic uncertainties introduced by ill-constrained microphysical parameters. When more massive models, $M \in (2.9, 3.1)\,M_\odot$, are considered, the difference in $F_{\rm peak}$ becomes larger than the systematic uncertainties, as models with BLQ EOS undergo prompt collapse, producing less energetic ejecta.

The effect of the phase transition on the peak time is, however, unclear. The largest difference is observed for the model with $1.4\ M_\odot - 1.4\ M_\odot$, where the $t_{\rm peak}$ of the model without phase transition is $\sim 9$ times larger. For the other models the difference is within the systematic uncertainties due to ill-constrained $n_{\rm ISM}$. As was the case for early-time kilonova, here too we observe the $1.45\ M_\odot - 1.45\ M_\odot$ binary with the BLh EOS to have the brightest overall afterglow. For this binary, the large kinetic energy of the ejecta is responsible for the early rise and subsequently large values of the synchrotron flux.

## 2.8 Conclusions

In this chapter we presented fully general relativistic neutrino-radiation hydrodynamics simulations of BNS mergers with a first order phase transition to deconfined quark matter. We considered and systematically analysed a wide range of BNS configurations. We studied their evolution using two EOSs with identical hadronic physics but that, respectively, included or excluded a QCD phase transition to deconfined quarks: the BLQ EOS and BLh EOS. The BLQ EOS is presented here for the first time. By comparing the results obtained with both the EOSs, we computed the observable signatures: GW, EM counterparts, and nucleosynthesis yields resulting from the phase transition.

The BLh EOS, which describes the hadronic phase of dense stellar matter, has been calculated making use of a finite temperature BHF approach [156–158] starting from modern two-body and three-body nuclear interactions derived within ChEFT. To model the quark phase we used a phenomenological bag model EOS which includes the effects of gluon mediated QCD interactions between quarks up to the second order in the QCD coupling $\alpha_s$. We assumed a first order transitions between the two phases and using the Gibbs construction [38] we derived the EOS for hadronic-quark mixed phase. When considering non-spinning isolated NSs, the differences in properties of matter modelled by the zero temperature version of the two EOSs, BLh and BLQ, begin to manifest for stars heavier than $\sim 1.7\,M_\odot$.

We find that the hot interface region created when the two NSs of a binary system start to merge is the first site where deconfined quark matter can be produced. In this region matter crosses the phase boundary at intermediate densities ($\rho \sim 2\ \rho_{\rm nuc}$)

and temperatures (T $\sim$ 30 MeV). As the merger proceeds and the cores of the two stars fuse, the inner core of the remnant is nearly-adiabatically compressed to high densities ($\rho \gtrsim 3\ \rho_{\rm nuc}$) and crosses the phase boundary at low temperatures (T $\sim$ 5 MeV). The phase transition results in a loss of pressure support in the merger remnants. In particular, the BLQ remnants become more compact and collapse to BH significantly earlier than the corresponding BLh remnants, which do not model the QCD phase transition. These results are in good qualitative agreement with the findings of Most et al. [52, 53]. Additionally, we find that the threshold mass above which prompt BH formation takes place is lowered by the inclusion of the phase transition in the BLQ EOS.

We employ Lagrangian tracer particles to record the thermodynamic evolution of the binaries by tracking the properties of individual fluid elements. We find that fluid elements repeatedly cross the phase boundary between the hadronic phase and the mixed quark phase as the remnants oscillate. Such dynamics was anticipated by Hanauske et al. [109], but it is shown here for the first time in the context of self-consistent simulation with a first order phase transition. Our analysis shows that BNS mergers probe a large region of the QCD phase diagram, with matter potentially crossing the phase boundary over a large range of temperatures and densities.

The QCD phase transition is most strongly imprinted in the postmerger GW signal. Owing to the rapid softening of the EOS caused by the phase transition, remnants evolved with the BLQ EOS are more compact than the corresponding BLh remnants. This influences the GW signal in two ways. First, because BLQ remnants have a larger gravitational binding energy in absolute value, they radiate a comparably larger amount of GW energy compared to the BLh binaries up to BH formation, at which point the GW emission terminates. Second, the change in the moment of inertia of the remnants due to the phase transition manifests itself as a shift in the postmerger frequency as observed in the GW spectra. While the presence of these shifts appears to be a robust feature of the phase transition [54, 55, 57], we find that for the EOS models we are considering their potential for GW astronomy is limited. On one hand, the magnitude of these shifts is found to be small. On the other hand, because of the early BH formation present in all binaries with phase transitions, the nominal uncertainty with which frequencies can be determined using Fourier analysis can be larger than the magnitude of the frequency shifts themselves. This means that a clean detection of the frequency shift for several of the binaries considered here would be impossible even in the limit of infinite SNRs. This issue is particularly severe for high mass binaries, for which BH formation occurs early. Lower mass binaries show measurable frequency shifts with $\Delta f_2 \lesssim 200$ Hz. However,

these deviations are not large compared to those normally present between different hadronic models. Indeed, we find that the postmerger peak frequencies of the binaries with first order phase transition are consistent with the quasi-universal relations that hold for hadronic EOSs [64].

We find the bulk properties of the dynamical ejecta, total mass, average composition and entropy, and geometry, are insensitive to the presence of a phase transition. Indeed, significant differences between the dynamical ejecta of the BLh and BLQ binaries are only present for those binaries that undergo prompt collapse according to the BLQ EOS, but not according to the BLh EOS. However, such differences are also expected when comparing purely hadronic EOSs with different prompt collapse mass thresholds [24], so this is not a genuine signature of phase transition. On the other hand, we find that the BLQ binaries generically produce a larger amount of ejecta with asymptotic velocities exceeding $0.6c$. This is due to the stronger bounce experienced by such binaries as a result of the phase transition.

We estimated the final abundances of different nuclear species in the dynamical ejecta arising from $r$-process nucleosynthesis. We find no significant difference between the BLh and the BLQ ejecta. This is not surprising given that the properties of the dynamical ejecta between the two set of simulations are very similar. Instead, we find that the nuclear abundances are sensitive to the mass ratio of the binaries. The elemental abundances from comparable mass ratio binaries are instead close to the Solar $r$-process residual. Higher mass ratio binary generate more tidally driven, neutron rich outflows, which preferentially produce heavy $r$-process elements ($A \gtrsim 130$) [24, 79, 80].

The remnant accretion disks for the BLQ and BLh binaries have significantly different masses at the end of our simulations. This is due to the fact that all the BLQ remnants form BHs within a short time of the merger ($\lesssim$20 ms). On the one hand, this terminates the process that leads to the formation of the disk in comparable mass ratio binaries: the shedding of hot material from the newly formed massive NS. On the other hand, BH formation is immediately followed by the rapid accretion of a significant portion of the disk. In contrast, many of the BLh binaries we have considered result in the formation of long-lived remnants. Thus, the variations in the remnant disk mass are entirely explained by the different life times of the BLh and the BLQ BNS merger remnants. Indeed, different hadronic models can also show large variations in the collapse times and the disk masses for BNS merger remnants [137].

Similarly, although substantial differences are found between the BLh and BLQ bolometric kilonova light curves, it will be challenging to use UVOIR observations of

kilonova events to constrain phase transitions. This is because the variations in kilonova properties observed in our simulations can be produced by effects others than phase transitions. For example, the appearance of hyperons, or the presence of strong magnetic fields [24]. More work is needed to understand whether these effects can be disentangled.

The fast-moving tail of the dynamical ejecta is expected to interact with the ISM and produce synchrotron radiation, the so-called kilonova afterglow. We find that, owing to the larger amount of fast ejecta, the BLQ binaries typically produce brighter synchrotron remnants than the BLh binaries. However, if prompt BH formation occurs, then the fast-moving tail of the ejecta is significantly reduced in mass and the synchrotron emission is suppressed. For this reason, the trend is reversed for binaries that undergo prompt BH formation according to the BLQ EOS, but not according to the BLh EOS. Overall, we conclude that kilonova afterglows are a promising avenue to probe a phase transition. Unfortunately, given the large uncertainties in the microphysics of the interaction between the ejecta and the ISM and the accuracy limitations of current simulations, our results cannot be used to quantitatively constrain the presence of phase transition with past or future observations. More work is needed to address these shortcomings.

Our study considered only one hadronic EOS and a specific model for the treatment of the quark phase and of the phase transition. Follow up studies should extend this work to include more hadronic models and different approaches to construct QCD phase transitions. For example, to compare the Gibbs and the Maxwell constructions. This will be the object of our future work.

## 2.9 Declaration

The author of this dissertation and Prof. David Radice were responsible for computing the majority of numerical simulations of BNS mergers and the consequent post-processing analysis. The credit for the development of the hadronic and quark EOS models goes to Prof. Ignazio Bombaci, Prof. Domenico Logoteta and Prof. Albino Perego. Dr. Vsevolod Nedroa and Dr. Rahul Kashyap assisted in the computation of electromagnetic signatures of such phase transitions. The contents of this chapter have been published in the journal Physical Review D of the American Physical Society (APS) with reference [159].

**Table 2.2.** A summary of the postmerger GW properties from all our simulations at 2 spatial resolutions. $t_{\rm merg}$ is the time of merger, $t_{\rm BH}$ is the time after merger when the system collapses to a black hole, $t_{\rm coll}$ is the time when the gravitational radiation from the 2,2 mode shuts down and $t_{\rm end}$ is the final time of the simulation. $f_2$ represents the dominant postmerger peak frequency of the 2,2 mode, $\Delta f_2$ represents the difference between the postmerger peak frequencies from the 2 EOSs and $\Delta$FT represents the numerical uncertainty in the Fourier transform. The binary labelled with BLh* is with GRLES (general-relativistic large-eddy simulation) and simulated using the calibrated turbulence model in [100].

| EOS | $M_1$ [$M_\odot$] | $M_2$ [$M_\odot$] | M [$M_\odot$] | q | Resolution | $t_{\rm BH}-t_{\rm merg}$ [ms] | $t_{\rm coll}-t_{\rm merg}$ [ms] | $t_{\rm end}-t_{\rm merg}$ [ms] | $f_2$ [kHz] | $\Delta f_2$ [kHz] | $\Delta$FT [kHz] | Prompt Collapse |
|---|---|---|---|---|---|---|---|---|---|---|---|---|
| BLh | 1.3 | 1.3 | 2.6 | 1.0 | SR | >18.69 | >18.69 | 18.69 | 2.8 | | | ✗ |
| BLQ | 1.3 | 1.3 | 2.6 | 1.0 | SR | 15.95 | 16.6 | 19.21 | 2.92 | 0.12 | 0.06 | ✗ |
| BLh | 1.3325 | 1.3325 | 2.67 | 1.0 | SR | >36.23 | >36.23 | 36.23 | 2.91 | | | ✗ |
| BLQ | 1.3325 | 1.3325 | 2.67 | 1.0 | SR | 7.44 | 8.17 | 10.55 | 3.11 | 0.19 | 0.12 | ✗ |
| BLh | 1.365 | 1.365 | 2.73 | 1.0 | SR | >101.2 | >101.2 | 101.2 | 3.06 | | | ✗ |
| BLh* | 1.365 | 1.365 | 2.73 | 1.0 | SR | >12.34 | >12.34 | 12.34 | 3.05 | | | ✗ |
| BLQ | 1.365 | 1.365 | 2.73 | 1.0 | SR | 4.1 | 4.82 | 12.15 | 3.18 | 0.12 | 0.21 | ✗ |
| BLh | 1.4 | 1.4 | 2.8 | 1.0 | SR | >38.57 | >38.57 | 38.57 | 3.2 | | | ✗ |
| BLQ | 1.4 | 1.4 | 2.8 | 1.0 | SR | 1.92 | 2.85 | 11.6 | ✗ | ✗ | ✗ | ✗ |
| BLh | 1.45 | 1.45 | 2.9 | 1.0 | SR | >14.4 | >14.4 | 14.4 | ✗ | | | ✗ |
| BLQ | 1.45 | 1.45 | 2.9 | 1.0 | SR | 0.67 | 1.68 | 4.39 | ✗ | ✗ | ✗ | ✓ |
| BLh | 1.475 | 1.475 | 2.95 | 1.0 | SR | 0.69 | 1.93 | 11.76 | ✗ | | | ✓ |
| BLQ | 1.475 | 1.475 | 2.95 | 1.0 | SR | 0.57 | 1.61 | 5.66 | ✗ | ✗ | ✗ | ✓ |
| BLh | 1.5 | 1.5 | 3.0 | 1.0 | SR | 0.56 | 1.69 | 4.76 | ✗ | | | ✓ |
| BLQ | 1.5 | 1.5 | 3.0 | 1.0 | SR | 0.51 | 1.54 | 3.63 | ✗ | ✗ | ✗ | ✓ |
| BLh | 1.6 | 1.6 | 3.2 | 1.0 | SR | 0.39 | 1.32 | 3.66 | ✗ | | | ✓ |
| BLQ | 1.6 | 1.6 | 3.2 | 1.0 | SR | 0.39 | 1.29 | 3.64 | ✗ | ✗ | ✗ | ✓ |
| BLh | 1.4 | 1.2 | 2.6 | 1.17 | SR | >105.0 | >105.0 | 105.0 | 2.75 | | | ✗ |
| BLQ | 1.4 | 1.2 | 2.6 | 1.17 | SR | 17.2 | 17.63 | 23.95 | 2.96 | 0.21 | 0.06 | ✗ |
| BLh | 1.482 | 1.259 | 2.74 | 1.18 | SR | >21.59 | >21.59 | 21.59 | 2.97 | | | ✗ |
| BLQ | 1.482 | 1.259 | 2.74 | 1.18 | SR | 3.54 | 4.42 | 9.03 | 3.2 | 0.23 | 0.23 | ✗ |
| BLh | 1.856 | 1.02 | 2.88 | 1.82 | SR | 1.02 | 1.61 | 8.31 | ✗ | | | ✓ |
| BLQ | 1.856 | 1.02 | 2.88 | 1.82 | SR | 0.65 | 1.74 | 8.74 | ✗ | ✗ | ✗ | ✓ |

**Table 2.3.** Same as Table 2.2 except that now we report the results for low-resolution (LR) simulations.

| EOS | $M_1$ [$M_\odot$] | $M_2$ [$M_\odot$] | M [$M_\odot$] | q | Resolution | $t_{BH} - t_{merg}$ [ms] | $t_{coll} - t_{merg}$ [ms] | $t_{end} - t_{merg}$ [ms] | $f_2$ [kHz] | $\Delta f_2$ [kHz] | $\Delta$FT [kHz] | Prompt Collapse |
|---|---|---|---|---|---|---|---|---|---|---|---|---|
| BLh | 1.3 | 1.3 | 2.6 | 1.0 | LR | >31.9 | >31.9 | 31.9 | 2.82 | | | ✗ |
| BLQ | 1.3 | 1.3 | 2.6 | 1.0 | LR | 12.28 | 12.81 | 19.66 | 2.94 | 0.13 | 0.08 | ✗ |
| BLh | 1.3325 | 1.3325 | 2.67 | 1.0 | LR | >26.35 | >26.35 | 26.35 | 2.88 | | | ✗ |
| BLQ | 1.3325 | 1.3325 | 2.67 | 1.0 | LR | 13.19 | 13.82 | 18.65 | 3.06 | 0.19 | 0.07 | ✗ |
| BLh | 1.365 | 1.365 | 2.73 | 1.0 | LR | >21.39 | >21.39 | 21.39 | 3.03 | | | ✗ |
| BLQ | 1.365 | 1.365 | 2.73 | 1.0 | LR | 4.84 | 5.44 | 8.59 | 3.06 | 0.04 | 0.18 | ✗ |
| BLh | 1.4 | 1.4 | 2.8 | 1.0 | LR | >23.63 | >23.63 | 23.63 | 3.15 | | | ✗ |
| BLQ | 1.4 | 1.4 | 2.8 | 1.0 | LR | 1.91 | 2.74 | 8.02 | ✗ | ✗ | ✗ | ✗ |
| BLh | 1.45 | 1.45 | 2.9 | 1.0 | LR | 1.85 | 2.93 | 13.3 | ✗ | | | ✗ |
| BLQ | 1.45 | 1.45 | 2.9 | 1.0 | LR | 0.67 | 1.53 | 9.44 | ✗ | ✗ | ✗ | ✓ |
| BLh | 1.475 | 1.475 | 2.95 | 1.0 | LR | 0.66 | 1.73 | 4.98 | ✗ | | | ✓ |
| BLQ | 1.475 | 1.475 | 2.95 | 1.0 | LR | 0.55 | 1.47 | 4.46 | ✗ | ✗ | ✗ | ✓ |
| BLh | 1.5 | 1.5 | 3.0 | 1.0 | LR | 0.56 | 1.54 | 5.06 | ✗ | | | ✓ |
| BLQ | 1.5 | 1.5 | 3.0 | 1.0 | LR | 0.52 | 1.43 | 4.65 | ✗ | ✗ | ✗ | ✓ |
| BLh | 1.6 | 1.6 | 3.2 | 1.0 | LR | 0.4 | 1.28 | 5.11 | ✗ | | | ✓ |
| BLQ | 1.6 | 1.6 | 3.2 | 1.0 | LR | 0.4 | 1.26 | 4.76 | ✗ | ✗ | ✗ | ✓ |
| BLh | 1.482 | 1.259 | 2.74 | 1.18 | LR | >20.71 | >20.71 | 20.71 | 2.98 | | | ✗ |
| BLQ | 1.482 | 1.259 | 2.74 | 1.18 | LR | 3.63 | 4.35 | 11.66 | 3.14 | 0.16 | 0.23 | ✗ |
| BLh | 1.856 | 1.02 | 2.88 | 1.82 | LR | 0.99 | 1.59 | 9.88 | ✗ | | | ✓ |
| BLQ | 1.856 | 1.02 | 2.88 | 1.82 | LR | 0.62 | 1.7 | 9.96 | ✗ | ✗ | ✗ | ✓ |

**Table 2.4.** A summary of the analysis of ejecta properties and disk masses for all our binaries at 2 spatial resolutions. $M_{\rm disk}^{\rm end}$ is the disk mass at the end of the simulation, $M_{\rm ej}$ is the total mass of the ejecta, $\langle v_\infty \rangle_{ej}$ is the ejecta's mass averaged asymptotic velocity, $\langle Y_{\rm e} \rangle_{\rm ej}$ its mass averaged electron fraction, $\langle s \rangle_{ej}$ the mass averaged specific entropy and $\langle \theta \rangle_{ej}$ is the rms angle with the orbital plane.

| EOS | $M_1$ $[M_\odot]$ | $M_2$ $[M_\odot]$ | q | Resolution | $M_{\rm disk}^{\rm end}$ $[10^{-3}\,M_\odot]$ | $M_{\rm ej}$ $[10^{-3}\,M_\odot]$ | $\langle v_\infty \rangle_{ej}$ [c] | $E_{\rm kin}$ $[10^{48}$erg] | $E_{\rm kin}(W\beta>1)$ $[10^{48}$erg] | $\langle Y_{\rm e} \rangle_{\rm ej}$ | $\langle s \rangle_{ej}$ $[k_B]$ | $\langle \theta \rangle_{ej}$ [rad] |
|---|---|---|---|---|---|---|---|---|---|---|---|---|
| BLh | 1.3 | 1.3 | 1.0 | SR | 110.29 | 1.22 | 0.14 | 34.48 | 0.22 | 0.25 | 21.51 | 0.65 |
| BLQ | 1.3 | 1.3 | 1.0 | SR | 58.89 | 1.73 | 0.15 | 50.55 | 0.23 | 0.25 | 21.67 | 0.61 |
| BLh | 1.3325 | 1.3325 | 1.0 | SR | 83.44 | 0.88 | 0.18 | 37.98 | 1.31 | 0.22 | 20.13 | 0.61 |
| BLQ | 1.3325 | 1.3325 | 1.0 | SR | 16.79 | 1.18 | 0.21 | 69.4 | 4.62 | 0.21 | 18.61 | 0.57 |
| BLh | 1.365 | 1.365 | 1.0 | SR | 49.44 | 1.4 | 0.16 | 45.3 | 0.16 | 0.26 | 21.14 | 0.65 |
| BLh* | 1.365 | 1.365 | 1.0 | SR | 53.35 | 1.51 | 0.2 | 75.47 | 3.33 | 0.25 | 22.16 | 0.64 |
| BLQ | 1.365 | 1.365 | 1.0 | SR | 6.95 | 2.05 | 0.2 | 97.53 | 0.76 | 0.24 | 18.56 | 0.6 |
| BLh | 1.4 | 1.4 | 1.0 | SR | 80.67 | 1.85 | 0.17 | 65.82 | 0.92 | 0.25 | 21.1 | 0.62 |
| BLQ | 1.4 | 1.4 | 1.0 | SR | 2.99 | 0.49 | 0.23 | 31.3 | 1.79 | 0.21 | 20.52 | 0.47 |
| BLh | 1.45 | 1.45 | 1.0 | SR | 76.05 | 6.84 | 0.19 | 309.73 | 7.7 | 0.25 | 17.03 | 0.57 |
| BLQ | 1.45 | 1.45 | 1.0 | SR | 0.13 | 0.12 | 0.26 | 8.36 | 0.0 | 0.25 | 28.65 | 0.4 |
| BLh | 1.475 | 1.475 | 1.0 | SR | 0.04 | 0.33 | 0.29 | 31.56 | 0.87 | 0.22 | 22.68 | 0.41 |
| BLQ | 1.475 | 1.475 | 1.0 | SR | 0.13 | 0.04 | 0.25 | 2.69 | 0.0 | 0.26 | 43.51 | 0.36 |
| BLh | 1.5 | 1.5 | 1.0 | SR | 0.1 | 0.2 | 0.29 | 19.21 | 0.3 | 0.24 | 23.58 | 0.32 |
| BLQ | 1.5 | 1.5 | 1.0 | SR | 0.04 | 0.01 | 0.15 | 0.19 | 0.0 | 0.19 | 65.38 | 0.34 |
| BLh | 1.6 | 1.6 | 1.0 | SR | 0.01 | 0.0 | 0.16 | 0.1 | 0.0 | 0.22 | 91.26 | 0.35 |
| BLQ | 1.6 | 1.6 | 1.0 | SR | 0.01 | 0.0 | 0.17 | 0.13 | 0.0 | 0.22 | 87.72 | 0.36 |
| BLh | 1.4 | 1.2 | 1.17 | SR | 107.27 | 1.98 | 0.19 | 92.57 | 2.39 | 0.18 | 14.06 | 0.55 |
| BLQ | 1.4 | 1.2 | 1.17 | SR | 67.01 | 1.82 | 0.2 | 96.53 | 4.09 | 0.17 | 14.09 | 0.5 |
| BLh | 1.482 | 1.259 | 1.18 | SR | 92.76 | 4.96 | 0.17 | 178.19 | 1.5 | 0.17 | 12.33 | 0.5 |
| BLQ | 1.482 | 1.259 | 1.18 | SR | 13.44 | 2.53 | 0.22 | 154.29 | 2.73 | 0.14 | 11.53 | 0.45 |
| BLh | 1.856 | 1.02 | 1.82 | SR | 60.99 | 7.51 | 0.11 | 102.35 | 0.15 | 0.04 | 3.8 | 0.11 |
| BLQ | 1.856 | 1.02 | 1.82 | SR | 59.46 | 7.42 | 0.11 | 101.71 | 0.08 | 0.04 | 4.04 | 0.12 |

**Table 2.5.** Same as table 2.4 except that now we report the results for low-resolution (LR) simulations.

| EOS | $M_1$ $[M_\odot]$ | $M_2$ $[M_\odot]$ | q | Resolution | $M_{disk}^{end}$ $[10^{-3} M_\odot]$ | $M_{ej}$ $[10^{-3} M_\odot]$ | $\langle v_\infty \rangle_{ej}$ [c] | $E_{kin}$ $[10^{48}$erg] | $E_{kin}(W\beta > 1)$ $[10^{48}$erg] | $\langle Y_e \rangle_{ej}$ | $\langle s \rangle_{ej}$ $[k_B]$ | $\langle \theta \rangle_{ej}$ [rad] |
|---|---|---|---|---|---|---|---|---|---|---|---|---|
| BLh | 1.3 | 1.3 | 1.0 | LR | 87.61 | 0.95 | 0.15 | 27.89 | 0.0 | 0.24 | 22.4 | 0.62 |
| BLQ | 1.3 | 1.3 | 1.0 | LR | 28.71 | 0.93 | 0.19 | 42.01 | 0.28 | 0.23 | 21.41 | 0.63 |
| BLh | 1.3325 | 1.3325 | 1.0 | LR | 95.56 | 1.28 | 0.18 | 50.3 | 0.07 | 0.26 | 22.91 | 0.64 |
| BLQ | 1.3325 | 1.3325 | 1.0 | LR | 43.02 | 1.16 | 0.17 | 40.1 | 0.0 | 0.27 | 23.53 | 0.64 |
| BLh | 1.365 | 1.365 | 1.0 | LR | 65.21 | 1.11 | 0.16 | 36.01 | 0.29 | 0.27 | 25.36 | 0.67 |
| BLQ | 1.365 | 1.365 | 1.0 | LR | 6.35 | 2.29 | 0.17 | 84.07 | 0.01 | 0.26 | 20.48 | 0.59 |
| BLh | 1.4 | 1.4 | 1.0 | LR | 72.59 | 1.68 | 0.19 | 77.06 | 0.41 | 0.26 | 20.11 | 0.67 |
| BLQ | 1.4 | 1.4 | 1.0 | LR | 9.07 | 0.51 | 0.25 | 37.22 | 0.43 | 0.23 | 22.66 | 0.53 |
| BLh | 1.45 | 1.45 | 1.0 | LR | 2.42 | 1.5 | 0.23 | 95.62 | 0.91 | 0.26 | 20.46 | 0.52 |
| BLQ | 1.45 | 1.45 | 1.0 | LR | 0.06 | 0.09 | 0.26 | 6.96 | 0.0 | 0.26 | 33.35 | 0.39 |
| BLh | 1.475 | 1.475 | 1.0 | LR | 0.14 | 0.58 | 0.33 | 69.26 | 4.32 | 0.22 | 20.47 | 0.44 |
| BLQ | 1.475 | 1.475 | 1.0 | LR | 0.13 | 0.04 | 0.27 | 2.98 | 0.0 | 0.29 | 52.87 | 0.41 |
| BLh | 1.5 | 1.5 | 1.0 | LR | 0.14 | 0.13 | 0.31 | 13.05 | 0.08 | 0.26 | 28.1 | 0.31 |
| BLQ | 1.5 | 1.5 | 1.0 | LR | 0.12 | 0.01 | 0.15 | 0.14 | 0.0 | 0.2 | 78.16 | 0.38 |
| BLh | 1.6 | 1.6 | 1.0 | LR | 0.01 | 0.01 | 0.18 | 0.21 | 0.0 | 0.21 | 60.81 | 0.29 |
| BLQ | 1.6 | 1.6 | 1.0 | LR | 0.0 | 0.0 | 0.17 | 0.14 | 0.0 | 0.22 | 82.65 | 0.34 |
| BLh | 1.482 | 1.259 | 1.18 | LR | 81.52 | 2.86 | 0.19 | 128.08 | 0.21 | 0.17 | 13.85 | 0.58 |
| BLQ | 1.482 | 1.259 | 1.18 | LR | 17.79 | 3.25 | 0.22 | 184.61 | 1.07 | 0.13 | 11.14 | 0.43 |
| BLh | 1.856 | 1.02 | 1.82 | LR | 60.78 | 7.46 | 0.11 | 109.1 | 0.0 | 0.05 | 4.37 | 0.13 |
| BLQ | 1.856 | 1.02 | 1.82 | LR | 60.78 | 7.46 | 0.11 | 102.74 | 0.05 | 0.05 | 4.27 | 0.13 |

# Chapter 3
# QCD Phase Transitions: Multimodal Gravitational Wave Signatures

## 3.1 Introduction

Binary neutron star (BNS) mergers produce some of the most extreme conditions in nature, compressing matter to several times the nuclear saturation density and to temperatures of tens of MeV [106]. Multimessenger observations of binary neutron star (BNS) mergers can be used to probe the properties of matter in these conditions, providing a unique avenue to study the non-perturbative regime of QCD [19, 20, 52–54, 108, 137, 159–177].

Presently, there are large uncertainties in the fundamental physics of strongly-interacting matter at densities of a few times nuclear saturation [178–180]. It is not even clear what the relevant degrees of freedom are for the densities and temperatures reached in the core of remnant massive neutron stars (RMNS) of BNS mergers. It is possible that matter remains composed of nucleons, together with leptons (electrons, positrons, and muons) and photons [21, 106]. The appearance of more exotic baryons, such as hyperons, is not excluded [19, 20, 181]. It is also possible for a transition to the deconfined quark-gluon plasma phase to take place in BNS mergers [52–54, 159]. The determination of the state of matter formed in BNS mergers is one of the most pressing scientific objectives of multimessenger astronomy [182, 183].

Previous work has shown that the presence of phase transitions (PTs) to deconfined quarks can be revealed by a shift of the postmerger gravitational wave (GW) peak frequency $f_2$ from the value expected for hadronic equations of state (EOSs) [54,56,57,184].

However, such frequency shifts can be degenerate with deviations from universal relations due to hadronic physics or other effects [3, 52, 56, 159, 177, 185]. It has also been suggested that the presence of a PT could be inferred from a measurement of the threshold mass for prompt collapse of BNS systems [108, 176, 186, 187]. In this work, we consider state-of-the-art numerical relativity simulations to show, for the first time, that the energy gap between a hadronic phase and a pure quark phase could be unambiguously determined through multimodal GW spectroscopy of RMNS thereby constraining an EOS that models a QCD PT of the first order. Such measurements will be possible with the next-generation of GW experiments like Cosmic Explorer [188], Einstein Telescope [189], and NEMO [190]. We vary many system properties including the mass ratio, eccentricity, and EOS model. Crucially, our simulations employ EOS models which cover a wide range of features for the PT, including different constructions and energy density gaps separating the two phases. The remainder of the chapter is organized as follows. In Sec. 3.2 we discuss the features of the EOS models we consider, with particular focus on a quantity that measures the energy density gap between a hadronic phase and a pure quark phase. In Sec. 3.3 we discuss our numerical methods and discuss the construction of the initial data for our simulations. In Sec. 3.4 we detail our main results and discuss the use of multimodal GW spectroscopy as a tool for understanding the nuclear structure of the NS EOS. Finally, we conclude in Sec. 3.5 and discuss future directions of investigation. Throughout the work we assume geometrized units, with $G = c = 1$, unless otherwise stated.

## 3.2 Equation of state models

For a clear understanding of the role that high-density deconfinement PTs could play in the development of the one-arm spiral instability, we consider a total of 5 quark EOS models with varying PT features. In particular, the size of the energy density gap which separates the hadronic and the pure quark phases is a useful way to classify hybrid hadron-quark EOS models [191]. This gap $\Delta\epsilon$ is given by

$$\Delta\epsilon \equiv \epsilon_{\rm quark} - \epsilon_{\rm trans}, \tag{3.1}$$

where $\epsilon_{\rm quark}$ is the energy density above which the EOS describes pure quark matter and $\epsilon_{\rm trans}$ is the energy density at the start of the phase transition below which the EOS describes hadronic matter. In principle, the parameters $\epsilon_{\rm trans}$, $p_{\rm trans}$, and $\Delta\epsilon$ are functions

**Table 3.1.** Summary of key properties for the EOS models considered in this work. We list the EOS model name, degrees of freedom considered (DOF), energy density gap $\Delta\epsilon$ in units of $10^{15}\mathrm{gcm}^{-3}$, type of EOS considered (where 'PP' stands for piecewise polytropic and 'FT' stands for a tabulated EOS model; all PP and FT type EOS models consider a $\Gamma$-law EOS with $\Gamma = 1.8$ and microphysical finite temperature thermal EOS treatment, respectively), and literature reference with further details on the model (Ref.). For EOS models that include a deconfinement PT to quark matter, we also list the counterpart hadronic EOS which is identical to the the model below the threshold densities for quark deconfinement (Count.).

| EOS | DOF | $\Delta\epsilon$ | Type | Ref. | Count. |
|---|---|---|---|---|---|
| BLh | h | 0.0 | FT | [71, 78, 159] | – |
| DD2F | h | 0.0 | FT | [159, 192] | – |
| DD2F-SF1 | h-q | 0.1967 | FT | [159, 192] | DD2F |
| DD2F-SF5 | h-q | 0.1967 | FT | [159, 192] | DD2F |
| BBKF1.5 | h-q | 0.2048 | PP | – | DD2F |
| BLQ | h-q | 0.319 | FT | [71, 78, 159] | BLh |
| T9 | h-q | 0.5922 | PP | [193–197] | DD2FPP |

of the electron fraction $Y_\mathrm{e}$ and temperature $T$, but for simplicity we assume that the values of these quantities are those for cold ($T \lesssim 1\,\mathrm{MeV}$), $\beta$-equilibrated matter when discussing them. We identify the end and beginning of each phase by considering the change in the approximate adiabatic index $\Gamma = \mathrm{d}\log p/\mathrm{d}\log(\rho)$, where $p$ and $\rho$ are the fluid pressure and rest mass density, respectively, of the cold, $\beta$-equilibrium, barotropic EOS for each EOS model considered. The region corresponding to the PT is always unambiguously marked by discontinuities in, or sudden changes in the slope of, the adiabatic index for the EOS models we consider.

The energy density gap $\Delta\epsilon$ tells us how much a system (e.g. a remnant neutron star) is prohibited from accessing the pure quark phase. Naturally, $\Delta\epsilon$ will depend upon the precise mechanism employed to construct the pure quark phase. For EOSs like DD2F-SF or CMF [52, 53, 58], the pure quark phase is accessible even at low temperatures and thus $\Delta\epsilon$ for such EOSs is small (see table 3.1). On the other hand, for EOSs like BLQ where the quark phase is modeled by the MIT Bag model, the pure quark phase is found to be energetically prohibited (based on our simulations of BNS remnants) to the remnant's thermodynamics (see section 2.4.2) and consequently $\Delta\epsilon$ is large (table 3.1). In a nutshell, $\Delta\epsilon$ is inversely related to the strength of a phase transition. By the strength of phase transition we mean the amount of softening the remnant undergoes upon the onset of the phase transition. More is the softening, more compact is the remnant and consequently, faster is its rotation. We also refer the reader to chapter 7 for a comparitive discussion on phase transitions.

In Tab. 3.1 we list the relevant details of the EOS models considered in our work, along with references to literature where the models are described in further detail or used in GRHD simulations. We consider EOS models that cover several sizes of the energy density gap, ranging from non-existent (i.e., a purely hadronic EOS) to significantly large, while maintaining consistency with current astrophysical constraints on the dense matter EOS. We consider both phenomenological EOS models [193–197] (in the form of piecewise polytropic approximations [198], abbreviated in Tab. 3.1 as 'PP') and microphysical, finite temperature EOS models [71, 78, 159, 192] (abbreviated in Tab. 3.1 as 'FT'). In simulations that employ piecewise polytropic approximations to the EOS, we consider a thermal treatment via the standard $\Gamma$-law EOS with thermal adiabatic index $\Gamma_{\rm th} = 1.8$. While a finer sampling of the $\Delta\epsilon$ parameter space would provide a more extensive study, the design of new EOS models consistent with astrophysical observations of NS properties was outside the scope of this work. As such, we considered as wide a range in $\Delta\epsilon$ as possible considering existing and available EOS models. We leave the exploration of a wider and more finely sampled (in $\Delta\epsilon$) EOS model space to future work.

## 3.3 Methods

We consider binaries in both quasi-circular orbits and highly eccentric encounters on nearly parabolic orbits. Initial data for the quasi-circular binaries is created using the conformal thin sandwich formalism [199] and assuming a helical Killing vector and irrotational flows. The resulting elliptic equations are solved using the pseudo-spectral code `LORENE` [101, 200, 201]. Initial data for the eccentric encounters is constructed by superimposing two isolated, boosted NS, following [23]. The initial separation of the stellar barycenters for parabolic encounters is set to 100 km, which is sufficiently large so that the level of constraint violation in the initial data is comparable to that of the quasi-circular binaries.

We perform NS merger simulations using the `WhiskyTHC` code [87–89]. `WhiskyTHC` makes use of the `CTGamma` spacetime solver [92], which is a part of the `Einstein Toolkit` [202]. The adaptive mesh refinement driver `Carpet` [95] is used to generate the dynamical grid structure employed in the simulations. All simulations considered here, with the exception of two, have been performed using at least two grid resolutions. Although there are small quantitative differences in the GW waveforms computed at different resolutions, the effects of PTs on the GW spectrum discussed here are robust across all simulations. Unless otherwise specified, we discuss results from simulations using the standard grid

**Table 3.2.** Summary of the modeling assumption and initial conditions for the simulations considered in this work. We list the EOS, degrees of freedom (DOF) modeled in the EOS, orbital condition imposed, neutrino model assumed, grid resolutions considered, total system mass, and mass ratio $q = M_1/M_2$ (where $M_1$ ($M_2$) is the mass of the less (more) massive star in the configuration).

| EOS | DOF | Orbit | $\nu$ | Res. | $M(M_\odot)$ | $q$ |
|---|---|---|---|---|---|---|
| BLh | h | Quasi-circular | M0 | LR/SR | 2.6 | 1 |
| BLh | h | Quasi-circular | M0 | SR | 2.6 | 0.85 |
| DD2F | h | Quasi-circular | M0 | LR/SR | 2.6 | 1 |
| DD2F | h | Quasi-circular | M0 | LR/SR | 2.7 | 1 |
| DD2F | h | Eccentric | – | LR/SR | 2.7 | 1 |
| DD2F-SF1 | h-q | Quasi-circular | M0 | LR/SR | 2.6 | 1 |
| DD2F-SF1 | h-q | Quasi-circular | M0 | LR/SR | 2.7 | 1 |
| DD2F-SF5 | h-q | Eccentric | – | LR/SR | 2.7 | 1 |
| BBKF1.5 | h-q | Eccentric | – | LR/SR | 2.7 | 1 |
| BLQ | h-q | Quasi-circular | M0 | LR/SR | 2.6 | 1 |
| BLQ | h-q | Quasi-circular | M0 | SR | 2.6 | 0.85 |
| T9 | h-q | Eccentric | – | LR/SR | 2.7 | 1 |

resolution (SR) (with grid spacing $\Delta x \simeq 184.6\,\mathrm{m}$ in the finest refinement level). The grid for lower resolution (LR) simulations is approximately 30% coarser than that of our SR grids. The grid structure for the simulations is the same adapted in [24] and [23]) for the quasi-circular and eccentric simulations, respectively. Neutrino emission and reabsorption are not included for binaries in eccentric orbits. All quasi-circular binaries include a neutrino treatment via the moment based M0 scheme [24]. Additionally, magnetic fields are not accounted for in any of our simulations, although all simulations (except with BLh and BLQ) account for angular momentum transport in the post-merger RMNS with the use of a subgrid viscosity large eddy simulation (LES) model which remains fixed across models.

The complete set of simulations considered in this work cover a wide variety of initial conditions and modeling assumptions. To further clarify the conditions considered we summarize in Tab. 3.2 the initial conditions and modeling assumptions that vary across the simulations. We note that several of the variable modeling assumptions are not expected to influence the development of the dynamics of the RMNS on the timescales we consider, including the use of an M0 neutrino scheme [25, 148] and the eccentricity of the orbit. The most relevant model assumptions are the subgrid viscosity LES model and the mass ratio. Specifically, the use of a subgrid viscosity model accounts for angular momentum transport in the RMNS, which largely dictates the differential rotation profile

crucial for the development of the one-armed spiral instability [122]. Moreover, the use of non-unity mass-ratio ensures an inherent perturbation in the system which reliably seeds the one-armed spiral instability. We emphasize that the important modeling assumptions, including the subgrid viscosity model and mass ratio (with the exception of a single pair of simulations to understand the effects of mass ratio), remain fixed across all of our simulations. We also emphasize that our main focus is the *relative* growth of the one-armed spiral instability in each pair of simulations and that we only compare simulations with identical initial conditions and modeling assumptions. The only difference between the pairs of simulations which we compare is whether the EOS includes a deconfinement phase transition or not. From this perspective, all potential modeling differences across our simulations should in principle not play a role in the effects we report.

## 3.4 Results

### 3.4.1 Development of the one-armed spiral instability in BNS mergers

The one-armed spiral instability is a non-axisymmetric mode in a rapidly rotating fluid which, when saturated, leads to the dominance of a single high-density mode in the fluid density that is displaced from the fluid barycenter [203–206]. The one-armed spiral instability has been observed to develop commonly in BNS merger simulations that produce long-lived, massive post-merger remnants on timescales of $\mathcal{O}(10\text{ms})$ [119,207–210] and in simulations of many other astrophysical systems including supernovae [211, 212], white dwarfs [213, 214] and accretion disks [214, 215].

A unique feature of the one-arm spiral mode is that it can be sustained on significantly longer timescales than other non-axisymmetric modes. In the context of BNS mergers, the growth and saturation of the one-arm spiral mode may be numerically observed by considering azimuthal decompositions of the rest mass density on the orbital plane. Specifically, we consider the amplitudes of these rest mass density decompositions as

$$C_m = \left| \int W \sqrt{\gamma} \rho e^{-im\phi} \mathrm{d}x\mathrm{d}y \right|, \tag{3.2}$$

where $W$ is the Lorentz factor, $\gamma$ is the determinant of the 3-metric, $\rho$ is the rest mass density, and $\phi = \tan^{-1}(y/x)$ is the azimuthal angle in the centre of mass frame. An indicative dynamical probe of the growth of the one-arm spiral instability is the dominance of the $C_1$ mode over the typically initially dominant $C_2$ mode. On dynamical timescales the one-arm instability leads to the growth of the $C_1$ density mode, while the $C_2$ mode

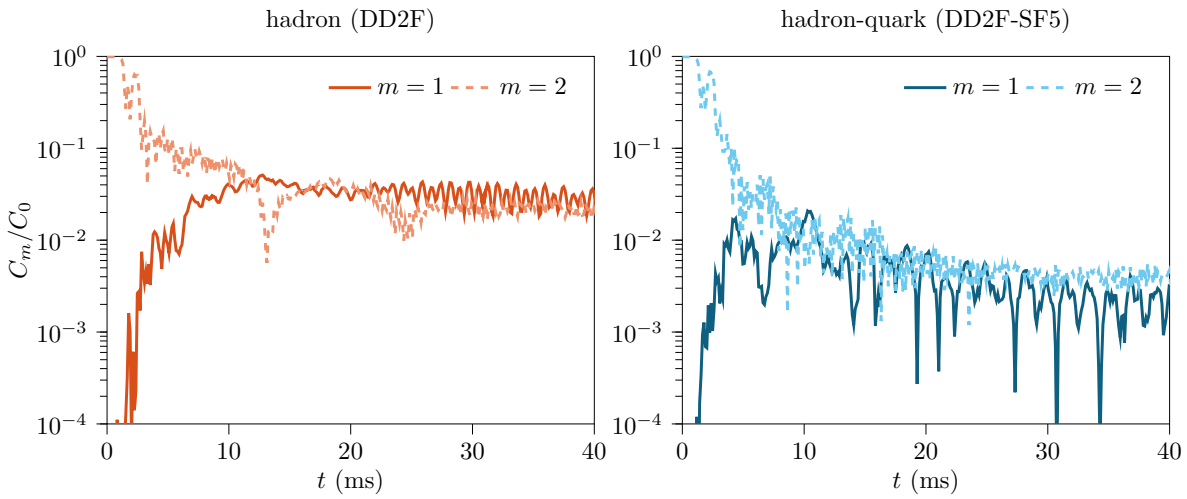


**Figure 3.1.** *Left panel:* Density mode decomposition following Eq. (3.2) for a simulation which employs a purely hadronic EOS (DD2F). We depict the dominant density modes ($C_2$ and $C_1$) scaled by the $C_0$ mode to show the relative strength of each fluid pattern. *Right panel:* Same as the left panel but for a simulation which employs an EOS with a hadron-quark PT (DD2F-SF5, which is identical to the hadronic DD2F model below the threshold densities for the phase transition). Such a suppression is even more evident in the case of BLQ EOS which has a larger $\Delta\epsilon$. See appendix 3.7

simultaneously decays.

Each fluid density mode that arises during the evolution of a massive NS remnant is associated with GW emission at a characteristic frequency stemming from its respective pattern speed. For example, the growth of the $C_1$ mode, which has half the pattern frequency as the $C_2$ mode, is associated with GW emission at half the characteristic frequency of the initially dominant $C_2$ mode. As such, the development of the one-armed spiral instability in astrophysical systems may be observed by considering multimodal GW spectroscopy [119]. For the simulations considered in this work we extract multimodal GW information within the Newman-Penrose formalism. We compute the coefficients of $s = -2$ spin-weighted spherical harmonic decompositions of the Newman-Penrose scalar $\Psi_4$ which we label as $\Psi_4^{\ell,m}$. The one-armed spiral instability can therefore be observed in the GW spectrum extracted from our simulations as a growth in the power and amplitude of the $\ell = 2, m = 1$ GW mode (i.e., $\Psi_4^{2,1}$) and simultaneous decay of the dominant $\ell = 2, m = 2$ GW mode (i.e., $\Psi_4^{2,2}$).

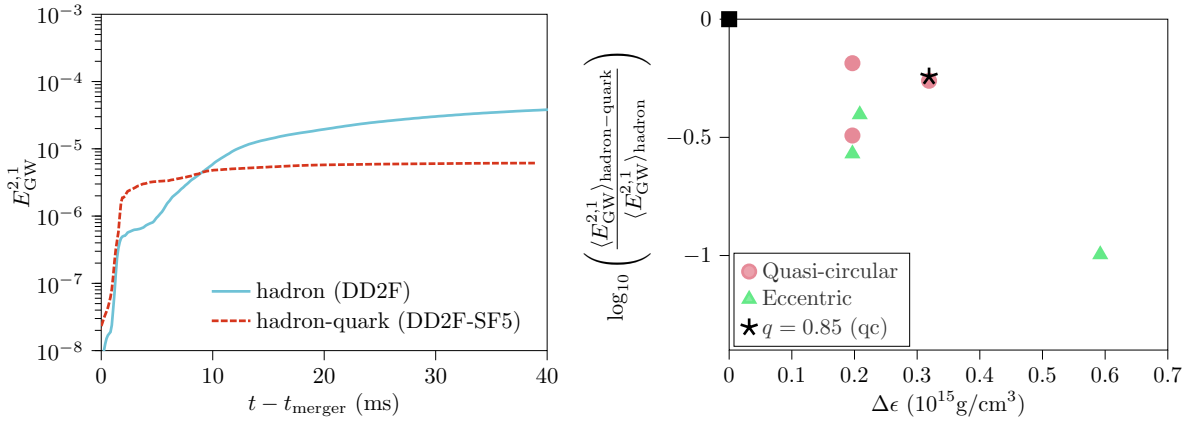


**Figure 3.2.** *Left panel:* Energy carried by GWs in the $\ell = 2, m = 1$ mode as a function of time. The development of the one-armed spiral instability can be observed in the purely hadronic simulation, as the energy in the $\ell = 2, m = 1$ GW mode continues to grow, but is suppressed in the hadron-quark simulation. *Right panel:* Time-averaged energy emitted by GWs in the $\ell = 2, m = 1$ mode, normalized by the same quantity for the corresponding hadronic EOS, as a function of the energy density gap separating the hadronic and quark phases. We depict results for quasi-circular and eccentric mergers with pink triangles and green circles, respectively. We find that the energy emitted by the $\ell = 2, m = 1$ GW mode decreases by up to approximately an order of magnitude for larger energy density gaps.

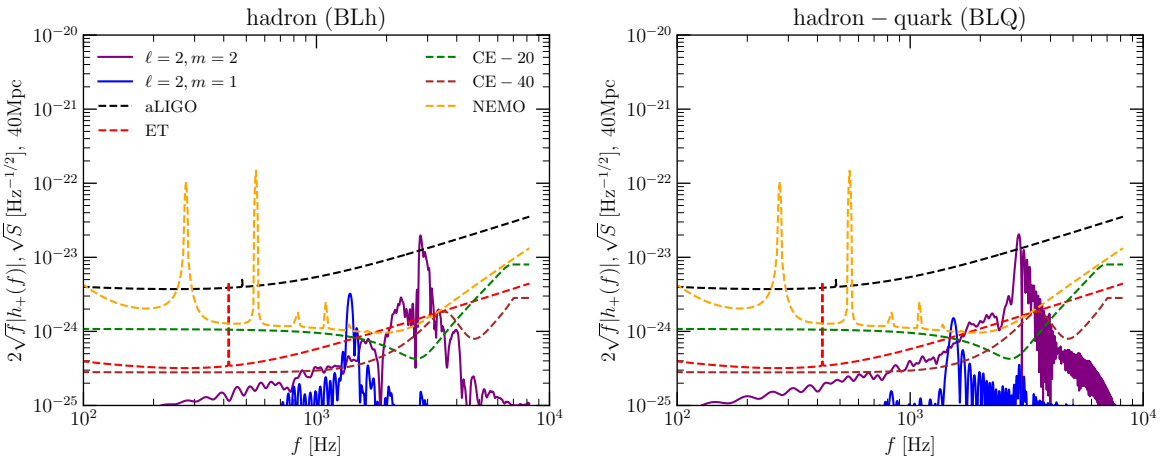


**Figure 3.3.** Multimodal GW amplitude spectral density computed for symmetric binaries of total mass $M = 2.6\ M_\odot$ in an edge-on configuration. Also shown are the noise sensitivity curves for advanced LIGO (aLIGO), Einstein Telescope (ET), the 20 km postmerger-optimized configuration for the Cosmic Explorer (CE20) and the 40 km configuration for Cosmic Explorer (CE40). A suppression in the amplitude spectral density as a result of the deconfinement PT may be detectable with the third generation detectors and most cleanly with CE40.

### 3.4.2 The effect of deconfinement phase transitions on the one-armed spiral instability

Our simulations show that *high-density deconfinement PTs may act to suppress the one-armed spiral instability*. Specifically, hadron-quark PTs lead to a relative suppression of the instability when compared to analogous cases with purely hadronic degrees of freedom. We refer to this effect simply as a 'relative suppression' throughout the manuscript for the sake of brevity. There are several potential mechanisms via which the instability may be relatively suppressed. For example, it has been shown that the physical extent of the remnant plays an important role in the development of the instability, with larger remnants being more conducive to the development of the instability on shorter timescales [119, 210, 216, 217]. The significant softening at high densities introduced by the PT results in more compact post-merger remnants (relative to scenarios that consider only hadronic degrees of freedom). As such, the more compact hybrid star remnants may see a weaker development of the one-armed spiral instability when compared to neutron star remnants.

In Fig. 3.1 we depict the density mode decomposition for two representative simulations which begin from the same initial conditions. The left and right panel of Fig. 3.1 depict the dominant density modes for a simulation employing a hadronic (DD2F) and hadron-quark (DD2F-SF5) EOS, respectively. In the left panel of Fig. 3.1 we see the clear growth and eventual dominance of the $C_1$ mode on dynamical timescales, which is indicative of the development of the one-armed spiral instability. On the other hand, the right panel of Fig. 3.1 clearly shows that the $C_1$ mode never dominates the fluid evolution, suggesting suppression of that density mode relative to the analogous hadronic case depicted in the left panel. Such suppression is even more pronounced for a quark EOS with larger $\Delta\epsilon$ (see appendix 3.7).

In the left panel of Fig. 3.2 we show the energy carried by the $\ell = 2, m = 1$ GW mode as a function of time for simulations employing the DD2F (hadronic) and DD2F-SF5 (hybrid hadron-quark) EOSs. We find that the energy carried in the $\ell = 2, m = 1$ mode of the GWs is significantly smaller in the simulation employing a hybrid hadron-quark EOS, indicating that the one-armed spiral instability is relatively suppressed in scenarios with deconfinement PTs at densities relevant for BNS mergers. We emphasize that in Fig. 3.1 and in the left panel of Fig. 3.2 we showcase results for a set of EOS models which are identical below the threshold for a PT, and as such the simulations have identical initial conditions. We find that this *relative* suppression exists for all of our simulations,

regardless of initial condition, modeling assumptions as listed in Tab. 3.2, or pair of EOS models considered.

In the right panel of Fig. 3.2, we show the time-averaged energy emitted by the $\ell = 2, m = 1$ GW mode $\langle E_{\rm GW}^{2,1} \rangle$ as a function of the energy density gap $\Delta\epsilon$ for all of our simulations. For the results depicted in the right panel of Fig. 3.2, we time-average over a window of $\Delta t \approx 40\,{\rm ms}$ after the merger except for cases that lead to a remnant collapse on shorter timescales (in such cases, we time-average until the collapse of the NS remnant). To account for differences and uncertainties in the hadronic sector of the NS EOS, we normalize all data by that corresponding to a complementary simulation that uses identical initial data and modeling assumptions but employs a purely hadronic EOS having the same low-density behavior below the PT threshold as the hybrid hadron-quark EOS. As such, we depict the point corresponding to all hadronic EOS simulations with a black square at $\Delta\epsilon = 0$. Each simulation is time-averaged to the same extent as its complementary hadronic simulation. The scatter of data suggest a potential *anti-correlation between the energy carried in the $\ell = 2, m = 1$ GW mode and the size of the energy density gap*, although we note significant variability in the trend. Our findings suggest that as the size of the energy density gap increases, GW emission in the $\ell = 2, m = 1$ mode decreases; the simulation employing the quark EOS with the largest energy gap leads to a relative suppression in $\langle E_{\rm GW}^{2,1} \rangle$ by approximately an order of magnitude.

Note that in Fig. 3.2 we also show the relative suppression of the GW energy in the $\ell = 2, m = 1$ mode, but for the case of a system with mass ratio $q = 0.85$, marked with a black star marker. The datum for the pair of unequal mass ratio simulations shown in Fig. 3.2 demonstrates that there is significant agreement in the relative suppression of the one-armed spiral instability between the unequal mass ratio and equal mass ratio cases at the same value of $\Delta\epsilon$. Specifically, we find that there is only a 3% difference in the relative growth of $E_{\rm GW}^{2,1}$ between the unequal and equal mass ratio cases of the same $\Delta\epsilon$. In principle, the one-armed spiral instability is expected to be seeded at a stronger level for systems with $q \neq 1$. However, in this work we consider the effect of deconfinement on the development of the one-armed spiral instability PTs, *relative to cases with identical initial conditions and modeling assumptions that employ purely hadronic EOSs.* As such, system properties such as the mass ratio and other modeling assumptions are expected to cancel out between comparison cases; the only difference between the simulations which we compare is whether or not the EOS contains a deconfinement PT to quark matter.

As the present work is the first ever to report the potential relative suppression of

the one-armed spiral instability due to deconfinement PTs, a significant amount of work remains to be done to understand whether the potential anti-correlation suggested by the right panel of Fig. 3.2 is robust, including the consideration of EOS models that more finely sample the parameter space of $\Delta\epsilon$ and a further investigation of the effects of system properties such as the mass ratio. We leave such investigations to future work.

## 3.5 Discussion and Conclusion

The characteristic frequency associated with peak emission in the $\ell = 2, m = 1$ GW mode has half the value of that associated with the $\ell = 2, m = 2$ mode (i.e., $f^{2,1}_{\rm peak} = f^{2,2}_{\rm peak}/2$). Observationally, a GW signal would contain information at all contributing frequencies. However, the dominant GW emission associated with binary coalescence is always expected to be from the $\ell = 2, m = 2$ contribution, such that $f_{\rm peak} = f^{2,2}_{\rm peak}$. Therefore, a potential observational signature of the one-armed spiral instability is the growth in power of an incoming GW signal at a frequency that is half of the dominant frequency; if it develops in the post-merger environment, the one-armed spiral instability will continuously power the emission of GWs at $f_{\rm peak}/2$, while emission in the dominant $f_{\rm peak}$ decays in time [113].

In Fig. 3.3 we show the post-merger GW amplitude spectrum density (ASD) for a symmetric, edge-on binary situated at a distance of 40 Mpc, which is consistent with the luminosity distance observed for GW170817 [218]. The edge-on configuration is the most optimal for the detection of an $m = 1$ mode. As expected, we see a relative suppression of power in the $m = 1$ mode (with respect to the complementary hadronic simulation) with the onset of a deconfinement PT. In this configuration, the appearance of quarks in the post-merger remnant results in a relative suppression of the postmerger signal-to-noise ratio (SNR) of the $(\ell = 2, m = 1)$ mode by a factor of 2, from 2.14 in the hadronic case to 1.08 in the hadron-quark case in the 40 km Cosmic Explorer detector [188]. The GW ASD peak of the $\ell = 2,\ m = 1$ mode (between 1-2 kHz) and the postmerger ASD peak of the $\ell = 2,\ m = 2$ mode (between 2-4 kHz), lie respectively in the most sensitive regions of the 40 km and the 20 km postmerger optimized Cosmic Explorer configurations. Our analysis recommends an increase in detector sensitivities in the high-frequency regimes (see also [219]) for best possible constraints on deconfinement PTs in BNS mergers, within the context of multimodal GW spectroscopy. In cases where the one-armed spiral instability develops, all binary inclinations except directly face on will produce GWs with a $l = 2, m = 1$ component. The one-armed spiral instability leads

to a unique bi-modal GW spectrum where the two most dominant peaks correspond exactly to $f_{\rm peak}$ and $f_{\rm peak}/2$. As such, a superposition of all signal modes may still in principle be used to extract the relative strength of the one-armed spiral instability. For instance, the SNR of a post-merger GW signal can be measured in a range of frequencies up to the inferred $f_{\rm peak}$; in cases where the one-armed spiral instability develops the dominant contribution to the signal in this range of frequencies is expected to be from the $l = 2, m = 1$ mode for all inclinations except directly face on. We note that the only way to completely remove the $l = 2, m = 1$ mode from the signal is in the highly specific scenario of an equal mass, directly face-on binary. Given reasonable expectations for distributions in the inclination and mass ratio of BNS systems, we may typically expect a contribution from the $l = 2, m = 1$ mode. However, deconfinement PTs may act to suppress the instability. In other words, except for the highly specific scenario of a face-on $q = 1$ binary, the lack of significant SNR over $f_{\rm peak}/2$ may be used to constrain the high- density EOS as highlighted by our work. For further detail on the detectability of the one-armed spiral instability via GW spectroscopy, we refer the reader to [119].

In [54] it was established that quasi-universal relations in the value of $f_{\rm peak}$ may be established for hadronic EOS models, and that EOS models which include a deconfinement PT unambiguously deviate from such universal relations (although recent work suggests that EOS features other than phase transitions may be responsible for deviations away from these quasi-universal relations [220]). As it is not presently understood whether similar relations exist in a quantity that measures the strength of the one-armed spiral instability (such as $\langle E^{2,1}_{\rm GW} \rangle$), we cannot establish whether the hadron-quark EOS models considered in this work deviate from such hypothetical quasi-universal relations. We may instead consider the effect showcased in this work as an additional tool to infer the presence and nature of PTs in BNS mergers. For example, when considered in combination with other known effects of PTs on BNS merger observables such as $f_{\rm peak}$ [54] and the associated KN brightness [159], the measurement of SNR($f_{\rm peak}/2$) (which is directly proportional to $\langle E^{2,1}_{\rm GW} \rangle$ as considered in our work) may allow for significant constraints on properties of the deconfinement PT. In principle the effects we discuss in this manuscript may be conflated with the effects of relatively soft EOS models [119] or potentially other effects such as non-convexity in the EOS [220]. In order to state definitively whether deconfinement PTs have a comparable effect on the one-armed spiral instability as relatively soft EOSs, we would need to consider hadronic EOS models over a significantly wider range of stiffness. Such a study would help establish whether quasi-universal relations exist in $\langle E^{2,1}_{\rm GW} \rangle$ or comparable metrics for the strength of the one-armed spiral

instability in the case of hadronic EOSs which we could then use as a standard against which to compare the effects presented in our work. We leave the investigation of quasi-universal relations for the strength of the one-armed spiral instability to future work.

In this work we have highlighted, for the first time, that high-density deconfinement PTs may act to relatively suppress the one-armed spiral instability. We find an anti-correlation between the energy carried in the $\ell = 2, m = 1$ GW mode and the size of the energy density gap which separates the hadronic and quark phases. Our findings reveal a potential deep connection between observable multimodal GW emission and the microphysical description of matter in the post-merger environment. We expect the one-armed spiral instability to be detectable at distances of 40 Mpc using future generation detectors [119]. If evidence of a strong one-armed spiral mode can be inferred from GW observations of the post-BNS merger environment, our findings suggest that a high-density deconfinement PT at the densities relevant to BNS mergers would be disfavored in favor of nucleonic EOS models. On the other hand, if evidence for the one-armed spiral instability is *not* found for close-by BNS mergers, this could also point to the possibility of a deconfinement PT taking place at densities relevant to BNS mergers with large values of $\Delta\epsilon$.

Similar studies considering the effect of PTs on BNS GW observables have not observed the relative suppression reflected in our simulations. For example, the Appendix of [56] considers a single comparison between a simulation with hadronic degrees of freedom and a hadron-quark PT. There, they show a potential relative *amplification* of the GW amplitude in the $\ell = 2, m = 1$ mode when allowing for a hadron-quark PT. However, that single comparison scenario is markedly different from those considered in this work. Specifically, in [56] the PT only occurs $t = 3 - 4$ ms after the merger, whereas the PT occurs within $t \approx 0.5$ ms for the simulations in this work. As such, the early development of the instability may not be impacted by the PT in the scenario considered in [56]. Moreover, we note that in our study we consider the time-averaged GW energy carried in the $l = 2, m = 1$ mode. Without comparing the same quantities used in our study to understand the development of the one-armed spiral, it is impossible to say whether the single comparison considered in [56] is contrary to the trend depicted in Fig. 3.2. Finally, we emphasize that [56] considers coarser numerical grids than our study for the single relevant comparison (a roughly 30% coarser numerical grid when compared to the standard resolution simulations in our work, which is consistent with our LR simulations), and does not consider an exploration of relevant effects as was done in our

study (e.g., the size of $\Delta\epsilon$ and different phase constructions). Importantly, [56] do not establish that their simulations, in the context of the one armed spiral instability, are in the convergent regime, as the amplification of the $\ell = 2, m = 1$ after a hadron-quark PT occurs in the remnant reported in that work is not observed using higher resolution simulations. As such, it remains unclear whether the potential deviation of that result from the trend established in Fig. 3.2 is not due to relatively higher numerical error in [56]. In App. 3.6 we discuss the complexity of understanding fluid instabilities in BNS mergers using LR grids.

Binary neutron star mergers with non-unity mass ratios are in principle more generic and common than the equal mass ratio systems considered in this work. Moreover, the inherent asymmetry in unequal mass ratio mergers may provide a reliable mechanism for efficiently seeding the one-armed spiral instability after the merger and has been shown to result in a stronger, faster development of the instability [210]. Although we present only a single case study for cases with unequal mass ratios in the present work, we find support for our main claim (that high-density deconfinement PTs may suppress the development of the one-armed spiral instability when compared to analogous cases with purely hadronic degrees of freedom) there as well. Due to the scope of the present work and the increased parameter space when considering unequal mass ratio cases, we find that a more systematic consideration of unequal mass ratio cases than can be presented in here is warranted. As such, we leave a full investigation of the effects of unequal mass ratio to future studies. We point out that other effects relevant in the post-merger environment - such as the presence of strong magnetic fields [221] and additional degrees of freedom that can cause a sudden softening of the EOS - may affect the development of the one-armed spiral instability. However, the relevant timescales and extent to which the aforementioned phenomena can affect the development of non-axisymmetric instabilities or the GW spectrum remains uncertain [119, 222], and may not impact our conclusions [223, 224]. The effects discussed in the present work arise on dynamical timescales $\sim \mathcal{O}(10\,\mathrm{ms})$, and may be the dominant mechanism for the relative suppression of the one-armed spiral instability. Additionally, although we find a trend in the decrease of energy carried by the $\ell = 2, m = 1$ GW mode for larger values of $\Delta\epsilon$, additional studies will help establish a more robust trend and provide an understanding of the potential spread in the trend. In particular, future lines of investigation will include: (1) considering the combined effects of the mass ratio and high-density PTs on the development of the one-armed spiral instability to a greater extent than could be done in this work; (2) considering the effects of accurate neutrino transport on high-density deconfinement PTs,

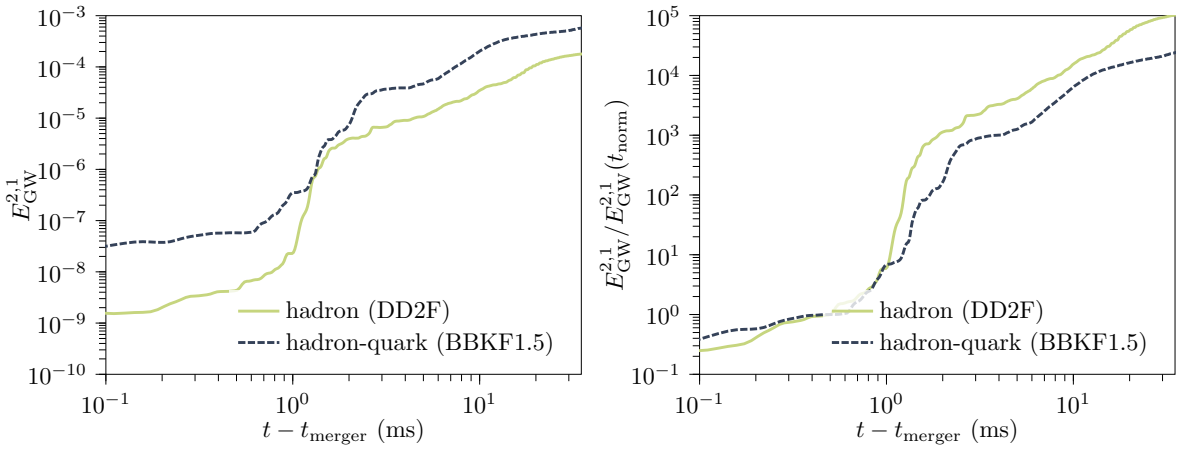


**Figure 3.4.** *Left panel*: Energy in the $\ell = 2, m = 1$ GW mode as a function of time for simulations employing a hadronic (DD2F) and hadron-quark (BBKF1.5) EOS; the simulations use identical initial conditions and are run with a grid resolution of $\Delta x = 369.2\,\mathrm{m}$ in the finest grid. These results showcase that the one-armed spiral instability may be seeded at different levels in the postmerger environment for different simulations. *Right panel:* Same quantity as the left panel, but normalized to the value at a time shortly after merger, $t_{\rm norm} = t_{\rm merger} + 0.5\,\mathrm{ms}$. Normalizing at this time accounts for the one-armed spiral instability being seeded at disparate levels across simulations.

as neutrinos may modify the composition of matter and thereby potentially affect the onset of the PT; (3) employing EOS models at systematically increasing values of $\Delta\epsilon$ while holding the hadronic region of the EOS fixed, as a limitation of the present work is the assumption that the $\ell = 2, m = 1$ GW mode is perfectly known in the case of hadronic EOSs; and (4) investigating the effects discussed in this work in scenarios with a *crossover* to quark matter, as our present work only considers EOS models with phase transitions. We leave such studies to future work.

## 3.6 Appendix 1: On the effects of grid resolution

Our main diagnostic for monitoring the development of the one-armed spiral instability is the energy carried in the $\ell = 2, m = 1$ mode of the GWs, which we further discuss in Sec. 3.4.2. We find that for most cases in our study, the relative suppression of the one armed spiral instability is observed at lower grid resolutions. However, there are notable exceptions for 2 pairs of simulations at lower resolutions. Specifically, we find that the low resolution (LR) versions for 2 of our simulations that employ high-density deconfinement phase transitions do not show a relative suppression of $\langle E^{2,1}_{\rm GW}\rangle$, but instead a relative *growth* with respect to the analogous simulations employing a purely hadronic EOS.

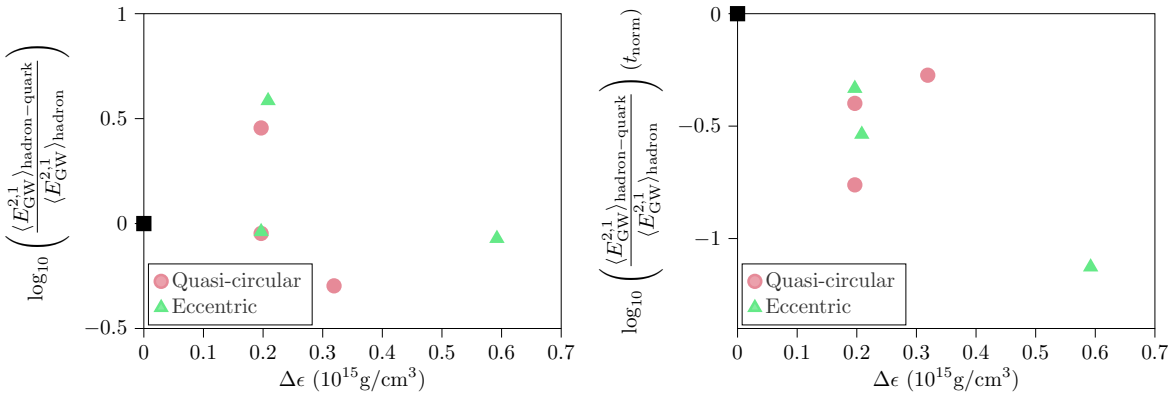


**Figure 3.5.** *Left panel:* Time-averaged energy emitted by GWs in the $\ell = 2, m = 1$ mode, normalized by the same quantity for the complementary hadronic EOS, as a function of the energy density gap separating the hadronic and quark phases. We show results for the LR simulations in our work. *Right panel:* Same as the left panel, but normalizing all data at a time shortly after merger, $t_{\rm norm} = t_{\rm merger} + 0.5\,{\rm ms}$ as consistent with Fig. 3.4

These cases seemingly contradict the discussion in the main text and are more consistent with the single case study showcased in [56]. However, we note that grid effects are crucial in determining the growth and saturation of the one-armed spiral instability. Specifically, the one-armed spiral instability may be seeded in a variable nature in the context of numerical studies. Unless it is explicitly excited as a non-axisymmetric perturbation of a known amplitude (e.g., as a fixed-amplitude perturbation in the rest mass density), the one-armed spiral instability arises numerically from error at the level of floating-point precision [225]. As such, small differences in the early post-merger evolution of the fluid can result in the instability being seeded at different strengths; this is potentially affected most strongly by the grid resolution. We do not explicitly seed the one-armed spiral instability using fluid perturbations in this work and, as a result, simulations that either run on different machines or use different grid resolutions libraries may result in different strengths for the initial instability seed.

To discuss the relative strength of the one-armed spiral instabilities across simulations which employ different grid structures, we consider $E^{2,1}_{\rm GW}$ normalized to its value at a time shortly after the merger; we depict normalized quantities because of the variable nature in which the one-armed spiral instability is seeded in the immediate post-merger environment in the context of numerical studies. In Fig. 3.4 we show the energy in the $\ell = 2, m = 1$ GW mode $E^{2,1}_{\rm GW}$ as a function of time for a set of low resolution simulations. The left panel of Fig. 3.4 shows $E^{2,1}_{\rm GW}$ as extracted from our simulations and appears to show that the simulation employing a hadron-quark EOS produces a larger energy

in the $\ell = 2, m = 1$ GW mode. However, it is clear that the energy at a time shortly after the merger $E_{\rm GW}^{2,1}(t_{\rm merger} + \tau_\epsilon)$ (where $\tau_\epsilon$ is a small additive time) is larger for the hadron-quark simulation, suggesting that the one-armed spiral instability was seeded at a larger amplitude in that case. In order to account for the different levels at which the one-armed spiral instability is seeded in the immediate post-merger environment, we normalize the quantities used to diagnose the relative strength of the instability at a time shortly *after* the merger $t_{\rm norm} = t_{\rm mer} + \tau_\epsilon$. We find that setting $\tau_\epsilon = 0.5\,{\rm ms}$ results in all simulations in our work having roughly equal values of $E_{\rm GW}^{2,1}$ in the few ms immediately following merger. We find that setting $\tau_\epsilon$ between 0.1 ms and 1 ms ensures that all simulations have approximate equality in the level at which the one-armed spiral instability is seeded, regardless of grid resolution or computational hardware used. We emphasize that our results at higher resolution are observed *without* the aforementioned normalization, but considering the normalization allows us to more suitably compare the development of the one-armed spiral instability across different grid resolutions. In Fig. 3.5 we show the time-averaged GW energy carried in the $l = 2, m = 1$ mode as a function of $\Delta\epsilon$ for all LR simulations in our work. We find that without accounting for disparate levels of the instability seed (left panel of Fig. 3.5), our data does not closely follow the potential trend established by the SR simulations in Fig. 3.2. However, normalizing all LR simulation data at a time consistent with Fig. 3.4 results in a much closer scatter of data between the LR and SR sets (right panel of Fig. 3.5). We leave the investigation of grid resolution effects, as well as the consideration of even higher resolution grids than could be included in this study, to future work.

## 3.7 Appendix 2: Azimuthal mode decomposition and suppression of $\ell = 2, m = 1$ GW mode for BLQ EOS

In this appendix, we provide additional evidence that large values of energy density gaps between a pure quark phase and a hadronic phase $\Delta\epsilon$ do indeed suppress the one-armed spiral instability developed in the postmerger remnant. To this aim, we show in figure 3.6, the time evolution of the azimuthal mode decomposition of rest mass density corresponding to the symmetric 1.30 $M_\odot$ - 1.30 $M_\odot$ binary. In the hadronic remnant simulated with the BLh EOS, the $m = 1$ density mode is seeded at the merger and grows to dominate the $m = 2$ mode eventually saturating over a time scale of 20 ms. On the other hand, the same binary when simulated with the BLQ EOS ($\Delta\epsilon = 3.2 \times 10^{14}{\rm gcm}^{-3}$)

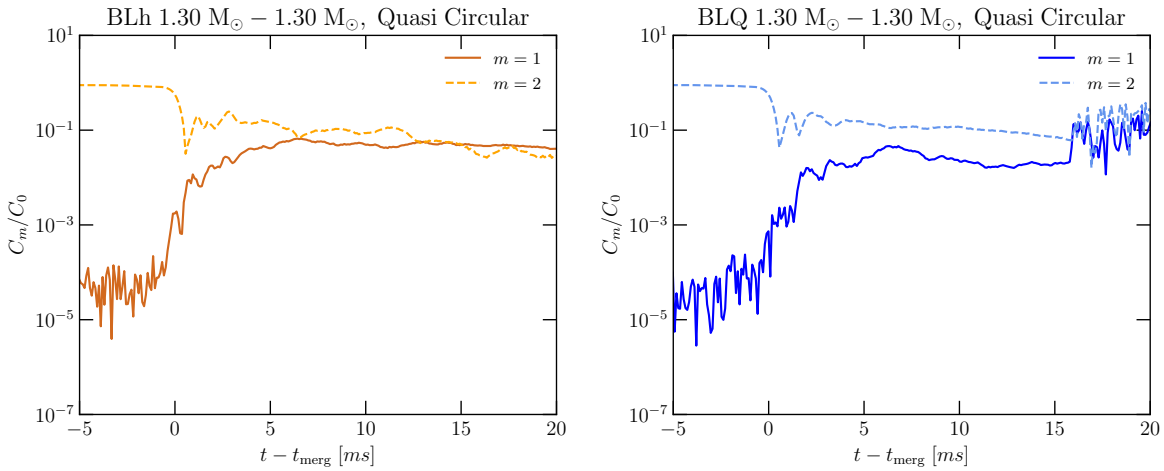


**Figure 3.6.** The decomposition of fluid density into azimuthal modes on the equatorial plane for a remnant neutron star (for the symmetric 1.30 $M_\odot$ - 1.30 $M_\odot$ binary) evolved with a hadronic EOS BLh (left panel) and a hybrid hadron-quark EOS BLQ (right panel). The quark EOS noticeably suppresses the $m = 1$ fluid density mode that manifests as a loss of SNR in the $\ell = 2, m = 1$ GW mode.

has a noticeable suppression of the $m = 1$ fluid density mode in the postmerger. This suppression is stronger as compared to the suppression of the $m = 1$ mode for the binary simulated with the DD2F-SF5 EOS (figure 3.1) with a smaller phase separation.

Finally, in figure 3.7, just like figure 3.2, we show the time evolution of GW energy carried by the $\ell = 2, m = 1$ mode and the fact that an onset of QCD phase transitions results in a suppression of this energy (equivalently the SNR in the $\ell = 2, m = 1$ mode).

## 3.8 Declaration

For this work, the numerical simulations of BNS mergers were shared between Pedro Espino and myself. Pedro was responsible for the post-processing analysis that established a suppression in the one-armed spiral instability with energy density gap and I contributed to the gravitational wave detectability prospects of the aforementioned suppression. The contents of this chapter have been published in the journal Physical Review D of the American Physical Society with refernce [226].

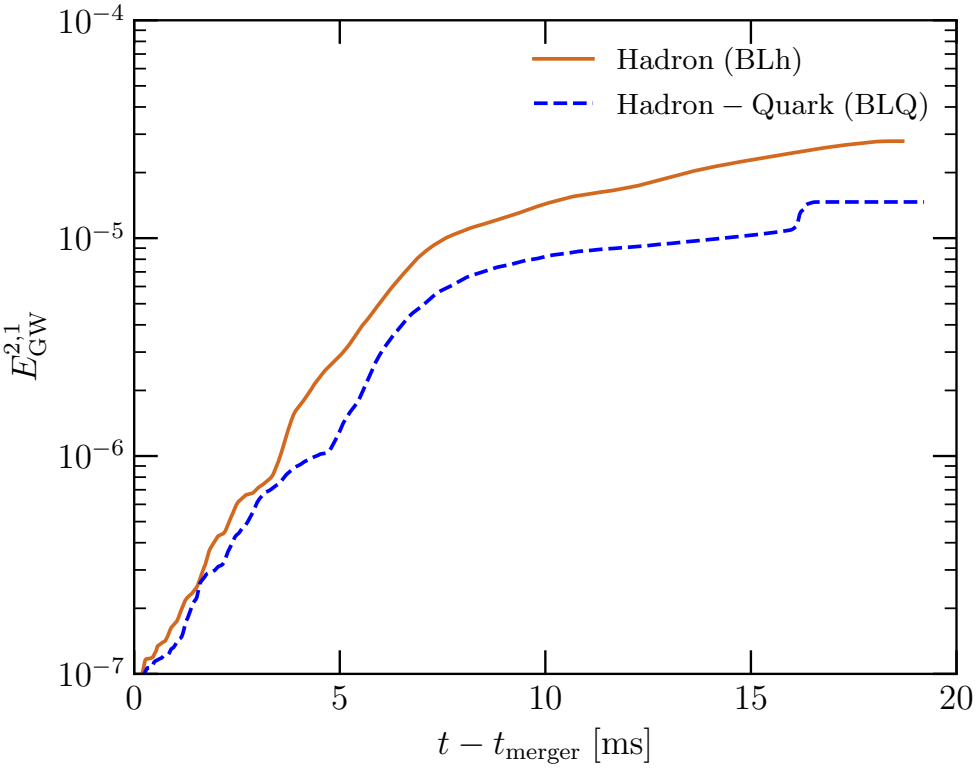


**Figure 3.7.** The time evolution of GW energy (equivalently SNR) carried by the $\ell = 2, m = 1$ mode in a merger of the symmetric 1.30 $M_\odot$ - 1.30 $M_\odot$ binary. Also shown is the relative suppression caused by an onset of QCD phase transitions.

# Chapter 4
# GRHD simulations of binary strange stars

## 4.1 Introduction

The detection of gravitational waves (GWs) from the coalescence of the binary neutron star (BNS) merger GW170817 [1] complemented by the subsequent observations of electromagnetic (EM) counterparts by a number of earth and space-based telescopes [2], has opened a new avenue for exploring the properties of matter under extreme densities (up to several times the nuclear saturation density $\rho_{\rm nuc} \sim 2.7 \times 10^{14}$ g cm$^{-3}$) and temperatures (up to 10s of MeVs) that can not be presently realized in any terrestrial laboratory. These extreme physical conditions are in fact expected to occur in the post-merger remnants generated in BNS mergers and in core-collapse supernovae [106, 227, 228]. The equation of state (EOS) describing the thermodynamic properties of this extreme matter primarily determines the evolution, the fate of the merger remnant, the GW signal, and to some extent the properties of the ejecta and associated electromagnetic counterparts. Other effects such as neutrino transport, [21, 23–25, 28, 224, 229–241], and magnetohydrodynamic turbulence [122, 242–244] may also influence the post-merger evolution.

In the aforementioned region of the phase diagram of strongly interacting matter, quantum chromodynamics (QCD) predicts a transition from a regime where quarks and gluons are confined within baryons and mesons (the hadronic matter phase) to a regime with deconfined quarks and gluons: the so-called quark matter phase. In this dense region of the phase diagram, it is still an open question as to whether such a transition is of the first order or proceeds continuously as in a crossover [245]. Experimental facilities under construction at future facilities, such as the Compressed Baryonic Matter (CBM)

experiment [51] at the Facility for Antiproton and Ion Research (FAIR) are expected to provide insight pertaining to the nature of strongly interacting matter.

For a long time, it has been proposed that a phase of matter composed of the three lightest flavors, namely the up ($u$), down ($d$), and strange ($s$) quarks together with an appropriate number of electrons to guarantee electrical charge neutrality, could exist in the core of sufficiently high-mass neutron stars (NS). This form of quark matter is referred to as strange quark matter (SQM) and NS possessing a SQM core are known as hybrid stars (see e.g., [34]). Even more intriguing than the existence of a SQM core in a NS is the possible existence of a new family of compact stars, called strange stars (SS), which are entirely (i.e., up to the surface) made up of SQM (bare SS). They could possibly be covered by a thin crust of 'normal' matter similar to the one found in the outer crust of a NS (crusted SS). The possible existence of SS is a consequence of the so-called Bodmer–Witten hypothesis [246, 247]. According to this hypothesis, SQM is absolutely stable, i.e., its energy per baryon $(E/A)_{uds}$ (at the baryon density where the pressure is equal to zero) is less than the energy per baryon of the most bound atomic nuclei ($^{56}$Fe,$^{58}$ Fe,$^{62}$ Ni) which is $\sim 930.4$ MeV. The absolute stability of SQM does not preclude the existence of "ordinary" matter [246, 247]. In fact, under this hypothesis, atomic nuclei can be considered as metastable states (with respect to the decay to SQM droplets) having a mean-life time many orders of magnitude larger than the age of the Universe.

Over several years a number of compact stars associated with different astrophysical phenomena have been proposed as possible strange star candidates [248–252]. Most recently, it has been argued that the low-mass companion (with a mass in the range $(2.50-2.67)\ M_\odot$) of the 23 $M_\odot$ black hole, whose merger generated the gravitational wave signal GW190814 [253], could be a strange star [254]. Massive strange stars could thus populate the so-called mass-gap between neutron stars (NSs) and black holes (BHs). It has been also recently suggested that the Central Compact Object within the supernova remnant HESS J1731-347 [255] could be interpreted as a low-mass ($M = 0.77^{+0.20}_{-0.17} M_\odot$) strange star [255–257].

Strange stars could be formed in supernova explosions [258, 259], during the early evolution of a protoneutron star [260–263], or by an external seeding of strangelets (chunks of SQM) [264] in ordinary neutron stars [265, 266]. Alternatively, the conversion of an ordinary neutron star into a strange star is a very likely formation mechanism. In fact, as it has been proposed and discussed in several works [267–269], if the hadronic-to-quark matter phase transition is of the first order, ordinary NSs above a threshold value of their

gravitational mass (corresponding to a threshold central density $n_{thr}$) become metastable with respect to the conversion to strange stars. These metastable NSs have a *mean-life time* related to the nucleation time $\tau$ to form the first critical-size SQM droplet in their center [1]. As shown in [267–269], $\tau$ decreases very steeply as a function of the stellar central density $n_c$ (or as a function of the corresponding gravitational mass $M_G(n_c)$), from $\tau = \infty$ when $n_c = n_{thr}$, to values much smaller than typical pulsar ages (see e.g. Fig. 1 in [267]). At this point (e.g. when $\tau \sim 1\,\mathrm{yr}$ [267, 268]) the conversion to a SS is very likely. This conversion process releases a huge amount of energy ($\mathcal{O} \sim 10^{53}\,\mathrm{erg}$) [270], mainly in a powerful neutrino burst that can possibly result in a short gamma-ray burst. Thus a way to produce SSs is through mass accretion onto neutron stars in binary systems [267, 271] or during the spin-down of a rapidly rotating neutron star [272]. By this mechanism, ordinary metastable neutron stars could be converted into strange stars and these two families of compact stars could coexist in the universe. It is important to emphasize that all the present observational data and our present experimental and theoretical knowledge of the properties of dense matter do not allow us to accept or exclude the validity of the Bodmer–Witten hypothesis and hence the existence of strange stars and the possibility of having two coexisting families of compact stars.

From the above discussion, it is clear that the existence of strange stars would have very far-reaching consequences not only for the physics of strong interactions in extreme matter but also for the many different astrophysical phenomena associated with compact stars.

In this work, we perform full general-relativistic hydrodynamic (GRHD) simulations of binary strange star (BSS) mergers. We note that although the merging of ordinary neutron stars has been widely discussed in literature [79, 148, 273], the case of BSS mergers has been relatively less explored. Only a few works have addressed the general features of the dynamics of this process by mainly employing zero temperature EOSs supplemented with a thermal correction [67, 274] or by using the conformal flatness approximation for the space-time evolution [66]. The main purpose of the present work is to use state-of-the-art numerical techniques to solve the equations of GRHD given a compact binary initial data. We compare numerical simulations of BSS mergers performed using a finite-temperature EOS (where thermal effects are calculated in a way consistent with the zero-temperature case) with those obtained using the zero-temperature EOS supplemented by a phenomenological thermal contribution (the so-called $\Gamma$-law) as done

[1] The actual mean-life time of the metastable NS depends on the mass accretion or on the spin-down rate which modifies the nucleation time via an explicit time dependence of the stellar central density $n_c$.

in previous works [67, 274]. We also make use of a modified version of the MIT bag model [275, 276] that allows for larger maximum masses of SS when compared to the classical MIT bag model [67, 264, 274]. To the best of our knowledge simulations of BSS mergers using the settings described above have never been performed.

The chapter is organized as follow. In Sec. 4.2 we describe the modified MIT Bag Model we employ to obtain the SQM EOS. Sec. 4.3 discusses the numerical setup we adopt and the initial data employed for simulations. An analysis of our results follows in Sec. 4.4. In particular in Sec. 4.4.1, we focus on the merger dynamics, and in Sec. 4.4.2, we study GW signatures. Sec. 4.4.3 is dedicated to a discussion of dynamical ejecta (4.4.3.1)from the BSS merger and accretion disks (4.4.3.2) for the remnant SS. We finally conclude in Sec. 4.5.

Throughout this chapter, we adopt a space-like signature $(-,+,+,+)$ with the Einstein's convention for summation over repeated indices. Unless otherwise stated, all quantities are expressed in geometrized units, i.e., $G = c = 1$.

## 4.2 The equation of state for strange quark matter

The EOS for strange quark matter that includes the effects of gluon-mediated QCD interactions between quarks up to $\mathcal{O}(\alpha_{\rm s}^2)$ particularly the one gluon exchange between quarks, can be written [81, 82, 275] in a straightforward and easy-to-use form similar to the popular version of the MIT bag model EOS [264]. The grand canonical potential per unit volume is given by (we use units where $\hbar = 1$, and $c = 1$)

$$\Omega = \sum_{i=u,d,s,e} \Omega_i^0 + \frac{3}{4\pi^2}(1 - a_4)\left(\frac{\mu_{\rm b}}{3}\right)^4 + B_{\rm eff}, \tag{4.1}$$

where $\Omega_i^0$ is the grand canonical potential density for $u$, $d$, $s$ quarks and electrons which are modeled as ideal relativistic Fermi gases. The second term on the right-hand side of Eq.(4.1) accounts for the perturbative QCD corrections up to $\mathcal{O}(\alpha_s^2)$ [81–83] and represents the degree of deviation from an ideal (non-interacting) relativistic Fermi gas, with $a_4 = 1$ corresponding to the ideal Fermi gas case. The baryon chemical potential $\mu_b$ can be written in terms of the $u$, $d$ and $s$ quark chemical potentials as $\mu_b = \mu_u + \mu_d + \mu_s$. $B_{\rm eff}$ is an effective bag constant that phenomenologically takes into account the non-perturbative aspects of QCD.

At a finite temperature, the ideal Fermi gas contributions to $\Omega$ provided by fermions and antifermions for a given temperature $T$ and chemical potential $\mu_i$ can be computed

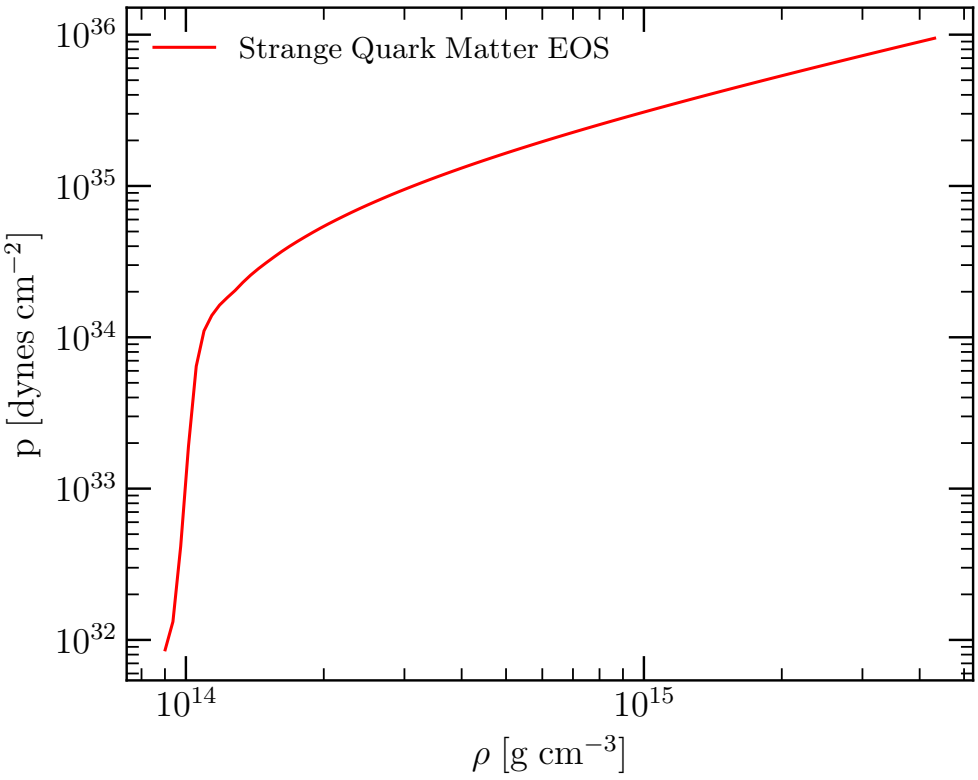


**Figure 4.1.** The pressure vs. rest mass density relation for the strange quark matter EOS at zero temperature, i.e., a completely degenerate Fermi gas of $u$, $d$, and $s$ quarks along with electrons for electrical neutrality. The pressure of strange quark matter begins dropping rapidly at densities near and less than nuclear saturation as is also seen in [66].

as (see e.g. [84]):

$$\begin{aligned} \Omega_i^0(T,\mu_i) &= -\frac{1}{3}\frac{g_i}{2\pi^2}\int_0^\infty k^2 dk\ k\,v \\ &\times \ [f(k,\mu_i)+f(k,-\mu_i)] \end{aligned} \tag{4.2}$$

where $v = k/E_i$ is the particle velocity (with total energy $E_i(k) = (k^2 + m_i^2)^{1/2}$), and $f(k, \pm\mu_i)$ are the Fermi-Dirac distribution functions with chemical potentials $+\mu_i$ for particles and $-\mu_i$ for antiparticles. The distribution functions are given as:

$$f(k,\pm\mu_i) = \frac{1}{e^{(E_i(k)\mp\mu_i)/T}+1}, \tag{4.3}$$

Here, the degeneracy factor is $g_i = 2$ for electrons and $g_i = 6$ for each quark flavor. The temperature dependence of the non-ideal Fermi gas term and that of the Bag constant in Eq.(4.1) has been neglected.

The total entropy density

$$s = \sum_{i=u,d,s,e} s_i \tag{4.4}$$

can be computed using the ideal Fermi gas approximation for each fermionic particle species [85]:

$$\begin{aligned} s_i(T,\mu_i) &= -\frac{g_i}{2\pi^2}\int_0^\infty k^2 dk\,[f(k,\mu_i)\ln f(k,\mu_i) \\ &+ (1-f(k,\mu_i))\ln(1-f(k,\mu_i)) \\ &+ f(k,-\mu_i)\ln f(k,-\mu_i) \\ &+ (1-f(k,-\mu_i))\ln(1-f(k,-\mu_i))] \end{aligned} \tag{4.5}$$

Using the standard relations for thermodynamic potentials, the energy density can be written as:

$$e = \Omega + \sum_{i=u,d,s,e} \mu_i n_i + Ts, \tag{4.6}$$

where $n_i$ is the number density for each particle species which can be given as:

$$n_i = -\left(\frac{\partial\Omega}{\partial\mu_i}\right)_{T,V} \tag{4.7}$$

The total baryon number density is:

$$n_B = \frac{1}{3}(n_u + n_d + n_s)\,. \tag{4.8}$$

Weak reactions involving quarks of the type:

$$d + u \leftrightarrow u + s \tag{4.9}$$

$$u + e^- \leftrightarrow s + \nu_e \tag{4.10}$$

occurring in the hot-dense merger remnant change the quark concentrations of matter to minimize the energy per baryon of the system. Since the typical time-scale for weak interaction processes $\tau_w \lesssim (10^{-8}\text{–}10^{-10})$ s is significantly shorter than the hydrodynamic timescales ($\tau_h \sim 10^{-3}$s) inside the remnant, we neglect detailed reaction rates involving quarks and neutrinos. Thus we consider $\beta$-stable strange quark matter satisfying equilibrium with respect to the weak interactions, i.e.,

$$\mu_s = \mu_d = \mu_u + \mu_e\,, \tag{4.11}$$

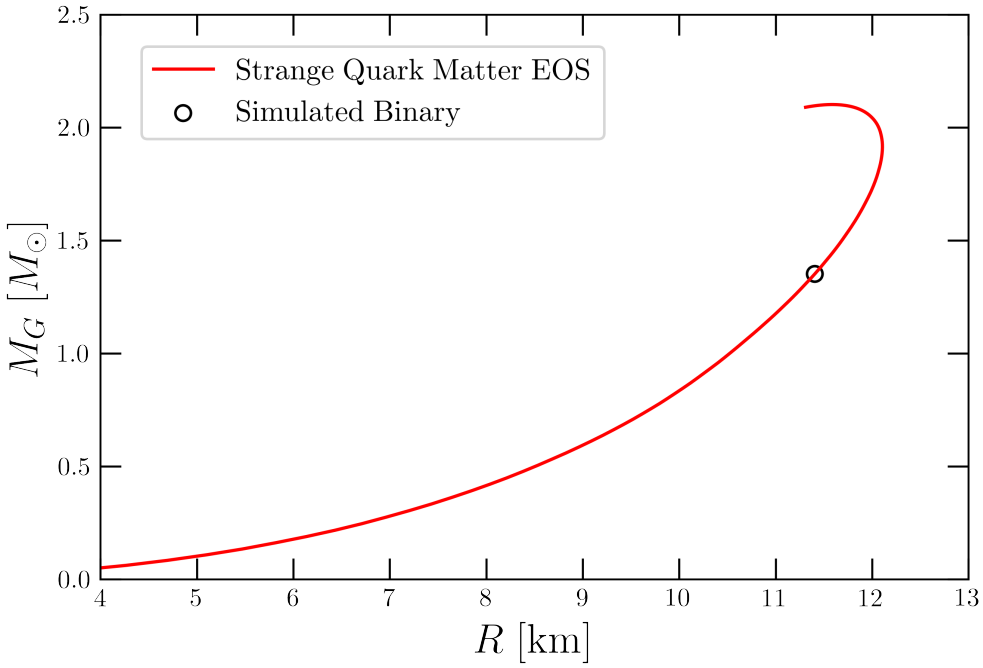


**Figure 4.2.** The mass-radius relationship for isolated and non-rotating strange stars computed from iterative solutions of the TOV equations for the cold strange quark matter EOS presented in this work. Contrary to the TOV sequences of neutron stars which have a negative slope, the TOV sequences for strange stars have $\partial M_{\rm G}/\partial R > 0$ for the stable branch. Strange stars are self-bound as a result of QCD interactions meaning that they will be bound even in the absence of gravity. In other words, their surfaces possess a surface tension and they can be very small in size $R \sim 4$km. We also denote the TOV configuration of the strange star, whose symmetric binary merger we simulate in this work with a black circle.

and electric charge neutrality.

In the present work we take $m_e = 0$, $m_u = m_d = 0$, $m_s = 100$ MeV, $B_{\rm eff}^{1/4} = 138\,{\rm MeV}$ and $a_4 = 0.8$. Using these values for the EOS parameters, SQM satisfies the Bodmer-Witten hypothesis and in addition, atomic nuclei are stable with respect to their possible decay to droplets of non-strange (i.e. $u$, $d$) quark matter [264, 272].

We show the cold and $\beta-$equilibrated EOS for SQM in figure 4.1. A steep drop in pressure for densities close to nuclear saturation is a characteristic of the strange quark matter EOS (see also [66]). In figure 4.2 we show the mass-radius curve for cold, isolated, and non-rotating strange stars described by our EOS model. Strange quark stars are self-bound instead of being gravitationally bound like other compact stars. This is due to the surface tension provided by the non-perturbative aspects of QCD and modeled by a negative Bag constant in the expression for pressure (see equation 1.112). This further implies that strange quark stars can support very small radii $\sim$ 4km. We obtain the

following values for the structure parameters characterizing the stellar maximum mass configuration: gravitational mass $M = 2.10\,M_\odot$, baryonic mass $M_B = 2.71\,M_\odot$, stellar radius $R = 11.57\,\mathrm{km}$, central baryon number density $n_{Bc} = 0.924\,\mathrm{fm}^{-3}$, central density $\rho_c = 1.7625 \times 10^{15}\mathrm{g/cm}^3$ and tidal deformability $\Lambda = 22.46$. For the SQM EOS model employed in this work, general relativistic equilibrium sequences of rapidly spinning bare strange stars have been constructed in [272]. In particular, it was shown (see Table 3, first line and figures 3 and 4 of Ref. [272]) that for the case of maximally spinning bare strange stars (i.e. at the mass shedding limit), the maximum gravitational and baryonic masses correspond to $M = 3.032 M_\odot$ and $M_B = 3.924 M_\odot$ respectively.

## 4.3 Numerical setup

All the simulations performed in this work are targeted to model a GW170817-like event in the sense that we consider BSS configurations with the same chirp mass as GW170817 [1], i.e., $M_{\rm chirp} = 1.18\ M_\odot$. To this aim, we simulate non-rotating, symmetric binaries of total mass $M = 2.72\ M_\odot$. This choice is aimed at simulating the cleanest scenario before possibly considering the effects of unequal mass ratios.

The initial data are generated using the pseudo-spectral code `LORENE` [101]. We consider irrotational binaries in quasi-circular orbits at an initial separation of 45 km. For bare strange stars, we have a large gradient in density as we transition from a tenuous atmosphere to the surface. To control spurious oscillations in the computation of density at the surface, in the computation of initial data, we reduce the relaxation factor for the gravitational potential to 0.05.

The evolution of BSS mergers in this work is carried out in full general relativity using our GRHD infrastructure `WhiskyTHC` [87, 88]. The spacetime is evolved using the Z4c formulation [90, 91] as implemented in the CTGamma [92, 93] thorn of Einstein Toolkit [277]. We employ the `Carpet` [95, 96] infrastructure for adaptive mesh refinement.

We assume the strange star matter to be a relativistic perfect fluid, i.e., a fluid without viscosity, heat conduction or shear. The stress-energy tensor for such a fluid is given by

$$T^{\mu\nu} = (e + p)u^\mu u^\nu + p g^{\mu\nu}\,, \tag{4.12}$$

where $e$ is the total energy density, $p$ the isotropic pressure, $u^\mu$ the relativistic 4-velocity of the fluid and $g^{\mu\nu}$ the spacetime metric. The energy density may be further expressed in terms of the rest mass density $\rho$ as $e = \rho(1 + \epsilon)$ where $\epsilon$ is the specific internal energy.

We also note that $\rho = nm_{\rm B}$ where $n$ is the baryon number density and $m_{\rm B}$ is a fiducial Baryonic mass.

As described in section 4.2, we neglect weak reactions in our simulations, i.e. we assume the net lepton number $n_e$ to be conserved. The equations of GRHD are therefore given by the conservation of rest mass (or baryon number) and the conservation of energy and momentum:

$$\nabla_\mu(\rho u^\mu) = 0, \tag{4.13}$$

$$\nabla_\mu T^{\mu\nu} = 0. \tag{4.14}$$

The system of equations (4.13)–(4.14) is closed by the EOS for strange quark matter as discussed in section 4.2. The flux terms in equations (4.13)–(4.14) are reconstructed using a positivity preserving limiter first introduced in [278] and later on implemented in `WhiskyTHC` [89].

All binaries are simulated at two spatial resolutions which we conventionally name as *low resolution* (LR) and *standard resolution* (SR). In the finest refinement level, the spatial grid's cell is $\sim 180$ m long for SR and $\sim 250$ m for LR. We shall primarily report results for the more accurate SR simulations. LR simulations will serve to provide an estimate of errors arising due to the finite spatial resolution. Our simulation dataset is summarized in table 4.1.

An interesting aspect of our work concerns the incorporation of thermal effects into the equation of state for SQM. We compare models of BSS mergers with a finite temperature EOS to models where we add an ideal-fluid thermal component to the cold $\beta$-equilibrated EOS. Finite temperature effects are modeled consistently through the numerical calculation of Fermi integrals for the various thermodynamic variables (eq.s (4.1)–(4.7)). This approach in which thermal contributions are consistently included with the zero-temperature EOS, has only been used in a few simulations of BSS mergers [66]. In this work, we will refer to numerical simulations that make use of this consistent treatment of thermal effects as the finite-T simulations. An approximate and still widely used treatment of thermal effects consists of adding a thermal contribution of an ideal fluid to the pressure and specific internal energy of the zero temperature EOS:

$$\begin{aligned} p &= p_{\rm c} + p_{\rm th} \\ \epsilon &= \epsilon_{\rm c} + \epsilon_{\rm th} \end{aligned} \tag{4.15}$$

where $p_{\rm c}$ is the pressure variation in the zero-temperature slice of the EOS and $p_{\rm th}$ is the

thermal contribution given by the so-called $\Gamma-$ law as

$$p_{\rm th} = (\Gamma_{\rm th} - 1)\rho\,\epsilon_{\rm th}. \tag{4.16}$$

$\epsilon_{\rm c}$ is the specific internal energy of the cold EOS and $\epsilon_{\rm th}$ is the thermal contribution to the same. We take the adiabatic index $\Gamma_{\rm th} = 1.7$. Typically, numerical simulations evolve $\epsilon$ and $\epsilon_{\rm th}$ is computed from $\epsilon - \epsilon_{\rm c}$, which is then used to compute $p_{\rm th}$. We will refer to numerical simulations based on the $\Gamma$-law treatment of the thermal contributions, as hybrid simulations.

## 4.4 Results

In this section, we present our results for a merger of BSS focusing on the overall dynamics of the merger, potential signatures on the gravitational wave emission, and the dynamical ejection of strange quark matter as a result of the merger.

### 4.4.1 Dynamics of the merger

In this sub-section, we present a qualitative overview of the merger dynamics. In figure 4.3, we report the evolution of the rest mass density of the strange star merger across the equatorial plane for the finite-T simulations. The snapshots are reported at instants relative to the merger so that the different stages of inspiral, merger, and post-merger can be distinguished. Starting from the initial data, the strange stars orbit for $\sim 7$ cycles in the inspiral, radiating away their energy and angular momentum via gravitational wave emission. As the orbit decays and the stars get closer, they become tidally deformed by their mutual gravitational attraction. We define the time of merger $t_{\rm merg}$ as the instant when the $\ell = 2, m = 2$ mode of the GW radiation attains a maximum. The merger results in a remnant that is highly deformed and undergoes violent radial pulsations and differential rotation that source gravitational wave emission in the kilohertz regime.

The remnant thus formed is stabilized by differential rotation over time scales of 10s of ms, thereby forming a rapidly rotating strange star. We refer the reader to table 4.1 for the eventual fates of the different models we simulate. We find that the only model that does not collapse over the simulation time scales is evolved using the hybrid EOS at SR. In the cases where the remnant is unable to support its shape and the outward quark degeneracy pressure gives in to the gravitational pressure, we characterize the lifetime of the remnant by the quantity $t_{\rm BH} - t_{\rm merg}$ which represents the approximate

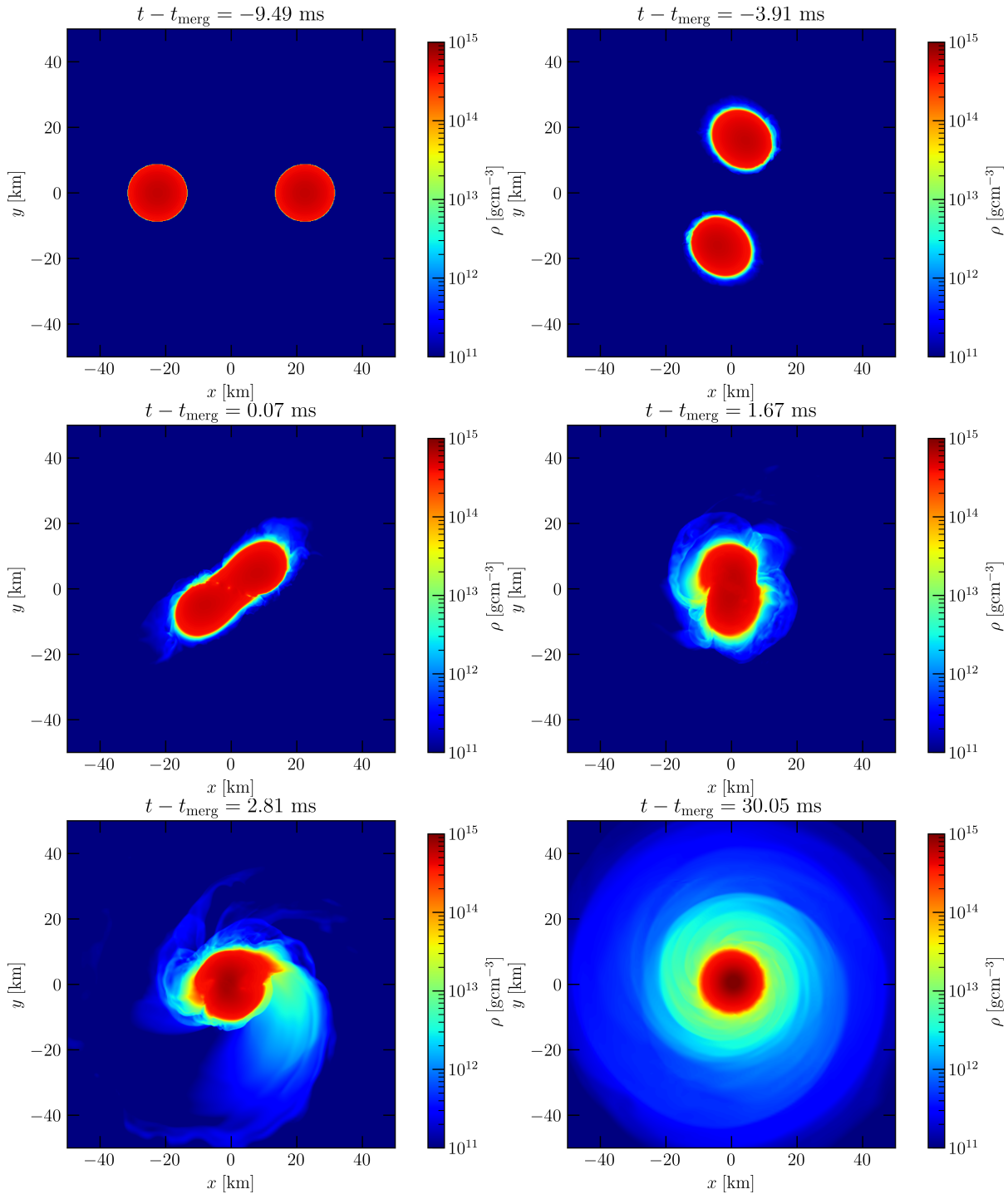


**Figure 4.3.** The evolution of rest mass density $\rho$ on the equatorial plane for a merger of BSS evolved with the finite-T EOS. The evolution time for each snapshot has been listed relative to the merger which we take to be at 0 ms.

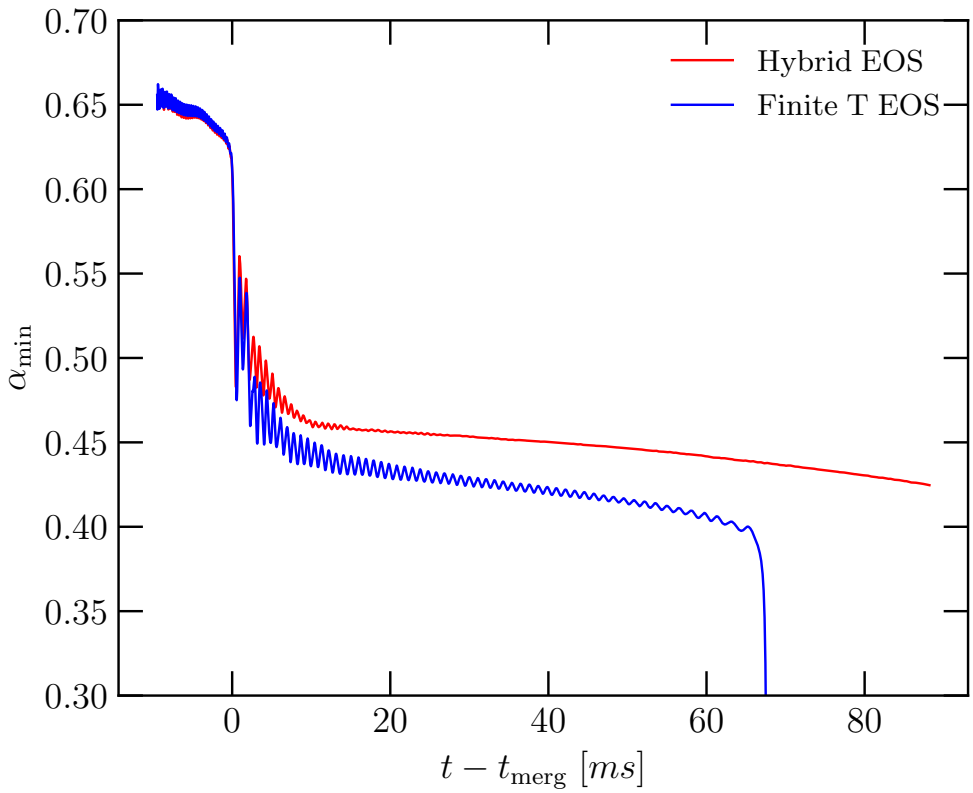


**Figure 4.4.** Time evolution of the minimum of lapse function $\alpha_{\rm min}$. We compare the evolution for the hybrid simulation and the finite-T simulation and observe that the lapse for the hybrid EOS's remnant saturates during the simulation time scale whereas for the finite-T EOS's remnant, it drops below 0.3 indicating the formation of an apparent horizon.

time from merger when an apparent horizon forms. We identify $t_{\rm BH}$ as the time when the minimum of the lapse function $\alpha_{\rm min} \leq 0.3$, which for non-spinning binaries (in the inspiral) is a good approximation. A similar definition for the remnant's lifetime was introduced in ref. [79] and has been utilized in refs. [108, 159, 279].

The finite-T EOS softens at high densities when compared to the hybrid EOS. This softening manifests as a difference in the lifetimes of the postmerger remnant. Indeed we note that the remnant evolved with the finite-T EOS collapses after 65.40 ms (for the SR) from the time of merger (see table 4.1). This is made explicit in Fig. 4.4 where we plot the time evolution of the minimum of the lapse function $\alpha_{\rm min}$, which for the remnant evolved with the finite-T EOS (SR) drops to below 0.3. On the other hand, the strange star remnant evolved with the hybrid EOS (SR) remains stable and does not undergo gravitational collapse over the full simulation time of 86.1 ms post-merger. This is evidenced by the near-constant evolution of the minimum lapse for postmerger. As

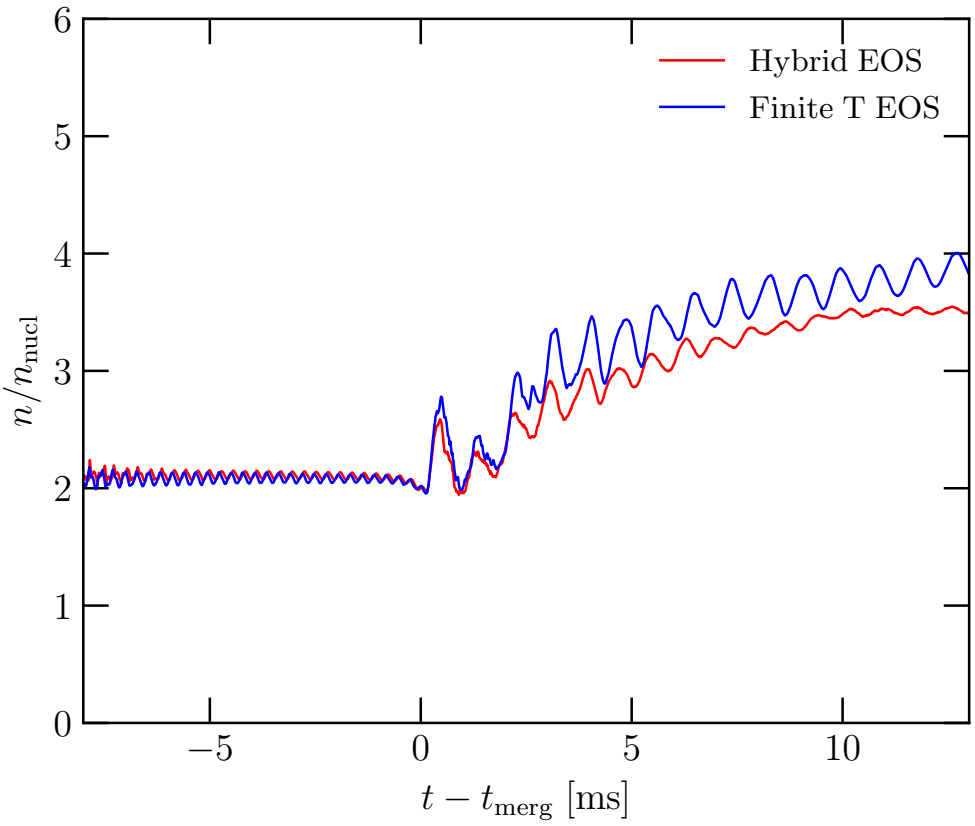


**Figure 4.5.** The time evolution of the central (maximum) rest mass density (normalized to nuclear saturation density) in a merger of strange stars for the two EOS treatments considered in this work. We observe that the finite-T remnant undergoes more violent oscillations in density owing to its softening at high densities relative to the hybrid EOS. These violent oscillations do not dampen away during the simulation time scale, eventually causing the finite-T remnant to collapse. On the other hand, oscillations in the hybrid remnant's central density saturate over a time scale of 20 ms, following which the hypermassive hybrid remnant remains stable.

is expected for remnant lifetimes, we find them to be strongly sensitive to a change in spatial resolution both for the finite-T simulations as well as the hybrid simulations (see table 4.1).

In figure 4.5, we show the evolution of the rest mass density in a merger of strange stars evolved with a hybrid EOS as well as a finite-T EOS at SR. During the inspiral, owing to the fact that both EOS treatments have the same cold $\beta-$ equilibrated behavior at low densities, the evolution of central density is very similar and undergoes mild oscillations. As the two stars merge, the central density undergoes strong oscillations sourced from the radial pulsations of the postmerger remnant. These oscillations are much more violent for the finite-T case than for the hybrid remnant reflecting a difference

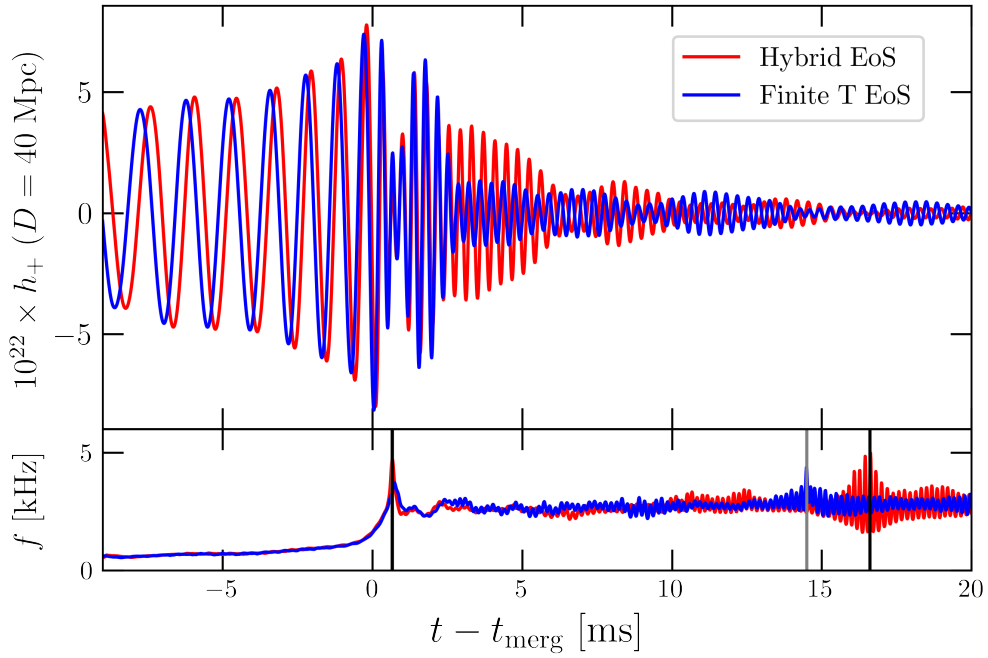


**Figure 4.6.** *Top panel*: The evolution of the + polarization of the gravitational wave strain computed from a hybrid simulation and a finite-T simulation. For both the EOS treatments, $h_+$ has been so oriented that the merger takes place at 0 ms. *Bottom Panel*: The time evolution of instantaneous frequency for both the EOS treatments.

in their thermal treatments. In particular, these strong pulsations of the finite-T EOS's remnant make it unstable towards a gravitational collapse to a black hole whereas the hybrid remnant can sustain its shape via differential rotation over the time scales of the simulation.

The differences in the postmerger dynamics as a result of differences in thermal treatments were also reported for BSS mergers in ref. [66] where it was found that including non-zero thermal effects in the EOS indeed influences the outer structure of the remnant strange star as well as its lifetime.

### 4.4.2 Gravitational waves

In this subsection, we will present an analysis of the gravitational wave emission from a merger of BSS and compare the evolution from a hybrid EOS model with a finite-T EOS model. To start with, we employ the Newman-Penrose formalism [8] (also see section 1.1.1.1 for a brief description) to compute the Weyl scalar $\Psi_4$ from a BSS merger. $\Psi_4$ thus obtained is integrated twice in time using fast frequency integration [280] to obtain the GW strain $h_+ - ih_\times$.

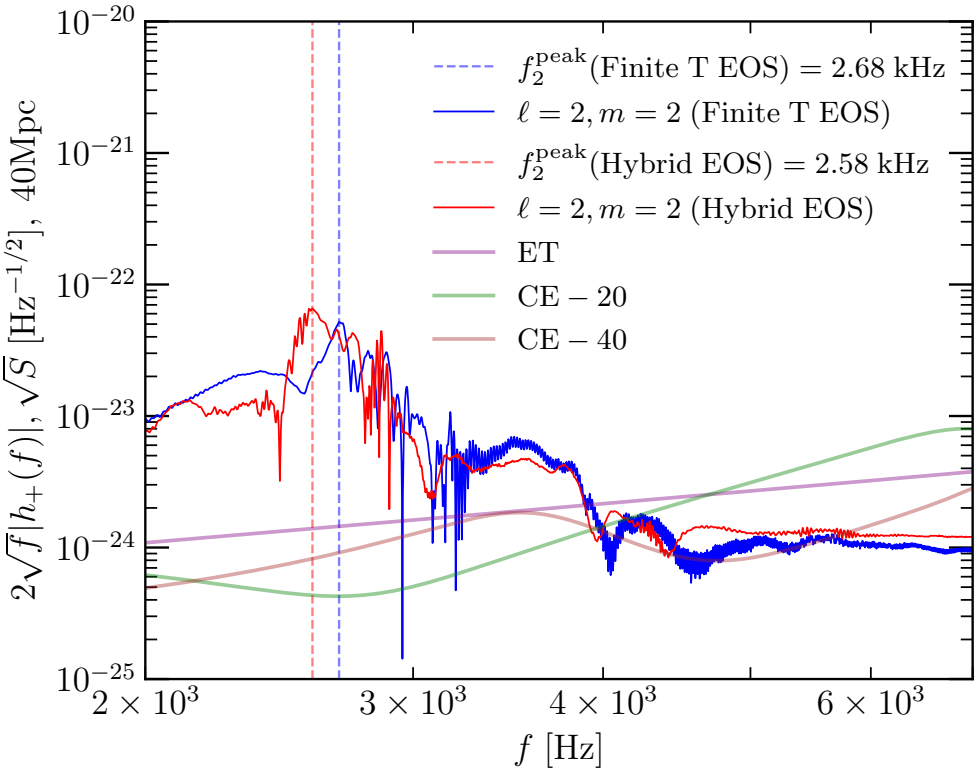


**Figure 4.7.** The amplitude spectral density of the postmerger gravitational wave strain from both the hybrid EOS treatment and the finite-T EOS treatment. Noticeable are the characteristic postmerger peak frequencies $f_2^{\rm peak}$ between 2-4 kHz. The finite-T EOS being softer at higher densities naturally predicts a more compact remnant thereby increasing its $f_2^{\rm peak}$. Also shown are the sensitivities of the next generation of GW detectors with the best detection prospects offered by the 20 km postmerger optimized CE-20 detector.

In figure 4.6, we show the + polarization of the GW strain as well as the instantaneous frequency from an inspiral, merger, and postmerger of a BSS evolved with a hybrid EOS and a finite-T EOS at SR. Notable attributes of these simulations are the pronounced modulations in the postmerger amplitude in both the EOS treatments (See [281] for a detailed discussion). These amplitude modulations are a beating pattern caused by the interaction of radial pulsations of the remnant (at a characteristic fundamental mode $f_0 \sim 1$ kHz) with the rotation of the remnant (at the characteristic postmerger peak frequency $f_2^{\rm peak} \sim 2 - 4$ kHz). Such features in the postmerger waveform morphology have also been encountered in [159, 282].

We report the postmerger amplitude spectral densities of our SR models for both the EOS treatments in figure 4.7. The inspiral contribution has been suppressed using a Tukey window to better compare the spectral contributions from the postmerger. We

notice that the peak $f_2^{\rm peak}$ frequencies are different between the two EOS models. This is to be expected because, as remarked before, the finite-T EOS is softer compared to the hybrid EOS at large densities that are typically probed during the postmerger. Such features in the postmerger spectra provide optimal detection avenues with the next generation of GW detectors. Quantitatively, for a BSS merger at a luminosity distance of 40 Mpc (same as that of GW170817), the CE-20 detector shall have a postmerger signal-to-noise ratio (SNR) of 38.4 for the hybrid EOS and 30.89 for the finite-T EOS. This relative decrease in the SNR could perhaps be attributed to the weaker amplitude modulations of the GW strain for the more compact finite-T remnant.

So far we have established that such signals could be potentialy detected with the next generation of GW experiments, however, it is also crucial to investigate whether we can differentiate between mergers of neutron stars (BNS) and mergers of binary strange stars (BSS). There have been a few works in this regard, most notably ref. [66], which claimed differentiability of BSS mergers from BNS mergers by citing smaller tidal parameters for strange stars as well as the fact that characteristic inspiral and postmerger frequencies are in general higher for binaries of strange stars. More recently, ref. [283] claimed distinguishability between BSS and BNS mergers from their respective inspiral signals. The authors made use of the empirical relations between the f-mode frequencies (frequency of density perturbations during the inspiral) and tidal deformations and cited a non-degeneracy between such relations for BSS and BNS inspirals as a claim of distinguishability. However, such a non-degeneracy could only be established with a weak statistical significance. On the other hand, Zhu et al. [67] showed that mergers of strange stars actually followed the same quasi-universal relations between merger/postmerger frequencies and tidal deformabilities as other hadronic binaries, thereby claiming that it will be difficult to distinguish the two classes of stars.

Our results appear to in agreement with the latter claim by Zhu et al. [67], in that, we too find that our strange star merger models follow the pre-established universal relations between the postmerger peak frequency $f_2^{\rm peak}$ and tidal deformabilities. In particular, in figure 4.8, we show a quasi-universal relation for neutron star binaries provided in refs. [284, 285] between the postmerger peak frequency $f_2^{\rm peak}$ and a tidal parameter $\kappa_2^T$ (see [284] for an expression of $\kappa_2^T$). These relations have been calibrated over 600 numerical relativity simulations of BNS mergers available publicly via the CoRe database. We also show (in red and blue circles), our SR models of BSS mergers and the fact that they are degenerate with the trends observed for neutron star binaries up to a credible interval of 90%. Thus in conclusion, up to 90% credible intervals, it is difficult

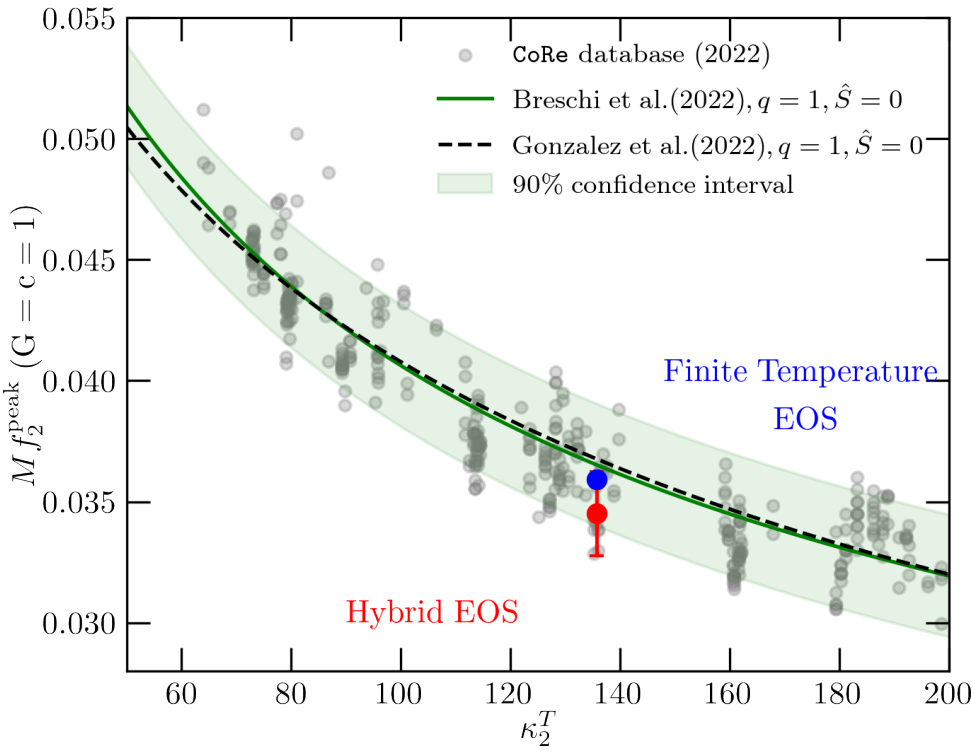


**Figure 4.8.** We show our BSS merger models (in red and blue circles) simulated at SR with both hybrid EOS and a finite-T EOS in conjunction with the pre-established quasi-universal relations for BNS mergers provided in refs. [284, 285]. The universal relations have been calibrated over 600 numerical relativity simulations of neutron star mergers from the CoRe database. Up to 90% credible intervals, BSS mergers are degenerate with BNS mergers implying that they are not mutually distinguishable. The error bars provide differences in $f_2^{\rm peak}$ from the corresponding lower resolution LR models. Owing to small $\Delta f_2^{\rm peak} \sim \mathcal{O}(10)$ Hz with a change in spatial resolution for the finite-T EOS model, its error bars are relatively obscured.

to distinguish between mergers of strange stars and mergers of neutron stars from their postmerger GW emission, at least for our EOS model.

### 4.4.3 Ejecta

In this subsection, we shall investigate the properties of nuggets of strange quark matter, also called strangelets, ejected in a BSS merger. It is noteworthy to mention that there exists a lack of modeling for the evaporation processes of these strangelets into ordinary nucleonic matter. Owing to this difficulty, we cannot comment upon the radioactive decay of ejecta, r-process nucleosynthesis, and the consequent kilonova signatures. We also refer the reader to ref. [65] for the production rates of strangelets from outflows of BSS mergers and the observational implications. This reference assumes that mergers of

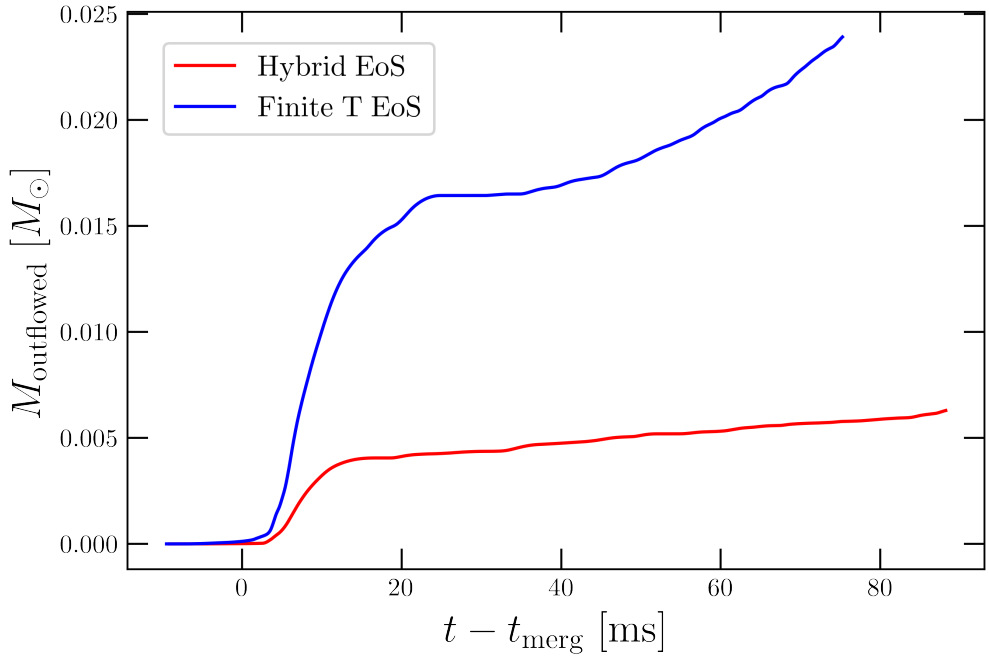


**Figure 4.9.** Evolution of the unbound (according to the geodesic criterion) strange quark matter as a function of time. Strong density pulsations with the softer finite-T EOS at high densities could result in more SQM being gravitationally unbound from the remnant.

binary strange stars are the only efficient mechanism for the production of strangelets and constrains an average SQM ejecta mass per event to be $\sim 10^{-4} M_\odot$. Furthermore, they find evidence of a strong correlation between the Bag constant for their EOS model and the ejected mass of SQM implying that a measurement of the cosmic ray flux of strangelets could in principle put observational constraints on the value of the Bag constant.

#### 4.4.3.1 Dynamical ejecta

We study the strange quark matter ejected from a merger of BSS on dynamical time scales. In particular, we make use of the geodesic criterion to flag the region of the flow that becomes gravitationally unbound with respect to the remnant. In other words, unbounded strange quark matter follows the condition $u_t < -1$ where $u_t$ is the time component of the 4-velocity of the flow. In figure 4.9, we show as a function of time, the mass of strange quark matter that has crossed a fiducial coordinate sphere of 200 $G\,\mathrm{M}_\odot/c^2$ ($\simeq 295.34$ km). We refer the reader to [126–128] for more discussions on the different criteria for the unbounded matter.

We note that the ejected SQM mass during the postmerger with the finite-T treatment

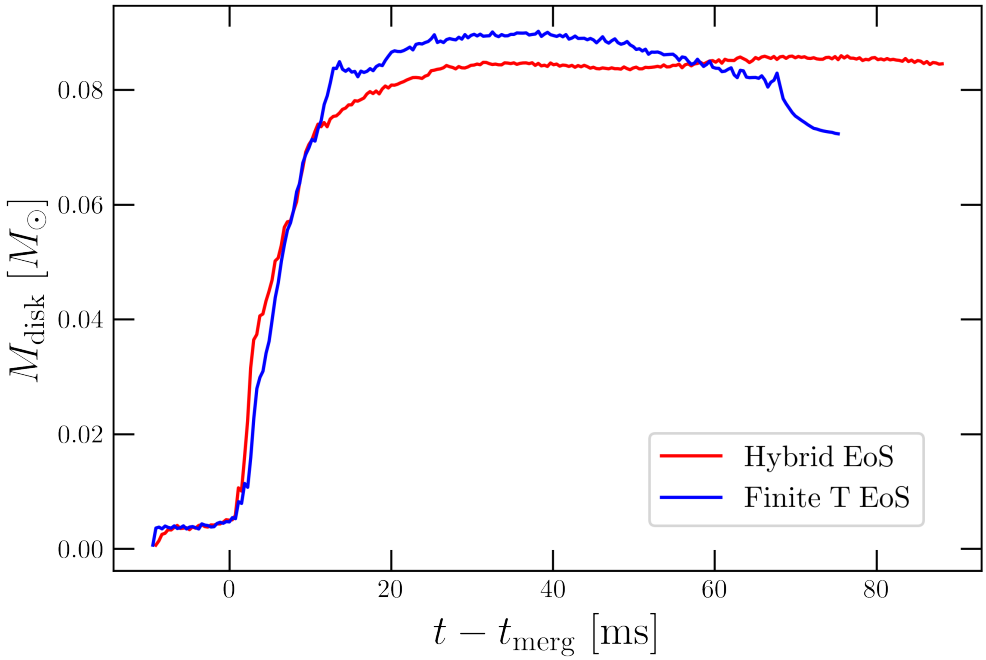


**Figure 4.10.** The evolution of disk mass as a function of time for the two treatments of the SQM EOS. We note that owing to violent oscillations in the remnant, the remnant for the finite-T model supports a more massive disk as compared to the hybrid model. This disk eventually starts getting accreted back as the remnant collapses into a black hole.

is a factor of $\gtrsim 4$ more massive than that simulated from the hybrid EOS. A possible explanation could be that violent postmerger pulsations of the remnant with the finite-T EOS could drive shocks that gravitationally unbound more strange quark matter than the case with the hybrid EOS.

#### 4.4.3.2 Accretion Disks

In this subsection, we shall investigate the properties of strangelets that are squeezed out of the collisional interface in a BSS merger but are still gravitationally bound so that their angular velocity is Keplerian [104]. Following the convention in [137], we compute the mass of the accretion disk as a function of time by computing the integral

$$M_{\rm disk} = \int_V \sqrt{\gamma}\rho W d^3x \tag{4.17}$$

over the 3D volume $V$ where the rest mass density of strange quark matter $\rho < 10^{13}$ g cm$^{-3}$ and where the strange quark matter lies outside the apparent horizon (if one has already been formed), i.e., $\alpha \geq 0.3$.

In figure 4.10, we present the time evolution (for SR) of disk mass as described above for the two SQM EOS treatments. We notice that the disk mass starts to increase after the merger and tends to saturate at about 20 ms for the hybrid model. On the other hand for the finite-T model, we have a slightly larger disk mass which could be attributed to more strange quark matter being ejected and becoming gravitationally bound as a result of violent density oscillations in the remnant. Interestingly, we also note a decay in the disk mass for the finite-T model near the time of the formation of an apparent horizon, i.e., $t_{\rm BH} - t_{\rm merg} \simeq 65.4$ms which can be attributed to the accretion of the disk back onto the collapsed black hole.

## 4.5 Conclusions

In this chapter, we have performed for the very first time, simulations of binary strange star mergers in full general relativity by employing a finite-T EOS model that is consistent with constraints from QCD. To describe the equilibrium behavior of the degrees of freedom ($u$, $d$, $s$ quarks and electrons) inside a strange star, we have employed an extended version of the MIT Bag model [275,276] which describes the degeneracy pressure of the Fermionic species as a non-interacting Fermi gas supplemented by phenomenological descriptions of gluon mediated interactions and non-perturbative aspects of QCD. Our model satisfies the Bodmer-Witten hypothesis [246,247] in that the energy per nucleon is less than that of the most bound $^{56}$Fe nuclei. Non-rotating TOV sequences of strange stars constructed from this model are self-bound and can have a very small size $R \sim 4$ km.

The qualitative dynamics of a merger of strange stars, in a broad-brush sense, are similar to that found in mergers of neutron stars. We consider four models of BSS mergers that differ in spatial resolution and the incorporation of thermal effects either by a thermal ideal gas correction or by the inclusion of non-zero thermal effects consistently within a finite-T EOS. We find that the remnants formed with the finite-T EOS are relatively more compact and more prone to gravitational collapse to a black hole as compared to remnants evolved with a hybrid EOS. This is attributed to a loss of pressure at high densities in the finite-T EOS when compared to a hybrid EOS.

The postmerger GW signals depict pronounced amplitude modulations as a result of the coupling between the fundamental pulsation mode and the characteristic rotational frequency of the remnant. The relative softness of the finite-T EOS manifests as a higher postmerger peak frequency $f_2^{\rm peak}$ when compared to the hybrid remnants. We also find that it is difficult to distinguish mergers of strange stars from those of neutron stars

owing to degeneracies in the quasi-universal relations which appear to be satisfied by both classes of stars.

Finally, we also investigate the properties of unbound strangelets that are ejected in a BSS merger. In particular, violent oscillations in the central density of the remnant with the finite-T EOS are responsible for a larger mass of the remnant becoming gravitationally unbound. This is also the reason why finite-T models support a more massive accretion disk around them at least up to the collapse of the remnant.

## 4.6 Declaration

The GRHD simulations and the post-processing analysis presented in this chapter were carried out by myself and a graduate student from the University of Pisa, Francesco Grippa. This chapter also forms a part of his Master's thesis. The draft of the publication is in the final stages of preparation for a potential submission to Physical Review D.

**Table 4.1.** A summary of our simulation dataset for two spatial resolutions. $m_1$ and $m_2$ are the gravitational masses of the two strange stars in the binary and $M$ is the total gravitational mass of the binary. $\Lambda$ represents the tidal deformability of the individual star in the binary and is the same for both stars in a symmetric binary. $f_2^{\rm peak}$ represents the dominant postmerger peak frequency of the $\ell = 2$, $m = 2$ mode. $t_{\rm BH} - t_{\rm merg}$ is the time of collapse to a black hole relative to merger.

| EOS | $m_1$ [$M_\odot$] | $m_2$ [$M_\odot$] | $M_{\rm tot}$ [$M_\odot$] | $\Lambda$ | Resolution | $f_2^{\rm peak}$ [kHz] | Collapse | $t_{\rm BH} - t_{\rm merg}$ [ms] |
|---|---|---|---|---|---|---|---|---|
| Hybrid EOS | 1.36 | 1.36 | 2.72 | 723.34 | LR | 2.836 | Yes | 63.35 |
| Hybrid EOS | 1.36 | 1.36 | 2.72 | 723.34 | SR | 2.576 | No | - |
| Finite T EOS | 1.36 | 1.36 | 2.72 | 723.34 | LR | 2.668 | Yes | 9.00 |
| Finite T EOS | 1.36 | 1.36 | 2.72 | 723.34 | SR | 2.682 | Yes | 65.40 |

# Chapter 5
# Thermal effects in neutron star mergers

## 5.1 Introduction

The extreme conditions found in neutron stars make them an ideal means for probing the nuclear equation of state (EOS). Electromagnetic (EM) observations of pulsars have provided valuable information about the mass distribution of neutron stars [286, 287], and recent results from NICER offer constraints on their radii [288–290]. Binary neutron star (BNS) mergers give additional astronomical constraints; the gravitational waves (GW) and EM counterpart of GW170817 contained details about the EOS via tidal deformability measurements and ejecta characteristics [291–297].

Due to the high Fermi temperature of matter in a neutron star, constraints obtained from pulsars and BNS inspirals are informative of the zero-temperature equation of state (EOS). On the other hand, temperatures as high as 100 MeV might be reached in the post-merger phase [106], making it a possible probe of the finite-temperature EOS. Current GW detectors have not yet observed a BNS post-merger [291, 298, 299]. Nevertheless, future detectors, like the proposed Einstein Telescope (ET) [300] and Cosmic Explorer (CE) [301] detectors, will feature improved sensitivity at the higher frequencies necessary to detect BNS post-merger signals. Inference on the EOS using post-merger data is possible at (post-merger) signal-to-noise ratios (SNR) as low as 8 [284]. Additionally, sensitivity upgrades to current instruments promise higher BNS detection counts with better sky localization [302].

State-of-the-art BNS merger simulations typically incorporate thermal effects via full finite-temperature EOSs, often in the form of a table [303, 304], and realistic neutrino transport, such as via elaborate moment approximations [305, 306] or Monte Carlo

methods [26]. Many studies perform simulations with multiple finite-temperature EOSs to demonstrate sensitivity (or lack thereof, as the case may be) of BNS merger observables under different scenarios, but the different cold-temperature behavior of each EOS makes it difficult to attribute specific outcomes to finite-temperature behavior [106,293,307–310]. Some studies have explored systematic changes in thermal effects through a so-called "hybrid EOS", which extends a cold nuclear EOS to finite temperatures using an ideal gas component with a fixed adiabatic constant $\Gamma_{\rm th}$ [303, 311]. However, this is only a very rough approximation, as the effective $\Gamma_{\rm th}$ of a full finite-temperature EOS varies considerably with density, temperature, and composition [312]. [313] more recently considered finite-temperature effects through a more sophisticated hybrid EOS based on an approximation to the effective mass, but they do not fully explore how their model affects post-merger GW signals, nor is this approach an entirely self-consistent model. Furthermore, none of these studies incorporate all the relevant physics for modeling thermal effects, particularly consistent neutrino transport.

In this chapter, we present a first GR neutrino-radiation hydrodynamics study of finite-temperature effects of a realistic nuclear EOS on BNS mergers through modifications to the specific heat capacity. Our simulations show that an increased heat capacity results in denser, cooler remnants. This leaves clear imprints on the GW signal in the post-merger phase, which we show can be recovered in a parameter estimation pipeline tuned to a next-generation GW observatory.

## 5.2 Methods

We select three non-relativistic Skyrme-type nucleonic EOSs built with the framework of [314] and parameterized to produce the same cold nuclear matter bulk properties but different specific heat content. In Skyrme EOSs, the specific heat is controlled by the *temperature-independent* effective masses of neutrons and protons, $m_n^*$ and $m_p^*$, respectively. These have a simple phenomenological description [314–316] that depends only on two parameters and on the nucleonic number densities, $n_n$ and $n_p$ (or, alternatively, the number density $n = n_n + n_p$ and the proton fraction $Y_p = n_p/n$ of matter), and converge toward the vacuum nucleon masses at zero density. The parameters were chosen to reproduce two nuclear matter observables at saturation density: the effective mass for symmetric nuclear matter, $m^* = m_n^* \simeq m_p^*$, and the neutron-proton effective mass splitting for pure neutron matter, $\Delta m^*$. Guided by theoretical and experimental efforts [316–319], the selected EOSs probe the average and extreme, but still plausible,

expected values for $m^*$, $m^* = \{0.55, 0.75, 0.95\}\, m_n$, while fixing the yet poorly constrained $\Delta m^*$ to $0.10\, m_n$. The same EOSs were used to study GW signals from core-collapse supernovae [320].

To first order, the baryonic contribution to the specific heat of degenerate matter found in the core of a neutron star, which dominates over the lepton contribution, is $c_v = \left(\frac{\pi}{3}\right)^{2/3} \frac{T}{n} \left(n_p^{1/3} m_p^* + n_n^{1/3} m_n^*\right)$, see Eq. (151) of [315]. Thus, all else being equal, increasing $m^*$ leads to a larger specific heat capacity for matter in the merger remnant, to which we attribute the differences seen across our simulations.

Using the pseudospectral code `LORENE` [321], we construct initial data for equal-mass binary neutron star systems in quasicircular orbit with a gravitational mass of $M = 1.35\ \mathrm{M}_\odot$ per star. We evolve each binary using `THC_M1` [306, 322], an extension of the `WhiskyTHC` numerical relativity code [323, 324] incorporating neutrino transport via a moment formalism [325, 326]. The implementation in `THC_M1` makes use of the Minerbo closure for the radiation pressure tensor, which is exact in the optically thick limit. Thus while our neutrino treatment is approximate overall, we can capture effects such as neutrino trapping and dissipative effects from out-of-equilibrium weak reactions in the BNS remnant exactly. Our runs, while not modeling the magnetic field explicitly, also account for the effects of heating and angular momentum transport from magnetohydrodynamic (MHD) turbulence via a general relativistic large eddy simulation (GRLES) formalism calibrated with high-resolution GRMHD BNS simulations [327–329].

We perform each simulation at two resolutions, designated as LR and SR, respectively corresponding to a grid spacing of $\Delta x \approx 250$ m and $\Delta x \approx 180$ m in the finest refinement level, which covers both stars during the inspiral and merger phases. We also run identical SR simulations with our older M0 solver [330] to validate our results; though the solver is less accurate and does not properly capture effects such as neutrino trapping, these runs support the major results of the M1 runs.

## 5.3 Results

Figures 5.1 and 5.2 show slices of the $x$-$y$ plane for the $m^* = 0.55$ and $m^* = 0.95$ SR simulations at approximately 5 ms post-merger and average temperatures for all three values of $m^*$[1] respectively. Even at this relatively early post-merger time, the density of the remnant's inner core is noticeably larger in the $m^* = 0.95$ model. Conversely, the temperature is lower for the $m^* = 0.95$ compared to the $m^* = 0.55$. The $m^* = 0.75$

[1] Unless otherwise noted, $m^*$ has units of $m_n$, the neutron mass.

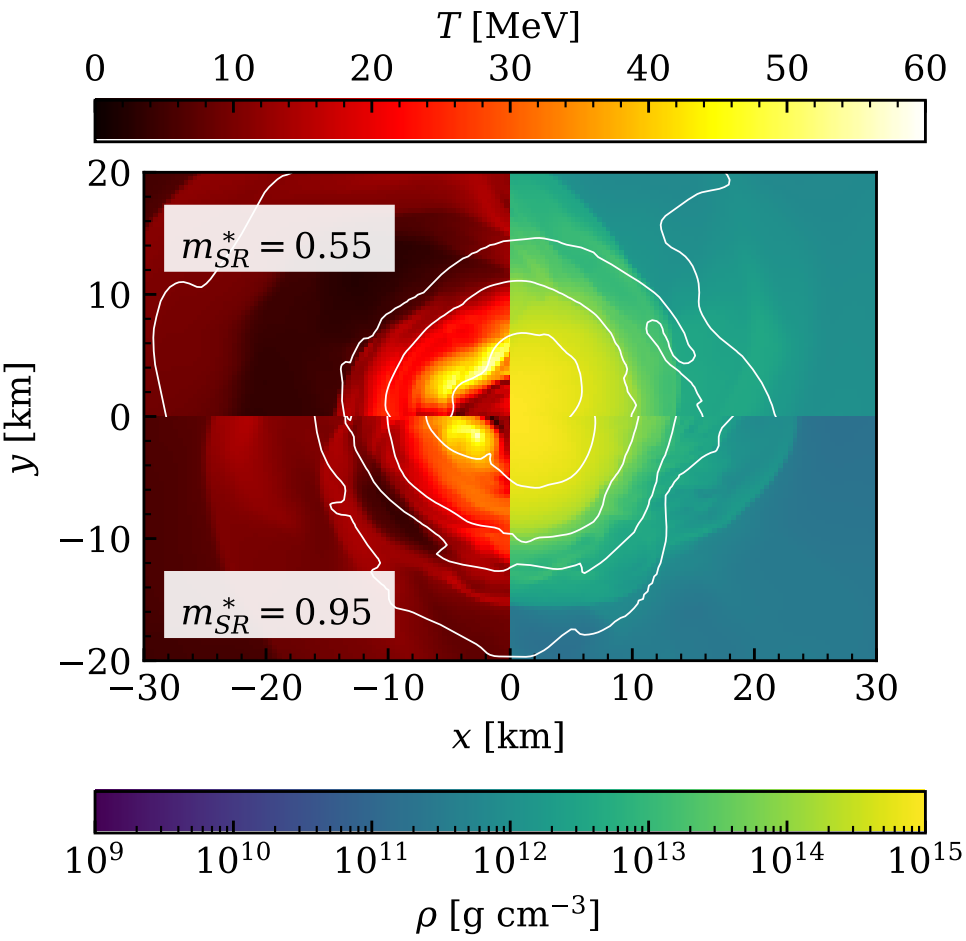


**Figure 5.1.** Temperature and rest-mass density slices in the $x$-$y$ plane of the $m^* = 0.55$ and $m^* = 0.95$ SR simulations at approximately 5 ms post-merger. Contour lines correspond to rest-mass densities $\rho = \{10^{12}, 10^{13}, 10^{14}, 5 \times 10^{14}\}$ g cm$^{-3}$. For visual clarity, the $m^* = 0.75$ model is not shown.

model has an intermediate behaviour compared to the other two. Interestingly, we find that the temperature trend reverses at lower densities (Figure 5.2), possibly because of the larger compactness of the merger remnant in the larger $m^*$ models. In other words, for higher $m^*$, surface material (where the differences between EOS models are much smaller) falls deeper into the gravitational potential, becoming hotter in the process. A similar trend was reported for CCSN simulations [314]. The top panel of Figure 5.3 shows that the maximum rest-mass density is highest in the $m^* = 0.95$ model and lowest for $m^* = 0.55$ at most post-merger times. As suggested in this plot, all of the models, independent of resolution or neutrino treatment, produce long-lived remnants.

The GW strain in Figure 5.3 (bottom panel) demonstrates identical behavior in the

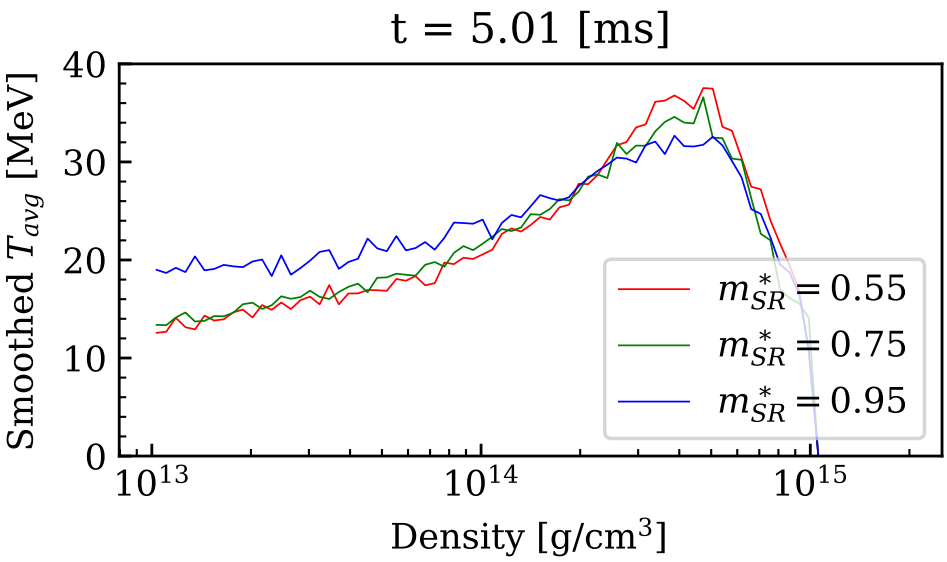


**Figure 5.2.** Average temperature as a function of density.

inspiral for all three models, but the waveforms begin to deviate in the post-merger due to finite-temperature effects in the EOS. The differences in morphology include frequency evolution, amplitude, damping times, and modulations. This is more quantitatively seen in the GW spectrum (see Figure 5.4), where there is a clear rightward shift in the peak postmerger frequency, $f_2$, as $m^*$ increases. Table 5.1 contains $f_2$ for both the LR and SR simulations. Although the precision of the NR waveform is limited by finite resolution and step size, the shift of $\Delta f \gtrsim 10$ Hz is robust across resolutions, which suggests it is an effect of the EOS and not an artifact of the simulations. The M0 SR simulation demonstrates a similar trend, although the $m^* = 0.75$ run is much closer to the $m^* = 0.95$ model than either of the M1 cases. This provides an important sanity check of our results, but we stress that it is only qualitative; the M1 results should be used for quantitative analysis of post-merger effects, as a self-consistent approach which accounts for neutrino trapping noticeably changing the remnant's evolution (see [322]; the appendix also contains a more detailed comparison).

To detect these thermal effects in the postmerger via next-generation GW detectors and possibly constrain the $m^*$ nuclear parameter, we perform full Bayesian inference on the postmerger GW signals. To compute injections, we extract the postmerger waveforms from the SR simulations by applying a Tukey window to suppress the inspiral and spline interpolate the GW waveforms to a sampling rate of 16384 Hz. We further zero pad the signals to a segment of 1 s. For brevity, we consider here only noise-less injections.

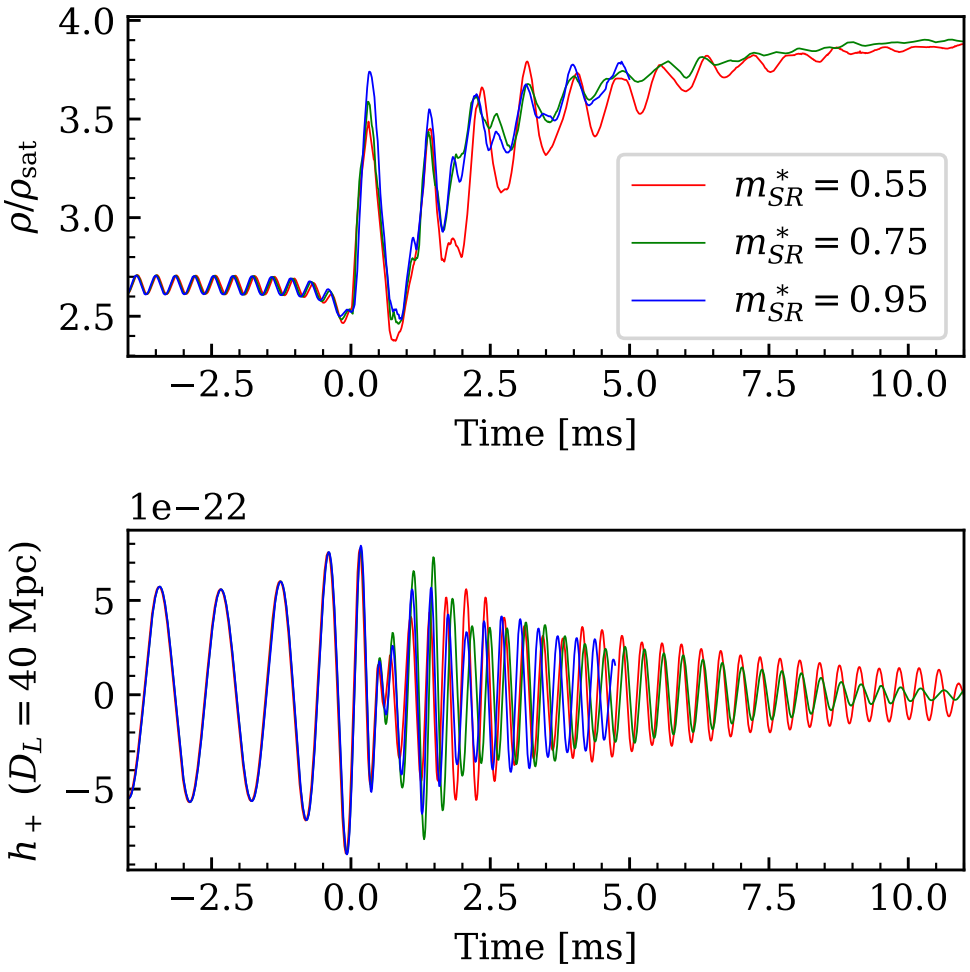


**Figure 5.3.** The maximum rest-mass density of the SR simulations (top) and the the gravitational-wave strain of the $\ell = 2$, $m = 2$ mode (bottom).

For parameter estimation, we employ the publicly available code `bajes` [331] and use the `UltraNest` [332] sampler available as part of the `bajes` pipeline. We recover the injections by using the postmerger model `NRPMw` from [284] and compute posteriors on its parameters. We inject all signals at a luminosity distance corresponding to a post-merger SNR of 15 (which corresponds to an inspiral SNR of $\mathcal{O}(100)$, see [300]), assuming the power spectral density of ET-D [333] to simulate the detector response. The priors are set in accordance to [334], section-IIB. In Figure 5.4, we show the reconstructed waveforms from `NRPMw` evaluated on the parameter space of the recovered posterior samples. We list the recovered SNRs and $f_2$ values in Table 5.1. At SNR = 15, the injected spectrum's $f_2$ frequencies sit well within the 90% credible intervals of the distribution of reconstructed waveform's $f_2$ frequencies. Furthermore, these intervals do not overlap, indicating that

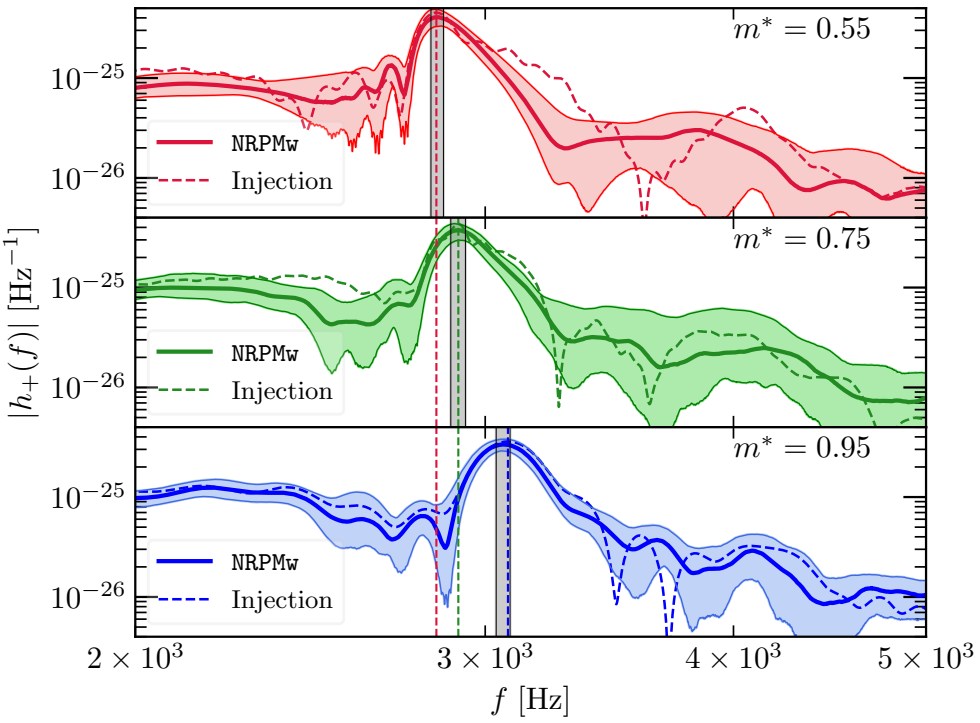


**Figure 5.4.** The reconstructed GW spectrum of the $\ell = 2$, $m = 2$ mode using the `NRPMw` model. The colored solid lines represent the median waveform and the colored shaded regions represent the 90% credible intervals on the posterior distribution of the spectra computed from the recovered parameter space of `NRPMw`. The colored dashed limes represent the injected spectra at an SNR of 15. Additionally, shown are the postmerger peak frequencies $f_2$ (in vertical dashed lines) and the 90% credible intervals (in grey) on the posterior distribution of $f_2$ from the reconstructed waveforms.

all three waveforms are clearly distinguishable at a post-merger SNR = 15 with 90% credibility.

## 5.4 Discussion

We have shown that $m^*$ significantly influences the GW signals in BNS mergers, and we have analyzed this effect in detail for $f_2$. The relationship between $m^*$ and $f_2$ is easily explained in terms of the specific heat. Increasing the specific heat appears to soften the equation of state; because it requires more energy to increase the temperature, there is less thermal pressure available to support the star, thus producing a more rapidly rotating and compact remnant with lower temperatures, in agreement with core-collapse supernovae studies [314, 320, 337].

The EOSs we use have a simple relationship between $m^*$ and the specific heat capacity

**Table 5.1.** Peak post-merger frequencies ($f_2$) of the gravitational wave spectrum for the LR (M1), M0, and SR (M1) simulations and the NRPMw model. For reference, the recovered matched-filter SNR values and corresponding luminosity distance $D_L$ are also provided. For consistency, all peaks are measured after suppressing the inspiral. We also provide the mismatch, $\mathcal{M}$ (see [335, 336]), between the $f_2^{\rm SR}$ runs, with one row measured against $m^* = 0.75$ and the other against $m^* = 0.95$.

| $m^*$ $[m_n]$ | $f_2^{\rm LR}$ [kHz] | $f_2^{\rm M0}$ [kHz] | $f_2^{\rm SR}$ [kHz] | $\mathcal{M}^{\rm SR}_{0.75}$ | $\mathcal{M}^{\rm SR}_{0.95}$ | $f_2^{\texttt{NRPMw}}$ [kHz] | $\rm SNR_{mf}$ | $D_L$ |
|---|---|---|---|---|---|---|---|---|
| 0.55 | 2.862 | 2.864 | 2.835 | 0.04 | 0.09 | $2.83^{+0.02}_{-0.02}$ | $13.6^{+1.6}_{-2.7}$ | 56.353 |
| 0.75 | 2.908 | 2.966 | 2.908 | N/A | 0.08 | $2.91^{+0.02}_{-0.02}$ | $13.4^{+1.6}_{-2.5}$ | 56.730 |
| 0.95 | 2.921 | 2.974 | 3.080 | 0.08 | N/A | $3.06^{+0.02}_{-0.02}$ | $13.8^{+1.8}_{-2.2}$ | 49.655 |

which may not be representative of the true nuclear EOS, which is expected to be both density and temperature dependent [312]. Nevertheless, this study serves as a proof of concept demonstrating that future detectors like ET and CE can use $f_2$ to constrain the finite-temperature EOS. We also reiterate that this effect *only* affects the finite-temperature evolution, which will not be observable until next-generation detectors sensitive to the post-merger phase come online. Furthermore, we also note that this study does not provide a method for measuring $m^*$ from $f_2$; we only assert that $m^*$ leaves an imprint on $f_2$.

We do acknowledge some limitations in our work; most notably, the length of the $m^* = 0.95$ M1 simulation is much shorter than both the $m^* = 0.55$ and $m^* = 0.75$ runs due to a limitation in the M1 neutrino solver which introduced unphysical effects past 5 ms post-merger. This short length may explain why $f_2^{m^*=0.95}$ increases between the LR and SR runs while both $f_2^{m^*=0.55}$ and $f_2^{m^*=0.75}$ instead decrease, as a shorter signal will introduce a extra spread of frequencies to the power spectrum and possibly shift the peak. Another possible limitation concerns the omission of magnetic fields. Our simulations include a GRLES model which can account for some, but not all MHD effects. On the other hand, other simulations suggest that MHD effects on the post-merger gravitational wave frequency are negligible for realistic initial magnetic field strengths [338].

We may consider several avenues for future work. Longer simulations would allow us to investigate the ejecta and consider possible effects on EM counterparts, as well as possible thermal effects on the lifetime of the remnants. Additionally, [322] indicate that resolution has a prominent influence on post-merger evolution, including collapse time and disk formation. Although we validate our results here with two resolutions, accurately determining the precise value of $f_2$ for each model would require higher resolution calculations. To investigate our hypothesis that this study's results are general, future simulations could also explore other EOS models with tunable finite-temperature behavior.

## 5.5 Appendix 1: Neutrino Effects

The presence of a trapped neutrino gas in optically-thick regions can affect the temperature and composition of the remnant [106, 322]. Many BNS simulations today employ leakage schemes, which do not explicitly model neutrino radiation, but instead estimate a cooling rate based on the local optical depth [304, 307, 330, 339, 340]. Because they do not perform consistent radiation transport, leakage schemes cannot capture the trapped

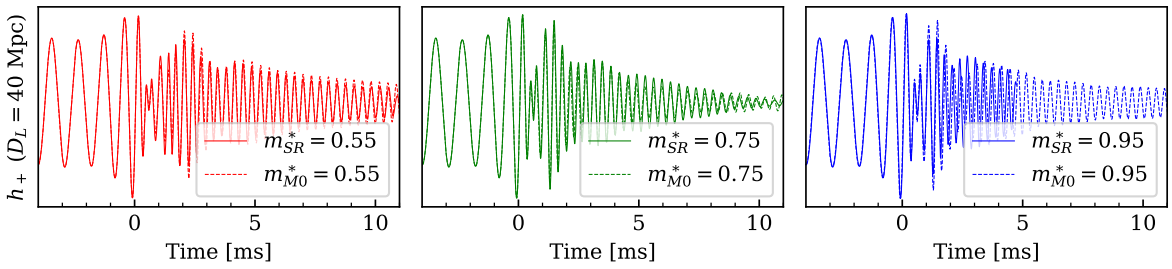


**Figure 5.5.** The GW strain of the $\ell = 2$, $m = 2$ mode at $D_L = 40$ Mpc for both the M1 (solid lines) and M0 (dashed lines) SR simulations.

neutrino gas in the remnant or potential out-of-equilibrium effects. The more accurate M1 scheme, however, directly models neutrino transport and can therefore capture both these effects [306, 322]. Because our study represents the first investigation of thermal effects in BNS mergers with self-consistent neutrino transport, we will demonstrate here the influence of neutrinos on our results by comparing our M0 (a leakage-style scheme) simulations to our M1 runs.

In Fig. 5.5, we show the GW strain for both the M0 and M1 simulations. All three values of $m^*$ show identical behavior in the inspiral, which is to be expected; neutrinos emissions are highly sensitive to the temperature, which is quite low prior to merger. In the post-merger signal, the $m^* = 0.55$ and $m^* = 0.75$ differ only very slightly in amplitude and frequency. The $m^* = 0.95$ runs show somewhat stronger deviations but are still quite similar in overall morphology. Nevertheless, the shifts in $f_2$ (see Table I in the main text) for changes in the neutrino solver are within a factor of two or three of the shifts due to changing $m^*$; were these results used to calibrate some model for determining $m^*$ from $f_2$, it may result in a fairly significant error.

In Fig. 5.6, we show the average temperature as a function of density at 5 ms post-merger for both the M0 and M1 SR simulations. We calculate this temperature by constructing two-dimensional histograms in temperature and density, then performing a weighted average over the temperature for each density bin. This data is smoothed by averaging five time steps centered around 5 ms. The M1 data demonstrates a clear trend at higher densities ($\rho \gtrsim \rho_{\rm sat}$) where higher values of $m^*$ lead to lower temperatures, and there is limited evidence suggesting an inverted trend in the outer layers of the star ($\rho \lesssim \rho_{\rm sat}$), a result which is consistent with core-collapse supernovae simulations [314]. One possible explanation is due to the increased compactness for higher $m^*$; material near the surface (where the density is low enough that $m^*$ has a much weaker effect on the EOS) falls deeper into the gravitational potential and heats up more as $m^*$ increases.

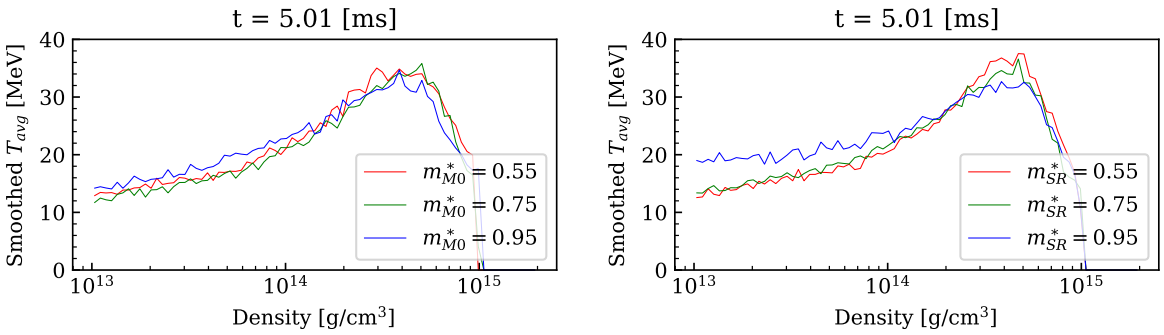


**Figure 5.6.** The average temperature as a function of density at $t \approx 5$ ms post-merger for the M0 (left) and M1 (right) SR simulations. Each average was calculated by constructing two-dimensional histograms in temperature and density, then averaging over the temperature with a weight corresponding to the mass of each density-temperature bin. To reduce noise in the data, five equally-spaced timesteps (with $\Delta t \approx 0.05$ ms) centered on $t \approx 5$ ms were averaged together.

However, the high-density trend is obscured in the M0 data, and there is no evidence of the low-density trend, as the $m^* = 0.55$ temperature is often higher than the $m^* = 0.75$ temperature at lower densities (where the M0 scheme suppresses neutrino absorption).

In weak equilibrium

$$\mu_{\nu_e} = \mu_p + \mu_e - \mu_n, \tag{5.1}$$

where $\mu_i$ is the chemical potential for particle species $i$, with $p$, $e$, $n$, and $\nu_e$ respectively representing the proton, electron, neutron, and electron neutrino.

On the other hand, for a trapped neutrino gas in thermal equilibrium with the nucleonic matter of density $\rho$, temperature $T$, and electron fraction $Y_e$, we have

$$Y_{\nu_i} = \frac{4\pi m_b}{\rho}\left(\frac{k_\mathrm{B}T}{hc}\right)^3 F_2\left(\frac{\mu_{\nu_i}}{k_\mathrm{B}T}\right), \tag{5.2}$$

where $m_b$ is the average baryon mass and $F_i(x)$ is the $i^{\text{th}}$ Fermi function. This is essentially a restatement of the fact that trapped neutrinos in thermal equilibrium can be treated as a massless (i.e. in the ultrarelativistic limit) ideal Fermi gas (see section 1.2.4.3). This suggests that one can monitor the deviation from equilibrium by calculating the quantity

$$\Delta\mu_{\nu_e} = \mu_p + \mu_e - \mu_n - \mu^T_{\nu_e}, \tag{5.3}$$

where $\mu^T_{\nu_e}$ is $\mu_{\nu_e}$ calculated under the assumption of thermal equilibrium (Eq. 5.2) using the evolved neutrino fractions from M1. For M0 this quantity should be set to zero,

as the trapped neutrino gas is not explicitly modeled. We plot this deviation for $\nu_e$ in Fig. 5.7. M0 shows noticeable deviations from weak equilibrium throughout the bulk of the remnant. This shows that the M0 simulations are not correctly capturing the thermal equilibrium of matter. On the other hand, the M1 simulations show that matter and neutrinos are in equilibrium in most regions in the remnant. We therefore conclude that a proper investigation of thermal effects must include full neutrino transport.

## 5.6 Declaration

While this manuscript was under review, [341] announced new results on the impact of thermal effects on $f_2$. Their work uses a semi-analytic prescription for the EOS and neglects neutrinos, but it is in good agreement with our findings.

The GRHD neutrino-radiation transport simulations were computed by Jacob Fields and the postmerger GW detectability analysis was computed by myself. This chapter will also form a part of Jacob Field's dissertation. In accordance with the terms of the Creative Commons CC BY 4.0 license, the contents of this chapter are based on the publication 'Thermal Effects in Binary Neutron Star Mergers', published in Astrophysical Journal Letters, Volume 952, number 2, pages L36 [342] with the modification that every occurence of the term 'letter' has been replaced with 'chapter'.

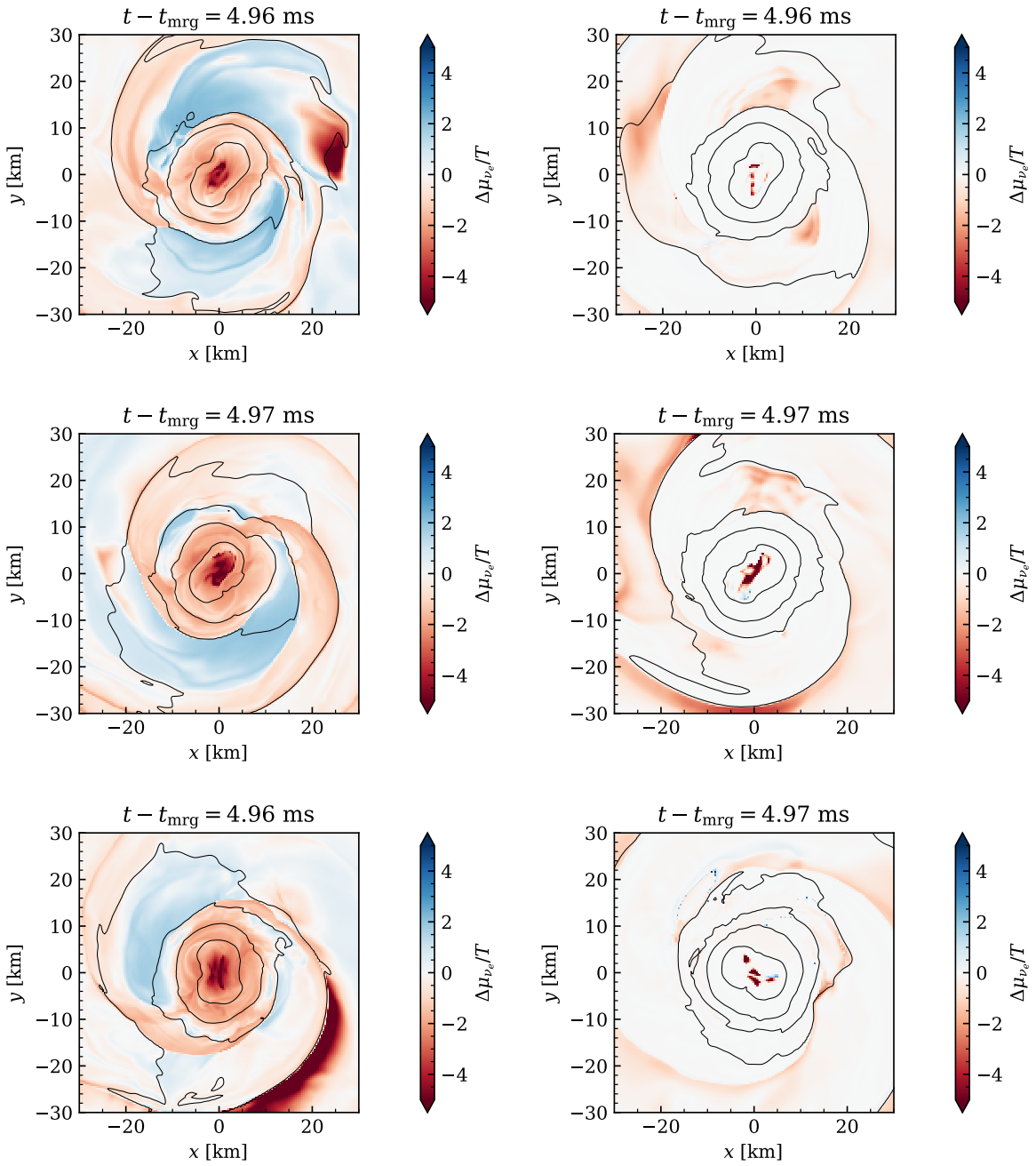


**Figure 5.7.** The deviation from weak equilibrium $\Delta\mu_{\nu_e}/T$ between M0 (left) and M1 (right) for $m^* = 0.55$ (top), $m^* = 0.75$ (middle), and $m^* = 0.95$ (bottom) at $t \approx 5$ ms. The contour lines correspond to the rest-mass densities $\rho = \{10^{12}, 10^{13}, 10^{14}, 5 \times 10^{14}\}$ g cm$^{-3}$.

# Part II

# Gravitational Wave Detectability

# Chapter 6
# Detectability of QCD Phase Transitions in neutron star mergers

## 6.1 Introduction

The discoveries of the gravitational wave (GW) event GW170817 [218] from a merger of two neutron stars, the associated short gamma ray burst GRB170817A and the optical transient AT2017gfo [343], revitalized the field of multimessenger astronomy. It is now possible to probe high-energy astrophysical phenomena through their GW signatures in addition to electromagnetic radiation. The emitted GW spectra from a merger of two neutron stars spans a broad range of frequencies. GWs from an inspiral (at frequencies $\lesssim 10^3$ Hz) signal provide a wealth of information about the intrinsic properties of a binary such as its component masses and tidal deformabilities. On the other hand, postmerger GW emission (at frequencies $\gtrsim 10^3$ Hz) can inform us about the dynamically evolving merger remnant. No postmerger signal from GW170817 was detected thereby leaving to speculation the fate of the remnant. We encourage the reader to refer to refs. [148, 344] for recent reviews.

With the upcoming generation of GW detectors like the Einstein Telescope (ET) [189, 333] or the Cosmic Explorer (CE) [182, 188, 345, 346], it is expected that the postmerger phase of evolution will be within reach of detector sensitivities [347, 348]. This would imply observational constraints on the physical processes in neutron star mergers, particularly the ones arising in the postmerger. The postmerger emission is characterized by GWs emitted in the kilohertz regime from the dynamically ($\mathcal{O} \sim 10^{-3}$ s) changing quadrupolar moment of the merger remnant. Changes in the quadrupolar moment depend strongly on the underlying equation of state (EOS) which describes the thermodynamic equilibrium state of matter in the neutron star bulk. EOSs may involve a multitude of

physical processes like temperature dependent effects [32, 106, 342, 349, 350], neutrino interactions and microphysics [21, 23–25, 28, 224, 229–241], appearance of hyperons [19, 20], and high-density phase transitions [3, 19, 20, 52–57, 159, 177, 184, 185, 226, 349, 351–355] which can leave imprints on the postmerger emission. Additionally, magnetic fields and magnetohydrodynamic turbulence [122, 242–244, 356] may influence the postmerger emission by redistributing the angular momentum in the remnant.

In recent years, there has been a significant impetus in understanding the behavior of supranuclear ($> 2.7 \times 10^{14}$ g cm$^{-3}$) matter expected to be realized in and around the core of heavy neutron stars, neutron star merger remnants or core collapse supernovae. Processes like a possible phase transition to deconfined quark matter or the appearance of hyperons have garnered particular interest in reference to binary neutron star (BNS) mergers as they are expected to influence the postmerger GW emission from a merger remnant which in turn can provide excellent test beds for probing strongly-interacting matter. Modelling efforts in this direction typically involve comparing GW emission from a nucleonic EOS to that computed from an EOS that has additional degrees of freedom. In this regard, the works by Sekiguchi et al. [19] and Radice et al. [20] explored the appearance of hyperons in a BNS merger and reported on their effects on the postmerger GW signal, i.e., a compactification of the merger remnant leading to shorter postmerger signals as compared to models without hyperons.

Most et al. [52, 53] considered a first order phase transition to deconfined quarks and obtained similar results for the postmerger GW emission along with a small dephasing. The works by Bauswein et al. [54, 55] identified large shifts (30-121 Hz) in the postmerger peak frequency (which we call $f_2^{\rm peak}$ in this work) of their quark models as compared to their hadronic models. They claimed that sufficiently large shifts in $f_2^{\rm peak}$, breaking the degeneracy of EOS-insensitive relations, could be a tell-tale sign of first order phase transitions. Extending this work, Blacker et al. [57] attempted to constrain the onset density of such phase transitions. In another work Blacker et al. [349] disentangled and explored the thermodynamics of deconfined quark matter with respect to BNS mergers. Weih et al. [56] reported on double-peaked frequency spectra as a signature of a delayed phase transition that resulted in a metastable hypermassive neutron star (HMNS). Studies by Prakash et al. [159] however, found no smoking-gun evidences of GW signatures and observed shifts in postmerger peak frequency that were degenerate with other hadronic EOSs. They also computed potential electromagnetic signatures of these phase transitions. Liebling et al. [3] computed similar postmerger GW signatures and observed changes in the magnetic field topology in the bulk of the

star. In contrast to modelling 1$^{st}$ order phase transitions, refs. [184, 351, 352] explored such deconfinement processes via a quark-hadron crossover (QHC) by constraining the $f_2^{peak}$ and chirp frequencies. In this regard, Fujimoto et al. [177] have compared GW signatures arising from a 1$^{st}$ order phase transition with those from a QHC and show the results from the QHC scenario to be consistent with electromagnetic counterparts observed from GW170817.

More recently, there have been efforts [185, 353] to employ the novel holographic V-QCD framework to construct EOSs with a deconfinement phase transition and compute their GW signals. Consistent with previous works, an early collapse for softer EOSs is observed. Espino et al. [226], for the first time, investigated multi-modal signatures of deconfinement phase transitions and reported on a weakening of the one-armed spiral instability that increased with the strength of the phase transition. Guo et al. [354] contrasted the GW signatures between EOSs that modelled such phase transitions via a Maxwell construction, a Gibbs construction and a QHC and showed that lower phase transition densities lead to more compact remnants that collapse into a black hole. In a parallel study, Haque et al. [355] varied the onset density of the phase transition and examined its impact on the postmerger GW frequency.

Both pre-merger (late inspiral) and postmerger phases of a BNS evolution can provide useful information with reference to phase transitions to deconfined quarks. Extensive efforts by several groups have gone into modelling the postmerger GW emission [60,64,284,357–361]. Chatziioannou et al. [362] and Wijngaarden et al. [363] employ model independent inference via `Bayeswave` to resconstruct the postmerger signals while using NR calibrated compact binary coalescence templates for the inspiral. While this kind of a hybrid model-agnostic approach does indeed offer more flexibility towards modelling particular waveform morphologies as compared to analytical models, an absence of a model implies no way for a likelihood computation and hence a comparison using Bayes' factors or odd's ratios to other approaches cannot be made. On the other hand, Tsang et al. [361] and Easter et al. [359] employed damped sinusoidal models to describe the postmerger emission. Breschi et al. [64, 284] constructed analytic models of postmerger emission which were calibrated by numerical relativity simulations. Subsequently, these models were employed in refs. [64, 334, 364] to potentially detect EOS softening via the production of $\Lambda$ hyperons. In particular, Breschi et al. [334] recovered differences in the postmerger peak frequency and remnant lifetimes to constrain the said effects in a BNS merger. In yet another recent work, Harada et al. [365] employ Bayesian model selection to distinguish between models that respectively include and exclude a smooth crossover

to a deconfined quark phase during the postmerger evolution.

To complement the above mentioned postmerger studies, there have also been several efforts to constrain nuclear properties of high-density matter using the late inspiral phase of a binary merger [362, 366–369]. In particular, Mondal et al. [370] employed a phenomenological meta-modelling approach to the EOSs and constrained QCD phase transitions via measurements of tidal parameters. Essick et al. [369] constructed non-parametric representations of EOSs and attempted to infer an onset of QCD phase transitions from the EOS itself. Raithel et al. [368] have examined the impact of phase transition on an inference of tidal deformability using inspiral GW signals and have found degeneracies between the EOS with phase transition and that with hadrons while keeping the tidal deformability constant. Raithel et al. [371] also present an interesting case of "tidal deformability doppelgängers" where they employ quark EOSs with differences in pressure at nuclear saturation but which predict tidal parameters consistent with that of exclusively hadronic EOSs. Pang et al. [372] have computed Bayes factors of binary mergers with and without a phase transition while also considering the strength of phase transitions as a paremeter for Bayesian inference.

While most of the works discussed above remark that such deconfinement phase transitions (and EOS softening effects in general) are potentially detectable, the refs. [64, 334, 352, 357, 359, 363, 364, 369, 370, 372] pave a concrete path in defining an observational strategy to observe their effects with kilohertz gravitational waves.

It has been shown from NR simulations of neutron star binaries [3, 59–63, 113, 124, 125] that there exists a correlation between the $f_2^{\rm peak}$ frequency of the postmerger and an inspiral property of the binary, e.g. a suitable combination of tidal parameters from the inspiral, the radius of a neutron star of a fixed mass or the compactness of a neutron star. Such relations are insensitive to the EOS and are also referred to as quasi universal relations (QURs). Indeed, such relations have been employed to construct analytical waveform models [64, 284]. Several works [54, 55] claim that a violation of a universal relation between $f_2^{\rm peak}$ and the tidal deformability of a $1.35M_\odot$ neutron star ($\Lambda_{1.35}$) can be taken to be a smoking-gun evidence of QCD phase transitions. Wijngaarden et al. [363] even demonstrate that Bayesian error estimates for a joint detection of $f_2^{\rm peak}$ and $\tilde{\Lambda}$ at sufficiently high signal to noise ratios (SNRs) can be distinguished from the established QURs. At the same time, Breschi et al. in ref. [364] perform a pre-postmerger consistency test and show that a breaking of an EOS insensitive relation between $f_2^{\rm peak}$ and tidal polarizability $\kappa_2^T$ to a given confidence level cannot be taken to be a confident signature of the softening of the EOS. In this work, we place our calculations in the context of

previous findings by applying error estimates from Bayesian inference to NR simulations.

We utilize Bayesian inference on the inspiral and postmerger signals to recover estimates on tidal properties and postmerger spectra respectively. We then use these estimates in reference to the universal relation by Breschi et al. [284] to show a potential detectability of QCD phase transitions at postmerger SNRs as low as 10. To this aim, we employ composition-dependent, finite-temperature EOSs describing the high-density behavior of strongly interacting matter and compute the postmerger GW emission of a BNS merger remnant. We employ the frequency domain waveform model `NRPMw` developed by Breschi et al. [284] to recover the spectra of the said NR waveforms assuming sensitivities of the next generation GW detectors. This chapter is organized as follows: in subsection 6.2.1, we describe the NR simulations used in this work. In subsection 6.2.2, we comment upon the procedure employed to create postmerger injections from our NR dataset. Following this in subsection 6.2.3, we briefly recapitulate the methodology for Bayesian inference of parameters given an analytic BNS waveform model. Finally in subsection 6.2.4, we describe two choices of priors employed in our work which are respectively informed and agnostic of the inspiral signal. We present our results in section 6.3 where we classify our (postmerger) parameter estimation (PE) analysis in two categories with different choices of priors. Primarily in subsection 6.3.1, we take inspiral-informed Gaussian priors on masses and tidal parameters for the postmerger. Secondarily, we present a test case in Appendix 6.5 wherein we assume broad priors for the postmerger model `NRPMw`'s parameters and perform an inspiral-agnostic PE. In subsection 6.3.2, we repeat the postmerger analysis with the CE detectors: the broadband CE-40 and the narrowband postmerger optimized CE-20. In subsection 6.3.3, we use an NR informed EOS insensitive relation to probe phase transitions at a given postmerger SNR. Finally, we conclude the chapter in section 6.4. In the appendices, we provide results for all our simulations as well as a miscellany of supplemental results. In appendices 6.5 and 6.6, we provide results for the entire simulation dataset. Finally, in appendix 6.7, we provide results from a flexible configuration of the `NRPMw` model aimed at addressing some of the biases encountered in recovering hadronic models.

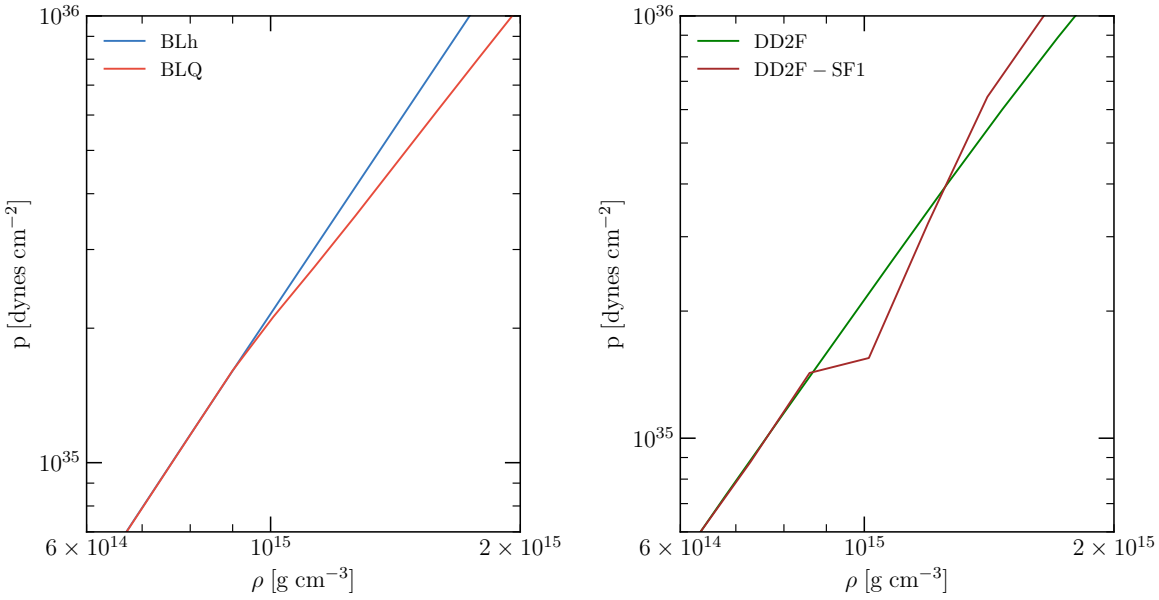


**Figure 6.1.** Pressure - density curves for the $T = 0$ (zero temperature) slice of the equations of state (EOSs) used in this work. BLh and DD2F EOSs contain only nucleonic degrees of freedom whereas BLQ and DD2F-SF1 also include a prescription for a $1^{\text{st}}$ order phase transition to deconfined quarks. Such a phase transition leads to a loss of pressure at high densities $\rho \sim 10^{15}$g cm$^{-3}$.

## 6.2 Methods

### 6.2.1 NR Simulations

We summarize the NR simulations used in this work in Table 6.1. Our dataset primarily consists of BNS merger simulations with hadronic and quark EOSs presented in ref. [159]. We also perform merger simulations with two additional EOSs DD2F [373, 374] and DD2F-SF1 [54, 58, 375] to include effects from different treatments of strongly-interacting matter. The mergers we consider produce remnants that do not collapse promptly and result in a finite postmerger GW signal (see Table 6.1). We employ the numerical infrastructure in ref. [159] and references therein for all our NR simulations. In particular, we solve the equations of General Relativistic Hydrodynamics (GRHD) in the 3+1 Valencia Formulation [16] using the publicly available code `WhiskyTHC` [87–89]. We employ the `CTGamma` [92, 93] code available as part of the `EinsteinToolkit` [277] to solve for the spacetime in the Z4c formulation [90, 91] of the Einstein's equations. We use the `WeylScal4` and `Multipole` thorns to compute the spin $s = -2$ weighted spherical harmonics of the Newman-Penrose scalar $\Psi_4$, from which we extract the GW strain of

the $\ell = 2, m = 2$ mode. Additionally, we employ a zeroth moment M0 scheme [23] to solve for the neutrino energies and neutrino number densities. We construct initial data assuming irrotational binaries in quasi-circular orbits using the pseudo spectral code `Lorene` [101]. The binaries are situated at an initial separation of 45 km (30.47 $M_\odot$). Finally, we employ the `Carpet` [95, 96] code for providing the adaptive mesh refinement (AMR) infrastructure.

To probe multiple possibilities in the high-density regime of QCD, we take a selection of 4 finite-temperature EOSs namely BLh [71,78], DD2F [373,374], BLQ [108,159,176,334] and DD2F-SF1 [54, 58]. For these EOSs, the pressure-density curves at 0 temperature are shown in Fig. 6.1. Of these, the BLh and DD2F EOSs contain only nucleonic degrees of freedom whereas the BLQ and DD2F-SF1 EOSs implement a first order phase transition to deconfined quark matter while having the same low-density behavior as the BLh and DD2F EOSs, respectively. The BLQ EOS employs a Gibbs construction to combine the hadronic and quark phases resulting in a mixed phase of deconfined quarks and hadrons. There is a gradual increase in the percentage of deconfined quarks with non-zero temperatures and densities $\gtrsim 3\rho_{\rm nuc}$ where $\rho_{\rm nuc} = 2.7 \times 10^{14}$g cm$^{-3}$ is the nuclear saturation density. The DD2F-SF1 EOS on the other hand employs a Maxwell construction that allows for a less gradual transition to the deconfined quark phase as compared to the BLQ EOS.

As previously found in Bauswein et al. [54], the BNS models evolved with the DD2F-SF family of EOSs display large deviations from the EOS insensitive relation between the postmerger peak frequency $f_2^{\rm peak}$ and tidal deformability $\Lambda$. On the other hand, models with the BLQ EOS [159] predict postmerger peak frequencies that are within range of those spanned by hadronic EOSs and obey the $f_2^{\rm peak} - \kappa_2^T$ relation obtained in ref. [64] where $\kappa_2^T$ is the tidal polarizability defined in the same reference. It is important to emphasize that the EOS insensitive relation obtained and the simulation setup employed in ref. [54] is not the same as the one used in ref. [64]. Therefore, for consistent comparison, we performed simulations with the DD2F-SF1 EOS with our GRHD infrastructure and find that models with this EOS also display large deviations with the $f_2^{\rm peak} - \kappa_2^T$ relation. We also note that the simulations presented in our work are computed in full general relativity (GR) whereas the ones from Bauswein et al. [54] consider a conformal flatness condition to solve for the Einstein's equations.

Additionally, we consider unequal mass mergers for the BLh and BLQ EOSs to account for the impact of mass ratios. With this diversity in the choice of EOSs and the masses of BNS mergers, our study provides reasonable estimates of the GW detectability

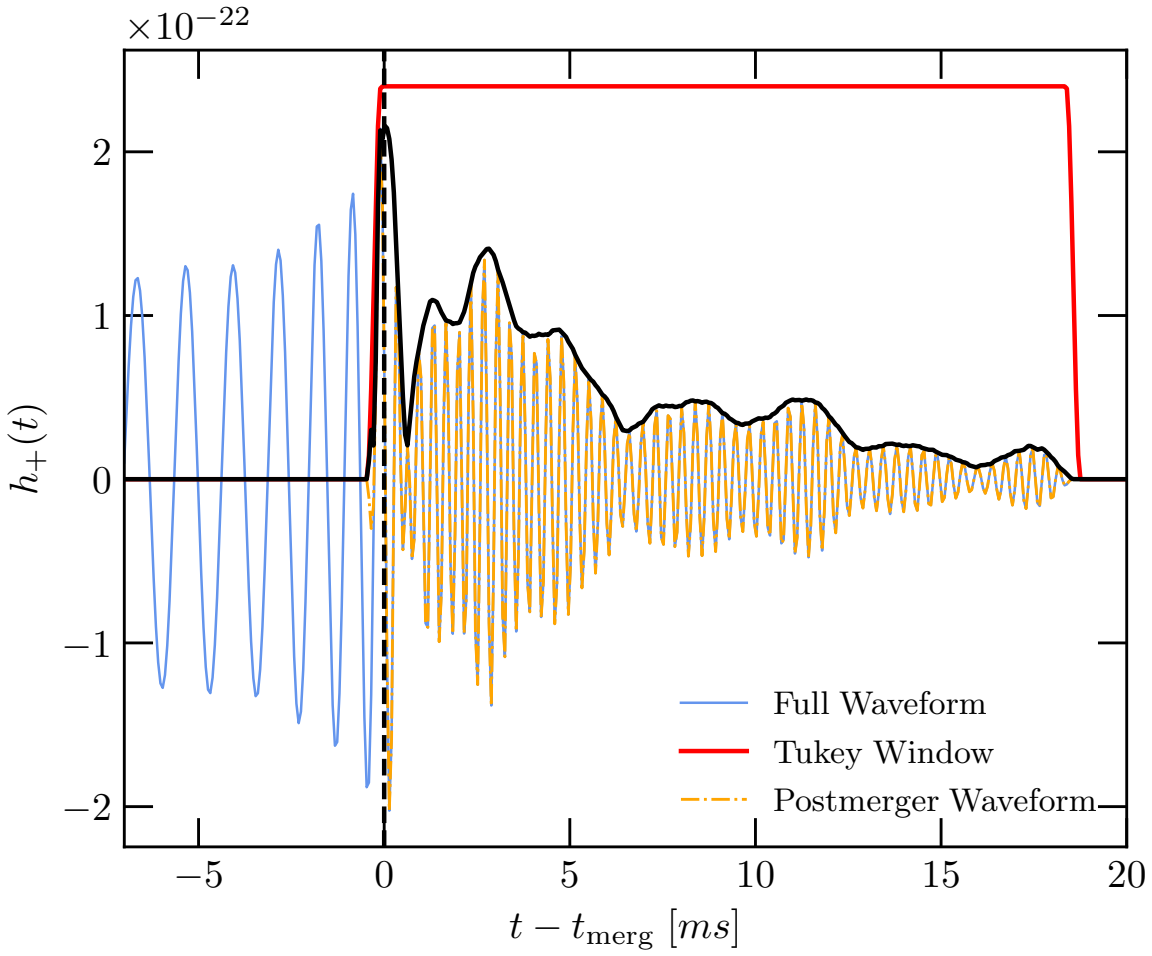


**Figure 6.2.** Extraction of the postmerger waveform from an NR waveform by applying a Tukey window. This windowed waveform upon spline interpolation and zero-padding is then injected in a noise-less configuration of the ET/CE detectors for parameter estimation using `NRPMw`.

of QCD phase transitions in BNS mergers. In addition to that, we would like to remark here that even though the waveform model `NRPMw` is trained on a large number of NR simulations spanning 21 EOSs, simulations with DD2F and DD2F-SF1 EOSs have not been utilized for training the model and therefore validate the model's performance.

### 6.2.2 Injection Settings

In this section, we describe the procedure for constructing postmerger injections from our NR simulations for a Bayesian inference study. In particular, we scale the GW strain obtained from NR simulations and introduce it in a data stream which serves to simulate

the incoming GW in a detector. To compute the $\ell = 2, m = 2$ GW strain output from the NR simulations, we first evaluate the Newman-Penrose scalar $\Psi_4$ on coordinate spheres in a multi-polar spherical harmonic basis. This scalar (for the $\ell = 2, m = 2$ mode) is then integrated twice in time using fixed frequency integration [280] to obtain the quadrupolar strain $h_+$ and $h_\times$. Fixed frequency integration also helps remove secular drifts in the strain amplitude that may arise because of direct integration of $\Psi_4$.

We define the time of merger $t_{\rm merg}$ as the time when the GW amplitude of the $\ell = 2,\ m = 2$ mode, i.e., $(h_+^2 + h_\times^2)^{1/2}$ is maximum. We construct the injections by considering only the postmerger portion of the NR waveform starting from $t_{\rm merg}$ up until the termination of the waveform. For the remnants that collapse into a black hole (BH), we define a time of BH formation $t_{\rm BH}$ (Table 6.1) as the time when the minimum value of the lapse function in the computational grid drops below 0.2 which approximately corresponds to the formation of an apparent horizon for remnants resulting from a merger of non-spinning binaries. This definition of the collapse of a remnant has been motivated from reference [79] and employed in works like [108, 159, 279]. We extract the postmerger signal ($t > t_{\rm merg}$) by employing a Tukey window [376] available as part of the `scipy` library. In particular, we use a windowing ansatz $w$ of the form

$$w(t, t_0, t_1, \delta) = \begin{cases} 0 \ \text{ if } t < t_0 \\ \tau(t, \delta) \ \text{ if } t \in [t_0, t_1] \\ 0 \ \text{ if } t > t_1 \end{cases} \tag{6.1}$$

where $\tau$ denotes the standard Tukey window of width $|t_1 - t_0|$ and a shape parameter $\delta$ that controls the fraction of the window inside the tapered region. Furthermore, we spline interpolate the waveforms to a sampling rate of 16,384 Hz and zero pad them to a signal segment of 1 s, as shown in Fig. 6.2. To systematically disentangle the effects of QCD phase transitions on the GW strain from the effects of detector noise, we construct noise-less injections. The posteriors on model parameters recovered in such a noise-less configuration approximate the average over those recovered from multiple Gaussian noise realizations. Finally, we scale the waveforms by a factor of the inverse luminosity distance $D_L^{-1}$ and the spin $s = -2$ weighted spherical harmonics ${}_{-2}Y_{2,2}(\iota = 0, \psi = 0)$ for a face-on configuration to consistently maintain a postmerger SNR of 10 in the ET detector network or in the CE-20 detector. This corresponds to placing each BNS system at different luminosity distances with respect to the detector as described in tables 6.4 and 6.5.

**Table 6.1.** A summary of NR simulations employed in this work. The corresponding postmerger waveforms are used in the construction of injections for the next generation GW detectors and for the subsequent Bayesian inference. EOS represents the equation of state, $m_1$ and $m_2$ the gravitational masses of the binary ($m_1 > m_2$), $q$ the mass ratio, $\Lambda_i$s the tidal deformabilities and $t_{\rm BH}$ the time of black hole formation expressed relative to the time of merger $t_{\rm merg}$. The acronym HMNS represents a hypermassive neutron star remnant that doesn't collapse within the simulation timescale.

| EOS | $m_1\ [M_\odot]$ | $m_2\ [M_\odot]$ | $q$ | $\Lambda_1$ | $\Lambda_2$ | $t_{\rm BH} - t_{\rm merg}$ [ms] |
|---|---|---|---|---|---|---|
| BLh | 1.298 | 1.298 | 1.0 | 701.901 | 701.901 | HMNS |
| BLQ | 1.298 | 1.298 | 1.0 | 701.901 | 701.901 | 15.95 |
| BLh | 1.481 | 1.257 | 1.178 | 295.467 | 856.064 | HMNS |
| BLQ | 1.481 | 1.257 | 1.178 | 295.467 | 856.064 | 3.54 |
| BLh | 1.398 | 1.198 | 1.167 | 435.735 | 1145.850 | HMNS |
| BLQ | 1.398 | 1.198 | 1.167 | 435.735 | 1145.850 | 17.2 |
| BLh | 1.363 | 1.363 | 1.0 | 515.379 | 515.379 | HMNS |
| BLQ | 1.363 | 1.363 | 1.0 | 515.379 | 515.379 | 4.1 |
| DD2F | 1.289 | 1.289 | 1.0 | 707.511 | 707.511 | HMNS |
| DD2F − SF1 | 1.289 | 1.289 | 1.0 | 707.511 | 707.511 | 42.36 |

### 6.2.3 Parameter Estimation

For our postmerger PE analysis, we employ the nested sampler `UltraNest` [332] included as part of the `bajes` code [377]. Our configuration employs $5 \times 10^3$ live points and a maximum of $5 \times 10^4$ iterations for the Monte Carlo sampler. We choose a Gaussian-noise likelihood [378] defined as

$$\begin{aligned} \log\left(\mathcal{L}(d|\boldsymbol{\theta})\right) = &-\frac{1}{2}\sum_j \log\left(2\pi S_j\right) \\ &-\frac{1}{2}\sum_j \langle d_j - \mu(\boldsymbol{\theta})|d_j - \mu(\boldsymbol{\theta})\rangle \end{aligned} \tag{6.2}$$

where the summation index $j$ runs over the three arms in the case of the ET detector, $S_j$ denotes the power spectral density (PSD) of the corresponding detector, $\mu(\boldsymbol{\theta})$ is the `NRPMw` model evaluated for the parameter set $\boldsymbol{\theta}$ and $d$ represents the data stream of the injection. In the case of the CE detector, we fix $j$ to correspond to the narrow-band 20km postmerger optimized configuration. The inner product $\langle .|. \rangle$ between two signals

say $a(f)$ and $b(f)$ in the frequency domain is given by

$$\langle a(f)|b(f)\rangle = 4\ \mathrm{Re}\int_{f_{\rm min}}^{f_{\rm max}} \frac{a^*(f)b(f)}{S_j(f)}df \tag{6.3}$$

The PSDs for the ET and the CE detectors employed by us are the same as those used in ref. [346–348]. We take $f_{min}$ and $f_{max}$ to be 1024 and 8192 Hz, respectively to include the postmerger domain of the signal.

We take $d_j$ to denote the data stream in each arm of the detector i.e. $d_j = s_j + n_j$, where $s_j$ and $n_j$ respectively denote the signal and noise in the detector. For noise-less injections, $d_j$ is given exclusively by the signal projected onto the individual detectors i.e.

$$\begin{aligned} d_j(f) = \mathrm{F}_{j;+}(\mathrm{RA.}, \mathrm{DEC.}, \psi)h_+(f) + \\ \mathrm{F}_{j;\times}(\mathrm{RA.}, \mathrm{DEC.}, \psi)h_\times(f) \end{aligned} \tag{6.4}$$

where $\mathrm{F}_{j;+}$ and $\mathrm{F}_{j;\times}$ denote the antenna pattern functions of the $j^{th}$ arm of the ET detector (or a CE-20 detector) and RA., DEC. and $\psi$ denote the right ascension, declination and the polarization angle of the binary respectively. The injected signal corresponds to the strain from NR simulations.

The joint posterior distribution function(PDF) of the posterior samples corresponding to the parameters of the `NRPMw` model is given by the Bayes' theorem as

$$p(\boldsymbol{\theta}|d) = \frac{\mathcal{L}(d|\boldsymbol{\theta})\pi(\boldsymbol{\theta})}{\mathcal{Z}} \tag{6.5}$$

where $\mathcal{Z}$ denotes the marginalized likelihood or the evidence for the data stream and $\pi(\boldsymbol{\theta})$ denotes the prior PDFs for the model parameters. Finally, to compute the individual posteriors ($\theta_i$) of the model parameters, we marginalize the joint PDF over the corresponding parameters to obtain

$$p(\theta_i|d) = \int \left(\prod_{k\neq i} d\theta_k\right) p(\boldsymbol{\theta}|d). \tag{6.6}$$

In the `NRPMw` model presented in Breschi et al. [284], the postmerger frequency parameter $f_2$ is decided by a fit to an EOS insensitive relation (see Table I of ref. [284]) with $\kappa_2^T$ and accounted for deviations by using the re-calibration parameter $\delta f_2$. In this work, we will assume $f_2$ to be an unconstrained parameter over which we can sample in a Bayesian framework. In other words, this means migrating $f_2$ from the set of $\boldsymbol{\theta}_{\rm fit}$ to $\boldsymbol{\theta}_{\rm free}$,

where $\boldsymbol{\theta}_{\rm fit}$ and $\boldsymbol{\theta}_{\rm free}$ are respectively the sets of fitted parameters and free parameters for `NRPMw`, as defined in ref. [284]. The motivation behind making $f_2$ unconstrained lies in the fact that we do not want our results to be informed in any way by the $f_2 - \kappa_2^T$ relation. Throughout this work, we will refer to the global maxima in the reconstructed postmerger spectra as $f_2^{\rm peak}$ to avoid confusion with the $f_2$ parameter of the `NRPMw` model which is a carrier frequency evolving linearly with time. We would like to stress that even though $f_2^{\rm peak}$ and $f_2$ are close numerically, they are not the same quantity. $f_2^{\rm peak}$ is a property of the reconstructed spectra whereas $f_2$ is a parameter of the `NRPMw` model. Posteriors on $f_2^{\rm peak}$ are computed from the global postmerger maxima of the reconstructed signal which in turn depends on $f_2$ and other parameters. In a nutshell, $f_2^{\rm peak}$ is influenced by the choice of $f_2$ but not the other way around. Throughout this work, we will refer to this updated model with the unconstrained $f_2$ parameter as `NRPMw`. For comparison, we have also presented calculations in subsection 6.3.3 with the original model of Breschi et al. [284] where $f_2$ is constrained by $\kappa_2^T$ and we call this model as `NRPMw_v1`. Finally, to explore a more flexible configuration of the model, we unconstrain not only $f_2$ but also $f_0$ which is the parameter for radial oscillation modes. We refer to this version of the model as `NRPMw_v2` and describe it in appendix 6.7.

### 6.2.4 Priors

With the advent of the next generation of GW detectors, it is expected for binaries that are loud enough that their postmergers can be detected, masses and tidal deformabilities will be measured accurately from the inspiral [347,348]. Therefore, the most accurate PE would result from an analysis of the full signal, i.e., inspiral and postmerger. However, performing Bayesian inference on the full signal is computationally expensive. In this work, we therefore adopt a two-fold approach in the sense that we analyze the inspiral and postmerger signals using separate inference codes. From the inspiral inference, we compute posteriors on total gravitational mass $M$, mass ratio $q$ and the tidal deformabilities $\Lambda_i$s, all of which for loud signals are Gaussians to a good approximation. Following this in a separate inference for the postmerger, we constrain the prior bounds of the postmerger model by supplying the Gaussian priors thus obtained. We refer the reader to 6.2.4.1 for the detailed procedure to compute these priors.

On the other hand, in 6.2.4.2, we describe a choice of priors that are broad and independent of the inspiral signal. We have summarized the two choices of priors in tables 6.2 and 6.3.

**Table 6.2.** Prior ranges for the parameters of the `NRPMw` model as well as the extrinsic and intrinsic parameters in an inspiral agnostic setting. In particular, the priors on $M$ and $q$ have been set in accordance to ref. [379] so as to maintain a uniform distribution in $m_1$ and $m_2$.

| parameter | min | max | Type |
|---|---|---|---|
| M [$M_\odot$] | 1 | 6 | ref. [379] |
| $q$ | 1 | 2 | ref. [379] |
| $\chi_1$ | -0.2 | 0.2 | aligned spin |
| $\chi_2$ | -0.2 | 0.2 | aligned spin |
| $\Lambda_1$ | 0 | 4000 | Uniform |
| $\Lambda_2$ | 0 | 4000 | Uniform |
| R.A. | 0 | $2\pi$ | Uniform |
| DEC. | $-\pi/2$ | $\pi/2$ | Cosinusoidal |
| $\cos\,\iota$ | -1 | 1 | Uniform |
| $\psi$ | 0 | $\pi$ | Uniform |
| $D_L$ [Mpc] | 5 | 500 | Volumetric |
| $t_{\rm coll}/M$ | 1 | 3000 | Uniform |
| $M^2\alpha_{\rm peak}$ | -$10^{-4}$ | $10^{-4}$ | Uniform |
| $\phi_{\rm PM}$ | 0 | $2\pi$ | Uniform |
| $f_2$ [kHz] | 1.5 | 5 | Uniform |
| $\delta(Mf_0)$ | -1 | 2 | $\text{Gaussian}^{\mu=0}_{\sigma=0.449}$ |
| $\delta(Mf_{\rm mrg}/\nu)$ | -0.2 | 0.2 | $\text{Gaussian}^{\mu=0}_{\sigma=0.026}$ |
| $\delta(A_{\rm mrg}/M)$ | -0.2 | 0.2 | $\text{Gaussian}^{\mu=0}_{\sigma=0.018}$ |
| $\delta(M/t_0)$ | -0.5 | 0.5 | $\text{Gaussian}^{\mu=0}_{\sigma=0.092}$ |
| $\delta(A_0/M)$ | -1 | 4 | $\text{Gaussian}^{\mu=0}_{\sigma=0.663}$ |
| $\delta(A_1/M)$ | -1 | 2 | $\text{Gaussian}^{\mu=0}_{\sigma=0.152}$ |
| $\delta(A_2/M)$ | -1 | 2 | $\text{Gaussian}^{\mu=0}_{\sigma=0.385}$ |
| $\delta(A_3/M)$ | -1 | 2 | $\text{Gaussian}^{\mu=0}_{\sigma=0.269}$ |
| $\delta(M^2\mathcal{I}m(\alpha_{\rm fus})/\nu)$ | -4 | 4 | $\text{Gaussian}^{\mu=0}_{\sigma=0.751}$ |
| $\delta(M\mathcal{R}e(\beta_{\rm peak}))$ | -1 | 2 | $\text{Gaussian}^{\mu=0}_{\sigma=0.27}$ |
| $\delta(M\Delta_{\rm fm})$ | -1 | 4 | $\text{Gaussian}^{\mu=0}_{\sigma=0.744}$ |
| $\delta(M\Gamma_{\rm fm})$ | -1 | 4 | $\text{Gaussian}^{\mu=0}_{\sigma=0.977}$ |

#### 6.2.4.1 Inspiral Informed Priors

Since the NR waveforms simulate only the last few orbits before merger and for a reliable estimate of masses and tidal parameters we require a longer inspiral data stream, we employ the `TaylorF2` waveform model [380–386] to simulate the inspiral signal targeted at the parameters of the binaries listed in table 6.4. The inspiraling binaries are assumed

to be non-spinning and situated at the most optimal sky location corresponding to the detectors (either ET or CE).

We perform a self-consistent injection recovery with the `TaylorF2` waveform model in the ET (or CE-40) noise configuration and compute posteriors on the chirp mass $\mathcal{M}_c$, tidal deformability $\tilde{\Lambda}$ as defined in ref. [99], mass ratio $q$, individual tidal parameters $\Lambda_i$s and the total mass $M$ for all the hadronic models listed in Table 6.4. For this purpose, we employ the publicly available `Bilby` framework [387–389] that utilizes relative binning [390, 391] for the computation of posteriors.

In Fig. 6.3, we show the posterior PDFs from the self-consistent injection recovery of the `TaylorF2` model targeted to simulate a long inspiral of the $1.398M_\odot - 1.198M_\odot$ binary with the BLh EOS. We see that the chirp mass $\mathcal{M}_c$ is extremely well measured with a standard deviation of $6.77 \times 10^{-7} M_\odot$. The posterior PDFs for the tidal parameters $\Lambda_i$s are refined by recomputing them via the universal relations presented in [392] by taking the $M$, $q$, $\Lambda_1$ and $\Lambda_2$ inspiral posteriors as inputs. This could be a potential source of systematic errors which we have underestimated given the uncertainties in these relations as pointed out in ref. [393]. For comparison, we have presented the posteriors on $\Lambda_i$s which have been obtained directly from the inspiral PE (not refined by the universal relations) and those which have been refined by the universal relations from [392] in figure 6.4. We note that this being an asymmetric merger ($q \neq 1$), we have an accurate determination of $q$ and consequently $\Lambda_1$ and $\Lambda_2$ . For an equal-mass merger, the injected value of $q = 1$, lies on the edge of the priors for the sampler, and the resulting posterior is one-sided as shown in Fig. 6.17. This one-sidedness of the mass ratio posterior also influences the measurement of $\Lambda_1$ and $\Lambda_2$ when refined by universal relations. Nevertheless, even for $q = 1$ mergers, symmetric tidal combinations such as $\kappa_2^T$ which is used as a probe for phase transitions are estimated to be well within the 90% credible intervals.

We approximate the inspiral posteriors on $M$, $q$, $\Lambda_1$ and $\Lambda_2$ with Gaussian distributions that have the same average as that of the inspiral posterior and a standard deviation equal to a quarter of the full 2 $\sigma$ width of the posterior. This choice allows us to be sufficiently conservative and establish a lower bound for measurement accuracy, which will only be improved if one chooses more restrictive priors and/or consider correlations between the priors. We remark that, at the moment, the `bajes` infrastructure does not support a specification of correlated priors. We extract these Gaussian profiles from the simulations run with hadronic EOSs and use them as priors for a postmerger PE for both hadronic and quark simulations. This is because, as discussed in 6.2.1, the

hadronic and quark EOSs have the same low-density EOS and therefore the same tidal deformabilities. We would like to emphasize that while this approach is not a replacement for a full inspiral-postmerger inference, it provides reliable estimates for masses and tidal polarizabilities from the inspiral signal. The signal in the inspiral corresponding to a postmerger SNR of 10, has an SNR of $\sim 600$. This corresponds to a detection rate of $0.5 - 1.5\ yr^{-1}$ [348] with the ET detector and a detection rate of $1 - 1.5\ yr^{-1}$ with the Cosmic Explorer CE-20 detector. The standard deviation in the inspiral estimates of the total mass ranges between $10^{-4}M_{\odot} - 10^{-3}M_{\odot}$. In addition to that, the percentage error in $\kappa_2^T$, i.e., deviation between the injected $\kappa_2^T$ and the $50^{\text{th}}$ percentile of the recovered posterior ranges from 0.1%-0.5%. The main advantage of employing a separate pipeline for the inspiral signal is the usage of relative binning which significantly reduces the computational cost. In addition, we have also shown an investigation of NRPMw's performance in tandem with the inspiral constraints.

#### 6.2.4.2 Inspiral Agnostic Priors

We now describe the priors for the parameters of the `NRPMw` model in an inspiral-agnostic setting. These broad ranges on the priors have been taken from the reference [334] to include a wide range of possibilities. Most importantly, the priors on $M$ and $q$ have been set according to [379] to maintain uniform priors on $m_1$ and $m_2$, the masses of the binary component stars. We also set uniform priors on $\Lambda_i$s ranging from 0 to 4000 to cover a wide range in stellar compactness.

Providing a comparison between results obtained from an inspiral-informed and inspiral-agnostic choice of priors is essential. We present such a comparison of priors in Fig. 6.5. As we will make explicit in this work, the choice of priors has minimal influence on the recovery of $f_2^{\text{peak}}$ which is solely estimated from the postmerger. However, estimating $f_2^{\text{peak}}$ is not the only pre-requisite for detecting phase transitions. Phase transitions are detected by quantifying violations of EOS insensitive relations between the postmerger $f_2$ and the inspiral $\kappa_2^T$. With the inspiral-agnostic priors, $f_2^{\text{peak}}$ is well measured but there are large uncertainties in the measurement of $\kappa_2^T$ (see appendix 6.5). This can be mitigated by supplying priors that are informed about the tidal properties and masses from the inspiral signal. This is precisely what we observe with the choice of inspiral-informed priors where our sampler essentially recovers the Gaussian priors set from the inspiral on masses and tidal deformabilities. Another motivation behind such a comparative study with different choices of priors is to demonstrate the `NRPMw` model's performance when subjected to different degrees of independence in the sampling of the

prior parameter space.

When a parameter of the NRPMw model is constrained by fits to EOS insensitive relations, we employ corresponding recalibration parameters to account for the uncertainties in these relations. The priors on all the recalibration parameters $\delta\boldsymbol{\theta}_{\rm fit}$ are distributed normally around a mean value of zero with a variance decided by the relative standard deviation between the scatter of NR simulations and the EOS insensitive relation. When we make a parameter independent of these fits as in the case of $f_2$, we ignore the corresponding recalibration parameter.

## 6.3 Results

### 6.3.1 Inspiral-Informed Postmerger PE with Einstein Telescope

In this subsection, we present results for the postmerger PE analysis using the ET detector and by taking the priors on $M$, $q$, $\Lambda_1$, and $\Lambda_2$ as Gaussian (normal) distributions that are informed from the inspiral signal.

In Fig. 6.6, we show our results for an inspiral informed PE for the representative case of the $1.398M_\odot - 1.198M_\odot$ merger with the BLh and BLQ EOSs. We note that for the model with the BLQ EOS, the 90% credible interval (CI) estimated by NRPMw for the posterior of $f_2^{\rm peak}$ contains the injected value whereas for the model with the BLh EOS, the 95% CI of the $f_2^{\rm peak}$ posterior contains the injection. Additionally, in Fig. 6.7, we present the reconstructed frequency spectra for the same pair of simulations using NRPMw. We emphasize that the 90% CIs for $f_2^{\rm peak}$ corresponding to the hadronic and quark cases do not overlap, implying that at a postmerger SNR of 10, the two models can be distinguished. In addition, we observe that the measurement of $f_2^{\rm peak}$ is insensitive (to within 90% CIs) to the choice of priors as it is an exclusively postmerger-determined quantity. The measurement of $\kappa_2^T$ on the other hand improves substantially upon employing the inspiral informed priors as it is decided exclusively from the inspiral signal.

We summarize our results for the detectability of $f_2^{\rm peak}$ for all other simulations in our work in Figs. 6.18, 6.19 and 6.20. We report that for the binaries $1.481M_\odot - 1.257M_\odot$ and $1.363M_\odot - 1.363M_\odot$ with the BLh EOS, the 90% CIs estimated for the $f_2^{\rm peak}$ posterior contain the injection. For the rest of the hadronic models, i.e., $1.398M_\odot - 1.198M_\odot$ with BLh, $1.289M_\odot - 1.289M_\odot$ with DD2F and $1.298M_\odot - 1.298M_\odot$ with BLh, 95 %, 98 % and 99.5 % CIs of $f_2^{\rm peak}$ contain the injection respectively. For the hadronic models, we

identify a systematic bias that leads to an overestimation of $f_2^{\rm peak}$ by `NRPMw`. This bias primarily arises because of the presence of multiple (>2) amplitude modulations in the postmerger signal. As mentioned in Fig. 2 of ref. [284], `NRPMw` is designed to capture the peaks of only the first two amplitude modulations, following which it models a damped sinusoidal decay of the postmerger amplitude. In the subsection 6.3.1.1, we discuss this bias in detail. On the other hand, for the quark EOSs, we observe that the 90% CIs for $f_2^{\rm peak}$ contain the injected $f_2^{\rm peak}$ except for the $1.363M_\odot - 1.363M_\odot$ merger where the 95% CIs contain the injection.

#### 6.3.1.1 Biases due to multiple amplitude modulations

A characteristic feature of our hadronic simulations, in particular the binaries $1.398M_\odot - 1.198M_\odot$ (BLh), $1.289M_\odot - 1.289M_\odot$ (DD2F) and $1.298M_\odot - 1.298M_\odot$ (BLh), is the existence of multiple amplitude modulations in the $\ell = 2, m = 2$ mode of the GW strain. From our NR simulations of hadronic EOSs, we note that these modulations are typically observed in the early postmerger signal, i.e., when the remnant has just formed and undergoes large dynamical deformations resulting in amplitude-modulated GW emissions. `NRPMw`, as of now, is unable to capture multiple modulations in the postmerger amplitude and attempts to reconstruct amplitude modulations beyond 2 via damped sinusoids. This leads to a biased overestimation of $f_2^{\rm peak}$ as is evidenced in Figs. 6.6, 6.18 and 6.19.

In this section, we explore in detail the major source of this systematic bias, i.e., the multiple amplitude modulations. In Fig. 6.8, we show the time domain waveform for the $1.398M_\odot - 1.198M_\odot$ binary with the BLh EOS that exhibits multiple amplitude modulations. In line with the convention for nodal points presented in ref. [284], we denote positions of the merger as $t_{\rm merg}$, the first two postmerger maxima as $t_1$ and $t_3$ and their corresponding intermediate minima as $t_0$ and $t_2$. `NRPMw` only includes amplitude modulations until $t_3$ beyond which the amplitude is described by a damped sinusoid. We introduce an exponential filtering function

$$F(t) = 1/(1 + \exp(t - t_{\rm cutoff})) \tag{6.7}$$

where $t_{\rm cutoff}$ denotes the point where the filter cuts off the strain. We take $t_{\rm cutoff}$ to be near the position of the third amplitude modulation and filter off the subsequent signal to disentangle the effects of subsequent modulations. In the right panel of Fig. 6.8, we show the frequency spectra of this filtered waveform against that of the unfiltered waveform. We note that the subsequent amplitude modulations for $t - t_{\rm merg} \gtrsim 5$ ms lead to multiple

oscillations near $f_2^{\rm peak}$. Such closely-spaced oscillations in the frequency domain are not a morphology that can be captured by `NRPMw` and the model tends to construct an average over these peaks leading to a bias. On the other hand, when such modulations have been filtered out, the model captures the peak of the filtered spectra much better.

We also refer the reader to appendix 6.7 for a brief discussion on how one can start to mitigate this bias by modifying the `NRPMw` model and making it more flexible to capture multiple modulations.

We would like to emphasize that even though we have shown for our hadronic systems that removing multiple (>2) amplitude oscillations can help remove biases in the measurement of $f_2^{\rm peak}$, we only report results from the unfiltered, i.e., complete waveforms for the purposes of detecting phase transitions. This is because, in a realistic detection scenario, it is rather artificial to engineer the waveforms to support a recovery of $f_2^{\rm peak}$ to within some confidence level. Additionally, we would like to emphasize that there is still scope for improvement in the contemporary BNS waveform models to capture the above-mentioned morphologies and that additional avenues apart from shifts in $f_2^{peak}$ need to be explored for a holistic examination of QCD phase transition effects.

### 6.3.2 Inspiral Informed Postmereger PE with Cosmic Explorer

In this subsection, we repeat the inspiral informed PE analysis described in 6.3.1 on the $1.289M_\odot - 1.289M_\odot$ binaries with the DD2F and DD2F-SF1 EOSs but with a difference that now we employ the Cosmic Explorer sensitivities for recovering our models. The configurations we employ are a broad-band 40 km detector and a narrow-band 20 km detector which has been optimized for postmerger and has increased sensitivity in the 2-4 kHz regime. The advantage of the enhanced sensitivities of the CE-20 detector is that for the same postmerger SNR of 10, we will observe more distant and therefore more frequent mergers. We inject the `TaylorF2` predicted inspiral for the hadronic model $1.289M_\odot - 1.289M_\odot$ with the DD2F EOS in the broad-band CE-40 configuration. This binary is now placed at a distance of 118.467 Mpc so as to produce a postmerger SNR of 10 in CE-20 configuration. This is because we would like to harness the sensitivities of the CE detectors most optimally. CE-40 has higher sensitivity at low frequencies corresponding to the inspiral signal and therefore it is utilized for estimating the mass and tidal parameters from an inspiral signal (as described in 6.3.1). On the other hand, CE-20 has increased sensitivities in the kilohertz regime corresponding to the emission frequencies of the BNS remnant and hence is utilized for the postmerger PE. For this analysis, we have assumed that both the CE-20 and CE-40 observatories are operating

simultaneously and are located at the same position on Earth.

In Fig. 6.9, we present a reconstruction of the postmerger amplitude spectrum recovered using the CE-20 detector by the `NRPMw` model. We see yet again that the measurement of $f_2^{\rm peak}$ for the hadronic model is overestimated due to the multiple amplitude modulations in the time-domain GWs from the hadronic model which we show explicitly in Fig. 6.10. The quality of the reconstruction of spectra and the accuracy of recovery of $f_2^{\rm peak}$ is similar in both the ET and CE-20 detectors with the only advantage being the increased rates of observation of BNS mergers with CE-20.

So far we have demonstrated that the `NRPMw` model along with the sensitivities of the ET detector and the CE detector can reliably detect and reconstruct the postmerger signal which is evidenced by the fact that we recover most ($\approx$8) of the injected SNR (Table 6.4). In addition, we have shown that our model is capable of recovering (albeit with some bias) the $f_2^{\rm peak}$ frequency and distinguishing the same between the hadronic and quark models at a postmerger SNR of 10. We would like to emphasize that detecting and distinguishing the $f_2^{\rm peak}$ frequency is not sufficient for inferring the occurrence of a phase transition in a realistic observational setting. The latter requires quantifying violations from EOS insensitive relations (see subsection 6.3.3). Since such relations involve inspiral tidal parameters in addition to the postmerger $f_2^{\rm peak}$, it is imperative that we have reliable estimates of the tidal parameters. In this regard, the utility of inspiral informed priors becomes clear. We can see that for all our models be it hadronic or quark, the 90% CIs for $\kappa_2^T$ posterior by the `NRPMw` model contain the injected value. There exists no information about masses or the tidal properties from the postmerger signal alone (at least at a postmerger SNR of 10) and our postmerger model essentially recovers these priors. In contrast, with the priors that are agnostic of the inspiral signal, as in appendix 6.5, the estimates of the tidal $\kappa_2^T$ are dominated by large errors which in turn will make an inference of QCD phase transitions difficult from the EOS insensitive quasi universal relations.

### 6.3.3 Probing QCD Phase Transitions

As we have previously remarked, detection of a postmerger signal and a reliable recovery and distinguishability of $f_2^{\rm peak}$ is necessary but not sufficient for probing QCD phase transitions. Previous works [54, 55, 364] suggest the utility of EOS insensitive relations, in particular between $f_2^{\rm peak}$ and a tidal parameter be it $\tilde{\Lambda}$ or $\kappa_2^T$, in probing such phase transitions. Specifically, if EOS softening effects by such phase transitions produce deviations from the aforementioned relations that are non-degenerate with other hadronic

models, one can ascertain the occurrence of a phase transition with some confidence. This requires that we have reliable estimates of not just $f_2^{\rm peak}$ but also of tidal properties. Comparing NR simulations of the postmerger signal at different resolutions can only provide the former as a one-dimensional error estimate because tidal properties are fixed upon assuming a specific equation of state. The only way we can compute a joint uncertainty of $f_2^{\rm peak}$ and $\kappa_2^T$ is by Bayesian inference of the postemrger signal which is informed of the tidal properties from the inspiral (and of course a Bayesian inference on the full signal).

We employ the fitting function obtained in ref. [284] with reference to the CoRe database. This fitting function improves upon the QUR obtained in refs. [64] by explicitly including the effects of inspiral spins and taking into account additional GRHD simulations performed with WhiskyTHC and BAM infrastructures. In Fig. 6.11, we plot the QUR fitting function for symmetric binaries that are non-spinning, along with an ensemble of simulations that form a part of the CoRe database. We also show the 90% confidence levels for the fit describing symmetric binaries. To this collection, we add the injections presented in this work with their error estimates that are essentially the 90% contour levels of the 2-dimensional joint posteriors for mass-rescaled $Mf_2^{\rm peak}$ and $\kappa_2^T$ obtained with the choice of inspiral informed priors.

In subsection 6.3.1 and appendix 6.6, we have provided evidence for mutual distinguishability between hadronic and quark models based on the non-degeneracy of the 90% CIs of the $f_2^{\rm peak}$ posteriors. In this section, we present a discussion on detecting phase transitions based on non-degeneracies between the joint $f_2^{\rm peak} - \kappa_2^T$ posteriors and comparing them with the EOS insensitive relation of Breschi et al. [284]. In the first (upper-left) panel of Fig.6.11, we present hadronic and quark models that, at a postmerger SNR of 10, are mutually distinguishable as is seen by the absence of any overlap between the corresponding joint $Mf_2^{\rm peak} - \kappa_2^T$ posteriors. These models are the $1.363M_\odot - 1.363M_\odot$ binary for the BLh and BLQ EOSs and the $1.289M_\odot - 1.289M_\odot$ binary for the DD2F and DD2F-SF1 EOSs. For the $1.363M_\odot - 1.363M_\odot$ binary, we notice that even though the hadronic and quark models are distinguishable (up to 90% confidence), the quark model's joint posterior is degenerate with other hadronic EOSs, implying that a postmerger SNR of 10, we cannot conclusively confirm a phase transition for this binary. On the other hand, for the $1.289M_\odot - 1.289M_\odot$ binary with the DD2F-SF1 EOSs, we notice that the injection and the corresponding joint posteriors do not overlap with the universal relation, implying that at a postmerger SNR of 10, we can confirm the presence of a phase transition. We do however caution the reader about a possible caveat.

The conclusion that whether we can confirm a phase transition to some confidence is sensitive to the particular universal relation used. The 90% contours of the joint posterior with DD2F-SF1 EOS, even though not overlapping with the universal relation's error margin, are very close to them and systematics in the universal relation may change our conclusions. Such systematics may result from updating the coefficients of the fit upon adding more simulations. At higher postmerger SNRs, detectability avenues will improve. This is made concrete by an additional model recovered at a higher postmerger SNR of 15, where we find that the DD2F-SF1 model's joint posteriors shrink and are even more removed from the universal relation than the same model at postmerger SNR 10.

Similarly, in the second panel (top right) of the figure 6.11, we repeat the calculations for the case of $1.289M_\odot - 1.289M_\odot$ binary with the DD2F and DD2F-SF1 EOS, assuming the Cosmic Explorer (CE-20) detector sensitivity. We notice here that the joint posteriors corresponding to the quark EOS are "more" non-degenerate with the universal relation as compared to the same model recovered from the Einstein Telescope sensitivity. Consequently, at a postmerger SNR of 10, we can confirm the presence of a phase transition. The better performance of the CE-20 detector as compared to the Einstein Telescope's recovery, is not entirely unexpected. Indeed we note that for the injected $f_2^{\rm peak}$ frequencies close to 3 kHz, the CE-20 detector is more sensitive than the ET detector.

On the other hand, in the third (bottom left) and fourth (bottom right) panels of figure 6.11, we show binaries for which the 90% contours of the joint posterior overlap between the hadronic and quark models. These models include the $1.298M_\odot - 1.298M_\odot$, $1.481M_\odot - 1.257M_\odot$ and $1.398M_\odot - 1.198M_\odot$ binaries with the BLh and BLQ EOSs. For the quark models of these binaries, at a postmerger SNR of 10, the presence of a QCD phase transition cannot be ascertained given the degeneracy with other hadronic EOSs.

Therefore, in a nutshell, even though postmerger waveforms from the hadronic models may be distinguishable from the corresponding quark models by virtue of non-degeneracy of $f_2^{\rm peak}$ posteriors, they may still be degenerate with each other in a two-dimensional space of $f_2^{\rm peak} - \kappa_2^T$ uncertainties. Furthermore, when there is no degeneracy in a joint measurement of $f_2^{\rm peak}$ and $\kappa_2^T$, a postmerger SNR of 10 can confirm the presence of a phase transition only if the model violates the universal relation strongly, i.e., $\Delta f_2^{\rm peak} \approx 455$ Hz ($\gtrsim 1.6\ \sigma$). At a postmerger SNR of 10, systematics in the universal relation may also play a role in influencing conclusions about the detectability of phase transitions. However, for louder binaries with SNR $\sim 15$, phase transitions of the type predicted by

the DD2F-SF1 model can be confirmed with a higher confidence.

At this stage we also present a test of the EOS insensitive relations with reference to detecting QCD phase transitions in Fig. 6.12. To this aim, we test two configurations of our model. Firstly, we use the `NRPMw` configuration employed throughout this work where the $f_2$ parameter is independent of the $f_2 - \kappa_2^T$ universal relation from Breschi et al. [284], i.e., the universal relation is ignored. Secondly, we employ the original model configuration of Breschi et al. (called `NRPMw_v1` in this work) where $f_2$ is decided by the universal relation. In particular, we are posing the question that given a signal, whether the inclusion of the $f_2 - \kappa_2^T$ universal relation in the model can play a role in detecting a "strong" phase transition. In the left panel of Fig.6.12, we present results for the $1.298M_\odot - 1.298M_\odot$ binary with the BLQ EOS whose injection is consistent with the universal relation. We note that for both model configurations, the 90% contour of the joint PDF contains the injection at a postmerger SNR of 10. To quantify this comparison we compute the Bayes' factor for the two hypotheses, i.e., inference with and without the universal relation respectively. We find that $\log \mathcal{B}^{\text{with QUR}}_{\text{without QUR}} = 2.53^{+0.27}_{-0.27}$ indicating a weak preference towards the QUR informed `NRPMw_v1` model. On the other hand, in the right panel of Fig. 6.12, we present the same calculation for the $1.289M_\odot - 1.289M_\odot$ binary with the DD2F-SF1 EOS. Since in this case, the injection is inconsistent with the universal relation, including the same in the model tends to drive the joint posterior toward the universal relation and away from the injection. This is evidenced by the fact that the 90% contour of the `NRPMw_v1` model does not contain the injection whereas the injection is well captured within the joint posterior of the more flexible `NRPMw` model. To quantify the same statement, the $\log \mathcal{B}^{\text{without QUR}}_{\text{with QUR}} = 2.24^{+0.27}_{-0.27}$ at a postmerger SNR of 10 indicating a weak preference towards the more flexible `NRPMw` model with respect to detecting phase transitions that strongly violate the universal relations.

## 6.4 Conclusions

In this work, we have shown that the next generation of GW experiments has the potential to identify QCD phase transitions in the postmerger phase of neutron star mergers, provided such phase transitions are sufficiently strong.

To model the influence of deconfined quarks on the dynamics of BNS merger remnants, we employ the BLQ and DD2F-SF1 EOSs which model the deconfined quark phase by Gibbs construction and Maxwell construction respectively. In the case of a merger, these treatments lead to remnants with very different properties, most notably differences in

the postmerger peak frequencies. We construct the postmerger signals by windowing out the inspiral signal from our NR waveforms and injecting the signal thus obtained in a noise-less configuration of ET or CE detectors.

We perform independent Bayesian inference calculations on the inspiral and the postmerger signals using the `Bilby` (via the `TaylorF2` model) and `bajes` (via the `NRPMw` model) codes, respectively. We compute the posteriors of total mass, mass ratio and tidal deformabilities which are expectedly Gaussian to a good approximation (except for the one-sided $q = 1$ posteriors). These posteriors help inform the priors for the postmerger PE analysis which provides the posteriors on $f_2^{\rm peak}$. We find that `NRPMw` model can reliably recover the postmerger signal as is evidenced by the recovered SNRs (Table 6.4 and Table 6.5). Additionally, at a postmerger SNR of 10, the model can also recover the $f_2^{\rm peak}$ frequency and distinguish the same between a hadronic and quark model to upto 90% confidence.

Our work also serves to present new test cases to which our waveform model has been applied as a means to evaluate its validity. We have presented for the first time, the behavior of the model in an inspiral-informed PE setting and tested its performance on morphologically complex NR waveforms. It is noteworthy that simulations from DD2F, DD2F-SF1 EOSs are also the ones that the model has not been trained on. For these cases too we get reliable signal reconstruction and recover most of the SNR.

We have provided a complimentary analysis by employing the CE-40 and CE-20 detectors. The advantage of utilizing the CE detectors for this purpose is two fold. First, with enhanced postmerger sensitivities, BNS mergers can be probed at larger luminosity distances and hence more frequently. Second, a combination of broad-band CE-40 detector and a narrow band postmerger optimized CE-20 detector is optimal for a holistic detection because of increased sensitivities in the inspiral (by CE-40) and the postmerger (by CE-20). For sources with postmerger SNR of 10 in CE-20, we have used the CE-40 detector to compute posteriors on masses and tidal parameters which serve as priors on the postmerger PE analysis via the CE-20 detector. We find no major differences in the inference of $f_2^{\rm peak}$ or the quality of signal reconstruction as compared to inference with the ET detcetor.

We emphasize that even though `NRPMw` coupled with the enhanced sensitivities of the upcoming generation of GW detectors, can reliably detect and distinguish the $f_2^{\rm peak}$ frequencies at a postmerger SNR of 10, it is not sufficient to probe QCD phase transitions. We compare the joint posterior estimates on $f_2^{\rm peak}$ and $\kappa_2^T$ in reference to the $f_2 - \kappa_2^T$ universal relation from Breschi et al. [284] and find that starting at postmerger SNRs

of 10, we can claim a detection of a first order phase transition but only for models that violate the universal relations by more than 1.6 $\sigma$. We also demonstrate a slight preference towards the model configuration which is independent of the universal relation in detecting "strong" phase transitions by a $\log \mathcal{B}^{\text{without QUR}}_{\text{with QUR}} = 2.24^{+0.27}_{-0.27}$.

For final remarks, Bayesian inference is done on waveforms that have a rich morphological structure and therefore we speculate that indicators of QCD phase transitions may not be exclusively encoded in $f_2^{\text{peak}}$. This warrants exploration of alternative signatures of phase transitions, e.g., imprints in the postmerger amplitude or the lifetimes of remnants. Our work calls for efforts in several directions. First, as we have shown, the current waveform models need to be improved to take into account additional waveform morphologies like multiple amplitude modulations which can be a significant source of bias at high enough SNRs. Additionally, a prescription for modeling the high-frequency black hole ringdown-spectrum can be accommodated in `NRPMw` however, we have omitted the same in favor of ease of computation. The ringdown spectrum and the ensuing quasi-normal modes can be important for constraining QCD phase transitions from short-lived remnants or promptly collapsing binaries where such phase transitions can play a role [108, 176, 186]. Second, the universal relations can themselves involve systematic biases which can be sourced from uncertainties in the physics modeled in the simulations. Such biases may shift the universal relations in the $f_2^{\text{peak}} - \kappa_2^T$ plane affecting conclusions about the occurrence of phase transitions. On a related note, it is also anticipated that modified-gravity theories [394] can distort the interpretation of tidal parameters [395] and produce effects [396] that may mimic QCD phase transitions [1]. Lastly, improvements are required in improving the postmerger convergence of contemporary NR codes [398] as will be required by large SNR detections from the next generation detectors. Overall, the prospects of detecting a QCD phase transition with the enhanced sensitivities of the upcoming detectors, seem not too pessimistic. A single GW170817-like event, provided a postmerger is also observed, can in theory constrain QCD phase transitions.

## 6.5 Appendix 1: Inspiral Agnostic PE: results for all simulations

In this appendix, we present results for a postmerger PE of the `NRPMw` model's parameters wherein we set a wide range of values to the priors as described in Table 6.2. The choice

[1] See also [397]

of priors follows that in [334] and is targeted at a wide range of possibilities for the GW event. To this aim, we present results for the postmerger PE of all the simulations listed in Table 6.5 performed with this choice of priors. In Figs. 6.13, 6.14 and 6.15 we present the posterior PDFs for $f_2^{\rm peak}$ and $\kappa_2^T$. We note that the $f_2^{\rm peak}$ frequencies are recovered accurately and the injection is contained in the 90% CIs. There appear to be no significant differences as compared to the estimation of $f_2^{\rm peak}$ from the inspiral informed choice of priors. At the same time, $\kappa_2^T$ is very poorly determined, serving to verify the fact that once the $f_2 - \kappa_2^T$ universal relation has been omitted from the model, there exists no tidal information solely from the postmerger signal.

Finally, in Fig. 6.16, we present the waveform reconstruction for the case of inspiral agnostic priors. Like in the case of the inspiral informed priors, the postmerger estimation of $f_2^{\rm peak}$ is accurate and distinguishable between hadronic and quark models. Additionally, the signal is reliably reconstructed as shown by the fact that most of the postmerger SNR is recovered (see Table 6.5).

## 6.6 Appendix 2: Inspiral Informed PE: results for all simulations

In this appendix, we present results analogous to Figs. 6.6 and 6.7 for all the systems as listed in Table 6.4 with the ET detector and the `NRPMw` model at a postmerger SNR of 10. In particular, in Figs. 6.18 and 6.19 we show the posterior PDFs for $f_2^{\rm peak}$ and $\kappa_2^T$. As mentioned previously in subsection 6.3.1, the `NRPMw` model performs very well with the quark EOSs, in that the 90% CI of $f_2^{\rm peak}$ posteriors contain the injection. However, for the hadronic simulations $1.398M_\odot - 1.198M_\odot$ (BLh), $1.289M_\odot - 1.289M_\odot$ (DD2F) and $1.298M_\odot - 1.298M_\odot$ (BLh), the estimation of $f_2^{\rm peak}$ is biased due to the presence of multiple amplitude modulations as explained in Fig. 6.21. We also show postmerger spectra for the waveform reconstructions in Fig. 6.20 that serve to re-affirm the detectability and distinguishability of the $f_2^{\rm peak}$ frequencies between the hadronic and quark models.

In Figs. 6.22 and 6.23, we show a comparison between posterior PDFs of the total mass $M$, mass ratio $q$ and tidal parameters $\Lambda_i$'s between the cases of inspiral informed and inspiral agnostic priors. We note the significant improvement in the estimation of masses and tidal parameters upon including inspiral information which is essentially a recovery of the priors that are informed of the inspiral signal. As we have stressed in the

main text, we require reliable estimates of the inspiral signal to consistently probe QCD phase transitions from the EOS insensitive relations.

## 6.7 Appendix 3 : Inference with unconstrained $f_2$ and $f_0$ parameters

In this appendix, we attempt to mitigate the source of bias in our hadronic models namely multiple amplitude modulations. We have seen in 6.3.1.1 that `NRPMw` can only capture the first two peaks of the postmerger amplitude modulations which leads to an overestimation of the $f_2^{\rm peak}$ frequency. We test a new model configuration, in which we attempt to increase the flexibility of the model by freeing from universal relations not just the postmerger peak frequency parameter $f_2$, but also the parameter that models the radial pulsation modes of the remnant, i.e., $f_0$. We call this model configuration as `NRPMw_v2` to distinguish from the other configurations employed in this work. This means that we do not use the recalibration parameter $\delta f_0$ which provided flexibility to the inference of $f_0$ when constrained from the universal relations instead, we set uniform priors on $f_0$ ranging between 0.1 to 2.5 kHz. The expectation is that making $f_0$ unconstrained can perhaps push the $\tilde{W}$pul wavelet that models amplitude modulations as defined in [284], to include more of the amplitude modulations.

We report however that this approach leads to only marginal improvements. We take the case of the $1.298M_\odot - 1.298M_\odot$ binary where the bias in measurement of $f_2^{\rm peak}$ is the largest. In figure 6.24, we report the same injection now being recovered from the modified `NRPMw_v2` model configuration. We report that with the `NRPMw` model, 99.5% CIs of the $f_2^{\rm peak}$ posterior contained the injection, which is now marginally improved to 97% CIs containing the injection with `NRPMw_v2`. Nevertheless, the model configuration still reliably reconstructs the postmerger signal with a recovered SNR of 8.6 corresponding to an injected SNR of 10.

Finally, in figure 6.25, we show a comparison of the joint $f_2^{\rm peak} - \kappa_2^T$ posterior between the `NRPMw` and the `NRPMw_v2` model configurations, with reference to the $f_2 - \kappa_2^T$ universal relation. For both the configurations, the 90% contours of the joint posterior capture the injection. We compute the Bayes' factor between the two models and find that $\log \mathcal{B}.\mathcal{F}^{\texttt{NRPMw}}_{\texttt{NRPMw\_v2}} = 0.06^{+0.28}_{-0.28}$ indicating that there is no preference to either models at a postmerger SNR of 10.

## 6.8 Declaration

The postmerger PE calculations and the consequent post-processing were performed by myself. Ish Gupta assisted in the computation of inspiral PE prior estimates. This chapter will also form a part of his dissertation. The contents of this chapter have been published in the journal Physical Review D of the American Physical Society (APS) with refernece [282].

**Table 6.3.** Prior ranges for the parameters of the `NRPMw` model, the extrinsic and intrinsic parameters in an inspiral informed setting. We constrain priors on $M$, $q$, $\Lambda_1$ and $\Lambda_2$ from the inspiral signal. In this table, we show details for the prior distribution employed for the $1.398M_\odot - 1.198M_\odot$ binary with the BLh EOS. The type of priors remains the same for all models in our work.

| parameter | min | max | Type |
|---|---|---|---|
| M [$M_\odot$] | 2.641 | 2.652 | $\text{Gaussian}^{\mu=2.646}_{\sigma=0.001}$ |
| $q$ | 1.11 | 1.22 | $\text{Gaussian}^{\mu=1.17}_{\sigma=0.01}$ |
| $\chi_1$ | -0.2 | 0.2 | aligned spin |
| $\chi_2$ | -0.2 | 0.2 | aligned spin |
| $\Lambda_1$ | 363.94 | 559.70 | $\text{Gaussian}^{\mu=448.24}_{\sigma=18.79}$ |
| $\Lambda_2$ | 1030.17 | 1203.71 | $\text{Gaussian}^{\mu=1123.61}_{\sigma=21.28}$ |
| R.A. | 0 | $2\pi$ | Uniform |
| DEC. | $-\pi/2$ | $\pi/2$ | Cosinusoidal |
| $\cos\,\iota$ | -1 | 1 | Uniform |
| $\psi$ | 0 | $\pi$ | Uniform |
| $D_L$ [Mpc] | 5 | 500 | Volumetric |
| $t_{\rm coll}/M$ | 1 | 3000 | Uniform |
| $M^2\alpha_{\rm peak}$ | $-10^{-4}$ | $10^{-4}$ | Uniform |
| $\phi_{\rm PM}$ | 0 | $2\pi$ | Uniform |
| $f_2$ [kHz] | 1.5 | 5 | Uniform |
| $\delta(Mf_0)$ | -1 | 2 | $\text{Gaussian}^{\mu=0}_{\sigma=0.449}$ |
| $\delta(Mf_{\rm mrg}/\nu)$ | -0.2 | 0.2 | $\text{Gaussian}^{\mu=0}_{\sigma=0.026}$ |
| $\delta(A_{\rm mrg}/M)$ | -0.2 | 0.2 | $\text{Gaussian}^{\mu=0}_{\sigma=0.018}$ |
| $\delta(M/t_0)$ | -0.5 | 0.5 | $\text{Gaussian}^{\mu=0}_{\sigma=0.092}$ |
| $\delta(A_0/M)$ | -1 | 4 | $\text{Gaussian}^{\mu=0}_{\sigma=0.663}$ |
| $\delta(A_1/M)$ | -1 | 2 | $\text{Gaussian}^{\mu=0}_{\sigma=0.152}$ |
| $\delta(A_2/M)$ | -1 | 2 | $\text{Gaussian}^{\mu=0}_{\sigma=0.385}$ |
| $\delta(A_3/M)$ | -1 | 2 | $\text{Gaussian}^{\mu=0}_{\sigma=0.269}$ |
| $\delta(M^2\mathcal{I}m(\alpha_{\rm fus})/\nu)$ | -4 | 4 | $\text{Gaussian}^{\mu=0}_{\sigma=0.751}$ |
| $\delta(M\mathcal{R}e(\beta_{\rm peak}))$ | -1 | 2 | $\text{Gaussian}^{\mu=0}_{\sigma=0.27}$ |
| $\delta(M\Delta_{\rm fm})$ | -1 | 4 | $\text{Gaussian}^{\mu=0}_{\sigma=0.744}$ |
| $\delta(M\Gamma_{\rm fm})$ | -1 | 4 | $\text{Gaussian}^{\mu=0}_{\sigma=0.977}$ |

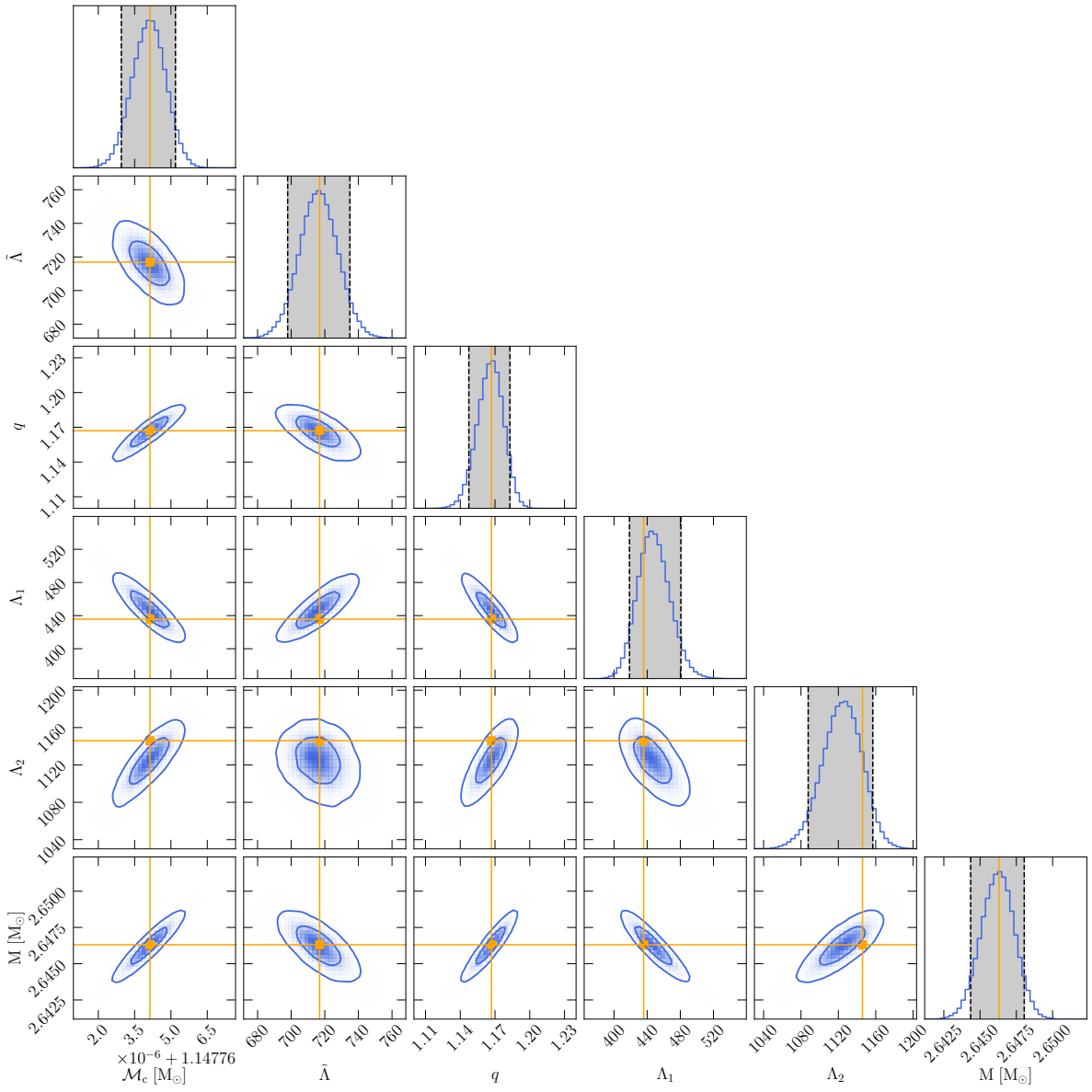


**Figure 6.3.** Corner plot depicting the posteriors on chirp mass $\mathcal{M}_c$, tidal deformability $\tilde{\Lambda}$, mass ratio $q$, individual tidal parameters $\Lambda_i$s and the total mass $M$ for the binary 1.398 $M_\odot$ - 1.198 $M_\odot$ with the BLh EOS. These posterior PDFs are computed from a self-consistent injection recovery of the `TaylorF2` waveform model corresponding to the binary parameters presented in Table 6.1 for the ET detector configuration. We show the 90% credible intervals in the 1-D posteriors in grey shaded regions and the 50% and 90% credible contours for the 2D joint posteriors.

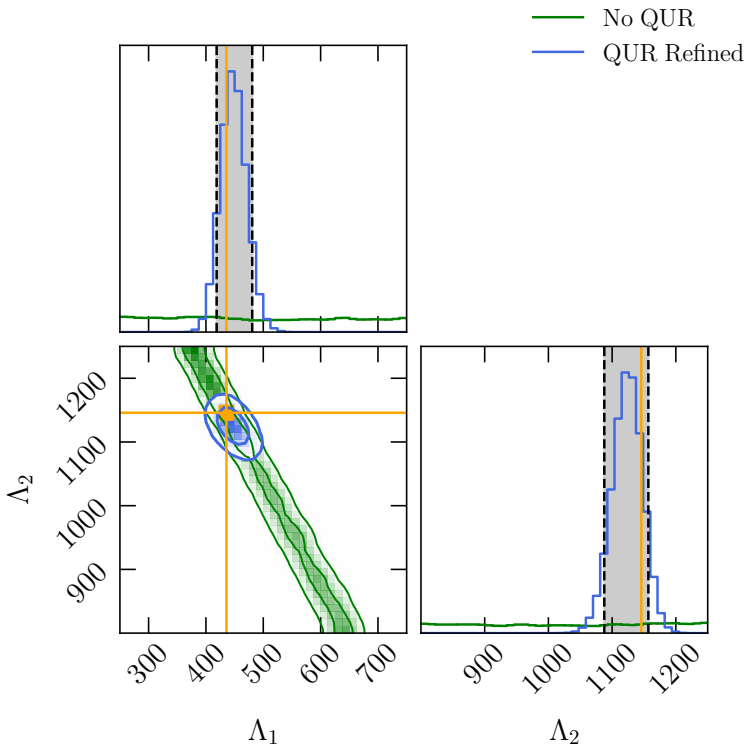


**Figure 6.4.** A corner plot showing a comparison between measurements of tidal parameters $\Lambda_1$ and $\Lambda_2$ when computed directly from inspiral and when refined using quasi-universal relations from [392]

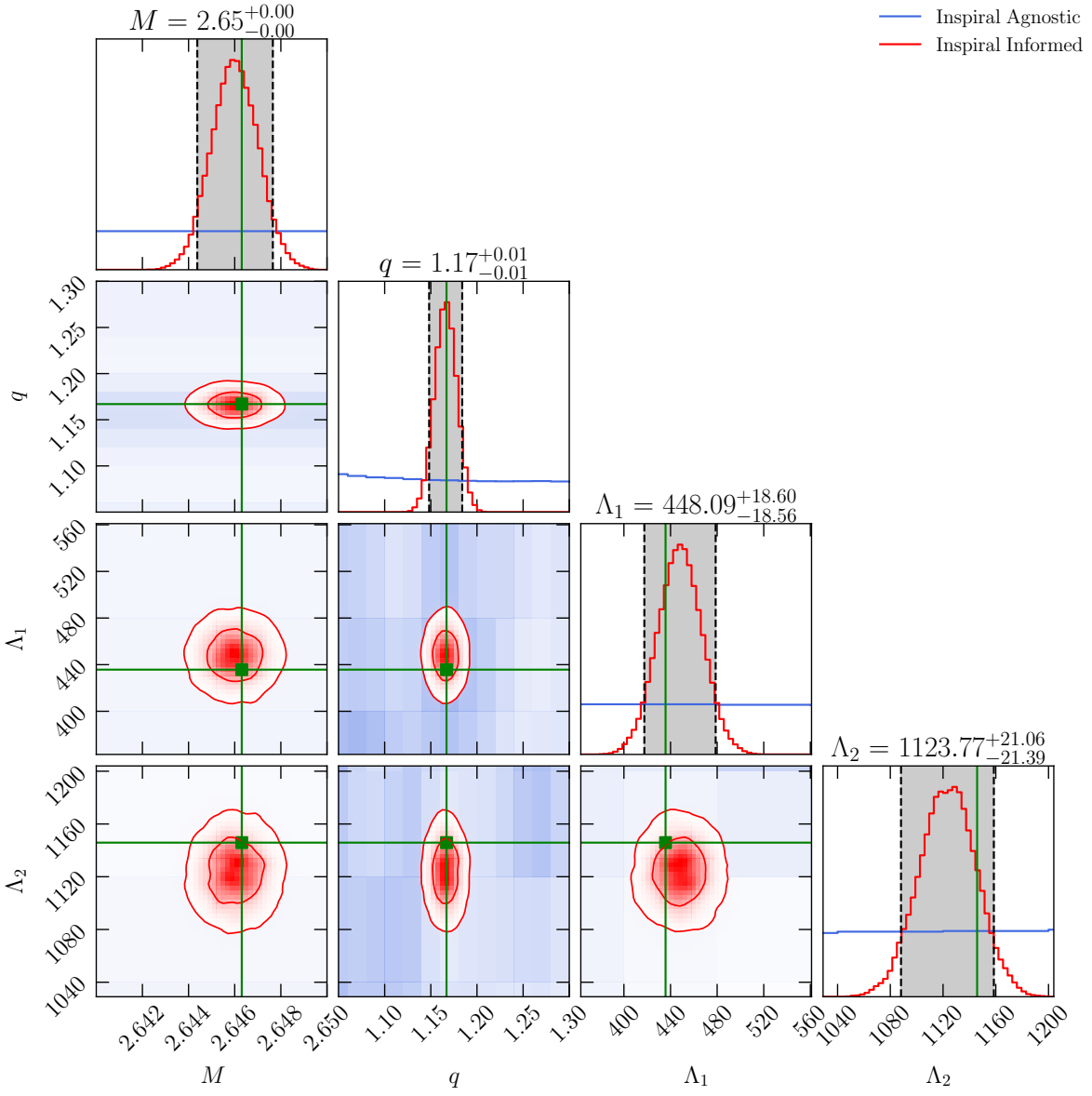


**Figure 6.5.** A corner plot showing a comparison between the two types of priors employed in our work, i.e., a broad prior on $M$, $q$, $\Lambda_1$ and $\Lambda_2$ and Gaussian distributions informed of these quantities from an independent parameter estimation of the inspiral signal.

**Table 6.4.** A summary of the properties of postmerger injections corresponding to the NR simulations reported in table 6.1. In this table we present these properties for the choice of priors that is informed by the inspiral signal as described in subsection 6.3.1. In particular, GW model represents the specific configuration of the NRPMw model utilized for the recovery. We us the NRPMw model in three configurations namely, `NRPMw`, where the $f_2$ parameter is **unconstrained** by the $f_2 - \kappa_2^T$ relation, `NRPMw_v1` where the $f_2$ parameter **is constrained** by the quasi universal relation, and the most flexible `NRPMw_v2` configuration where both $f_2$ and $f_0$ are unconstrained from their respective quasi universal relations. Detector is the GW datector used for the recovery of postmerger injections, $f^{\rm peak}_{2;\rm Injected}$ and $f^{\rm peak}_{2;\rm Recovered}$ are respectively the injected and recovered postmerger peak frequencies and $D_\ell$ is the luminosity distance of the binary from the detector. In the last two columns, we report the postmerger signal to noise ratios of the injected and recovered signals.

| Index | EOS | $m_1\ [M_\odot]$ | $m_2\ [M_\odot]$ | GW Model | Detector | $f^{\rm peak}_{2;\rm Injected}$ [kHz] | $f^{\rm peak}_{2;\ \rm Recovered}$ [kHz] | $D_\ell$ [Mpc] | $\rho_{\rm injected}$ | $\rho_{\rm recovered}$ |
|---|---|---|---|---|---|---|---|---|---|---|
| 1 | BLh | 1.298 | 1.298 | `NRPMw` | ET | 2.804 | $2.842^{+0.041}_{-0.025}$ | 89.049 | 10 | $8.73^{+1.08}_{-1.62}$ |
| 2 | BLQ | 1.298 | 1.298 | `NRPMw` | ET | 2.927 | $2.924^{+0.016}_{-0.025}$ | 93.474 | 10 | $8.61^{+1.10}_{-1.71}$ |
| 3 | BLh | 1.481 | 1.257 | `NRPMw` | ET | 2.962 | $2.948^{+0.016}_{-0.025}$ | 97.503 | 10 | $8.66^{+1.17}_{-1.49}$ |
| 4 | BLQ | 1.481 | 1.257 | `NRPMw` | ET | 3.143 | $3.145^{+0.303}_{-0.106}$ | 83.434 | 10 | $8.75^{+1.20}_{-1.19}$ |
| 5 | BLh | 1.398 | 1.198 | `NRPMw` | ET | 2.758 | $2.825^{+0.082}_{-0.066}$ | 87.027 | 10 | $7.82^{+0.95}_{-1.22}$ |
| 6 | BLQ | 1.398 | 1.198 | `NRPMw` | ET | 2.955 | $2.957^{+0.025}_{-0.033}$ | 87.500 | 10 | $8.75^{+1.17}_{-1.70}$ |
| 7 | BLh | 1.363 | 1.363 | `NRPMw` | ET | 3.074 | $3.055^{+0.033}_{-0.025}$ | 97.282 | 10 | $7.97^{+1.16}_{-1.66}$ |
| 8 | BLQ | 1.363 | 1.363 | `NRPMw` | ET | 3.197 | $3.268^{+0.09}_{-0.066}$ | 78.449 | 10 | $8.60^{+1.33}_{-1.35}$ |
| 9 | DD2F | 1.289 | 1.289 | `NRPMw` | ET | 2.889 | $2.916^{+0.025}_{-0.025}$ | 93.284 | 10 | $8.56^{+1.13}_{-1.70}$ |
| 10 | DD2F − SF1 | 1.289 | 1.289 | `NRPMw` | ET | 3.354 | $3.284^{+0.213}_{-0.172}$ | 78.247 | 10 | $8.53^{+1.25}_{-1.25}$ |
| 11 | DD2F − SF1 | 1.289 | 1.289 | `NRPMw` | ET | 3.354 | $3.325^{+0.106}_{-0.041}$ | 52.165 | 15 | $12.34^{+2.17}_{-1.87}$ |
| 12 | DD2F | 1.289 | 1.289 | `NRPMw` | CE-20 | 2.888 | $2.916^{+0.025}_{-0.025}$ | 118.467 | 10 | $8.59^{+1.12}_{-2.14}$ |
| 13 | DD2F − SF1 | 1.289 | 1.289 | `NRPMw` | CE-20 | 3.375 | $3.276^{+0.221}_{-0.09}$ | 89.078 | 10 | $8.48^{+1.15}_{-1.78}$ |
| 14 | DD2F − SF1 | 1.289 | 1.289 | `NRPMw_v1` | ET | 3.354 | $3.243^{+0.066}_{-0.106}$ | 78.247 | 10 | $8.40^{+1.23}_{-1.21}$ |
| 15 | BLQ | 1.298 | 1.298 | `NRPMw_v1` | ET | 2.927 | $2.924^{+0.016}_{-0.025}$ | 93.474 | 10 | $8.55^{+1.12}_{-1.65}$ |
| 16 | BLh | 1.298 | 1.298 | `NRPMw_v2` | ET | 2.804 | $2.834^{+0.033}_{-0.025}$ | 89.049 | 10 | $8.60^{+1.12}_{-1.62}$ |

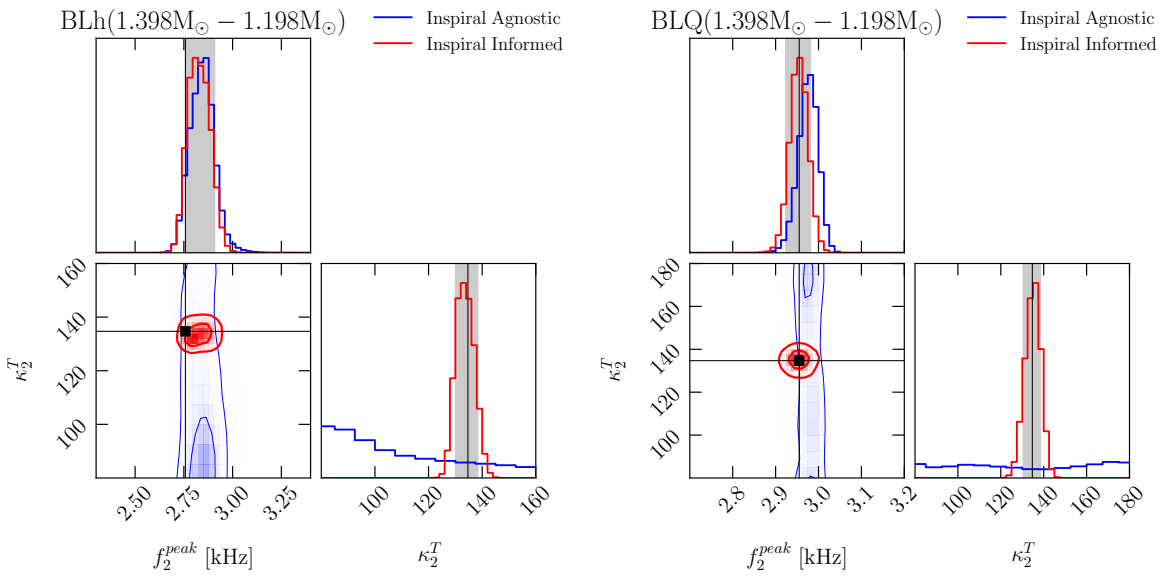


**Figure 6.6.** *Left Panel:* The posterior distribution on the postmerger peak frequency $f_2^{\rm peak}$ and the tidal polarizability $\kappa_2^T$ for the binary $1.398M_\odot - 1.198M_\odot$ with the BLh EOS at a postmerger SNR of 10. We also show the 90% and 50 % contour levels for the joint PDF. Additionally, we compare the posteriors obtained from the two choices of priors namely an inspiral agnostic choice (in blue) and an inspiral informed choice (in red). We observe that using inspiral informed priors has marginal influence on $f_2^{\rm peak}$ but substantially improves the measurement of $\kappa_2^T$ as expected. *Right panel:* The same calculation for the corresponding quark model. Shown in grey shaded regions are the 90% CIs for the respective posteriors with inspiral informed priors. We note that for the quark EOS, `NRPMw` is able to recover the injected $f_2^{\rm peak}$ to within 90% CIs however, for the BLh (hadronic) case, the injected value lies at the boundary of the $5^{\rm th}$ percentile. Nevertheless, for both the cases the injection lies within the 90% contour of the joint PDF.

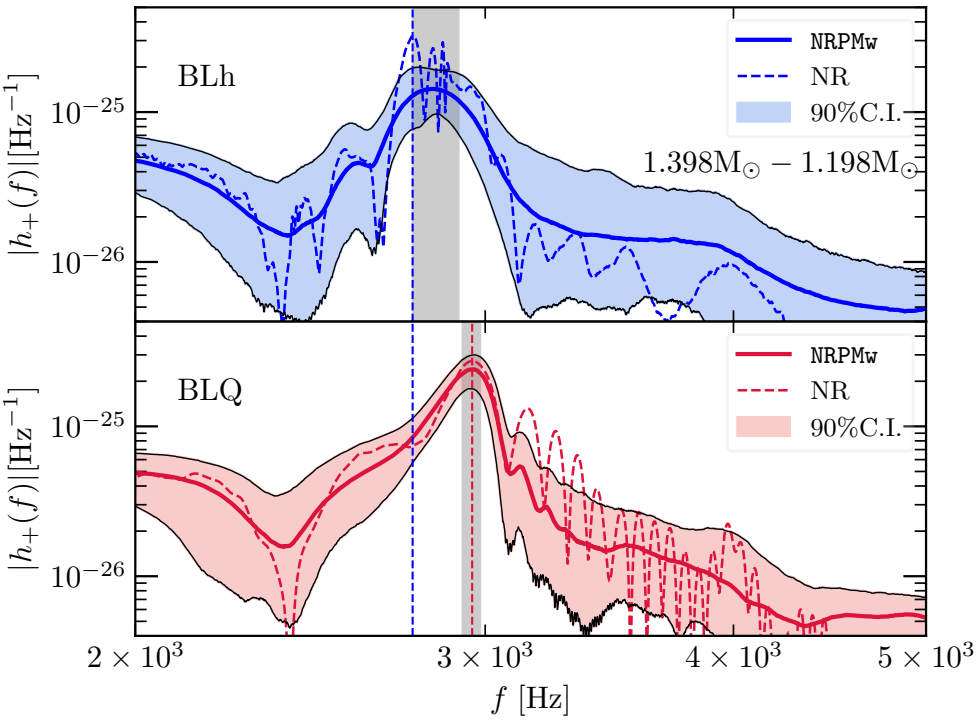


**Figure 6.7.** Reconstructed spectra for the binary $1.398M_\odot - 1.198M_\odot$ with the BLh and BLQ EOSs at a postmerger SNR of 10. The dotted curves represnt the injected spectra and the solid curves represent the median reconstructed signal by `NRPMw`. We also show 90% CIs on the reconstructed signal in the shaded regions. Vertical dotted lines correspond to the injected $f_2^{\mathrm{peak}}$ and the grey shaded regions represent the 90% CIs on the $f_2^{\mathrm{peak}}$ posteriors.

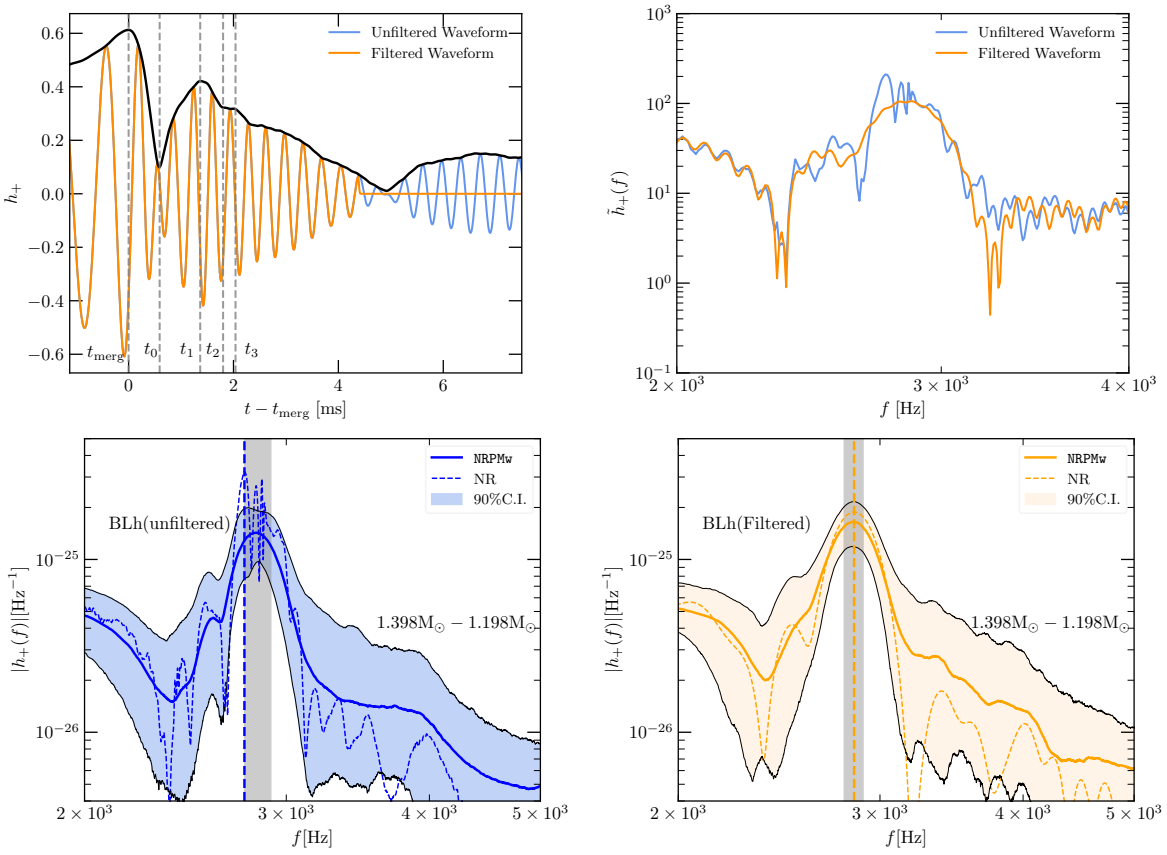


**Figure 6.8.** *Upper Left panel:* The time domain postmerger waveform for the BLh - $1.398M_\odot - 1.198M_\odot$ binary with and without an exponential filter. `NRPMw` works best for the early postmerger where it can capture the 1$^{\rm st}$ two amplitude modulations that peak at $t_1$ and $t_3$ respectively. The model, as of now, cannot capture subsequent amplitude modulations. *Upper Right Panel:* The frequency spectra of the corresponding unfiltered and filtered waveforms that show a shift in $f_2^{\rm peak}$ upon exclusion of amplitude modulations at $t - t_{\rm merg} \gtrsim 5$ ms. *Bottom Panel:* The reconstructed spectra for the unfiltered waveform (left) and the filtered waveform (right) that show the bias in $f_2^{\rm peak}$'s measurement because of the $3^{rd}$ and subsequent amplitude modulations. We see that upon filtering these modulations, the model is able to capture the $f_2^{\rm peak}$ to within 90% CIs.

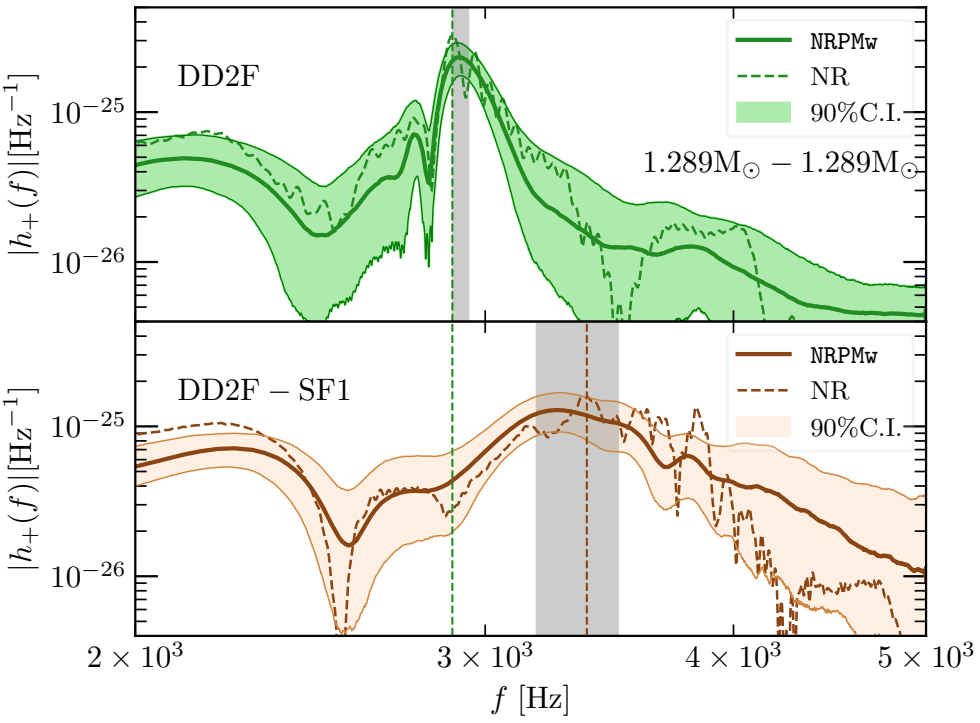


**Figure 6.9.** The reconstructed spectra corresponding to an inspiral informed postmerger PE for the binary $1.289M_\odot - 1.289M_\odot$ with the DD2F and DD2F-SF1 EOSs, computed with the postmerger optimized CE-20 detector. Like in the case of recovery from Einstein Telescope (Fig. 6.20), here also we see that multiple amplitude modulations can bias the recovery of $f_2^{\rm peak}$ for DD2F.

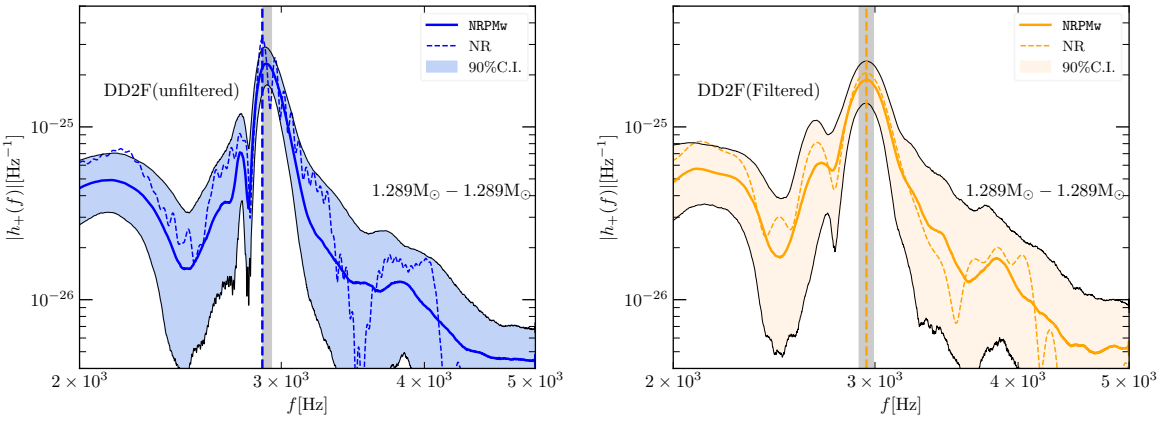


**Figure 6.10.** Same calculation as in fig. 6.8 to show the impact of multiple amplitude modulations on the recovery of $f_2^{\rm peak}$ for the hadronic DD2F simulation computed with the CE-20 detector. Here also we observe that filtering out the 3$^{\rm rd}$ and subsequent modulation in the postmerger amplitude can result in an accurate recovery of $f_2^{\rm peak}$ to within 90% CIs.

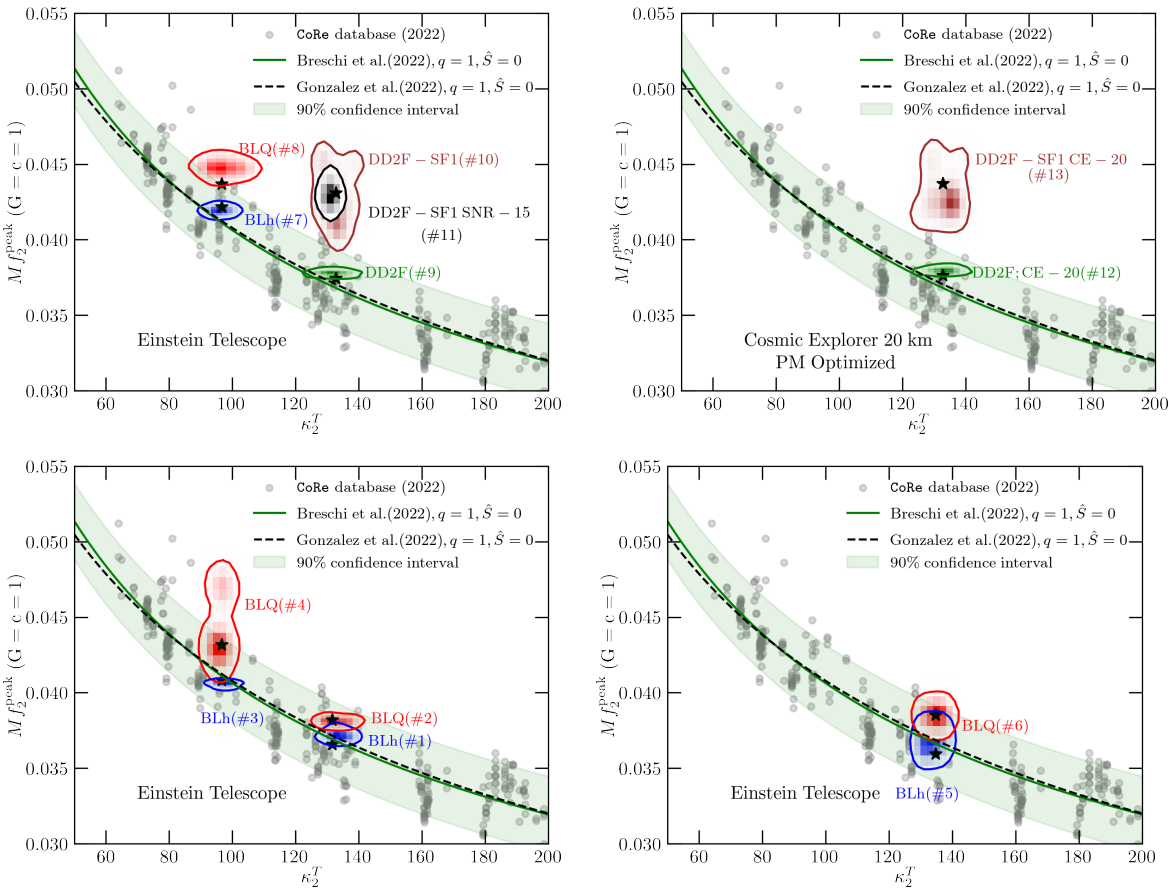


**Figure 6.11.** Quasi Universal relation from Breschi et al. [284] shown along with this work's Bayesian inference error estimates. Shown in grey scatter points, are the hadronic simulations from the `CoRe` database along with the fitting functions from [284] and [285] for non-spinning and symmetric binaries. The light green shaded region represents a 90% confidence interval corresponding to the fit function from [284] which is also implemented in the `NRPMw` model. Even though [285] updates upon the fit coefficients in [284], the two are within 90% confidence of each other. Black stars denote the injected values in a 2D parameter space of $Mf_2$ and $\kappa_2^T$. The colored shaded regions represent the 90% contours of the 2D joint posteriors on $Mf_2$ and $\kappa_2^T$ obtained in this study. In parenthesis we depict the simulation index of the binaries as defined in Table 6.4. *Top Panels:* We show binaries which are non-degenerate with respect to each other upto 90% CIs and with the universal relation. *Bottom Panels:* We show models which are not mutually distinguishable to 90 %.

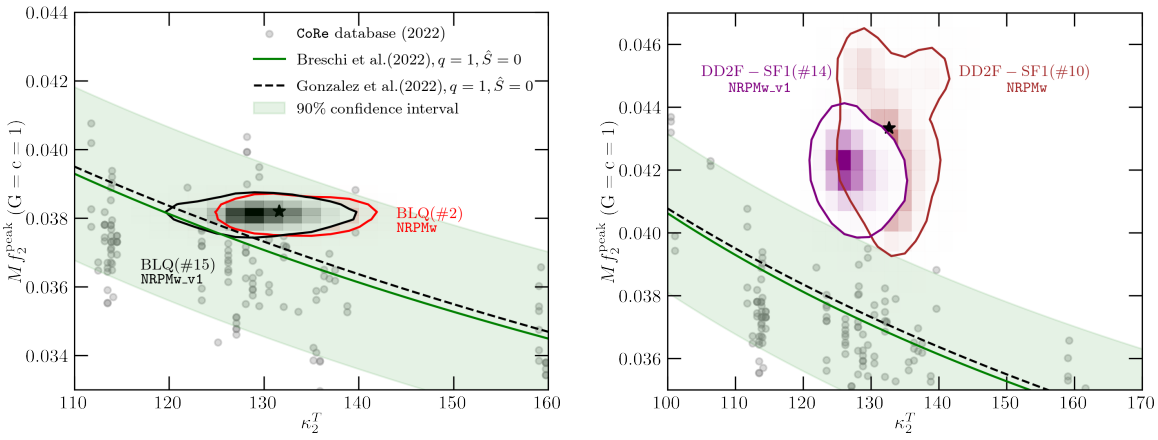


**Figure 6.12.** A comparison of the joint inference of $f_2^{\rm peak}$ and $\kappa_2^T$ between two configurations of `NRPMw`, i.e., excluding the $f_2^{\rm peak} - \kappa_2^T$ universal relation (`NRPMw`) and including the $f_2^{\rm peak}$ universal relation (`NRPMw_v1`). *Left Panel:* Results for the $1.298M_\odot - 1.298M_\odot$ binary with the BLQ EOS whose injection follows the universal relation. Both the model configurations can recover the injection with the data (injection) slightly preferring the QUR informed model `NRPMw_v1`. *Right panel*: Results for the $1.289M_\odot - 1.289M_\odot$ binary with the DD2F-SF1 EOS whose injection strongly violates the universal relation. The data (injection) slightly prefers the more flexible QUR uninformed model (`NRPMw`) as it has larger flexibility than `NRPMw_v1` in reference to recovering injections that violate the universal relation.

**Table 6.5.** Same properties as presented in table 6.4 but now for the choice of inspiral agnostic priors.

| Index | EOS | $m_1$ $[M_\odot]$ | $m_2$ $[M_\odot]$ | GW Model | Detector | $f^{\rm peak}_{2;\rm Injected}$ [kHz] | $f^{\rm peak}_{2;\rm Recovered}$ [kHz] | $D_\ell$ [Mpc] | $\rho_{\rm injected}$ | $\rho_{\rm recovered}$ |
|---|---|---|---|---|---|---|---|---|---|---|
| 1 | BLh | 1.298 | 1.298 | NRPMw | ET | 2.804 | $2.825^{+0.033}_{-0.025}$ | 89.049 | 10 | $8.88^{+1.07}_{-1.59}$ |
| 2 | BLQ | 1.298 | 1.298 | NRPMw | ET | 2.927 | $2.924^{+0.025}_{-0.025}$ | 93.474 | 10 | $8.64^{+1.08}_{-1.61}$ |
| 3 | BLh | 1.481 | 1.257 | NRPMw | ET | 2.962 | $2.957^{+0.016}_{-0.025}$ | 97.503 | 10 | $8.79^{+1.12}_{-1.47}$ |
| 4 | BLQ | 1.481 | 1.257 | NRPMw | ET | 3.143 | $3.284^{+0.139}_{-0.246}$ | 83.434 | 10 | $8.72^{+1.15}_{-1.11}$ |
| 5 | BLh | 1.398 | 1.198 | NRPMw | ET | 2.758 | $2.842^{+0.098}_{-0.09}$ | 87.027 | 10 | $7.89^{+0.88}_{-1.15}$ |
| 6 | BLQ | 1.398 | 1.198 | NRPMw | ET | 2.955 | $2.973^{+0.033}_{-0.033}$ | 87.500 | 10 | $8.66^{+1.22}_{-1.43}$ |
| 7 | BLh | 1.363 | 1.363 | NRPMw | ET | 3.073 | $3.055^{+0.025}_{-0.033}$ | 97.282 | 10 | $7.97^{+1.19}_{-1.52}$ |
| 8 | BLQ | 1.363 | 1.363 | NRPMw | ET | 3.197 | $3.284^{+0.279}_{-0.147}$ | 78.449 | 10 | $8.13^{+1.21}_{-1.29}$ |
| 9 | DD2F | 1.289 | 1.289 | NRPMw | ET | 2.889 | $2.907^{+0.025}_{-0.025}$ | 93.284 | 10 | $8.51^{+1.12}_{-1.48}$ |
| 10 | DD2F − SF1 | 1.289 | 1.289 | NRPMw | ET | 3.354 | $3.432^{+0.066}_{-0.139}$ | 78.247 | 10 | $8.60^{+1.38}_{-1.20}$ |

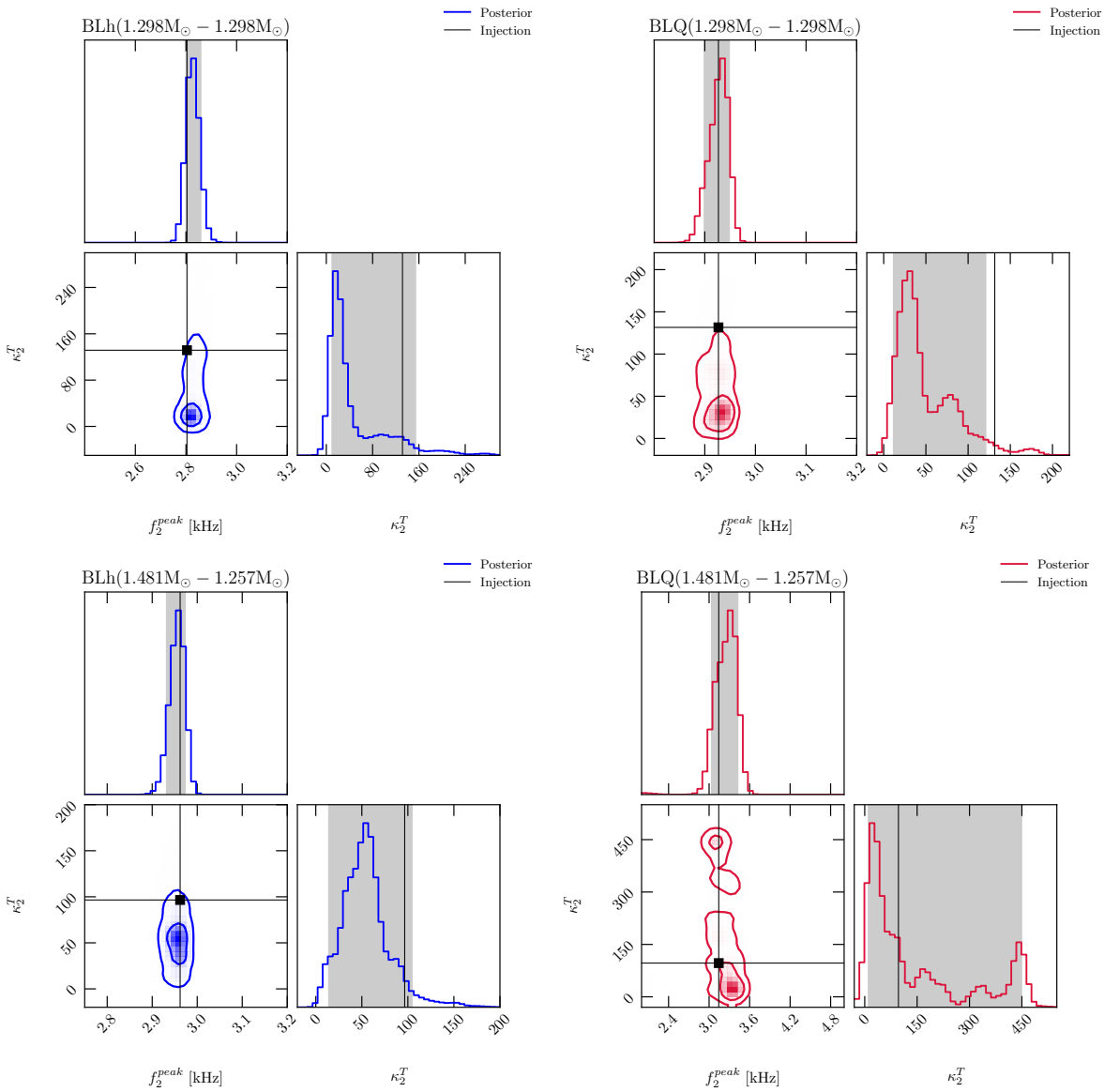


**Figure 6.13.** Same calculations as in Fig. 6.6, i.e., a measurement of $f_2^{\rm peak}$ and $\kappa_2^T$ for the $1.298M_\odot - 1.298M_\odot$ and $1.481M_\odot - 1.257M_\odot$ binaries with the BLh and BLQ EOSs. In contrast to Fig. 6.6, here we use a different choice of priors that are uninformed of the inspiral signal and set to wide ranges as described in Table 6.2. We note that the `NRPMw` model captures to within 90% CIs the $f_2^{\rm peak}$ frequency for the quark and hadronic models however, the tidal polarizability $\kappa_2^T$ is poorly determined owing to the fact that no tidal information is present in the postmerger signal.

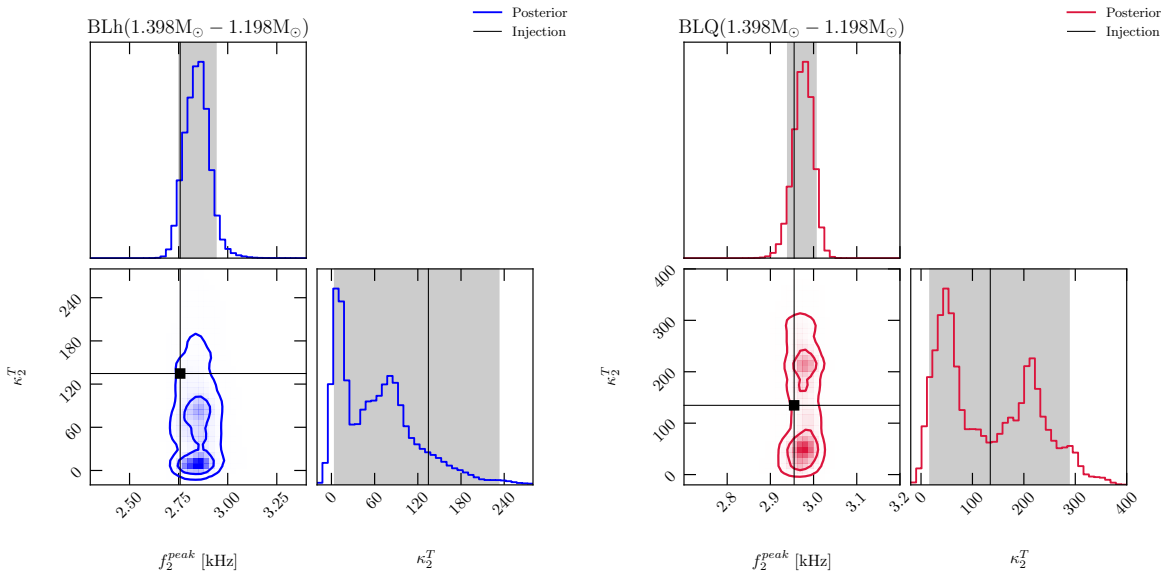


**Figure 6.14.** Same calculations as in Figure 6.13 for the binary $1.398M_\odot - 1.198M_\odot$ simulated with the BLh and BLQ EOSs.

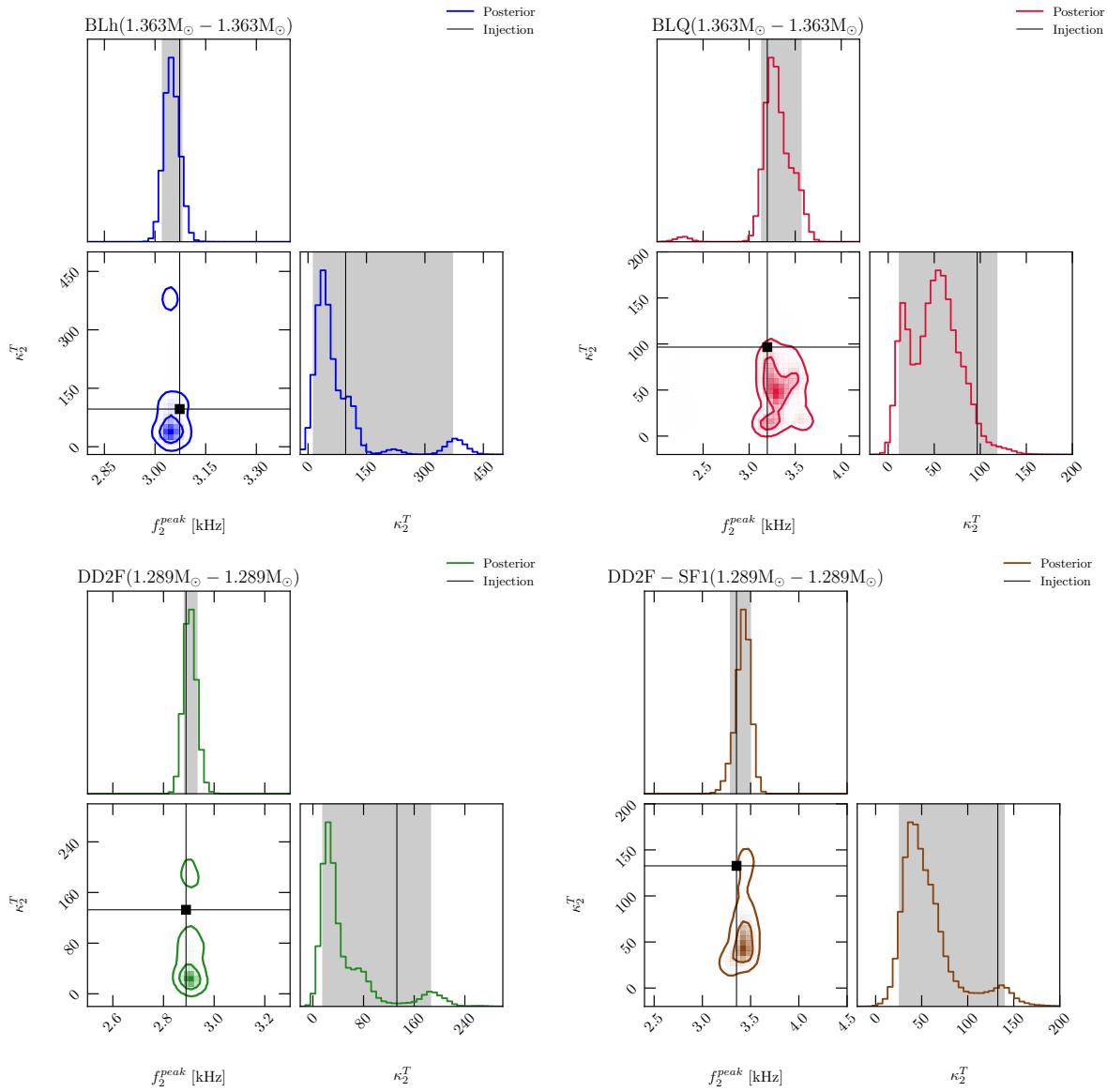


**Figure 6.15.** Same calculations as in Figure 6.13 for the binary $1.363M_\odot - 1.363M_\odot$ simulated with the BLh and BLQ EOSs and the binary $1.289M_\odot - 1.289M_\odot$ simulated with the DD2F and DD2F-SF1 EOS.

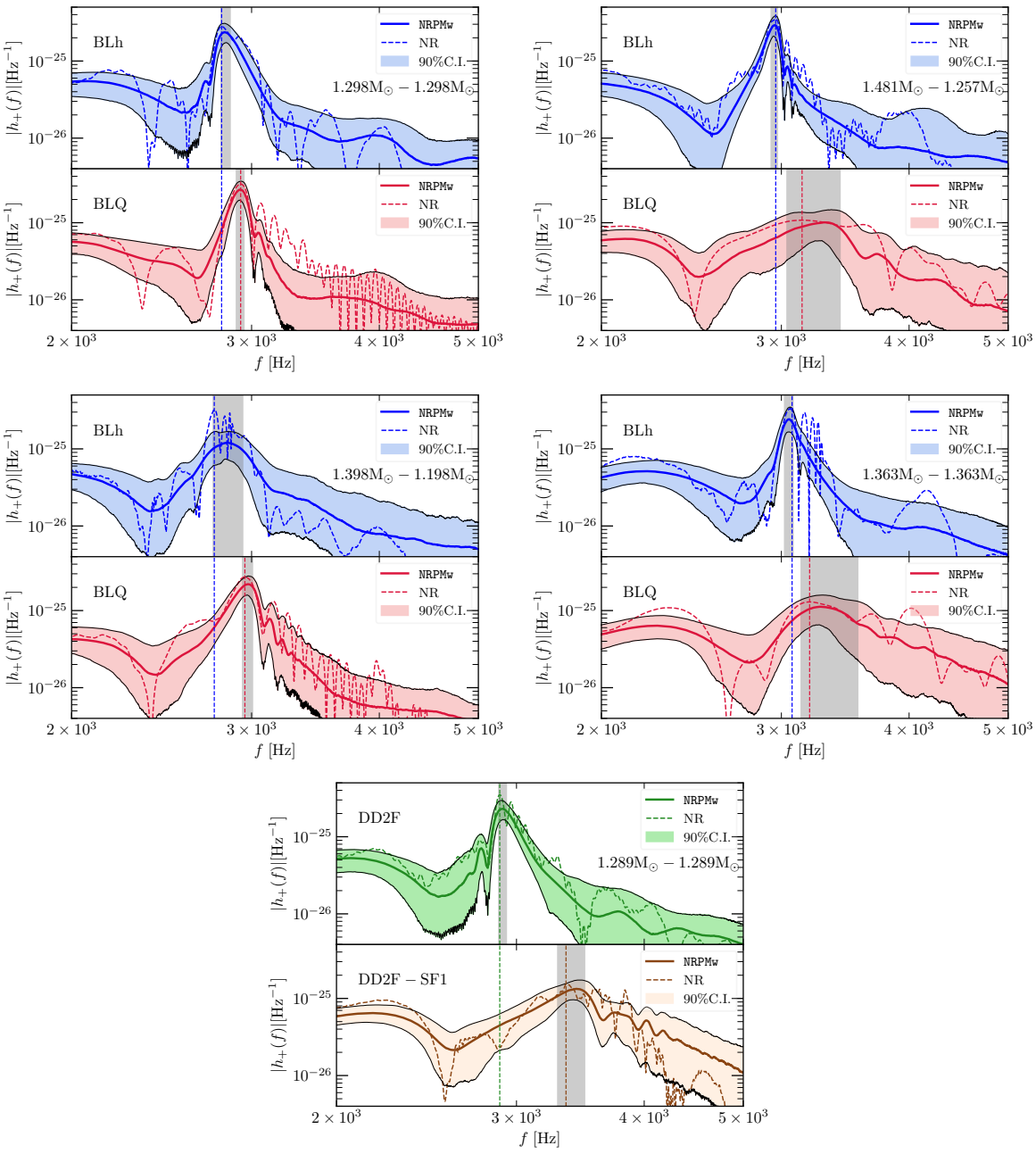


**Figure 6.16.** Same calculation as in Fig. 6.7, i.e. reconstructed spectra for all the binaries in our work but computed with priors that are uninformed of the inspiral signal. We observe an accurate recovery of $f_2^{\rm peak}$ and distinguishability between hadronic and quark models to 90% at a postmerger SNR of 10.

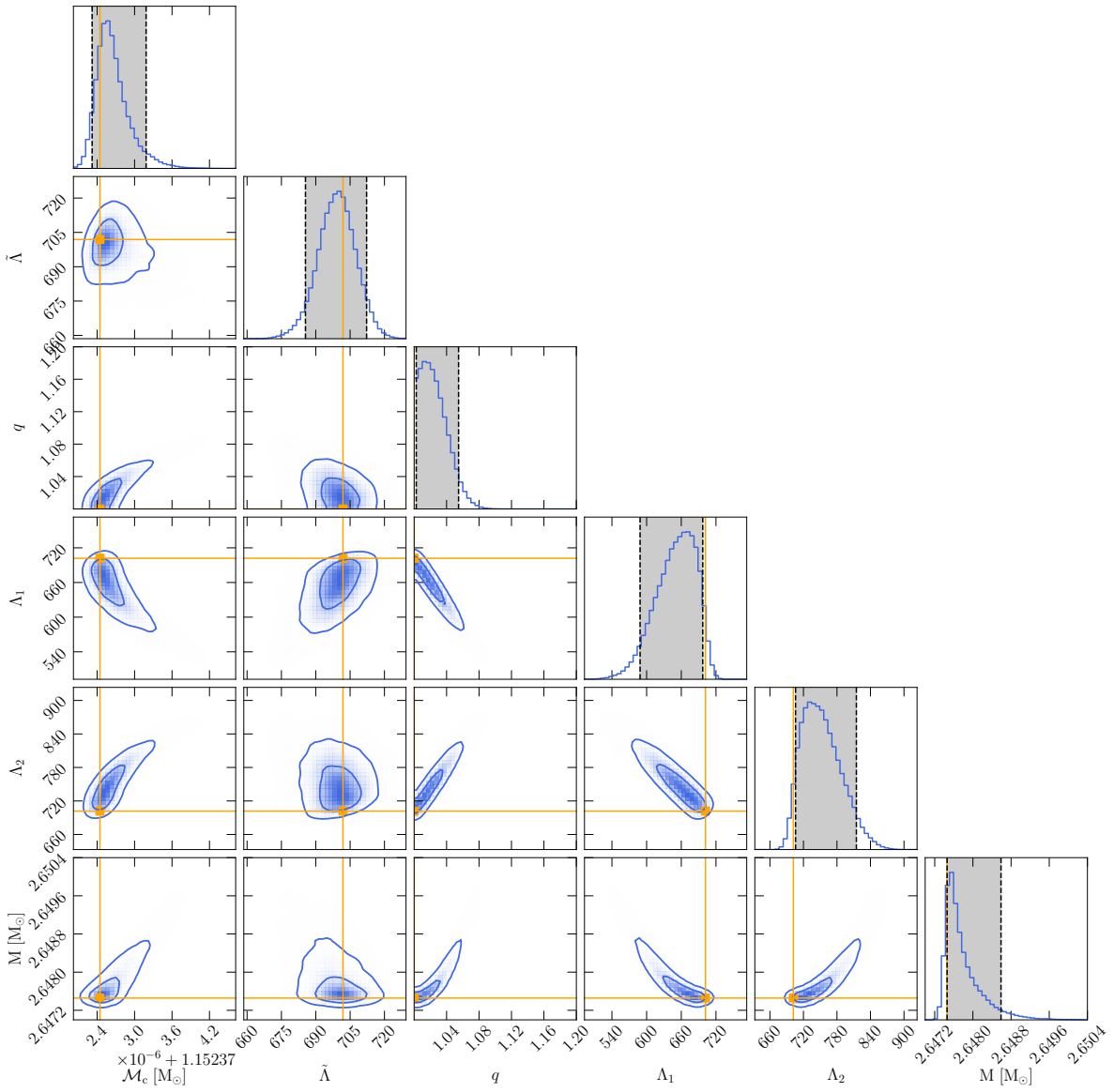


**Figure 6.17.** Corner plot depicting the posteriors on chirp mass $\mathcal{M}_c$, tidal deformability $\tilde{\Lambda}$, mass ratio $q$, individual tidal parameters $\Lambda_i$s and the total mass $M$ for the binary 1.298 $M_\odot$ - 1.298 $M_\odot$ with the BLh EOS. The fact that the posteriors on mass ratio are one-sided influences the measurements of $\Lambda_1$, $\Lambda_2$ and $M$.

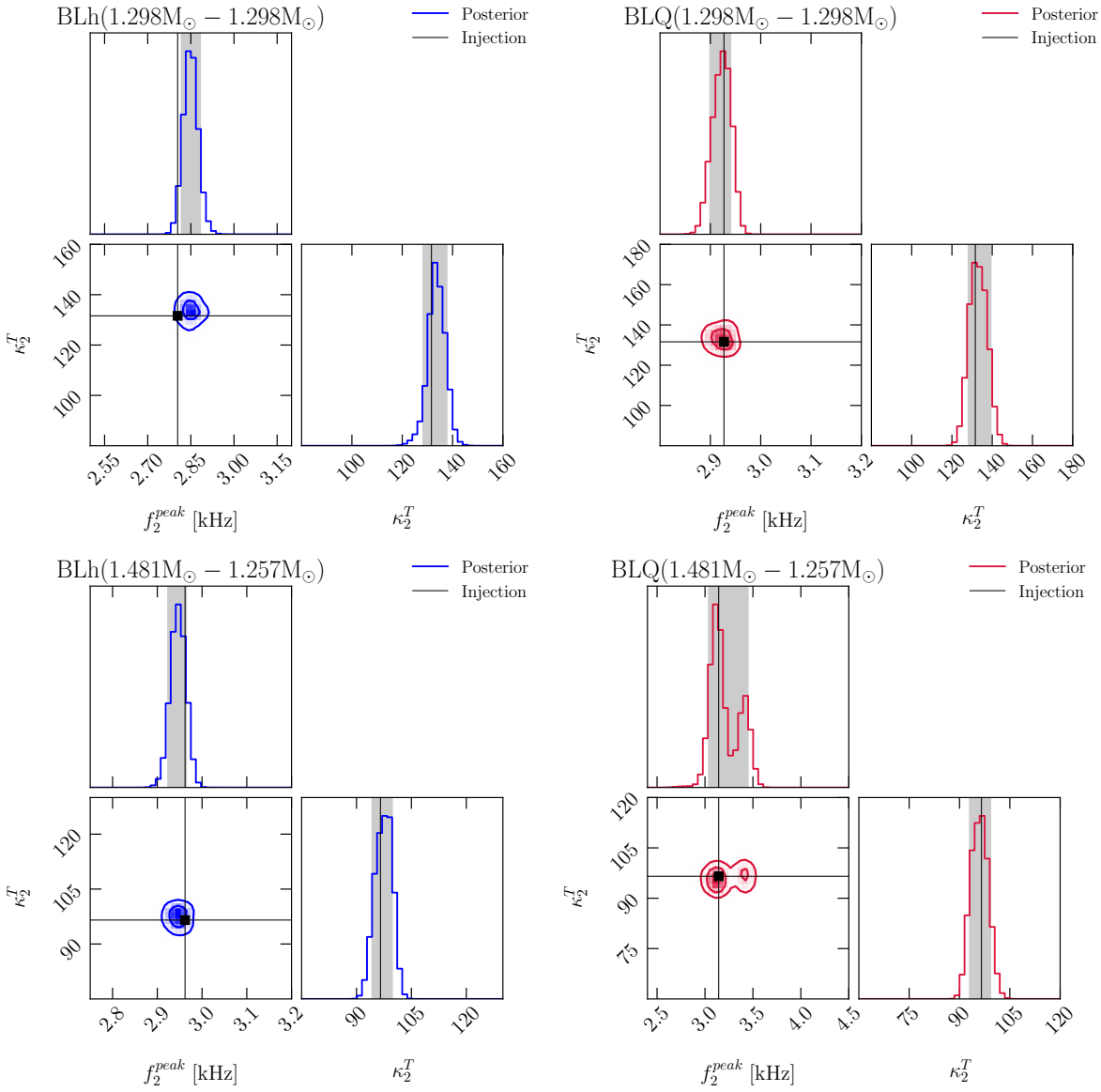


**Figure 6.18.** Same calculations as in Fig. 6.6 for the binaries $1.298M_\odot - 1.298M_\odot$ and $1.481M_\odot - 1.257M_\odot$ with the BLh and BLQ EOSs. We note that the `NRPMw` model captures to within 90% CIs the $f_2^{\rm peak}$ frequency for the quark EOSs however the measurement of the same for hadronic model $1.298M_\odot - 1.298M_\odot$ suffers from a systematic bias that of multiple amplitude modulations. The double-peaked feature in the 1.481 $M_\odot$ - 1.257 $M_\odot$ binary is because this system is the shortest-lived of all our simulations due to which the uncertainties in the measurement of postmerger frequency are the highest.

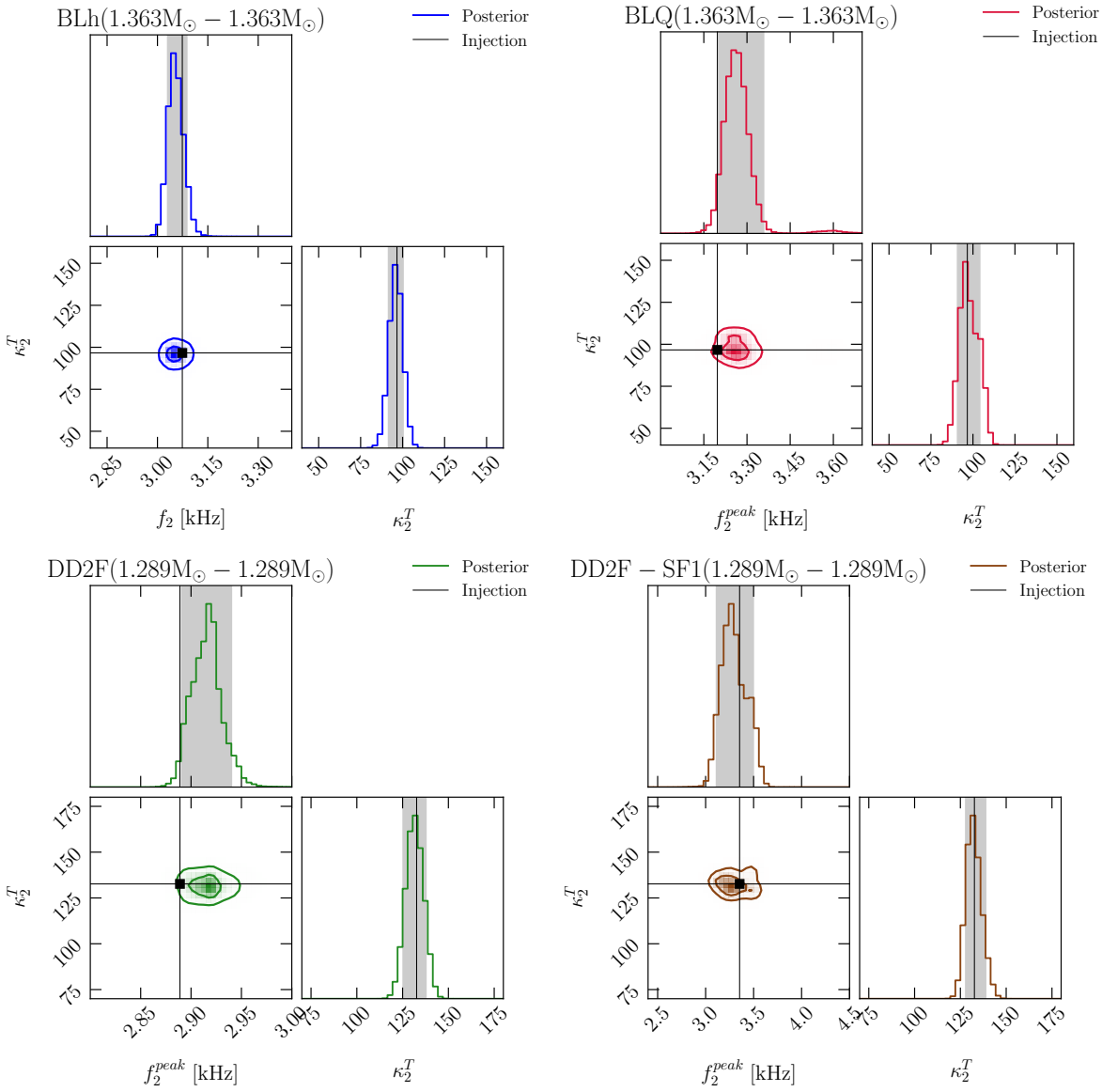


**Figure 6.19.** Same calculations as in Fig. 6.6 for the binary $1.363M_\odot - 1.363M_\odot$ with the BLh and BLQ EOS and the binary $1.289M_\odot - 1.289M_\odot$ with the DD2F and DD2F-SF1 EOS.

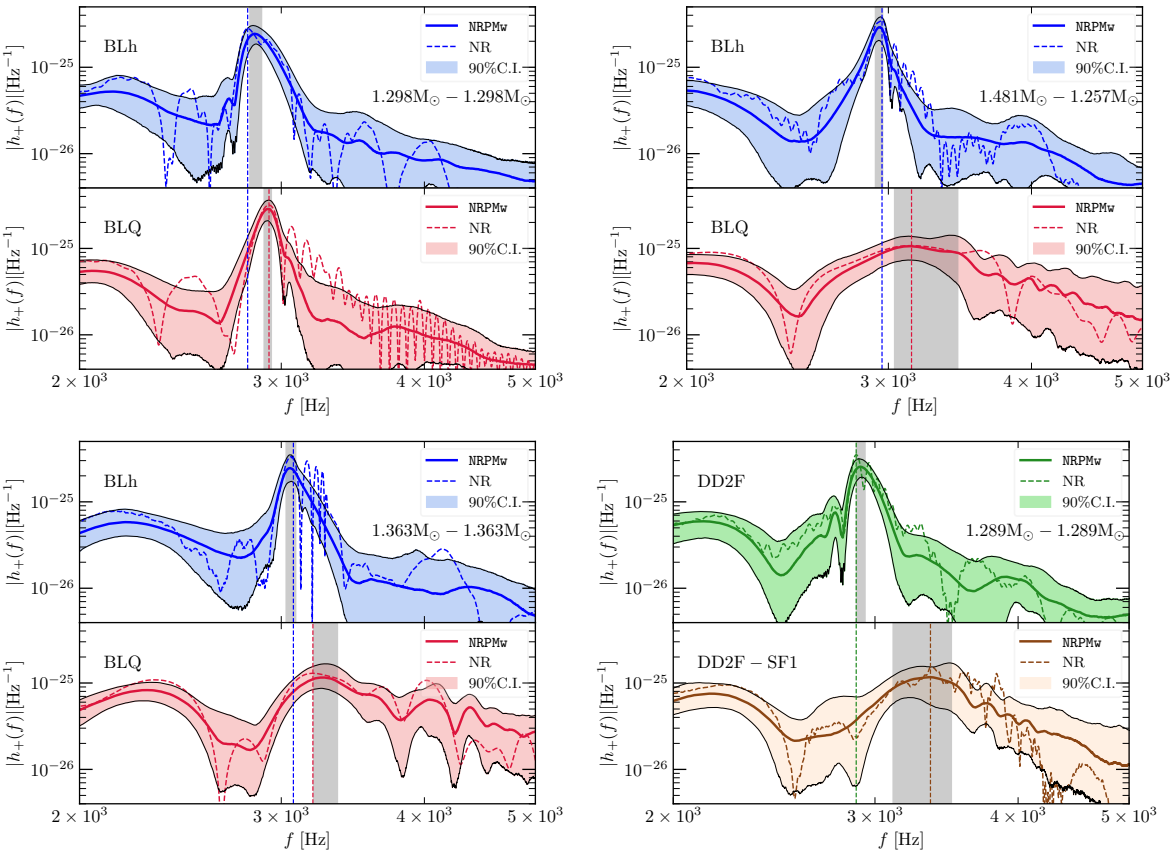


**Figure 6.20.** Same calculation as in Fig. 6.7, i.e., reconstructed spectra for the binaries $1.298M_\odot - 1.298M_\odot$, $1.481M_\odot - 1.257M_\odot$ and $1.363M_\odot - 1.363M_\odot$ with the BLh and BLQ EOS as well as for the binary $1.289M_\odot - 1.289M_\odot$ with the DD2F and DD2F-SF1 EOS.

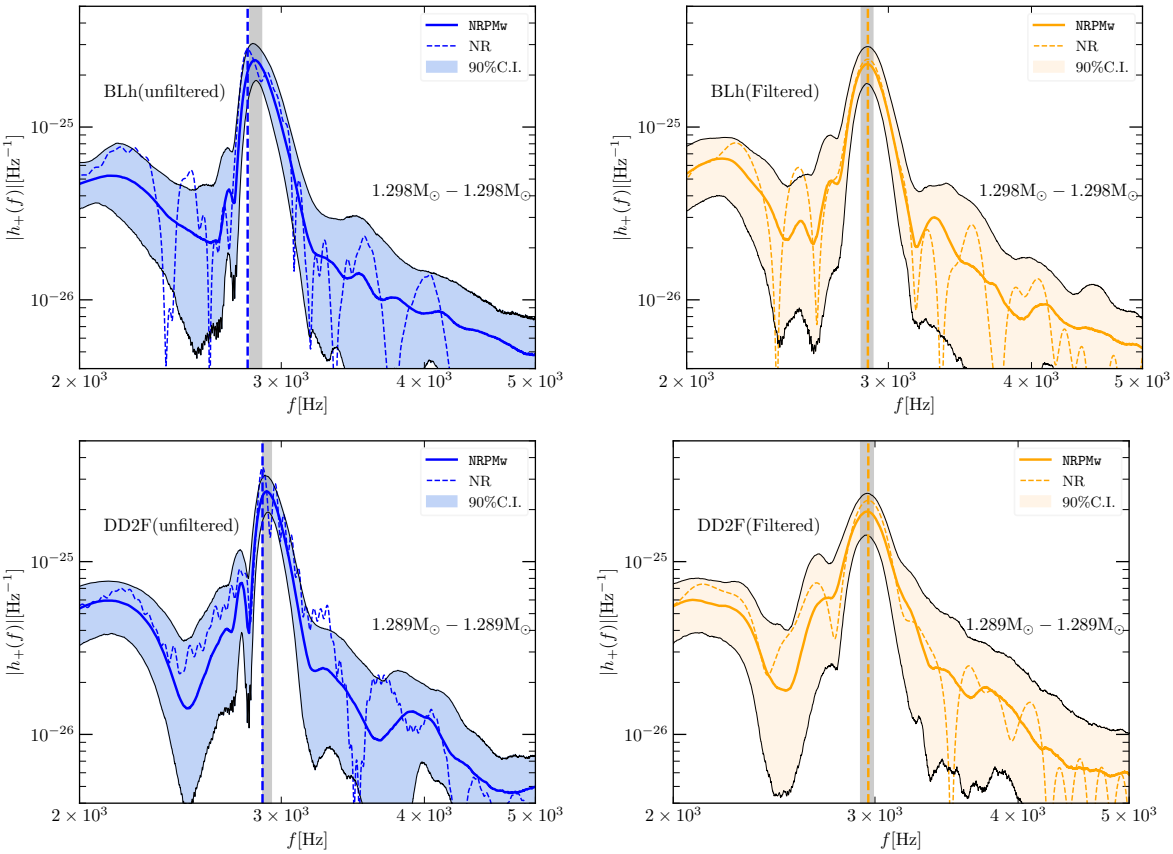


**Figure 6.21.** Same calculations as in Figure 6.8 for the binary $1.298M_\odot - 1.298M_\odot$ with the BLh EOS and the binary $1.289M_\odot - 1.289M_\odot$ with the DD2F EOS. Here, we show that the exclusion of more than 2 amplitude modulations in the strain can lead to recovery of the $f_2^{\rm peak}$ to within 90% CIs at a postmerger SNR of 10.

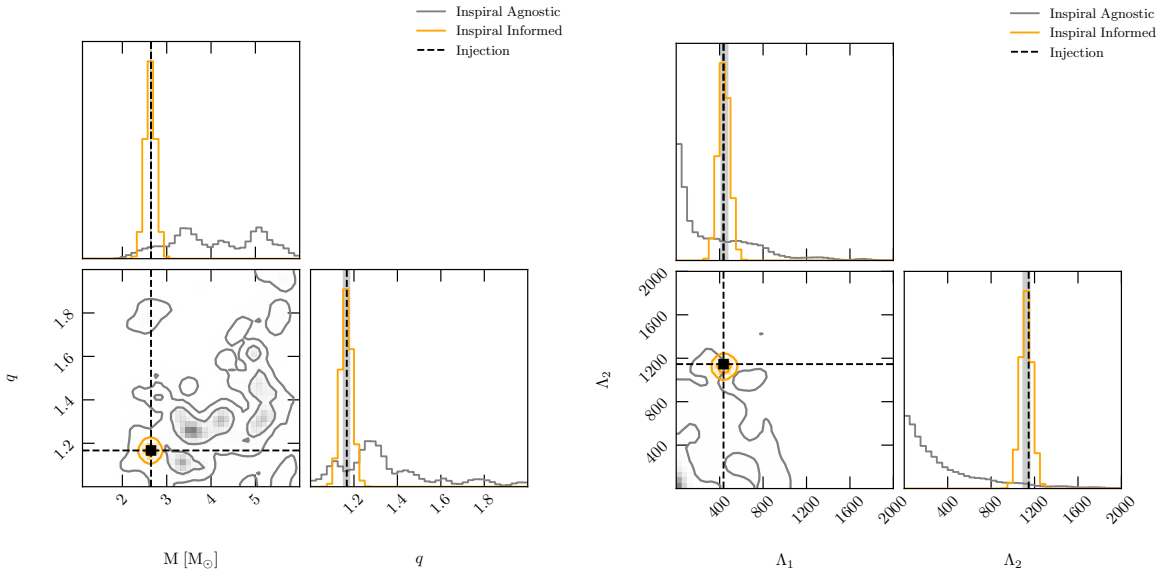


**Figure 6.22.** *Left Panel*: The posterior distributions of the total mass and mass ratio from a postmerger PE of the binary $1.398M_{\odot} - 1.198M_{\odot}$ with the BLh EOS compared between the two choice of priors used in this work. *Right Panel*: the posterior PDFs for the component tidal deformabilities. In both cases we notice a clear improvement in accuracy for the measurement of $M, q, \Lambda_1$ and $\Lambda_2$.

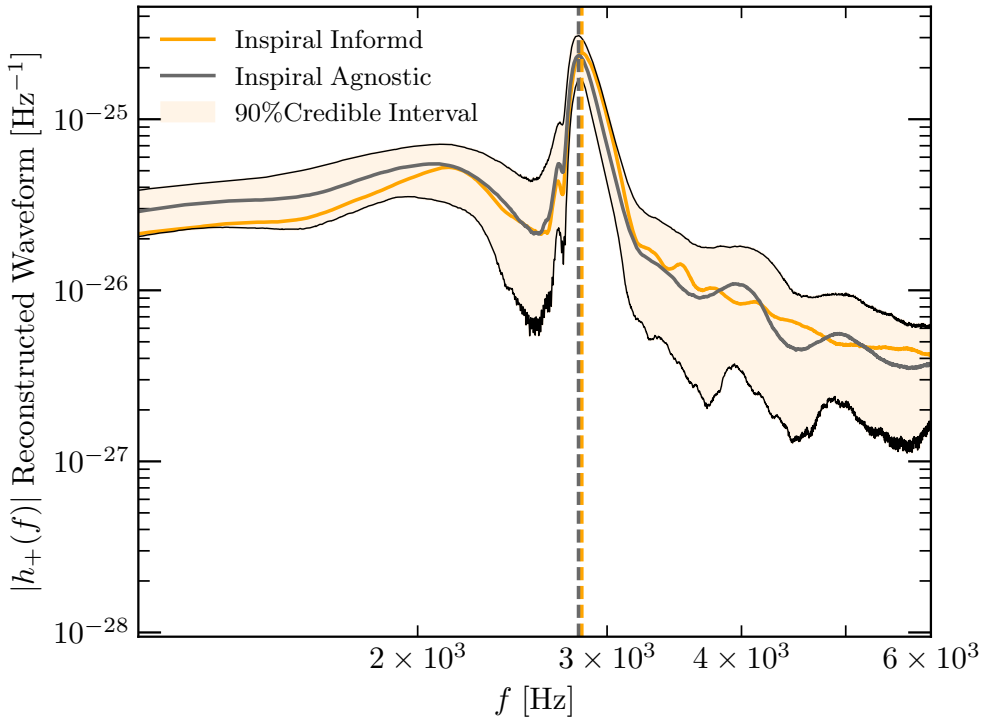


**Figure 6.23.** The reconstructed `NRPMw` waveforms for a postmerger PE of the binary $1.398M_\odot - 1.198M_\odot$ with the BLh EOS corresponding to both the choices of priors. Both the reconstructions lie within the 90% CIs of each injection and the $f_2^{\rm peak}$ frequency shows only a miniscule deviation of $\approx$0.3%.

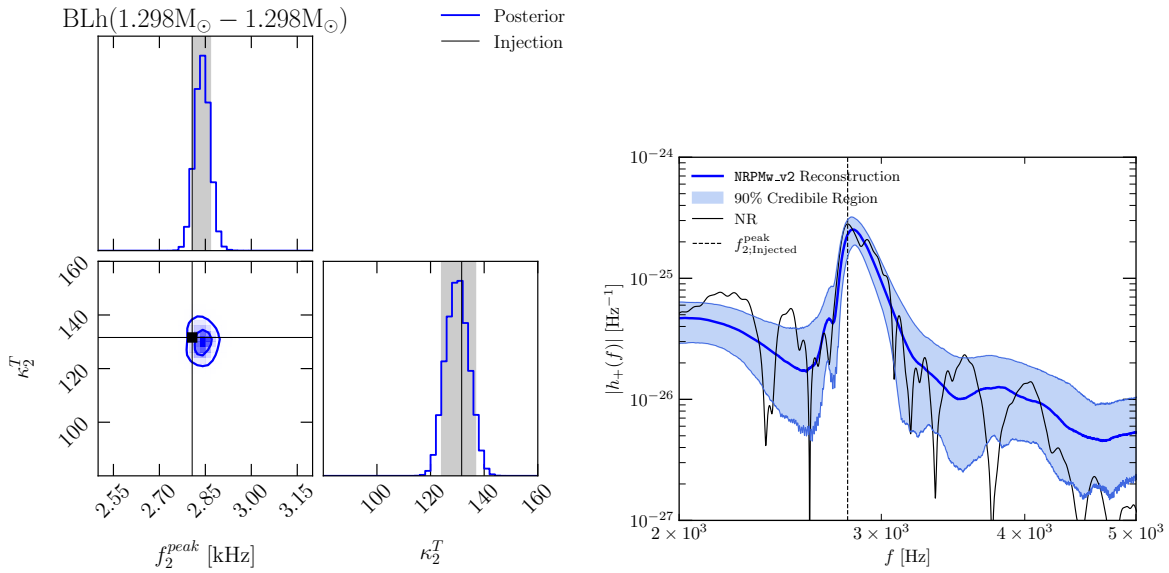


**Figure 6.24.** *Left Panel*: The posterior distributions of the postmerger peak frequency $f_2^{\mathrm{peak}}$ and the tidal polarizability $\kappa_2^T$ corresponding to the $1.298M_\odot - 1.298M_\odot$ binary with the BLh EOS. Also shown is the lack of covariance of $f_2^{\mathrm{peak}}$ with $\kappa_2^T$ owing to the corresponding QUR being not used. The contours correspond to the 50 % and 90% CIs of the joint PDF. *Right Panel*: The median reconstructed waveform from `NRPMw_v2` shown along with the NR waveform.

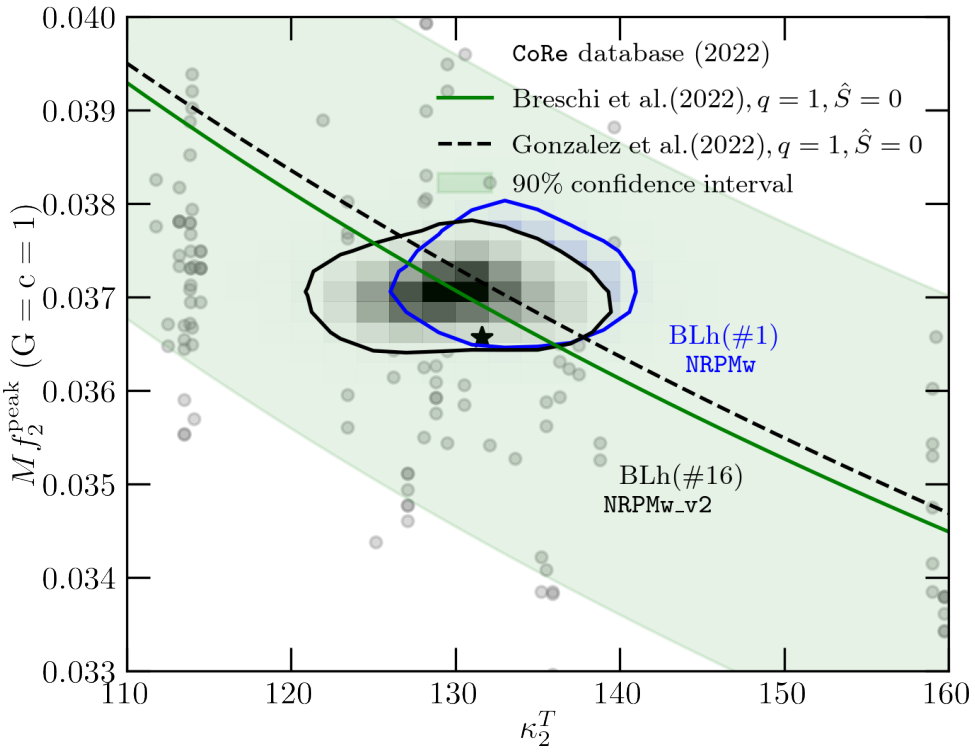


**Figure 6.25.** A comparison of the joint $f_2^{\rm peak} - \kappa_2^T$ posterior for the $1.298M_\odot - 1.298M_\odot$ binary between the `NRPMw` and `NRPMw_v2` model configurations. We see that the 90% contours of the joint posteriors for both the model configuratios contain the injection.

# Chapter 7
# Conclusions and Outlook

This dissertation is a small step towards understanding the nature of strongly interacting matter in the purview of neutron star mergers. We employ state-of-the-art general relativistic neutrino-radiation hydrodynamic simulations to model compact binary objects, in particular, mergers of neutron stars and mergers of strange stars. Throughout this dissertation we attempt to study models of QCD phase transitions from a phase of matter where quarks are confined within nucleons to a deconfined phase of quarks and gluons. Neutron stars and their mergers prove to be excellent test beds in this regard as they can probe extreme densities (several times the nuclear saturation density) and high temperatures (up to 10s of MeV or even higher) thereby providing access to thermodynamic regimes that are impregnable via any terrestrial laboratory.

In chapter 1, we provide the reader with a detailed introduction to the physics behind the several moving parts in a numerical relativity simulation and how the problem of QCD phase transitions interfaces with these simulations. Beginning in chapter 2, we compute several gravitational wave and electromagnetic signatures assuming a first-order phase transition were to take place within the remnant of a neutron star merger. In particular, we find that an onset of a deconfinement phase transition in the hot and dense parts of the remnant can compactify it thus making the remnant spin faster. This manifests as a relative increase in the postmerger peak frequency $f_2^{\rm peak}$ when compared to remnants that are evolved without a prescription of such a phase transition. However, the increments in $f_2^{\rm peak}$ are found to be degenerate with BNS mergers simulated from other hadronic equations of state. Therefore a gravitational wave distinguishability of quark models of the type described in the chapter against hadronic models, based solely on the values of $f_2^{\rm peak}$, is not feasible. We also note that owing to violent bounces in the quark remnant, the dynamical ejecta corresponding to a quark model can attain large relativistic velocities resulting in a brighter synchrotron afterglow as compared to the

afterglow from hadronic models.

In chapter 3, we discuss a novel signature of such phase transitions coming from multi-modal gravitational wave spectroscopy. We find that the growth of a one-armed spiral instability, which is a characteristic of differentially rotating remnants over time scales of $\mathcal{O}(10)$ ms, is suppressed by an onset of a deconfinement phase transition. Additionally, the greater the energy gap between the hadronic phase and the pure quark phase in the equation of state for quark matter, the more suppressed the growth of this instability. The one-armed spiral instability links directly to the emission of the sub-dominant $\ell = 2, m = 1$ GW mode which is also suppressed by a deconfinement phase transition. Such a suppression could be potentially measurable with the next generation of GW detectors.

We explore the general relativistic hydrodynamics of a merger of strange stars in chapter 4. To this aim, we provide a comparative discussion of the merger dynamics from treatments of thermal effects in the equation of state for a strange star. In particular, we compare the dynamics of a binary strange star merger from a cold $\beta-$equilibrated equation of state supplemented with a thermal ideal gas correction to the dynamics from an equation of state that consistently includes finite temperature effects. We find that for either treatment, the gravitational wave signatures are degenerate with mergers of binary neutron stars with a hadronic EOS, and therefore distinguishing between the two classes of compact binary mergers is difficult based on the values of $f_2^{\rm peak}$.

Chapter 5 deals with the manifestation of thermal effects in neutron star matter in the postmerger gravitational wave signature of a merger of neutron stars. In particular, we control the effective nucleon mass $m^*$, a parameter for the equation of state that influences the specific heat capacity of the merger remnant. We find that large values of $m^*$ lead to higher specific heats and therefore colder and more compact remnants. Additionally, the impact of changing $m^*$ is imprinted as increments in the postmerger peak frequency $f_2^{\rm peak}$, much like a QCD phase transition. We show that a postmerger SNR of 15 in the Einstein Telescope detector will be sufficient to constrain the effective nucleon mass parameter from the postmerger GW emission. However, at the moment it is unclear whether the source of such shifts in $f_2^{\rm peak}$ could be attributed to QCD phase transitions or to specific thermal effects.

In tandem with numerical simulations, we investigate the potential GW detectability of QCD phase transitions by measuring shifts in $f_2^{\rm peak}$ in chapter 6. To this aim, we use the simulation dataset computed in chapter 2 involving the BLQ quark EOS. To this dataset, we add additional numerical simulations of BNS mergers involving another

quark EOS DD2F-SF1. We find that the remnants of binaries evolved with the latter quark model exhibit a stronger phase transition in that they lead to large shifts in $f_2^{\rm peak}$, i.e., $\Delta f_2^{\rm peak} \approx 455$Hz. We show that at postmerger SNRs as low as 10, strong QCD phase transitions can be gravitationally detected and distinguished from other hadronic models by the next generation of gravitational wave detectors. On the other hand, EOSs like BLQ that model a more continuous (weaker) phase transition lead to effects degenerate with mergers from other hadronic EOSs not containing quarks.

We shall now conclude this dissertation by asking the million-dollar question that will encapsulate the crux of these works. The question is, what is it precisely in the quark EOSs BLQ and DD2F-SF1 that causes such drastic changes in the dynamics of the merger remnant to the point that phase transitions in one model (DD2F-SF1) are detectable with gravitational waves but not in the other model (BLQ) ? As it turns out, the answer to this question is multifaceted. The two EOS models BLQ and DD2F-SF1 differ not only in the description of the low density nucleonic phase or the high density deconfined quark phase, but also in the way these two phases are connected with each other. On one hand, the BLQ EOS utilizes the phenomenological MIT Bag model to describe the deconfined quark phase and uses the Gibbs construction (see section 1.2.5.2) to stitch it to its hadronic phase. On the other hand, the DD2F-SF1 EOS models the deconfined quark phase in a density functional approach [375] and uses the Maxwell construction (see section 1.2.5.2) to connect the hadronic and quark phases together. These differences in modeling the nature of strongly interacting matter lend their contributions to the differences in the dynamics of the merger remnant. In these works, it is not possible to disentangle the remnant dynamics arising as a result of differences in hadron/quark treatments or Maxwell/Gibbs constructions. We postpone such explorations to a future work wherein we propose to explore the effects of using different phase constructions (Maxwell and Gibbs) on the phase transition dynamics in the remnant, while keeping the hadronic and quark treatments identical. However, we can still draw important insights by observing a few important diagnostics.

In figure 7.1, we show the oscillations in central density of the merger remnant as it evolves with time. We compare this quantity for two representative scenarios: those of symmetric binaries with total mass $M = 2.6 M_\odot$ evolved with the BLQ and DD2F-SF1 EOSs. This pair of binaries is chosen because they are the closest in gravitational mass and therefore the detectability of the DD2F-SF1 model (see chapter 6) and the non-detectability of the BLQ model can be attributed to differences in the underlying EOS. We can see that the remnant evolved with the DD2F-SF1 EOS undergoes stronger

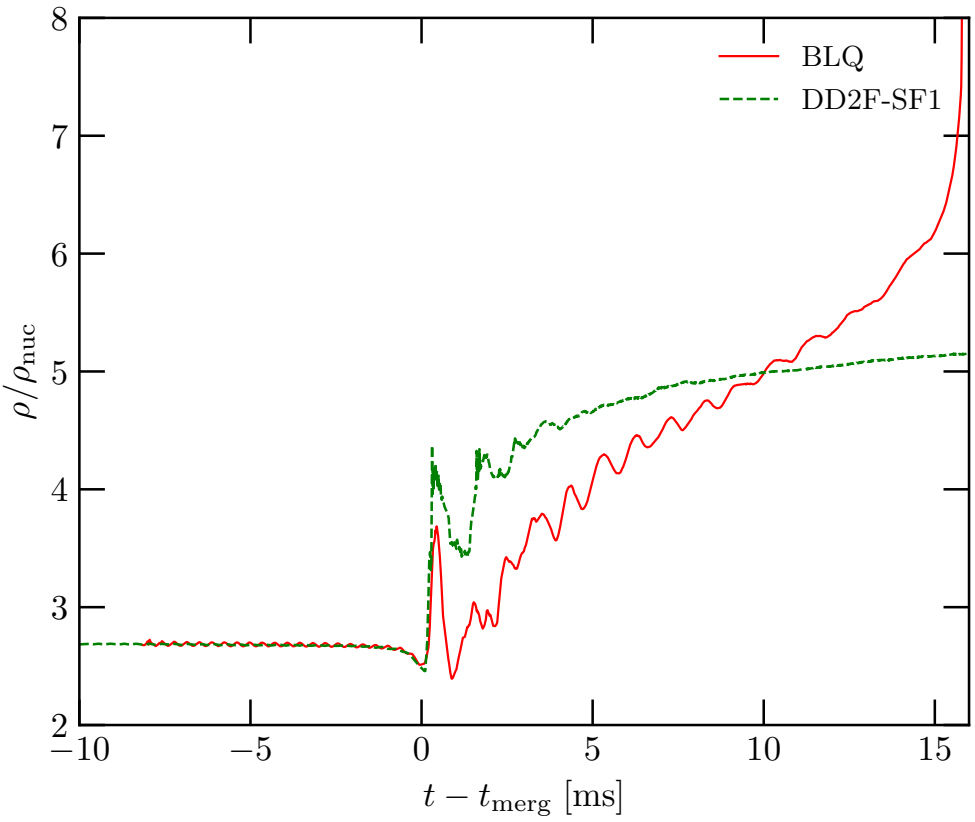


**Figure 7.1.** A comparison of the evolution of central density in the remnant (scaled to nuclear saturation) with time for a merger of 1.3 $M_\odot$ - 1.3 $M_\odot$ binary corresponding to the EOSs BLQ and DD2F-SF1. These EOSs construct the phase transitions via a Gibbs and a Maxwell construction respectively. The remnant with the DD2F-SF1 EOS is more compact which is evidenced by the stronger density oscillations it undergoes.

density oscillations when compared to the BLQ remnant and as a result is relatively more compactified. For a perect fluid (that with stress-energy tensor of a perfect fluid), it is straightforward to show (see chapter 3 in [7]) that angular momentum is conserved provided one assumes azimuthal symmetry (i.e., $\vec{\partial}_\varphi$ is assumed to be a Killing vector field). For a remnant of symmetric binary mergers, to an approximation, it is reasonable to assume azimuthal symmetry and therefore conservation of angular momentum. Larger compactification of the DD2F-SF1 remnant implies a reduction in the moment of inertia and consequently an increase in the angular velocity of the remnant. It is this increase in angular velocity which manifests as increased values of $f_2^{\rm peak}$. There is also an increase in $f_2^{\rm peak}$ for the BLQ model however it is modest and degenerate with other hadronic EOSs, whereas for the DD2F-SF1 model the increase exceeds 1.6 $\sigma$.

Another interesting aspect of an onset of deconfinement phase transitions is revealed

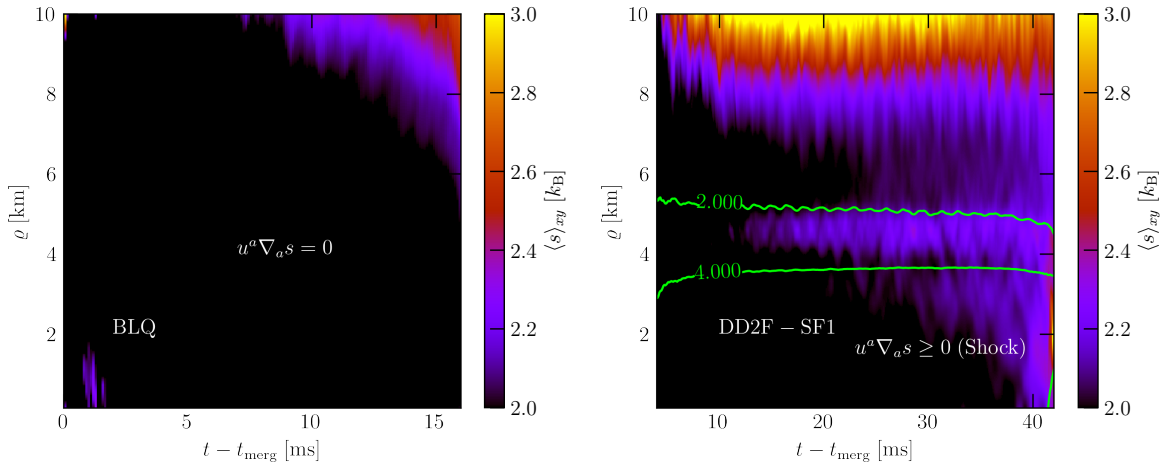


**Figure 7.2.** Azimuthally averaged radial profiles of specific entropy (per baryon) for the two BNS models shown in figure 7.1. For the BLQ remnant, the flow near the core of the remnant is adiabatic as is seen by a largely constant entropy distribution. On the other hand, the fluid near the core of of the remnant with the DD2F-SF1 EOS experiences a shock which is evidenced by local entropy production near the core. The green contours represent constant density profiles in units of nuclear saturation.

by our simulations in figure 7.2. Following the analysis in [58, 230, 399], we compute azimuthaly averaged profiles of specific entropy (i.e., entropy per baryon) for the postmerger evolution of the merger remnant as a function of cylindrical radii and time from merger. Considering an equatorial slice of the remnant, we obtain specific entropy $s = s(x, y)$ in Cartesian coordinates from the hydrodynamic evolution. Following this, we interpolate the specific entropy $s$ onto a cylindrical grid and compute the azimuthally averaged entropy profile as

$$\langle s \rangle_{xy} = \frac{1}{\Delta} \oint_{C(\varrho)} \sqrt{\gamma} \varrho d\varphi \; s(\varrho, \varphi) \text{ where} \tag{7.1}$$

$$\Delta = \oint_{C(\varrho)} \sqrt{\gamma} \varrho d\varphi. \tag{7.2}$$

Here $\varrho$ represents the cylindrical coordinate, $\varphi$ the azimuthal coordinate and $\sqrt{\gamma}$ is the volume form (also interpolated to the 2D cylindrical grid). The integral is evaluated over the contour $C(\varrho)$ where $C$ is a concentric circle of radius $\varrho$ centred at the origin. The entropy profile is a useful diagnostic to monitor the local production of entropy during the postmerger evolution. We show these profiles for both the BLQ and DD2F-SF1 models in figure 7.2.

For a perfect fluid like the ones assumed by our GRHD infrastructure, one can show

that smooth fluid flow is adiabatic (see chapter 3 in [7]). In other words, specific entropy $s$ is conserved along the fluid lines provided the flow is smooth, i.e., in the absence of shocks the following condition holds true

$$u^a \nabla_a s = 0. \tag{7.3}$$

In the presence of shocks however, entropy is no longer conserved and there is local production of entropy, i.e., $u^a \nabla_a s \geq 0$. In the figure 7.2, we see that for both BLQ and DD2F-SF1 models, at large $\varrho$ corresponding to the edges of the merger remnant, entropy is produced locally indicating the presence of shocks. These shocks are hydrodynamic in origin arising due to the violent collision dynamics taking place along the interface of the merging stars. On the other hand at small values of $\varrho$ corresponding to the fluid flow near the core of the remnant, the BLQ model predicts an almost adiabatic flow evidenced by the constant entropy profile. On the other hand, the remnant with the DD2F-SF1 EOS exhibits shocked fluid flow near the remnant's core. This shock, unlike the ones discussed before, is not hydrodynamic rather nuclear in origin. It arises due to the fact that in the DD2F-SF1 model, the phase transition proceeds at a constant pressure (the so-called Maxwell construction, see figure 1 in [58] and figure 4 in [375]). In the transition region or the mixed phase, a consequence of constant pressure is that local sound speed vanishes and consequently all fluid flow in the mixed phase becomes supersonic. In order to increase entropy, this supersonic fluid flows in a way that makes it subsonic. In other words, a shock front is produced that tends to engulf regions of mixed phase making the fluid flow subsonic. This shock arises due to the Maxwell construction and is responsible for the local entropy production near the core of the remnant. We postpone the consequences and further treatments of this shocked flow in models with Maxwell construction to future work.

In conclusion, this dissertation reflects a synergy between two mutually dependent fields of study: numerical relativistic simulations and gravitational wave data analysis in addressing the problem of QCD phase transitions. To put this interplay into perspective, with the advent of the next generation of GW detectors, the SNR for an inspiral signal from a GW event a 100 Mpc away could be as high as several 100s. This means that we require GW waveforms of high accuracy because at high SNRs, waveform systematics play an increasingly dominant role. Improvements in several avenues like conservative fomulations of GRHD [18] or novel numerical methods [400, 401] for existing formulations could play a key role in the generation of more accurate waveforms. On the other hand,

rigorous treatments of relevant physics modules like GRMHD, accurate neutrino radiation transport or non-perfect fluids should be considered for adding realism to the simulations. Advances in computational infrastructure with the development of Graphic Processing Units (GPUs) are being exploited by adapting contemporary codes to these architectures. This dissertation is a small step in simulating science that will be within reach with the next generation of GW detectors.

# Bibliography


[1] LIGO Scientific, Virgo collaboration, *GW170817: Observation of Gravitational Waves from a Binary Neutron Star Inspiral*, *Phys. Rev. Lett.* **119** (2017) 161101 [1710.05832].

[2] LIGO Scientific, Virgo, Fermi GBM, INTEGRAL, IceCube, AstroSat Cadmium Zinc Telluride Imager Team, IPN, Insight-Hxmt, ANTARES, Swift, AGILE Team, 1M2H Team, Dark Energy Camera GW-EM, DES, DLT40, GRAWITA, Fermi-LAT, ATCA, ASKAP, Las Cumbres Observatory Group, OzGrav, DWF (Deeper Wider Faster Program), AST3, CAASTRO, VINROUGE, MASTER, J-GEM, GROWTH, JAGWAR, CaltechNRAO, TTU-NRAO, NuSTAR, Pan-STARRS, MAXI Team, TZAC Consortium, KU, Nordic Optical Telescope, ePESSTO, GROND, Texas Tech University, SALT Group, TOROS, BOOTES, MWA, CALET, IKI-GW Follow-up, H.E.S.S., LOFAR, LWA, HAWC, Pierre Auger, ALMA, Euro VLBI Team, Pi of Sky, Chandra Team at McGill University, DFN, ATLAS Telescopes, High Time Resolution Universe Survey, RIMAS, RATIR, SKA South Africa/MeerKAT collaboration, *Multi-messenger Observations of a Binary Neutron Star Merger*, *Astrophys. J. Lett.* **848** (2017) L12 [1710.05833].

[3] S.L. Liebling, C. Palenzuela and L. Lehner, *Effects of High Density Phase Transitions on Neutron Star Dynamics*, *Class. Quant. Grav.* **38** (2021) 115007 [2010.12567].

[4] C.W. Misner, K.S. Thorne and J.A. Wheeler, *Gravitation* (1973).

[5] B. Schutz, *A First Course in General Relativity* (2009).

[6] R.M. Wald, *General Relativity* (1984).

[7] L. Rezzolla and O. Zanotti, *Relativistic Hydrodynamics* (2013).

[8] E. Newman and R. Penrose, *An Approach to gravitational radiation by a method of spin coefficients*, *J. Math. Phys.* **3** (1962) 566.

[9] R.J. LeVeque and R.J. Leveque, *Numerical methods for conservation laws*, vol. 214, Springer (1992).

[10] E.F. Toro, *Riemann solvers and numerical methods for fluid dynamics: a practical introduction*, Springer Science & Business Media (2013).

[11] T.W. Baumgarte and S.L. Shapiro, *Numerical Relativity: Solving Einstein's Equations on the Computer*, Cambridge University Press (2010), 10.1017/CBO9781139193344.

[12] M. Shibata, *Numerical Relativity* (2016), 10.1142/9692.

[13] M. Alcubierre, *Introduction to 3+1 Numerical Relativity* (2008).

[14] F. de Felice and C.J.S. Clarke, *Relativity on curved manifolds.* (1990).

[15] R.L. Arnowitt, S. Deser and C.W. Misner, *The Dynamics of general relativity*, *Gen. Rel. Grav.* **40** (2008) 1997 [gr-qc/0405109].

[16] F. Banyuls, J.A. Font, J.M.A. Ibanez, J.M.A. Marti and J.A. Miralles, *Numerical 3+1 General Relativistic Hydrodynamics: A Local Characteristic Approach*, *Astrophys. J.* **476** (1997) 221.

[17] Y.-F. Jiang, M. Belyaev, J. Goodman and J.M. Stone, *A New Way to Conserve Total Energy for Eulerian Hydrodynamic Simulations with Self-Gravity*, *New Astron.* **19** (2013) 48 [1208.1795].

[18] L. Landau and E. Lifshitz, *The Classical Theory of Fields: Volume 2*, Course of theoretical physics, Elsevier Science (1975).

[19] Y. Sekiguchi, K. Kiuchi, K. Kyutoku and M. Shibata, *Effects of hyperons in binary neutron star mergers*, *Phys. Rev. Lett.* **107** (2011) 211101 [1110.4442].

[20] D. Radice, S. Bernuzzi, W. Del Pozzo, L.F. Roberts and C.D. Ott, *Probing Extreme-Density Matter with Gravitational Wave Observations of Binary Neutron Star Merger Remnants*, *Astrophys. J. Lett.* **842** (2017) L10 [1612.06429].

[21] E. Loffredo, A. Perego, D. Logoteta and M. Branchesi, *Muons in the aftermath of neutron star mergers and their impact on trapped neutrinos*, *Astron. Astrophys.* **672** (2023) A124 [2209.04458].

[22] C. Cercignani and G.M. Kremer, *The relativistic Boltzmann equation: theory and applications* (2002).

[23] D. Radice, F. Galeazzi, J. Lippuner, L.F. Roberts, C.D. Ott and L. Rezzolla, *Dynamical Mass Ejection from Binary Neutron Star Mergers*, *Mon. Not. Roy. Astron. Soc.* **460** (2016) 3255 [1601.02426].

[24] D. Radice, A. Perego, K. Hotokezaka, S.A. Fromm, S. Bernuzzi and L.F. Roberts, *Binary Neutron Star Mergers: Mass Ejection, Electromagnetic Counterparts and Nucleosynthesis*, *Astrophys. J.* **869** (2018) 130 [1809.11161].

[25] D. Radice, S. Bernuzzi, A. Perego and R. Haas, *A new moment-based general-relativistic neutrino-radiation transport code: Methods and first applications to neutron star mergers*, *Mon. Not. Roy. Astron. Soc.* **512** (2022) 1499 [2111.14858].

[26] F. Foucart, M.D. Duez, R. Haas, L.E. Kidder, H.P. Pfeiffer, M.A. Scheel et al., *General relativistic simulations of collapsing binary neutron star mergers with Monte Carlo neutrino transport*, *Phys. Rev. D* **107** (2023) 103055 [2210.05670].

[27] F. Foucart, M.D. Duez, F. Hebert, L.E. Kidder, P. Kovarik, H.P. Pfeiffer et al., *Implementation of Monte Carlo Transport in the General Relativistic SpEC Code*, *Astrophys. J.* **920** (2021) 82 [2103.16588].

[28] F. Foucart, *Neutrino transport in general relativistic neutron star merger simulations*, *Liv. Rev. Comput. Astrophys.* **9** (2023) 1 [2209.02538].

[29] M.K. Bhattacharyya and D. Radice, *A finite element method for angular discretization of the radiation transport equation on spherical geodesic grids*, *Journal of Computational Physics* **491** (2023) 112365.

[30] P.L. Espino, P. Hammond, D. Radice, S. Bernuzzi, R. Gamba, F. Zappa et al., *Neutrino Trapping and Out-of-Equilibrium Effects in Binary Neutron-Star Merger Remnants*, *Phys. Rev. Lett.* **132** (2024) 211001 [2311.00031].

[31] P.L. Espino, D. Radice, F. Zappa, R. Gamba and S. Bernuzzi, *Impact of moment-based, energy integrated neutrino transport on microphysics and ejecta in binary neutron star mergers*, *Phys. Rev. D* **109** (2024) 103027 [2311.12923].

[32] P. Hammond, I. Hawke and N. Andersson, *Thermal aspects of neutron star mergers*, *Phys. Rev. D* **104** (2021) 103006 [2108.08649].

[33] N. Glendenning, *Compact Stars. Nuclear Physics, Particle Physics and General Relativity.* (1996).

[34] N.K. Glendenning, *Compact stars. Nuclear physics, particle physics, and general relativity* (1997).

[35] I.S. Gradshteyn and I.M. Ryzhik, *Table of integrals, series and products* (1965).

[36] A. Chodos, R.L. Jaffe, K. Johnson, C.B. Thorn and V.F. Weisskopf, *A New Extended Model of Hadrons*, *Phys. Rev. D* **9** (1974) 3471.

[37] A. Bhattacharyya, I.N. Mishustin and W. Greiner, *Deconfinement Phase Transition in Compact Stars : Maxwell vs. Gibbs Construction of the Mixed Phase*, *J. Phys. G* **37** (2010) 025201 [0905.0352].

[38] N.K. Glendenning, *First order phase transitions with more than one conserved charge: Consequences for neutron stars*, *Phys. Rev. D* **46** (1992) 1274.

[39] S. Chandrasekhar, *The maximum mass of ideal white dwarfs*, *Astrophys. J.* **74** (1931) 81.

[40] T. Gorda, O. Komoltsev and A. Kurkela, *Ab-initio QCD Calculations Impact the Inference of the Neutron-star-matter Equation of State*, *Astrophys. J.* **950** (2023) 107 [2204.11877].

[41] C. Ecker, T. Gorda, A. Kurkela and L. Rezzolla, *Listening to the long ringdown: a novel way to pinpoint the equation of state in neutron-star cores*, [2403.03246].

[42] J.R. Oppenheimer and G.M. Volkoff, *On massive neutron cores*, *Phys. Rev.* **55** (1939) 374.

[43] E.C. Nambo and O. Sarbach, *Static spherical perfect fluid stars with finite radius in general relativity: a review*, *Rev. Mex. Fis. E* **18** (2021) 020208 [2010.02859].

[44] M. Shibata, K. Kiuchi, Y.-i. Sekiguchi and Y. Suwa, *Truncated Moment Formalism for Radiation Hydrodynamics in Numerical Relativity*, *Prog. Theor. Phys.* **125** (2011) 1255 [1104.3937].

[45] P. Braun-Munzinger and J. Wambach, *The Phase Diagram of Strongly-Interacting Matter*, *Rev. Mod. Phys.* **81** (2009) 1031 [0801.4256].

[46] M.G. Alford, A. Schmitt, K. Rajagopal and T. Schäfer, *Color superconductivity in dense quark matter*, *Reviews of Modern Physics* **80** (2008) 1455 [0709.4635].

[47] R. Anglani, R. Casalbuoni, M. Ciminale, N. Ippolito, R. Gatto, M. Mannarelli et al., *Crystalline color superconductors*, *Rev. Mod. Phys.* **86** (2014) 509 [1302.4264].

[48] Y. Aoki, G. Endrodi, Z. Fodor, S.D. Katz and K.K. Szabo, *The Order of the quantum chromodynamics transition predicted by the standard model of particle physics*, *Nature* **443** (2006) 675 [hep-lat/0611014].

[49] A. Bazavov et al., *The chiral and deconfinement aspects of the QCD transition*, *Phys. Rev. D* **85** (2012) 054503 [1111.1710].

[50] W. Busza, K. Rajagopal and W. van der Schee, *Heavy Ion Collisions: The Big Picture, and the Big Questions*, *Ann. Rev. Nucl. Part. Sci.* **68** (2018) 339 [1802.04801].

[51] P. Senger, *Probing dense nuclear matter in the laboratory: Experiments at fair and nica*, *Universe* **7** (2021) .

[52] E.R. Most, L.J. Papenfort, V. Dexheimer, M. Hanauske, S. Schramm, H. Stöcker et al., *Signatures of quark-hadron phase transitions in general-relativistic neutron-star mergers*, *Phys. Rev. Lett.* **122** (2019) 061101 [1807.03684].

[53] E.R. Most, L. Jens Papenfort, V. Dexheimer, M. Hanauske, H. Stoecker and L. Rezzolla, *On the deconfinement phase transition in neutron-star mergers*, *Eur. Phys. J. A* **56** (2020) 59 [1910.13893].

[54] A. Bauswein, N.-U.F. Bastian, D.B. Blaschke, K. Chatziioannou, J.A. Clark, T. Fischer et al., *Identifying a first-order phase transition in neutron star mergers through gravitational waves*, *Phys. Rev. Lett.* **122** (2019) 061102 [1809.01116].

[55] A. Bauswein and S. Blacker, *Impact of quark deconfinement in neutron star mergers and hybrid star mergers*, *Eur. Phys. J. ST* **229** (2020) 3595 [2006.16183].

[56] L.R. Weih, M. Hanauske and L. Rezzolla, *Postmerger Gravitational-Wave Signatures of Phase Transitions in Binary Mergers*, *Phys. Rev. Lett.* **124** (2020) 171103 [1912.09340].

[57] S. Blacker, N.-U.F. Bastian, A. Bauswein, D.B. Blaschke, T. Fischer, M. Oertel et al., *Constraining the onset density of the hadron-quark phase transition with gravitational-wave observations*, *Phys. Rev. D* **102** (2020) 123023 [2006.03789].

[58] T. Fischer, N.-U.F. Bastian, M.-R. Wu, P. Baklanov, E. Sorokina, S. Blinnikov et al., *Quark deconfinement as a supernova explosion engine for massive blue supergiant stars*, *Nature Astron.* **2** (2018) 980 [1712.08788].

[59] A. Bauswein and H.T. Janka, *Measuring neutron-star properties via gravitational waves from binary mergers*, *Phys. Rev. Lett.* **108** (2012) 011101 [1106.1616].

[60] K. Hotokezaka, K. Kiuchi, K. Kyutoku, T. Muranushi, Y.-i. Sekiguchi, M. Shibata et al., *Remnant massive neutron stars of binary neutron star mergers: Evolution process and gravitational waveform*, *Phys. Rev. D* **88** (2013) 044026 [1307.5888].

[61] S. Bernuzzi, A. Nagar, S. Balmelli, T. Dietrich and M. Ujevic, *Quasiuniversal properties of neutron star mergers*, *Phys. Rev. Lett.* **112** (2014) 201101 [1402.6244].

[62] L. Rezzolla and K. Takami, *Gravitational-wave signal from binary neutron stars: a systematic analysis of the spectral properties*, *Phys. Rev. D* **93** (2016) 124051 [1604.00246].

[63] F. Zappa, S. Bernuzzi, D. Radice, A. Perego and T. Dietrich, *Gravitational-wave luminosity of binary neutron stars mergers*, *Phys. Rev. Lett.* **120** (2018) 111101 [1712.04267].

[64] M. Breschi, S. Bernuzzi, F. Zappa, M. Agathos, A. Perego, D. Radice et al., *kiloHertz gravitational waves from binary neutron star remnants: time-domain model and constraints on extreme matter*, *Phys. Rev. D* **100** (2019) 104029 [1908.11418].

[65] A. Bauswein, H.T. Janka, R. Oechslin, G. Pagliara, I. Sagert, J. Schaffner-Bielich et al., *Mass Ejection by Strange Star Mergers and Observational Implications*, *Phys. Rev. Lett.* **103** (2009) 011101 [0812.4248].

[66] A. Bauswein, R. Oechslin and H.T. Janka, *Discriminating Strange Star Mergers from Neutron Star Mergers by Gravitational-Wave Measurements*, *Phys. Rev. D* **81** (2010) 024012 [0910.5169].

[67] Z. Zhu and L. Rezzolla, *Fully general-relativistic simulations of isolated and binary strange quark stars*, *Phys. Rev. D* **104** (2021) 083004 [2102.07721].

[68] R. De Pietri, A. Drago, A. Feo, G. Pagliara, M. Pasquali, S. Traversi et al., *Merger of compact stars in the two-families scenario*, *Astrophys. J.* **881** (2019) 122 [1904.01545].

[69] J. Madsen, *Astrophysical Limits on the Flux of Quark Nuggets*, *Phys. Rev. Lett.* **61** (1988) 2909.

[70] A. Bauswein, N.-U. Friedrich Bastian, D. Blaschke, K. Chatziioannou, J.A. Clark, T. Fischer et al., *Equation-of-state Constraints and the QCD Phase Transition in the Era of Gravitational-Wave Astronomy*, *AIP Conf. Proc.* **2127** (2019) 020013 [1904.01306].

[71] I. Bombaci and D. Logoteta, *Equation of state of dense nuclear matter and neutron star structure from nuclear chiral interactions*, *Astron. Astrophys.* **609** (2018) A128 [1805.11846].

[72] R. Machleidt and D.R. Entem, *Chiral effective field theory and nuclear forces*, *Phys. Rept.* **503** (2011) 1 [1105.2919].

[73] H.W. Hammer, S. König and U. van Kolck, *Nuclear effective field theory: status and perspectives*, *Rev. Mod. Phys.* **92** (2020) 025004 [1906.12122].

[74] D. Logoteta, I. Bombaci and A. Kievsky, *Nuclear matter properties from local chiral interactions with $\Delta$ isobar intermediate states*, *Phys. Rev. C* **94** (2016) 064001 [1609.00649].

[75] P. Danielewicz, R. Lacey and W.G. Lynch, *Determination of the equation of state of dense matter*, *Science* **298** (2002) 1592 [nucl-th/0208016].

[76] D. Logoteta and I. Bombaci, *Constraints on Microscopic and Phenomenological Equations of State of Dense Matter from GW170817*, *Universe* **5** (2019) 204.

[77] A. Endrizzi, D. Logoteta, B. Giacomazzo, I. Bombaci, W. Kastaun and R. Ciolfi, *Effects of Chiral Effective Field Theory Equation of State on Binary Neutron Star Mergers*, *Phys. Rev. D* **98** (2018) 043015 [1806.09832].

[78] D. Logoteta, A. Perego and I. Bombaci, *Microscopic equation of state of hot nuclear matter for numerical relativity simulations*, *Astron. Astrophys.* **646** (2021) A55 [2012.03599].

[79] S. Bernuzzi et al., *Accretion-induced prompt black hole formation in asymmetric neutron star mergers, dynamical ejecta and kilonova signals*, *Mon. Not. Roy. Astron. Soc.* **497** (2020) 1488 [2003.06015].

[80] V. Nedora, S. Bernuzzi, D. Radice, B. Daszuta, A. Endrizzi, A. Perego et al., *Numerical Relativity Simulations of the Neutron Star Merger GW170817: Long-Term Remnant Evolutions, Winds, Remnant Disks, and Nucleosynthesis*, *Astrophys. J.* **906** (2021) 98 [2008.04333].

[81] E.S. Fraga, R.D. Pisarski and J. Schaffner-Bielich, *Small, dense quark stars from perturbative QCD*, *Phys. Rev. D* **63** (2001) 121702 [hep-ph/0101143].

[82] M. Alford, M. Braby, M.W. Paris and S. Reddy, *Hybrid stars that masquerade as neutron stars*, *Astrophys. J.* **629** (2005) 969 [nucl-th/0411016].

[83] S. Weissenborn, I. Sagert, G. Pagliara, M. Hempel and J. Schaffner-Bielich, *Quark Matter in Massive Compact Stars*, Oct., 2011. 10.1088/2041-8205/740/1/L14.

[84] S.L. Shapiro and S.A. Teukolsky, *Black Holes, White Dwarfs and Neutron Stars: The Physics of Compact Objects* (1986).

[85] A.L. Fetter and J.D. Walecka, *Quantum Theory of Many-Particle Systems*, McGraw-Hill, Boston (1971).

[86] I. Bombaci, D. Logoteta, I. Vidaña and C. Providência, *Quark matter nucleation in neutron stars and astrophysical implications*, *Eur. Phys. J. A* **52** (2016) 58 [1601.04559].

[87] D. Radice and L. Rezzolla, *THC: a new high-order finite-difference high-resolution shock-capturing code for special-relativistic hydrodynamics*, *Astron. Astrophys.* **547** (2012) A26 [1206.6502].

[88] D. Radice, L. Rezzolla and F. Galeazzi, *Beyond second-order convergence in simulations of binary neutron stars in full general-relativity*, *Mon. Not. Roy. Astron. Soc.* **437** (2014) L46 [1306.6052].

[89] D. Radice, L. Rezzolla and F. Galeazzi, *High-Order Fully General-Relativistic Hydrodynamics: new Approaches and Tests*, *Class. Quant. Grav.* **31** (2014) 075012 [1312.5004].

[90] S. Bernuzzi and D. Hilditch, *Constraint violation in free evolution schemes: Comparing BSSNOK with a conformal decomposition of Z4*, *Phys. Rev. D* **81** (2010) 084003 [0912.2920].

[91] D. Hilditch, S. Bernuzzi, M. Thierfelder, Z. Cao, W. Tichy and B. Bruegmann, *Compact binary evolutions with the Z4c formulation*, *Phys. Rev. D* **88** (2013) 084057 [1212.2901].

[92] D. Pollney, C. Reisswig, E. Schnetter, N. Dorband and P. Diener, *High accuracy binary black hole simulations with an extended wave zone*, *Phys. Rev. D* **83** (2011) 044045 [0910.3803].

[93] C. Reisswig, C.D. Ott, E. Abdikamalov, R. Haas, P. Moesta and E. Schnetter, *Formation and Coalescence of Cosmological Supermassive Black Hole Binaries in Supermassive Star Collapse*, *Phys. Rev. Lett.* **111** (2013) 151101 [1304.7787].

[94] F. Loffler et al., *The Einstein Toolkit: A Community Computational Infrastructure for Relativistic Astrophysics*, *Class. Quant. Grav.* **29** (2012) 115001 [1111.3344].

[95] E. Schnetter, S.H. Hawley and I. Hawke, *Evolutions in 3-D numerical relativity using fixed mesh refinement*, *Class. Quant. Grav.* **21** (2004) 1465 [gr-qc/0310042].

[96] C. Reisswig, R. Haas, C.D. Ott, E. Abdikamalov, P. Mösta, D. Pollney et al., *Three-Dimensional General-Relativistic Hydrodynamic Simulations of Binary Neutron Star Coalescence and Stellar Collapse with Multipatch Grids*, *Phys. Rev. D* **87** (2013) 064023 [1212.1191].

[97] M.J. Berger and J. Oliger, *Adaptive Mesh Refinement for Hyperbolic Partial Differential Equations*, *J. Comput. Phys.* **53** (1984) 484.

[98] M.J. Berger and P. Colella, *Local Adaptive Mesh Refinement for Shock Hydrodynamics*, *Journal of Computational Physics* **82** (1989) 64.

[99] L. Wade, J.D.E. Creighton, E. Ochsner, B.D. Lackey, B.F. Farr, T.B. Littenberg et al., *Systematic and statistical errors in a bayesian approach to the estimation of the neutron-star equation of state using advanced gravitational wave detectors*, *Phys. Rev. D* **89** (2014) 103012 [1402.5156].

[100] D. Radice, *Binary Neutron Star Merger Simulations with a Calibrated Turbulence Model*, *Symmetry* **12** (2020) 1249 [2005.09002].

[101] E. Gourgoulhon, P. Grandclement, K. Taniguchi, J.-A. Marck and S. Bonazzola, *Quasiequilibrium sequences of synchronized and irrotational binary neutron stars in general relativity: 1. Method and tests*, *Phys. Rev. D* **63** (2001) 064029 [gr-qc/0007028].

[102] D.J. Champion, D.R. Lorimer, M.A. McLaughlin, J.M. Cordes, Z. Arzoumanian, J.M. Weisberg et al., *PSR J1829+2456: A Relativistic binary pulsar*, *Mon. Not. Roy. Astron. Soc.* **350** (2004) L61 [astro-ph/0403553].

[103] S. Bernuzzi, D. Radice, C.D. Ott, L.F. Roberts, P. Moesta and F. Galeazzi, *How loud are neutron star mergers?*, *Phys. Rev. D* **94** (2016) 024023 [1512.06397].

[104] M. Hanauske, K. Takami, L. Bovard, L. Rezzolla, J.A. Font, F. Galeazzi et al., *Rotational properties of hypermassive neutron stars from binary mergers*, *Phys. Rev. D* **96** (2017) 043004 [1611.07152].

[105] W. Kastaun, R. Ciolfi and B. Giacomazzo, *Structure of Stable Binary Neutron Star Merger Remnants: a Case Study*, *Phys. Rev. D* **94** (2016) 044060 [1607.02186].

[106] A. Perego, S. Bernuzzi and D. Radice, *Thermodynamics conditions of matter in neutron star mergers*, *Eur. Phys. J. A* **55** (2019) 124 [1903.07898].

[107] N. Sarin, P.D. Lasky and G. Ashton, *Gravitational waves or deconfined quarks: what causes the premature collapse of neutron stars born in short gamma-ray bursts?*, *Phys. Rev. D* **101** (2020) 063021 [2001.06102].

[108] R. Kashyap et al., *Numerical relativity simulations of prompt collapse mergers: Threshold mass and phenomenological constraints on neutron star properties after GW170817*, *Phys. Rev. D* **105** (2022) 103022 [2111.05183].

[109] M. Hanauske, J. Steinheimer, A. Motornenko, V. Vovchenko, L. Bovard, E.R. Most et al., *Neutron Star Mergers: Probing the EoS of Hot, Dense Matter by Gravitational Waves*, *Particles* **2** (2019) 44.

[110] L. Baiotti, B. Giacomazzo and L. Rezzolla, *Accurate evolutions of inspiralling neutron-star binaries: prompt and delayed collapse to black hole*, *Phys. Rev. D* **78** (2008) 084033 [0804.0594].

[111] S. Bernuzzi, A. Nagar, M. Thierfelder and B. Brugmann, *Tidal effects in binary neutron star coalescence*, *Phys. Rev. D* **86** (2012) 044030 [1205.3403].

[112] K. Takami, L. Rezzolla and L. Baiotti, *Spectral properties of the post-merger gravitational-wave signal from binary neutron stars*, *Phys. Rev. D* **91** (2015) 064001 [1412.3240].

[113] S. Bernuzzi, T. Dietrich and A. Nagar, *Modeling the complete gravitational wave spectrum of neutron star mergers*, *Phys. Rev. Lett.* **115** (2015) 091101 [1504.01764].

[114] T. Dietrich, M. Ujevic, W. Tichy, S. Bernuzzi and B. Bruegmann, *Gravitational waves and mass ejecta from binary neutron star mergers: Effect of the mass-ratio*, *Phys. Rev. D* **95** (2017) 024029 [1607.06636].

[115] T. Dietrich, S. Bernuzzi, M. Ujevic and W. Tichy, *Gravitational waves and mass ejecta from binary neutron star mergers: Effect of the stars' rotation*, *Phys. Rev. D* **95** (2017) 044045 [1611.07367].

[116] M. Shibata and K. Uryu, *Gravitational waves from the merger of binary neutron stars in a fully general relativistic simulation*, *Prog. Theor. Phys.* **107** (2002) 265 [gr-qc/0203037].

[117] N. Stergioulas, A. Bauswein, K. Zagkouris and H.-T. Janka, *Gravitational waves and nonaxisymmetric oscillation modes in mergers of compact object binaries*, *Mon. Not. Roy. Astron. Soc.* **418** (2011) 427 [1105.0368].

[118] K. Takami, L. Rezzolla and L. Baiotti, *Constraining the Equation of State of Neutron Stars from Binary Mergers*, *Phys. Rev. Lett.* **113** (2014) 091104 [1403.5672].

[119] D. Radice, S. Bernuzzi and C.D. Ott, *One-armed spiral instability in neutron star mergers and its detectability in gravitational waves*, *Phys. Rev. D* **94** (2016) 064011 [1603.05726].

[120] L. Lehner, S.L. Liebling, C. Palenzuela, O.L. Caballero, E. O'Connor, M. Anderson et al., *Unequal mass binary neutron star mergers and multimessenger signals*, *Class. Quant. Grav.* **33** (2016) 184002 [1603.00501].

[121] K. Kiuchi, K. Kyutoku, Y. Sekiguchi and M. Shibata, *Global simulations of strongly magnetized remnant massive neutron stars formed in binary neutron star mergers*, *Phys. Rev. D* **97** (2018) 124039 [1710.01311].

[122] D. Radice, *General-Relativistic Large-Eddy Simulations of Binary Neutron Star Mergers*, *Astrophys. J. Lett.* **838** (2017) L2 [1703.02046].

[123] T. Dietrich, D. Radice, S. Bernuzzi, F. Zappa, A. Perego, B. Brügmann et al., *CoRe database of binary neutron star merger waveforms*, *Class. Quant. Grav.* **35** (2018) 24LT01 [1806.01625].

[124] A. Bauswein, H.T. Janka, K. Hebeler and A. Schwenk, *Equation-of-state dependence of the gravitational-wave signal from the ring-down phase of neutron-star mergers*, *Phys. Rev. D* **86** (2012) 063001 [1204.1888].

[125] G. Lioutas, A. Bauswein and N. Stergioulas, *Frequency deviations in universal relations of isolated neutron stars and postmerger remnants*, *Phys. Rev. D* **104** (2021) 043011 [2102.12455].

[126] W. Kastaun and F. Galeazzi, *Properties of hypermassive neutron stars formed in mergers of spinning binaries*, *Phys. Rev. D* **91** (2015) 064027 [1411.7975].

[127] L. Bovard, D. Martin, F. Guercilena, A. Arcones, L. Rezzolla and O. Korobkin, *r-process nucleosynthesis from matter ejected in binary neutron star mergers*, *Phys. Rev. D* **96** (2017) 124005 [1709.09630].

[128] V. Nedora, S. Bernuzzi, D. Radice, A. Perego, A. Endrizzi and N. Ortiz, *Spiral-wave wind for the blue kilonova*, *Astrophys. J. Lett.* **886** (2019) L30 [1907.04872].

[129] A. Bauswein, S. Goriely and H.T. Janka, *Systematics of dynamical mass ejection, nucleosynthesis, and radioactively powered electromagnetic signals from neutron-star mergers*, *Astrophys. J.* **773** (2013) 78 [1302.6530].

[130] Y. Sekiguchi, K. Kiuchi, K. Kyutoku and M. Shibata, *Dynamical mass ejection from binary neutron star mergers: Radiation-hydrodynamics study in general relativity*, *Phys. Rev. D* **91** (2015) 064059 [1502.06660].

[131] B.D. Metzger, A. Bauswein, S. Goriely and D. Kasen, *Neutron-powered precursors of kilonovae*, *Mon. Not. Roy. Astron. Soc.* **446** (2015) 1115 [1409.0544].

[132] K. Hotokezaka, K. Kiuchi, M. Shibata, E. Nakar and T. Piran, *Synchrotron radiation from the fast tail of dynamical ejecta of neutron star mergers*, *Astrophys. J.* **867** (2018) 95 [1803.00599].

[133] D. Radice, A. Perego, K. Hotokezaka, S. Bernuzzi, S.A. Fromm and L.F. Roberts, *Viscous-Dynamical Ejecta from Binary Neutron Star Merger*, *Astrophys. J. Lett.* **869** (2018) L35 [1809.11163].

[134] V. Nedora, D. Radice, S. Bernuzzi, A. Perego, B. Daszuta, A. Endrizzi et al., *Dynamical ejecta synchrotron emission as a possible contributor to the changing behaviour of GRB170817A afterglow*, *Mon. Not. Roy. Astron. Soc.* **506** (2021) 5908 [2104.04537].

[135] Y. Sekiguchi, K. Kiuchi, K. Kyutoku, M. Shibata and K. Taniguchi, *Dynamical mass ejection from the merger of asymmetric binary neutron stars: Radiation-hydrodynamics study in general relativity*, *Phys. Rev. D* **93** (2016) 124046 [1603.01918].

[136] F.K. Thielemann, M. Eichler, I.V. Panov and B. Wehmeyer, *Neutron Star Mergers and Nucleosynthesis of Heavy Elements*, *Ann. Rev. Nucl. Part. Sci.* **67** (2017) 253 [1710.02142].

[137] D. Radice, A. Perego, F. Zappa and S. Bernuzzi, *GW170817: Joint Constraint on the Neutron Star Equation of State from Multimessenger Observations*, *Astrophys. J. Lett.* **852** (2018) L29 [1711.03647].

[138] S. Fujibayashi, K. Kiuchi, N. Nishimura, Y. Sekiguchi and M. Shibata, *Mass Ejection from the Remnant of a Binary Neutron Star Merger: Viscous-Radiation Hydrodynamics Study*, *Astrophys. J.* **860** (2018) 64 [1711.02093].

[139] R. Fernández, A. Tchekhovskoy, E. Quataert, F. Foucart and D. Kasen, *Long-term GRMHD simulations of neutron star merger accretion discs: implications for electromagnetic counterparts*, *Mon. Not. Roy. Astron. Soc.* **482** (2019) 3373 [1808.00461].

[140] R. Fernández, F. Foucart and J. Lippuner, *The landscape of disc outflows from black hole–neutron star mergers*, *Mon. Not. Roy. Astron. Soc.* **497** (2020) 3221 [2005.14208].

[141] R. Fernández and B.D. Metzger, *Delayed outflows from black hole accretion tori following neutron star binary coalescence*, *Mon. Not. Roy. Astron. Soc.* **435** (2013) 502 [1304.6720].

[142] W.D. Arnett, *Type I supernovae. I - Analytic solutions for the early part of the light curve*, *Astrophys. J.* **253** (1982) 785.

[143] E. Chatzopoulos, J.C. Wheeler and J. Vinko, *Generalized Semi-Analytical Models of Supernova Light Curves*, *Astrophys. J.* **746** (2012) 121 [1111.5237].

[144] V.A. Villar et al., *The Combined Ultraviolet, Optical, and Near-Infrared Light Curves of the Kilonova Associated with the Binary Neutron Star Merger GW170817: Unified Data Set, Analytic Models, and Physical Implications*, *Astrophys. J. Lett.* **851** (2017) L21 [1710.11576].

[145] M. Tanaka, D. Kato, G. Gaigalas and K. Kawaguchi, *Systematic Opacity Calculations for Kilonovae*, *Mon. Not. Roy. Astron. Soc.* **496** (2020) 1369 [1906.08914].

[146] O. Korobkin, S. Rosswog, A. Arcones and C. Winteler, *On the astrophysical robustness of neutron star merger r-process*, *Mon. Not. Roy. Astron. Soc.* **426** (2012) 1940 [1206.2379].

[147] J. Barnes, D. Kasen, M.-R. Wu and G. Martínez-Pinedo, *Radioactivity and thermalization in the ejecta of compact object mergers and their impact on kilonova light curves*, *Astrophys. J.* **829** (2016) 110 [1605.07218].

[148] D. Radice, S. Bernuzzi and A. Perego, *The Dynamics of Binary Neutron Star Mergers and GW170817*, *Ann. Rev. Nucl. Part. Sci.* **70** (2020) 95 [2002.03863].

[149] D. Radice, A. Perego, S. Bernuzzi and B. Zhang, *Long-lived Remnants from Binary Neutron Star Mergers*, *Mon. Not. Roy. Astron. Soc.* **481** (2018) 3670 [1803.10865].

[150] E. Nakar and T. Piran, *Radio Remnants of Compact Binary Mergers - the Electromagnetic Signal that will follow the Gravitational Waves*, *Nature* **478** (2011) 82 [1102.1020].

[151] K. Hotokezaka and T. Piran, *Mass ejection from neutron star mergers: different components and expected radio signals*, *Mon. Not. Roy. Astron. Soc.* **450** (2015) 1430 [1501.01986].

[152] B. Margalit and T. Piran, *Shock within a shock: revisiting the radio flares of NS merger ejecta and GRB-supernovae*, 4, 2020. 10.1093/mnras/staa1486.

[153] A. Hajela et al., *Evidence for X-Ray Emission in Excess to the Jet-afterglow Decay 3.5 yr after the Binary Neutron Star Merger GW 170817: A New Emission Component*, *Astrophys. J. Lett.* **927** (2022) L17 [2104.02070].

[154] W. Ishizaki, K. Ioka and K. Kiuchi, *Fallback Accretion Model for the Years-to-decades X-Ray Counterpart to GW170817*, *Astrophys. J. Lett.* **916** (2021) L13 [2104.04433].

[155] A. Hajela et al., *Two Years of Nonthermal Emission from the Binary Neutron Star Merger GW170817: Rapid Fading of the Jet Afterglow and First Constraints on the Kilonova Fastest Ejecta*, *Astrophys. J. Lett.* **886** (2019) L17 [1909.06393].

[156] I. Bombaci, T.T.S. Kuo and U. Lombardo, *The incompressibility of hot asymmetric nuclear matter*, *Physics Letters B* **311** (1993) 9.

[157] I. Bombaci, T.T.S. Kuo and U. Lombardo, *Temperature and asymmetry dependence of nuclear incompressibility and supernova explosions*, July, 1994. 10.1016/0370-1573(94)90149-X.

[158] M. Baldo and L.S. Ferreira, *Nuclear liquid-gas phase transition*, *Phys. Rev. C* **59** (1999) 682.

[159] A. Prakash, D. Radice, D. Logoteta, A. Perego, V. Nedora, I. Bombaci et al., *Signatures of deconfined quark phases in binary neutron star mergers*, *Phys. Rev. D* **104** (2021) 083029 [2106.07885].

[160] M. Shibata, *Constraining nuclear equations of state using gravitational waves from hypermassive neutron stars*, *Phys. Rev. Lett.* **94** (2005) 201101 [gr-qc/0504082].

[161] T. Hinderer, B.D. Lackey, R.N. Lang and J.S. Read, *Tidal deformability of neutron stars with realistic equations of state and their gravitational wave signatures in binary inspiral*, *Phys. Rev. D* **81** (2010) 123016 [0911.3535].

[162] T. Damour, A. Nagar and L. Villain, *Measurability of the tidal polarizability of neutron stars in late-inspiral gravitational-wave signals*, *Phys. Rev. D* **85** (2012) 123007 [1203.4352].

[163] K. Hotokezaka, K. Kyutoku, H. Okawa, M. Shibata and K. Kiuchi, *Binary Neutron Star Mergers: Dependence on the Nuclear Equation of State*, *Phys. Rev. D* **83** (2011) 124008 [1105.4370].

[164] A. Bauswein, T.W. Baumgarte and H.T. Janka, *Prompt merger collapse and the maximum mass of neutron stars*, *Phys. Rev. Lett.* **111** (2013) 131101 [1307.5191].

[165] LIGO Scientific, Virgo collaboration, *Search for Post-merger Gravitational Waves from the Remnant of the Binary Neutron Star Merger GW170817*, *Astrophys. J. Lett.* **851** (2017) L16 [1710.09320].

[166] B. Margalit and B.D. Metzger, *Constraining the Maximum Mass of Neutron Stars From Multi-Messenger Observations of GW170817*, *Astrophys. J. Lett.* **850** (2017) L19 [1710.05938].

[167] A. Bauswein, O. Just, H.-T. Janka and N. Stergioulas, *Neutron-star radius constraints from GW170817 and future detections*, *Astrophys. J. Lett.* **850** (2017) L34 [1710.06843].

[168] M.W. Coughlin, T. Dietrich, B. Margalit and B.D. Metzger, *Multimessenger Bayesian parameter inference of a binary neutron star merger*, *Mon. Not. Roy. Astron. Soc.* **489** (2019) L91 [1812.04803].

[169] S. De, D. Finstad, J.M. Lattimer, D.A. Brown, E. Berger and C.M. Biwer, *Tidal Deformabilities and Radii of Neutron Stars from the Observation of GW170817*, *Phys. Rev. Lett.* **121** (2018) 091102 [1804.08583].

[170] LIGO Scientific, Virgo collaboration, *Properties of the binary neutron star merger GW170817*, *Phys. Rev. X* **9** (2019) 011001 [1805.11579].

[171] LIGO Scientific, Virgo collaboration, *GW170817: Measurements of neutron star radii and equation of state*, *Phys. Rev. Lett.* **121** (2018) 161101 [1805.11581].

[172] D. Radice and L. Dai, *Multimessenger Parameter Estimation of GW170817*, *Eur. Phys. J. A* **55** (2019) 50 [1810.12917].

[173] T. Dietrich, M.W. Coughlin, P.T.H. Pang, M. Bulla, J. Heinzel, L. Issa et al., *Multimessenger constraints on the neutron-star equation of state and the Hubble constant*, *Science* **370** (2020) 1450 [2002.11355].

[174] M. Breschi, A. Perego, S. Bernuzzi, W. Del Pozzo, V. Nedora, D. Radice et al., *AT2017gfo: Bayesian inference and model selection of multicomponent kilonovae and constraints on the neutron star equation of state*, *Mon. Not. Roy. Astron. Soc.* **505** (2021) 1661 [2101.01201].

[175] M. Breschi, S. Bernuzzi, D. Godzieba, A. Perego and D. Radice, *Constraints on the Maximum Densities of Neutron Stars from Postmerger Gravitational Waves with Third-Generation Observations*, *Phys. Rev. Lett.* **128** (2022) 161102 [2110.06957].

[176] A. Perego, D. Logoteta, D. Radice, S. Bernuzzi, R. Kashyap, A. Das et al., *Probing the Incompressibility of Nuclear Matter at Ultrahigh Density through the Prompt Collapse of Asymmetric Neutron Star Binaries*, *Phys. Rev. Lett.* **129** (2022) 032701 [2112.05864].

[177] Y. Fujimoto, K. Fukushima, K. Hotokezaka and K. Kyutoku, *Gravitational Wave Signal for Quark Matter with Realistic Phase Transition*, *Phys. Rev. Lett.* **130** (2023) 091404 [2205.03882].

[178] C.D. Capano, I. Tews, S.M. Brown, B. Margalit, S. De, S. Kumar et al., *Stringent constraints on neutron-star radii from multimessenger observations and nuclear theory*, *Nature Astron.* **4** (2020) 625 [1908.10352].

[179] P.T.H. Pang, I. Tews, M.W. Coughlin, M. Bulla, C. Van Den Broeck and T. Dietrich, *Nuclear Physics Multimessenger Astrophysics Constraints on the Neutron Star Equation of State: Adding NICER's PSR J0740+6620 Measurement*, *Astrophys. J.* **922** (2021) 14 [2105.08688].

[180] E. Annala, T. Gorda, E. Katerini, A. Kurkela, J. Nättilä, V. Paschalidis et al., *Multimessenger Constraints for Ultradense Matter*, *Phys. Rev. X* **12** (2022) 011058 [2105.05132].

[181] D. Logoteta, *Hyperons in Neutron Stars*, *Universe* **7** (2021) 408.

[182] M. Evans et al., *A Horizon Study for Cosmic Explorer: Science, Observatories, and Community*, [2109.09882].

[183] A. Lovato et al., *Long Range Plan: Dense matter theory for heavy-ion collisions and neutron stars*, [2211.02224].

[184] A. Kedia, H.I. Kim, I.-S. Suh and G.J. Mathews, *Binary neutron star mergers as a probe of quark-hadron crossover equations of state*, *Phys. Rev. D* **106** (2022) 103027 [2203.05461].

[185] S. Tootle, C. Ecker, K. Topolski, T. Demircik, M. Järvinen and L. Rezzolla, *Quark formation and phenomenology in binary neutron-star mergers using V-QCD*, *SciPost Phys.* **13** (2022) 109 [2205.05691].

[186] A. Bauswein, S. Blacker, V. Vijayan, N. Stergioulas, K. Chatziioannou, J.A. Clark et al., *Equation of state constraints from the threshold binary mass for prompt collapse of neutron star mergers*, *Phys. Rev. Lett.* **125** (2020) 141103 [2004.00846].

[187] A. Bauswein, S. Blacker, G. Lioutas, T. Soultanis, V. Vijayan and N. Stergioulas, *Systematics of prompt black-hole formation in neutron star mergers*, *Phys. Rev. D* **103** (2021) 123004 [2010.04461].

[188] D. Reitze et al., *Cosmic Explorer: The U.S. Contribution to Gravitational-Wave Astronomy beyond LIGO*, *Bull. Am. Astron. Soc.* **51** (2019) 035 [1907.04833].

[189] M. Punturo et al., *The Einstein Telescope: A third-generation gravitational wave observatory*, *Class. Quant. Grav.* **27** (2010) 194002.

[190] K. Ackley et al., *Neutron Star Extreme Matter Observatory: A kilohertz-band gravitational-wave detector in the global network*, *Publ. Astron. Soc. Austral.* **37** (2020) e047 [2007.03128].

[191] M.G. Alford and S. Han, *Characteristics of hybrid compact stars with a sharp hadron-quark interface*, *Eur. Phys. J. A* **52** (2016) 62 [1508.01261].

[192] N.-U.F. Bastian, *Phenomenological quark-hadron equations of state with first-order phase transitions for astrophysical applications*, *Phys. Rev. D* **103** (2021) 023001 [2009.10846].

[193] V. Paschalidis, K. Yagi, D. Alvarez-Castillo, D.B. Blaschke and A. Sedrakian, *Implications from GW170817 and I-Love-Q relations for relativistic hybrid stars*, *Phys. Rev.* **D97** (2018) 084038 [1712.00451].

[194] D.E. Alvarez-Castillo and D.B. Blaschke, *High-mass twin stars with a multipolytrope equation of state*, *Phys. Rev. C* **96** (2017) 045809 [1703.02681].

[195] M.G. Alford and A. Sedrakian, *Compact stars with sequential QCD phase transitions*, *Phys. Rev. Lett.* **119** (2017) 161104 [1706.01592].

[196] G. Bozzola, P.L. Espino, C.D. Lewin and V. Paschalidis, *Maximum mass and universal relations of rotating relativistic hybrid hadron-quark stars*, *Eur. Phys. J. A* **55** (2019) 149 [1905.00028].

[197] P.L. Espino and V. Paschalidis, *Fate of twin stars on the unstable branch: Implications for the formation of twin stars*, *Phys. Rev. D* **105** (2022) 043014 [2105.05269].

[198] J.S. Read, B.D. Lackey, B.J. Owen and J.L. Friedman, *Constraints on a phenomenologically parameterized neutron-star equation of state*, *Phys. Rev. D* **79** (2009) 124032 [0812.2163].

[199] J.W. York, Jr., *Conformal 'thin sandwich' data for the initial-value problem*, *Phys. Rev. Lett.* **82** (1999) 1350 [gr-qc/9810051].

[200] K. Taniguchi, E. Gourgoulhon and S. Bonazzola, *Quasiequilibrium sequences of synchronized and irrotational binary neutron stars in general relativity. 2. Newtonian limits*, *Phys. Rev. D* **64** (2001) 064012 [gr-qc/0103041].

[201] K. Taniguchi and E. Gourgoulhon, *Equilibrium sequences of synchronized and irrotational binary systems composed of different mass stars in newtonian gravity*, *Phys. Rev. D* **65** (2002) 044027 [astro-ph/0108086].

[202] Y. Zlochower, S.R. Brandt, P. Diener, W.E. Gabella, M. Gracia-Linares, R. Haas et al., *The einstein toolkit*, May, 2022. 10.5281/zenodo.6588641.

[203] B.K. Pickett, R.H. Durisen and G.A. Davis, *The dynamic stability of rotating protostars and protostellar disks. i. the effects of the angular momentum distribution*, *The Astrophysical Journal* **458** (1996) 714.

[204] J.M. Centrella, K.C.B. New, L.L. Lowe and J.D. Brown, *Dynamical rotational instability at low T/W*, *Astrophys. J. Lett.* **550** (2001) L193 [astro-ph/0010574].

[205] M. Saijo, T.W. Baumgarte and S.L. Shapiro, *One-armed spiral instability in differentially rotating stars*, *Astrophys. J.* **595** (2002) 352 [astro-ph/0302436].

[206] S. Ou and J. Tohline, *Unexpected dynamical instabilities in differentially rotating neutron stars*, *Astrophys. J.* **651** (2006) 1068 [astro-ph/0604099].

[207] V. Paschalidis, W.E. East, F. Pretorius and S.L. Shapiro, *One-arm Spiral Instability in Hypermassive Neutron Stars Formed by Dynamical-Capture Binary Neutron Star Mergers*, *Phys. Rev.* **D92** (2015) 121502 [1510.03432].

[208] W.E. East, V. Paschalidis and F. Pretorius, *Equation of state effects and one-arm spiral instability in hypermassive neutron stars formed in eccentric neutron star mergers*, *Class. Quant. Grav.* **33** (2016) 244004 [1609.00725].

[209] W.E. East, V. Paschalidis, F. Pretorius and S.L. Shapiro, *Relativistic simulations of eccentric binary neutron star mergers: One-arm spiral instability and effects of neutron star spin*, *prd* **93** (2016) 024011 [1511.01093].

[210] L. Lehner, S.L. Liebling, C. Palenzuela and P.M. Motl, *m=1 instability and gravitational wave signal in binary neutron star mergers*, *Phys. Rev.* **D94** (2016) 043003 [1605.02369].

[211] C.D. Ott, S. Ou, J.E. Tohline and A. Burrows, *One-armed spiral instability in a slowly rotating, post-bounce supernova core*, *Astrophys. J. Lett.* **625** (2005) L119 [astro-ph/0503187].

[212] T. Kuroda, T. Takiwaki and K. Kotake, *Gravitational Wave Signatures from Low-mode Spiral Instabilities in Rapidly Rotating Supernova Cores*, *Phys. Rev. D* **89** (2014) 044011 [1304.4372].

[213] R. Kashyap, R. Fisher, E. García-Berro, G. Aznar-Siguán, S. Ji and P. Lorén-Aguilar, *Spiral Disk Instability Can Drive Thermonuclear Explosions in Binary White Dwarf Mergers*, *Astrophys. J.* **800** (2015) L7 [1501.05645].

[214] R. Kashyap, R. Fisher, E. García-Berro, G. Aznar-Siguán, S. Ji and P. Lorén-Aguilar, *One-Armed Spiral Instability in Double-Degenerate Post-Merger Accretion Disks*, *Astrophys. J.* **840** (2017) 16 [1704.01584].

[215] E. Wessel, V. Paschalidis, A. Tsokaros, M. Ruiz and S.L. Shapiro, *Gravitational Waves from Disks Around Spinning Black Holes: Simulations in Full General Relativity*, *Phys. Rev. D* **103** (2021) 043013 [2011.04077].

[216] M. Saijo and S. Yoshida, *Unstable normal modes of low T/W dynamical instabilities in differentially rotating stars*, *Phys. Rev. D* **94** (2016) 084032 [1610.05328].

[217] M. Saijo, *Determining the stiffness of the equation of state using low T/W dynamical instabilities in differentially rotating stars*, *Phys. Rev. D* **98** (2018) 024003 [1807.00841].

[218] LIGO Scientific, Virgo collaboration, *GW170817: Observation of Gravitational Waves from a Binary Neutron Star Inspiral*, *Phys. Rev. Lett.* **119** (2017) 161101 [1710.05832].

[219] T. Zhang, H. Yang, D. Martynov, P. Schmidt and H. Miao, *Gravitational-Wave Detector for Postmerger Neutron Stars: Beyond the Quantum Loss Limit of the Fabry-Perot-Michelson Interferometer*, *Phys. Rev. X* **13** (2023) 021019 [2212.12144].

[220] G. Rivieccio, D. Guerra, M. Ruiz and J.A. Font, *Gravitational-wave imprints of nonconvex dynamics in binary neutron star mergers*, *Phys. Rev. D* **109** (2024) 064032 [2401.06849].

[221] L. Franci, R. De Pietri, K. Dionysopoulou and L. Rezzolla, *Dynamical bar-mode instability in rotating and magnetized relativistic stars*, *Phys. Rev. D* **88** (2013) 104028 [1308.3989].

[222] C.D. Muhlberger, F.H. Nouri, M.D. Duez, F. Foucart, L.E. Kidder, C.D. Ott et al., *Magnetic effects on the low-T/|W| instability in differentially rotating neutron stars*, *Phys. Rev. D* **90** (2014) 104014 [1405.2144].

[223] C. Palenzuela, R. Aguilera-Miret, F. Carrasco, R. Ciolfi, J.V. Kalinani, W. Kastaun et al., *Turbulent magnetic field amplification in binary neutron star mergers*, *Phys. Rev. D* **106** (2022) 023013 [2112.08413].

[224] F. Zappa, S. Bernuzzi, D. Radice and A. Perego, *Binary neutron star merger simulations with neutrino transport and turbulent viscosity: impact of different schemes and grid resolution*, *Monthly Notices of the Royal Astronomical Society* **520** (2023) 1481 [https://academic.oup.com/mnras/article-pdf/520/1/1481/49116821/stad107.pdf].

[225] P.L. Espino, V. Paschalidis, T.W. Baumgarte and S.L. Shapiro, *Dynamical stability of quasitoroidal differentially rotating neutron stars*, *Phys. Rev. D* **100** (2019) 043014 [1906.08786].

[226] P.L. Espino, A. Prakash, D. Radice and D. Logoteta, *Revealing phase transition in dense matter with gravitational wave spectroscopy of binary neutron star mergers*, *Phys. Rev. D* **109** (2024) 123009 [2301.03619].

[227] I. BOMBACI, M. PRAKASH, M. PRAKASH, P. ELLIS, J. LATTIMER and G. BROWN, *Newborn hot neutron-stars*, *NUCLEAR PHYSICS A* **583** (1995) C623.

[228] M. Prakash, I. Bombaci, M. Prakash, P.J. Ellis, J.M. Lattimer and R. Knorren, *Composition and structure of protoneutron stars*, *Phys. Rept.* **280** (1997) 1 [nucl-th/9603042].

[229] F. Schianchi, H. Gieg, V. Nedora, A. Neuweiler, M. Ujevic, M. Bulla et al., *M1 neutrino transport within the numerical-relativistic code BAM with application to low mass binary neutron star mergers*, *Phys. Rev. D* **109** (2024) 044012 [2307.04572].

[230] D. Radice and S. Bernuzzi, *Ab-initio General-relativistic Neutrino-radiation Hydrodynamics Simulations of Long-lived Neutron Star Merger Remnants to Neutrino Cooling Timescales*, *Astrophys. J.* **959** (2023) 46 [2306.13709].

[231] A. Camilletti, L. Chiesa, G. Ricigliano, A. Perego, L.C. Lippold, S. Padamata et al., *Numerical relativity simulations of the neutron star merger GW190425: microphysics and mass ratio effects*, *Monthly Notices of the Royal Astronomical Society* **516** (2022) 4760 [https://academic.oup.com/mnras/article-pdf/516/4/4760/45992630/stac2333.pdf].

[232] E.R. Most, S.P. Harris, C. Plumberg, M.G. Alford, J. Noronha, J. Noronha-Hostler et al., *Projecting the likely importance of weak-interaction-driven bulk viscosity in neutron star mergers*, *Mon. Not. Roy. Astron. Soc.* **509** (2021) 1096 [2107.05094].

[233] E.R. Most, A. Haber, S.P. Harris, Z. Zhang, M.G. Alford and J. Noronha, *Emergence of Microphysical Bulk Viscosity in Binary Neutron Star Postmerger Dynamics*, *Astrophys. J. Lett.* **967** (2024) L14 [2207.00442].

[234] L. Combi and D.M. Siegel, *GRMHD Simulations of Neutron-star Mergers with Weak Interactions: r-process Nucleosynthesis and Electromagnetic Signatures of Dynamical Ejecta*, *Astrophys. J.* **944** (2023) 28 [2206.03618].

[235] M. George, M.-R. Wu, I. Tamborra, R. Ardevol-Pulpillo and H.-T. Janka, *Fast neutrino flavor conversion, ejecta properties, and nucleosynthesis in newly-formed hypermassive remnants of neutron-star mergers*, *Phys. Rev. D* **102** (2020) 103015 [2009.04046].

[236] D.M. Siegel and B.D. Metzger, *Three-dimensional GRMHD simulations of neutrino-cooled accretion disks from neutron star mergers*, *Astrophys. J.* **858** (2018) 52 [1711.00868].

[237] D. Martin, A. Perego, W. Kastaun and A. Arcones, *The role of weak interactions in dynamic ejecta from binary neutron star mergers*, *Class. Quant. Grav.* **35** (2018) 034001 [1710.04900].

[238] S. Fujibayashi, M. Shibata, S. Wanajo, K. Kiuchi, K. Kyutoku and Y. Sekiguchi, *Mass ejection from disks surrounding a low-mass black hole: Viscous neutrino-radiation hydrodynamics simulation in full general relativity*, *Phys. Rev. D* **101** (2020) 083029 [2001.04467].

[239] E. Grohs, S. Richers, S.M. Couch, F. Foucart, J.P. Kneller and G.C. McLaughlin, *Neutrino fast flavor instability in three dimensions for a neutron star merger*, *Phys. Lett. B* **846** (2023) 138210 [2207.02214].

[240] E. Grohs, S. Richers, S.M. Couch, F. Foucart, J. Froustey, J.P. Kneller et al., *Two-moment Neutrino Flavor Transformation with Applications to the Fast Flavor Instability in Neutron Star Mergers*, *Astrophys. J.* **963** (2024) 11 [2309.00972].

[241] S.A. Richers, G.C. McLaughlin, J.P. Kneller and A. Vlasenko, *Neutrino Quantum Kinetics in Compact Objects*, *Phys. Rev. D* **99** (2019) 123014 [1903.00022].

[242] R. Ciolfi, *The key role of magnetic fields in binary neutron star mergers*, *Gen. Rel. Grav.* **52** (2020) 59 [2003.07572].

[243] R. Ciolfi, W. Kastaun, B. Giacomazzo, A. Endrizzi, D.M. Siegel and R. Perna, *General relativistic magnetohydrodynamic simulations of binary neutron star mergers forming a long-lived neutron star*, *Phys. Rev. D* **95** (2017) 063016 [1701.08738].

[244] M. Shibata and K. Kiuchi, *Gravitational waves from remnant massive neutron stars of binary neutron star merger: Viscous hydrodynamics effects*, *Phys. Rev. D* **95** (2017) 123003 [1705.06142].

[245] G. Baym, T. Hatsuda, T. Kojo, P.D. Powell, Y. Song and T. Takatsuka, *From hadrons to quarks in neutron stars: a review*, *Rept. Prog. Phys.* **81** (2018) 056902 [1707.04966].

[246] A.R. Bodmer, *Collapsed nuclei*, *Phys. Rev. D* **4** (1971) 1601.

[247] E. Witten, *Cosmic Separation of Phases*, *Phys. Rev. D* **30** (1984) 272.

[248] M. Dey, I. Bombaci, J. Dey, S. Ray and B.C. Samanta, *Strange stars with realistic quark vector interaction and phenomenological density dependent scalar potential*, *Phys. Lett. B* **438** (1998) 123 [astro-ph/9810065].

[249] X.D. Li, I. Bombaci, M. Dey, J. Dey and E.P.J. van den Heuvel, *Is SAX J1808.4-3658 a strange star?*, *Phys. Rev. Lett.* **83** (1999) 3776 [hep-ph/9905356].

[250] X.-D. Li, S. Ray, J. Dey, M. Dey and I. Bombaci, *On the Nature of the compact star in 4u 1728-34*, *Astrophys. J. Lett.* **527** (1999) L51 [astro-ph/9908274].

[251] J.J. Drake et al., *Is RXJ1856.5-3754 a quark star?*, *Astrophys. J.* **572** (2002) 996 [astro-ph/0204159].

[252] F. Weber, *Strange quark matter and compact stars*, *Prog. Part. Nucl. Phys.* **54** (2005) 193 [astro-ph/0407155].

[253] LIGO Scientific, Virgo collaboration, *GW190814: Gravitational Waves from the Coalescence of a 23 Solar Mass Black Hole with a 2.6 Solar Mass Compact Object*, *Astrophys. J. Lett.* **896** (2020) L44 [2006.12611].

[254] I. Bombaci, A. Drago, D. Logoteta, G. Pagliara and I. Vidaña, *Was GW190814 a Black Hole–Strange Quark Star System?*, *Phys. Rev. Lett.* **126** (2021) 162702 [2010.01509].

[255] V. Doroshenko, V. Suleimanov, G. Puehlhofer and A. Santangelo, *A strangely light neutron star within a supernova remnant*, *NATURE ASTRONOMY* **6** (2022) 1444+.

[256] F. Di Clemente, A. Drago and G. Pagliara, *Is the Compact Object Associated with HESS J1731-347 a Strange Quark Star? A Possible Astrophysical Scenario for Its Formation*, *Astrophys. J.* **967** (2024) 159 [2211.07485].

[257] J.E. Horvath, L.S. Rocha, L.M. de Sá, P.H.R.S. Moraes, L.G. Barão, M.G.B. de Avellar et al., *A light strange star in the remnant HESS J1731−347: Minimal consistency checks*, *Astron. Astrophys.* **672** (2023) L11 [2303.10264].

[258] O. BENVENUTO and J. HORVATH, *Evidence for strange matter in supernovae*, *PHYSICAL REVIEW LETTERS* **63** (1989) 716.

[259] T. Fischer, I. Sagert, G. Pagliara, M. Hempel, J. Schaffner-Bielich, T. Rauscher et al., *Core-collapse supernova explosions triggered by a quark-hadron phase transition during the early post-bounce phase*, *Astrophys. J. Suppl.* **194** (2011) 39 [1011.3409].

[260] B.W. Mintz, E.S. Fraga, G. Pagliara and J. Schaffner-Bielich, *Nucleation of quark matter in protoneutron star matter*, *Phys. Rev. D* **81** (2010) 123012 [0910.3927].

[261] I. Bombaci, D. Logoteta, P.K. Panda, C. Providencia and I. Vidana, *Quark matter nucleation in hot hadronic matter*, *Phys. Lett. B* **680** (2009) 448 [0910.4109].

[262] I. Bombaci, D. Logoteta, C. Providencia and I. Vidana, *Effects of quark matter nucleation on the evolution of proto-neutron stars*, *Astron. Astrophys.* **528** (2011) A71 [1102.1665].

[263] G. Lugones, *From quark drops to quark stars: some aspects of the role of quark matter in compact stars*, *Eur. Phys. J. A* **52** (2016) 53 [1508.05548].

[264] E. Farhi and R.L. Jaffe, *Strange Matter*, *Phys. Rev. D* **30** (1984) 2379.

[265] A.V. Olinto, *On the Conversion of Neutron Stars Into Strange Stars*, *Phys. Lett. B* **192** (1987) 71.

[266] N. Bucciantini, A. Drago, G. Pagliara, S. Traversi and A. Bauswein, *Formation and evaporation of strangelets during the merger of two compact stars*, *Phys. Rev. D* **106** (2022) 103032 [1908.02501].

[267] Z. Berezhiani, I. Bombaci, A. Drago, F. Frontera and A. Lavagno, *Gamma-ray bursts from delayed collapse of neutron stars to quark matter stars*, *Astrophys. J.* **586** (2003) 1250 [astro-ph/0209257].

[268] I. Bombaci, I. Parenti and I. Vidana, *Quark deconfinement and implications for the radius and the limiting mass of compact stars*, *Astrophys. J.* **614** (2004) 314 [astro-ph/0402404].

[269] A. Drago, A. Lavagno and G. Pagliara, *Effects of color superconductivity on the structure and formation of compact stars*, *Phys. Rev. D* **69** (2004) 057505 [nucl-th/0401052].

[270] I. Bombaci and B. Datta, *Conversion of neutron stars to strange stars as the central engine of gamma-ray bursts*, *Astrophys. J. Lett.* **530** (2000) L69 [astro-ph/0001478].

[271] G. Wiktorowicz, A. Drago, G. Pagliara and S.B. Popov, *Strange quark stars in binaries: formation rates, mergers and explosive phenomena*, *Astrophys. J.* **846** (2017) 163 [1707.01586].

[272] S. Bhattacharyya, I. Bombaci, D. Logoteta and A.V. Thampan, *Fast spinning strange stars: possible ways to constrain interacting quark matter parameters*, *Mon. Not. Roy. Astron. Soc.* **457** (2016) 3101 [1601.06120].

[273] L. Baiotti and L. Rezzolla, *Binary neutron star mergers: a review of Einstein's richest laboratory*, *Rept. Prog. Phys.* **80** (2017) 096901 [1607.03540].

[274] E. Zhou, K. Kiuchi, M. Shibata, A. Tsokaros and K. Uryu, *Evolution of equal mass binary bare quark stars in full general relativity: Could a supramassive merger remnant experience prompt collapse?*, *Phys. Rev. D* **106** (2022) 103030 [2111.00958].

[275] S. Weissenborn, I. Sagert, G. Pagliara, M. Hempel and J. Schaffner-Bielich, *Quark Matter In Massive Neutron Stars*, *Astrophys. J. Lett.* **740** (2011) L14 [1102.2869].

[276] S. Bhattacharyya, I. Bombaci, D. Logoteta and A.V. Thampan, *Two coexisting families of compact stars: observational implications for millisecond pulsars*, *Astrophys. J.* **848** (2017) 65 [1709.02415].

[277] L. Werneck, S. Cupp, T. Assumpção, S.R. Brandt, C.-H. Cheng, P. Diener et al., *The einstein toolkit*, May, 2023. 10.5281/zenodo.7942541.

[278] X.Y. Hu, N.A. Adams and C.-W. Shu, *Positivity-preserving method for high-order conservative schemes solving compressible euler equations*, *Journal of Computational Physics* **242** (2013) 169.

[279] H. Bandyopadhyay, D. Radice, A. Prakash, A. Dhani, D. Logoteta, A. Perego et al., *Do black holes remember what they are made of?*, *Classical and Quantum Gravity* (2024) .

[280] C. Reisswig and D. Pollney, *Notes on the integration of numerical relativity waveforms*, *Class. Quant. Grav.* **28** (2011) 195015 [1006.1632].

[281] W. Kastaun, R. Ciolfi, A. Endrizzi and B. Giacomazzo, *Structure of Stable Binary Neutron Star Merger Remnants: Role of Initial Spin*, *Phys. Rev. D* **96** (2017) 043019 [1612.03671].

[282] A. Prakash, I. Gupta, M. Breschi, R. Kashyap, D. Radice, S. Bernuzzi et al., *Detectability of QCD phase transitions in binary neutron star mergers: Bayesian inference with the next generation gravitational wave detectors*, *Phys. Rev. D* **109** (2024) 103008 [2310.06025].

[283] B.K. Pradhan, S. Shirke and D. Chatterjee, *Prospects of identifying the presence of Strange Stars using Gravitational Waves from binary systems*, [2311.15745].

[284] M. Breschi, S. Bernuzzi, K. Chakravarti, A. Camilletti, A. Prakash and A. Perego, *Kilohertz gravitational waves from binary neutron star mergers: Numerical-relativity informed postmerger model*, *Phys. Rev. D* **109** (2024) 064009 [2205.09112].

[285] A. Gonzalez et al., *Second release of the CoRe database of binary neutron star merger waveforms*, *Class. Quant. Grav.* **40** (2023) 085011 [2210.16366].

[286] J.M. Lattimer and M. Prakash, *Neutron star structure and the equation of state*, *Astrophys. J.* **550** (2001) 426 [astro-ph/0002232].

[287] J. Alsing, H.O. Silva and E. Berti, *Evidence for a maximum mass cut-off in the neutron star mass distribution and constraints on the equation of state*, *Mon. Not. Roy. Astron. Soc.* **478** (2018) 1377 [1709.07889].

[288] T.E. Riley et al., *A NICER View of the Massive Pulsar PSR J0740+6620 Informed by Radio Timing and XMM-Newton Spectroscopy*, *Astrophys. J. Lett.* **918** (2021) L27 [2105.06980].

[289] R.M. Ludlam et al., *Radius Constraints from Reflection Modeling of Cygnus X-2 with NuSTAR and NICER*, *Astrophys. J.* **927** (2022) 112 [2201.11767].

[290] T. Salmi et al., *The Radius of PSR J0740+6620 from NICER with NICER Background Estimates*, *Astrophys. J.* **941** (2022) 150 [2209.12840].

[291] LIGO Scientific Collaboration and Virgo Collaboration collaboration, *Gw170817: Observation of gravitational waves from a binary neutron star inspiral*, *Phys. Rev. Lett.* **119** (2017) 161101.

[292] B. Margalit and B.D. Metzger, *Constraining the Maximum Mass of Neutron Stars From Multi-Messenger Observations of GW170817*, *Astrophys. J. Lett.* **850** (2017) L19 [1710.05938].

[293] D. Radice, A. Perego, F. Zappa and S. Bernuzzi, *GW170817: Joint Constraint on the Neutron Star Equation of State from Multimessenger Observations*, *Astrophys. J. Lett.* **852** (2018) L29 [1711.03647].

[294] S. De, D. Finstad, J.M. Lattimer, D.A. Brown, E. Berger and C.M. Biwer, *Tidal Deformabilities and Radii of Neutron Stars from the Observation of GW170817*, *Phys. Rev. Lett.* **121** (2018) 091102 [1804.08583].

[295] LIGO Scientific, Virgo collaboration, *GW170817: Measurements of neutron star radii and equation of state*, *Phys. Rev. Lett.* **121** (2018) 161101 [1805.11581].

[296] T. Dietrich, M.W. Coughlin, P.T.H. Pang, M. Bulla, J. Heinzel, L. Issa et al., *Multimessenger constraints on the neutron-star equation of state and the Hubble constant*, *Science* **370** (2020) 1450 [2002.11355].

[297] R. Kashyap et al., *Numerical relativity simulations of prompt collapse mergers: Threshold mass and phenomenological constraints on neutron star properties after GW170817*, *Phys. Rev. D* **105** (2022) 103022 [2111.05183].

[298] LIGO Scientific Collaboration and Virgo Collaboration collaboration, *Multi-messenger observations of a binary neutron star merger*, *Astrophys. J. Lett.* **848** (2017) L12.

[299] LIGO Scientific, Virgo collaboration, *GW190425: Observation of a Compact Binary Coalescence with Total Mass* $\sim 3.4 M_{\odot}$, *Astrophys. J. Lett.* **892** (2020) L3 [2001.01761].

[300] M. Maggiore et al., *Science Case for the Einstein Telescope*, *JCAP* **2020** (2020) 050 [1912.02622].

[301] LIGO Scientific collaboration, *Exploring the Sensitivity of Next Generation Gravitational Wave Detectors*, *Class. Quant. Grav.* **34** (2017) 044001 [1607.08697].

[302] KAGRA, LIGO Scientific, Virgo, VIRGO collaboration, *Prospects for observing and localizing gravitational-wave transients with Advanced LIGO, Advanced Virgo and KAGRA*, *Living Rev. Rel.* **21** (2018) 3 [1304.0670].

[303] A. Bauswein, H.T. Janka and R. Oechslin, *Testing Approximations of Thermal Effects in Neutron Star Merger Simulations*, *Phys. Rev. D* **82** (2010) 084043 [1006.3315].

[304] Y. Sekiguchi, K. Kiuchi, K. Kyutoku and M. Shibata, *Gravitational waves and neutrino emission from the merger of binary neutron stars*, *Phys. Rev. Lett.* **107** (2011) 051102 [1105.2125].

[305] F. Foucart, E. O'Connor, L. Roberts, L.E. Kidder, H.P. Pfeiffer and M.A. Scheel, *Impact of an improved neutrino energy estimate on outflows in neutron star merger simulations*, *Phys. Rev. D* **94** (2016) 123016 [1607.07450].

[306] D. Radice, S. Bernuzzi, A. Perego and R. Haas, *A new moment-based general-relativistic neutrino-radiation transport code: Methods and first applications to neutron star mergers*, *Mon. Not. Roy. Astron. Soc.* **512** (2022) 1499 [2111.14858].

[307] D. Neilsen, S.L. Liebling, M. Anderson, L. Lehner, E. O'Connor and C. Palenzuela, *Magnetized Neutron Stars With Realistic Equations of State and Neutrino Cooling*, *Phys. Rev. D* **89** (2014) 104029 [1403.3680].

[308] E.R. Most, L.J. Papenfort, V. Dexheimer, M. Hanauske, S. Schramm, H. Stöcker et al., *Signatures of quark-hadron phase transitions in general-relativistic neutron-star mergers*, *Phys. Rev. Lett.* **122** (2019) 061101 [1807.03684].

[309] P. Hammond, I. Hawke and N. Andersson, *Thermal aspects of neutron star mergers*, *Phys. Rev. D* **104** (2021) 103006 [2108.08649].

[310] A. Camilletti, L. Chiesa, G. Ricigliano, A. Perego, L.C. Lippold, S. Padamata et al., *Numerical relativity simulations of the neutron star merger GW190425: microphysics and mass ratio effects*, *Mon. Not. Roy. Astron. Soc.* (2022) [2204.05336].

[311] A. Figura, J.J. Lu, G.F. Burgio, Z.H. Li and H.J. Schulze, *Hybrid equation of state approach in binary neutron-star merger simulations*, *Phys. Rev. D* **102** (2020) 043006 [2005.08691].

[312] A. Carbone and A. Schwenk, *Ab initio constraints on thermal effects of the nuclear equation of state*, *Phys. Rev. C* **100** (2019) 025805 [1904.00924].

[313] C. Raithel, V. Paschalidis and F. Özel, *Realistic finite-temperature effects in neutron star merger simulations*, *Phys. Rev. D* **104** (2021) 063016 [2104.07226].

[314] A.S. Schneider, L.F. Roberts, C.D. Ott and E. O'connor, *Equation of state effects in the core collapse of a 20-$M_\odot$ star*, *Phys. Rev. C* **100** (2019) 055802 [1906.02009].

[315] C. Constantinou, B. Muccioli, M. Prakash and J.M. Lattimer, *Thermal properties of supernova matter: The bulk homogeneous phase*, *Phys. Rev. C* **89** (2014) 065802 [1402.6348].

[316] J. Margueron, R. Hoffmann Casali and F. Gulminelli, *Equation of state for dense nucleonic matter from metamodeling. I. Foundational aspects*, *Phys. Rev. C* **97** (2018) 025805 [1708.06894].

[317] B.-A. Li, B.-J. Cai, L.-W. Chen and J. Xu, *Nucleon Effective Masses in Neutron-Rich Matter*, *Prog. Part. Nucl. Phys.* **99** (2018) 29 [1801.01213].

[318] S. Huth, C. Wellenhofer and A. Schwenk, *New equations of state constrained by nuclear physics, observations, and QCD calculations of high-density nuclear matter*, *Phys. Rev. C* **103** (2021) 025803 [2009.08885].

[319] Z. Zhang, X.-B. Feng and L.-W. Chen, *Bayesian inference on isospin splitting of nucleon effective mass from giant resonances in $^{208}Pb$*, *Chin. Phys. C* **45** (2021) 064104 [2103.04643].

[320] O.E. Andersen, S. Zha, A. da Silva Schneider, A. Betranhandy, S.M. Couch and E.P. O'Connor, *Equation-of-state Dependence of Gravitational Waves in Core-collapse Supernovae*, *Astrophys. J.* **923** (2021) 201 [2106.09734].

[321] E. Gourgoulhon, P. Grandclément, J.-A. Marck, J. Novak and K. Taniguchi, "LORENE: Spectral methods differential equations solver." Astrophysics Source Code Library, record ascl:1608.018, Aug., 2016.

[322] F. Zappa, S. Bernuzzi, D. Radice and A. Perego, *Binary neutron star merger simulations with neutrino transport and turbulent viscosity: impact of different schemes and grid resolution*, *Mon. Not. Roy. Astron. Soc.* (2023) [2210.11491].

[323] D. Radice, L. Rezzolla and F. Galeazzi, *Beyond second-order convergence in simulations of binary neutron stars in full general-relativity*, *Mon. Not. Roy. Astron. Soc.* **437** (2014) L46 [1306.6052].

[324] D. Radice, L. Rezzolla and F. Galeazzi, *High-order fully general-relativistic hydrodynamics: new approaches and tests*, *Classical and Quantum Gravity* **31** (2014) 075012.

[325] K.S. Thorne, *Relativistic radiative transfer - Moment formalisms*, *Mon. Not. Roy. Astron. Soc.* **194** (1981) 439.

[326] M. Shibata, K. Kiuchi, Y.-i. Sekiguchi and Y. Suwa, *Truncated Moment Formalism for Radiation Hydrodynamics in Numerical Relativity*, *Prog. Theor. Phys.* **125** (2011) 1255 [1104.3937].

[327] D. Radice, *General-Relativistic Large-Eddy Simulations of Binary Neutron Star Mergers*, *Astrophys. J. Lett.* **838** (2017) L2 [1703.02046].

[328] K. Kiuchi, K. Kyutoku, Y. Sekiguchi and M. Shibata, *Global simulations of strongly magnetized remnant massive neutron stars formed in binary neutron star mergers*, *Phys. Rev. D* **97** (2018) 124039 [1710.01311].

[329] D. Radice, *Binary Neutron Star Merger Simulations with a Calibrated Turbulence Model*, *Symmetry* **12** (2020) 1249 [2005.09002].

[330] D. Radice, F. Galeazzi, J. Lippuner, L.F. Roberts, C.D. Ott and L. Rezzolla, *Dynamical Mass Ejection from Binary Neutron Star Mergers*, *Mon. Not. Roy. Astron. Soc.* **460** (2016) 3255 [1601.02426].

[331] M. Breschi, R. Gamba and S. Bernuzzi, *Bayesian inference of multimessenger astrophysical data: Methods and applications to gravitational waves*, *Phys. Rev. D* **104** (2021) 042001 [2102.00017].

[332] J. Buchner, *UltraNest - a robust, general purpose Bayesian inference engine*, Mar., 2021. 10.5281/zenodo.4636924.

[333] S. Hild et al., *Sensitivity Studies for Third-Generation Gravitational Wave Observatories*, *Class. Quant. Grav.* **28** (2011) 094013 [1012.0908].

[334] M. Breschi, R. Gamba, S. Borhanian, G. Carullo and S. Bernuzzi, *Kilohertz Gravitational Waves from Binary Neutron Star Mergers: Inference of Postmerger Signals with the Einstein Telescope*, [2205.09979].

[335] L. Lindblom, B.J. Owen and D.A. Brown, *Model Waveform Accuracy Standards for Gravitational Wave Data Analysis*, *Phys. Rev. D* **78** (2008) 124020 [0809.3844].

[336] T. Damour, A. Nagar and M. Trias, *Accuracy and effectualness of closed-form, frequency-domain waveforms for non-spinning black hole binaries*, *Phys. Rev. D* **83** (2011) 024006 [1009.5998].

[337] H. Yasin, S. Schäfer, A. Arcones and A. Schwenk, *Equation of state effects in core-collapse supernovae*, *Phys. Rev. Lett.* **124** (2020) 092701 [1812.02002].

[338] C. Palenzuela, R. Aguilera-Miret, F. Carrasco, R. Ciolfi, J.V. Kalinani, W. Kastaun et al., *Turbulent magnetic field amplification in binary neutron star mergers*, *Phys. Rev. D* **106** (2022) 023013 [2112.08413].

[339] C. Palenzuela, S.L. Liebling, D. Neilsen, L. Lehner, O.L. Caballero, E. O'Connor et al., *Effects of the microphysical Equation of State in the mergers of magnetized Neutron Stars With Neutrino Cooling*, *Phys. Rev. D* **92** (2015) 044045 [1505.01607].

[340] D. Radice, A. Perego, K. Hotokezaka, S.A. Fromm, S. Bernuzzi and L.F. Roberts, *Binary Neutron Star Mergers: Mass Ejection, Electromagnetic Counterparts and Nucleosynthesis*, *Astrophys. J.* **869** (2018) 130 [1809.11161].

[341] C.A. Raithel and V. Paschalidis, *Influence of stellar compactness on finite-temperature effects in neutron star merger simulations*, *Phys. Rev. D* **108** (2023) 083029 [2306.13144].

[342] J. Fields, A. Prakash, M. Breschi, D. Radice, S. Bernuzzi and A. da Silva Schneider, *Thermal Effects in Binary Neutron Star Mergers*, *Astrophys. J. Lett.* **952** (2023) L36 [2302.11359].

[343] LIGO Scientific, Virgo, Fermi GBM, INTEGRAL, IceCube, AstroSat Cadmium Zinc Telluride Imager Team, IPN, Insight-Hxmt, ANTARES, Swift, AGILE Team, 1M2H Team, Dark Energy Camera GW-EM, DES, DLT40, GRAWITA, Fermi-LAT, ATCA, ASKAP, Las Cumbres Observatory Group, OzGrav, DWF (Deeper Wider Faster Program), AST3, CAASTRO, VINROUGE, MASTER, J-GEM, GROWTH, JAGWAR, CaltechNRAO, TTU-NRAO, NuSTAR, Pan-STARRS, MAXI Team, TZAC Consortium, KU, Nordic Optical Telescope, ePESSTO, GROND, Texas Tech University, SALT Group, TOROS, BOOTES, MWA, CALET, IKI-GW Follow-up, H.E.S.S., LOFAR, LWA, HAWC, Pierre Auger, ALMA, Euro VLBI Team, Pi of Sky, Chandra Team at McGill University, DFN, ATLAS Telescopes, High Time Resolution Universe Survey, RIMAS, RATIR, SKA South Africa/MeerKAT collaboration, *Multi-messenger Observations of a Binary Neutron Star Merger*, *Astrophys. J. Lett.* **848** (2017) L12 [1710.05833].

[344] S. Bernuzzi, *Neutron Star Merger Remnants*, *Gen. Rel. Grav.* **52** (2020) 108 [2004.06419].

[345] LIGO Scientific collaboration, *Exploring the Sensitivity of Next Generation Gravitational Wave Detectors*, *Class. Quant. Grav.* **34** (2017) 044001 [1607.08697].

[346] M. Evans et al., *Cosmic Explorer: A Submission to the NSF MPSAC ngGW Subcommittee*, [2306.13745].

[347] M. Branchesi et al., *Science with the Einstein Telescope: a comparison of different designs*, *JCAP* **07** (2023) 068 [2303.15923].

[348] I. Gupta et al., *Characterizing Gravitational Wave Detector Networks: From A$^\sharp$ to Cosmic Explorer*, [2307.10421].

[349] S. Blacker, A. Bauswein and S. Typel, *Exploring thermal effects of the hadron-quark matter transition in neutron star mergers*, *Phys. Rev. D* **108** (2023) 063032 [2304.01971].

[350] E.R. Most and C.A. Raithel, *Impact of the nuclear symmetry energy on the post-merger phase of a binary neutron star coalescence*, *Phys. Rev. D* **104** (2021) 124012 [2107.06804].

[351] G.J. Mathews, A. Kedia, H.I. Kim and I.-S. Suh, *Neutron Star Mergers and the Quark Matter Equation of State*, *EPJ Web Conf.* **274** (2022) 01013 [2302.12897].

[352] Y.-J. Huang, L. Baiotti, T. Kojo, K. Takami, H. Sotani, H. Togashi et al., *Merger and Postmerger of Binary Neutron Stars with a Quark-Hadron Crossover Equation of State*, *Phys. Rev. Lett.* **129** (2022) 181101 [2203.04528].

[353] T. Demircik, C. Ecker, M. Järvinen, L. Rezzolla, S. Tootle and K. Topolski, *Exploring the Phase Diagram of V-QCD with Neutron Star Merger Simulations*, *EPJ Web Conf.* **274** (2022) 07006 [2211.10118].

[354] L.-J. Guo, W.-C. Yang, Y.-L. Ma and Y.-L. Wu, *Probing hadron-quark transition through binary neutron star merger*, [2308.01770].

[355] S. Haque, R. Mallick and S.K. Thakur, *Effects of onset of phase transition on binary neutron star mergers*, *Mon. Not. Roy. Astron. Soc.* **527** (2023) 11575 [2207.14485].

[356] B. Margalit, A.S. Jermyn, B.D. Metzger, L.F. Roberts and E. Quataert, *Angular-momentum Transport in Proto-neutron Stars and the Fate of Neutron Star Merger Remnants*, *Astrophys. J.* **939** (2022) 51 [2206.10645].

[357] A. Bauswein, N. Stergioulas and H.-T. Janka, *Exploring properties of high-density matter through remnants of neutron-star mergers*, *Eur. Phys. J. A* **52** (2016) 56 [1508.05493].

[358] S. Bose, K. Chakravarti, L. Rezzolla, B.S. Sathyaprakash and K. Takami, *Neutron-star Radius from a Population of Binary Neutron Star Mergers*, *Phys. Rev. Lett.* **120** (2018) 031102 [1705.10850].

[359] P.J. Easter, S. Ghonge, P.D. Lasky, A.R. Casey, J.A. Clark, F.H. Vivanco et al., *Detection and parameter estimation of binary neutron star merger remnants*, *Phys. Rev. D* **102** (2020) 043011 [2006.04396].

[360] T. Soultanis, A. Bauswein and N. Stergioulas, *Analytic models of the spectral properties of gravitational waves from neutron star merger remnants*, *Phys. Rev. D* **105** (2022) 043020 [2111.08353].

[361] K.W. Tsang, T. Dietrich and C. Van Den Broeck, *Modeling the postmerger gravitational wave signal and extracting binary properties from future binary neutron star detections*, *Phys. Rev. D* **100** (2019) 044047 [1907.02424].

[362] K. Chatziioannou, J.A. Clark, A. Bauswein, M. Millhouse, T.B. Littenberg and N. Cornish, *Inferring the post-merger gravitational wave emission from binary neutron star coalescences*, *Phys. Rev. D* **96** (2017) 124035 [1711.00040].

[363] M. Wijngaarden, K. Chatziioannou, A. Bauswein, J.A. Clark and N.J. Cornish, *Probing neutron stars with the full premerger and postmerger gravitational wave signal from binary coalescences*, *Phys. Rev. D* **105** (2022) 104019 [2202.09382].

[364] M. Breschi, G. Carullo and S. Bernuzzi, *Pre/post-merger consistency test for gravitational signals from binary neutron star mergers*, *Particles* **6** (2023) 731.

[365] R. Harada, K. Cannon, K. Hotokezaka and K. Kyutoku, *On the Testability of the Quark-Hadron Transition Using Gravitational Waves From Merging Binary Neutron Stars*, [2310.13603].

[366] S. Han and A.W. Steiner, *Tidal deformability with sharp phase transitions in (binary) neutron stars*, *Phys. Rev. D* **99** (2019) 083014 [1810.10967].

[367] M. Sieniawska, W. Turczanski, M. Bejger and J.L. Zdunik, *Tidal deformability and other global parameters of compact stars with strong phase transitions*, *Astron. Astrophys.* **622** (2019) A174 [1807.11581].

[368] C.A. Raithel and E.R. Most, *Degeneracy in the Inference of Phase Transitions in the Neutron Star Equation of State from Gravitational Wave Data*, *Phys. Rev. Lett.* **130** (2023) 201403 [2208.04294].

[369] R. Essick, I. Legred, K. Chatziioannou, S. Han and P. Landry, *Phase transition phenomenology with nonparametric representations of the neutron star equation of state*, *Phys. Rev. D* **108** (2023) 043013 [2305.07411].

[370] C. Mondal, M. Antonelli, F. Gulminelli, M. Mancini, J. Novak and M. Oertel, *Detectability of a phase transition in neutron star matter with third-generation gravitational wave interferometers*, *Mon. Not. Roy. Astron. Soc.* **524** (2023) 3464 [2305.05999].

[371] C.A. Raithel and E.R. Most, *Tidal deformability doppelgänger: Implications of a low-density phase transition in the neutron star equation of state*, *Phys. Rev. D* **108** (2023) 023010 [2208.04295].

[372] P.T.H. Pang, T. Dietrich, I. Tews and C. Van Den Broeck, *Parameter estimation for strong phase transitions in supranuclear matter using gravitational-wave astronomy*, *Phys. Rev. Res.* **2** (2020) 033514 [2006.14936].

[373] S. Typel, G. Ropke, T. Klahn, D. Blaschke and H.H. Wolter, *Composition and thermodynamics of nuclear matter with light clusters*, *Phys. Rev. C* **81** (2010) 015803 [0908.2344].

[374] D. Alvarez-Castillo, A. Ayriyan, S. Benic, D. Blaschke, H. Grigorian and S. Typel, *New class of hybrid EoS and Bayesian M-R data analysis*, *Eur. Phys. J. A* **52** (2016) 69 [1603.03457].

[375] M.A.R. Kaltenborn, N.-U.F. Bastian and D.B. Blaschke, *Quark-nuclear hybrid star equation of state with excluded volume effects*, *Phys. Rev. D* **96** (2017) 056024 [1701.04400].

[376] F. Harris, *On the use of windows for harmonic analysis with the discrete fourier transform*, *Proceedings of the IEEE* **66** (1978) 51.

[377] M. Breschi, R. Gamba and S. Bernuzzi, *Bayesian inference of multimessenger astrophysical data: Methods and applications to gravitational waves*, *Phys. Rev. D* **104** (2021) 042001 [2102.00017].

[378] E. Thrane and C. Talbot, *An introduction to Bayesian inference in gravitational-wave astronomy: parameter estimation, model selection, and hierarchical models*, *Publ. Astron. Soc. Austral.* **36** (2019) e010 [1809.02293].

[379] T. Callister, *A Thesaurus for Common Priors in Gravitational-Wave Astronomy*, [2104.09508].

[380] B.S. Sathyaprakash and S.V. Dhurandhar, *Choice of filters for the detection of gravitational waves from coalescing binaries*, *Phys. Rev. D* **44** (1991) 3819.

[381] A. Bohé, S. Marsat and L. Blanchet, *Next-to-next-to-leading order spin–orbit effects in the gravitational wave flux and orbital phasing of compact binaries*, *Class. Quant. Grav.* **30** (2013) 135009 [1303.7412].

[382] K.G. Arun, A. Buonanno, G. Faye and E. Ochsner, *Higher-order spin effects in the amplitude and phase of gravitational waveforms emitted by inspiraling compact binaries: Ready-to-use gravitational waveforms*, *Phys. Rev. D* **79** (2009) 104023 [0810.5336].

[383] B. Mikoczi, M. Vasuth and L.A. Gergely, *Self-interaction spin effects in inspiralling compact binaries*, *Phys. Rev. D* **71** (2005) 124043 [astro-ph/0504538].

[384] A. Bohé, G. Faye, S. Marsat and E.K. Porter, *Quadratic-in-spin effects in the orbital dynamics and gravitational-wave energy flux of compact binaries at the 3PN order*, *Class. Quant. Grav.* **32** (2015) 195010 [1501.01529].

[385] C.K. Mishra, A. Kela, K.G. Arun and G. Faye, *Ready-to-use post-Newtonian gravitational waveforms for binary black holes with nonprecessing spins: An update*, *Phys. Rev. D* **93** (2016) 084054 [1601.05588].

[386] E. Poisson, *Gravitational waves from inspiraling compact binaries: The Quadrupole moment term*, *Phys. Rev. D* **57** (1998) 5287 [gr-qc/9709032].

[387] G. Ashton et al., *BILBY: A user-friendly Bayesian inference library for gravitational-wave astronomy*, *Astrophys. J. Suppl.* **241** (2019) 27 [1811.02042].

[388] I.M. Romero-Shaw et al., *Bayesian inference for compact binary coalescences with bilby: validation and application to the first LIGO–Virgo gravitational-wave transient catalogue*, *Mon. Not. Roy. Astron. Soc.* **499** (2020) 3295 [2006.00714].

[389] G. Ashton and C. Talbot, *B ilby-MCMC: an MCMC sampler for gravitational-wave inference*, *Mon. Not. Roy. Astron. Soc.* **507** (2021) 2037 [2106.08730].

[390] B. Zackay, L. Dai and T. Venumadhav, *Relative Binning and Fast Likelihood Evaluation for Gravitational Wave Parameter Estimation*, [1806.08792].

[391] K. Krishna, A. Vijaykumar, A. Ganguly, C. Talbot, S. Biscoveanu, R.N. George et al., *Accelerated parameter estimation in Bilby with relative binning*, [2312.06009].

[392] K. Chatziioannou, C.-J. Haster and A. Zimmerman, *Measuring the neutron star tidal deformability with equation-of-state-independent relations and gravitational waves*, *Phys. Rev. D* **97** (2018) 104036 [1804.03221].

[393] W. Kastaun and F. Ohme, *Finite tidal effects in GW170817: Observational evidence or model assumptions?*, *Phys. Rev. D* **100** (2019) 103023 [1909.12718].

[394] M. Aparicio Resco, A. de la Cruz-Dombriz, F.J. Llanes Estrada and V. Zapatero Castrillo, *On neutron stars in $f(R)$ theories: Small radii, large masses and large energy emitted in a merger*, *Phys. Dark Univ.* **13** (2016) 147 [1602.03880].

[395] E. Lope-Oter and A. Wojnar, *Constraining Palatini gravity with GR-independent equations of state for neutron stars*, *JCAP* **02** (2024) 017 [2306.00870].

[396] D.D. Doneva, C.J. Krüger, K.V. Staykov and P.Y. Yordanov, *Neutron stars in Gauss-Bonnet gravity: Nonlinear scalarization and gravitational phase transitions*, *Phys. Rev. D* **108** (2023) 044054 [2306.16988].

[397] E. Lope-Oter and F.J. Llanes-Estrada, *Maximum latent heat of neutron star matter independently of General Relativity*, *Phys. Rev. C* **105** (2022) L052801 [2103.10799].

[398] P.L. Espino, G. Bozzola and V. Paschalidis, *Quantifying uncertainties in general relativistic magnetohydrodynamic codes*, *Phys. Rev. D* **107** (2023) 104059 [2210.13481].

[399] E.R. Most, A. Motornenko, J. Steinheimer, V. Dexheimer, M. Hanauske, L. Rezzolla et al., *Probing neutron-star matter in the lab: Similarities and differences between binary mergers and heavy-ion collisions*, *Phys. Rev. D* **107** (2023) 043034 [2201.13150].

[400] F. Guercilena, D. Radice and L. Rezzolla, *Entropy-limited hydrodynamics: a novel approach to relativistic hydrodynamics*, *Comput. Astrophys. Cosmol.* **4** (2017) 3 [1612.06251].

[401] G. Doulis, S. Bernuzzi and W. Tichy, *Entropy based flux limiting scheme for conservation laws*, [2401.04770].

# Vita

## Aviral Prakash

Aviral Prakash obtained his Master's degree in Physics from the Indian Institute of Technology in Madras, India in the year 2018. As part of his master's thesis, he worked on the parameter estimation of binary black hole mergers under the supervision of Prof. Chandra Kant Mishra. In the Fall of 2018, he started at The Pennsylvania State University as a graduate student and in the following year, commenced research in the field of numerical relativity with Prof. David Radice. His research interests include numerical simulations of binary neutron star mergers, exploring the nature of dense nuclear matter formed in such mergers, and the development of numerical methods for simulating relativistic flows. In the fall of 2024, he is expected to start as an N3AS Postdoctoral fellow at The University of California Berkeley where he will be mentored by Prof. François Foucart from the University of New Hampshire. His selected publications include:

1. Detectability of QCD phase transitions in binary neutron star mergers: Bayesian inference with the next generation gravitational wave detectors
   **Aviral Prakash**, Ish Gupta, Matteo Breschi, Rahul Kashyap, David Radice, Sebastiano Bernuzzi, Domenico Logoteta, and B.S. Sathyaprakash,
   arXiv: 2310.06025 [gr − qc]; [astro − ph.HE]

2. Thermal Effects in Binary Neutron Star Mergers
   Jacob Fields, **Aviral Prakash**, Matteo Breschi, David Radice, Sebastiano Bernuzzi and André da Silva Schneider, *ApJL 952 L36*, arXiv: 2302.11359 [astro − ph.HE]

3. Revealing Phase Transition in Dense Matter with Gravitational Wave Spectroscopy of Binary Neutron Star Mergers
   Pedro Luis Espino, **Aviral Prakash**, David Radice and Domenico Logoteta, arXiv: 2301.03619 [astro − ph.HE]

4. Numerical relativity simulations of prompt collapse mergers: Threshold mass and phenomenological constraints on neutron star properties after GW170817
   Rahul Kashyap, Abhishek Das, David Radice, Surendra Padamata, **Aviral Prakash**, Domenico Logoteta, Albino Perego, Daniel A. Godzieba, Sebastiano Bernuzzi, Ignazio Bombaci, Farrukh J. Fattoyev, Brendan T. Reed and André da Silva Schneider, *Phys. Rev. D 105, 103022*, arXiv: 2111.05183 [astro − ph.HE]

5. Signatures of deconfined quark phases in binary neutron star mergers.
   **Aviral Prakash**, David Radice, Domenico Logoteta, Albino Perego, Vsevolod Nedora, Ignazio Bombaci, Rahul Kashyap, Sebastiano Bernuzzi, and Andrea Endrizzi, *Phys. Rev. D 104, 083029*, arXiv: 2106.07885 [astro − ph.HE]